

COLLECTED PAPERS
ON
QUANTUM OPTICS AND TECHNOLOGY

Volume 10
August 1994—July 1995

Professor
Motoichi OHTSU

TOKYO INSTITUTE OF TECHNOLOGY
Interdisciplinary Graduate School of Science and Engineering
4259 Nagatsuta, Midori-ku, Yokohama,
Kanagawa 226, JAPAN

各位殿

拝啓 時下ますますご清祥のこととお慶び申し上げます。

さて、このたび、前回に引き続きまして、最近の私どもの発表論文をまとめましたので、ここにお送り致します。よろしくご査収下されば幸いです。いずれも未熟な論文ばかりでございますので、ご意見、ご批評を賜ればと、お待ちしております。

(財) 神奈川科学技術アカデミー「フォトン制御」プロジェクトも順調に進展しており、フォトンSTMシステムの開発とナノ・フォトニクスへの展開、レーザ周波数/位相制御、に関して研究を遂行しております。今後ともご指導ご鞭撻のほど、よろしくお願い申し上げます。

敬具

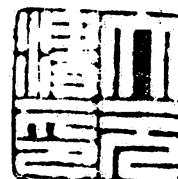
平成7年8月

東京工業大学

大学院・総合理工学研究科

電子システム専攻

大津 元一

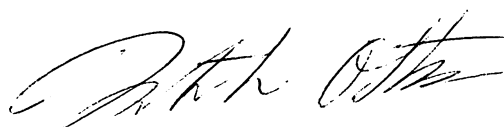


PREFACE

In order to realize the ultimate status of light and matter, M. Ohtsu tries to control spatial and temporal properties of light. The former corresponds to the research of photon scanning tunneling microscopy (photon STM) and its application to nano-fabrication which can open new era of nano-photonics. The latter corresponds to developing laser frequency/phase controlling technology. It should be pointed out that the photon STM is closely related to the quantum optics, atom manipulation, high density optical storage, biochemistry, and so on. And by this relationship with a variety of field, photon STM and near-field photonics exhibit rapid progresses. Further research will be done to realize novel nanometric materials and devices by using nano-structural optical probes of photon STM.

A "PHOTON CONTROL" project of Kanagawa Academy of Science and Technology (KAST)(*), directed by Ohtsu is also engaged in the research subjects described above. Twelve research staffs including three visiting scientists from industries and three visiting fellows from Sweden, Italy, and France have obtained several results on photon STM and laser frequency/phase control. Their details are reviewed in this issue of the COLLECTED PAPERS.

August 1994



Motoichi OHTSU

(*) Address:

Photon Control Project,
Kanagawa Academy of Science and Technology,
KSP East, Rm 408, 3-2-1 Sakado, Takatsu-ku,
Kawasaki-shi, Kanagawa 213, Japan

Phone: +81-44-819-2071

Fax: +81-44-819-2072

MEMBERS

(From April 1, 1995)

Professor

Motoichi OHTSU (Dr. Eng.)^{a)}

Research Associate

Motonobu KOUROGI (Dr. Eng.)^{b)}

Graduate Students (Doctor Candidates)

Yoshinari AWAJI (M. Eng.)

Yasunori TODA (M. Eng.)

Mikio KOZUMA (M. Eng.)

Shuji SAYAMA (M. Eng.)

Andrei Vasilyevich ZVYAGIN (M. Sci.)

Graduate Students (Master Course)

Kazuhiro IMAI (B. Eng.)

Takeshi NAKATA (B. Sci.)

Takuya MATSUMOTO (B. Eng.)

Keiji SAKAKI (B. Eng.)

Shintaro TAKEHARA (B. Eng.)

Takashi YATSUI (B. Eng.)

Yoshitaka YOKOYAMA (B. Sci.)

Undergraduate Students

Masaru HATAKEHAMA

Taro KOBAYASHI

Kazumi WATANABE

Visiting Scientists

Sudong JIANG

Wonho JHE (July 10, 1995 - Aug. 10, 1995)^{c)}

Kwan-il LEE (July 10, 1995 - Sept. 8, 1995)^{c)}

Secretaries

Sanae OKAMOTO

Kaoru OGURA

Maki SASAKI (July 1, 1995 - July 28, 1995)

- a) Also with Kanagawa Academy of Science and Technology
(Director, "Photon Control" Project)
- b) Also with Kanagawa Academy of Science and Technology
(Research staff member, "Photon Control" Project)
- c) Permanent affiliation: Dept. of Phys, Seoul National Univ.,
Seoul, Korea

LIST OF PAPERS

[1] PHOTON CONTROL IN THE SPATIAL DOMAIN

(a) Journal Papers

[1] M. Ohtsu, "Progress of High-Resolution Photon Scanning Tunneling Microscopy Due to a Nanometric Fiber Probe", J. Lightwave Technol., Vol.13, No.7, July 1995, pp.1200-1221 (Invited paper)

[pp.1 - 22]

[2] H. Ito, K. Sakaki, T. Nakata, W. Jhe, and M. Ohtsu, "Optical potential for atom guidance in a cylindrical-core hollow fiber", Opt. Commun., Vol.115, March, 1995, pp.57-64

[pp.23 - 30]

[3] Y. Toda and M. Ohtsu, "High Spatial Resolution Diagnostics of Optical Waveguides Using a Photon-Scanning Tunneling Microscope", IEEE Photonics Technol. Lett., Vol.7, No.1, Jan. 1995, pp.84-86

[pp.31 - 33]

[4] M. Ohtsu, "Photon Scanning Tunneling Microscopes", Jpn. J. Optics, Vol.23, No.12, Dec. 1994, pp.733-739 (Review paper, in Japanese)

[pp.34 - 40]

[5] W. Jhe, M. Ohtsu, H. Hori, and S.R. Friberg, "Atomic Waveguide Using Evanescent Waves Near Optical Fibers", Jpn. J. Appl. Phys., Vol.33, Part 2, No.12A, Dec. 1994, pp.L1680-L1682

[pp.41 - 43]

[6] T. Pangaribuan, S. Jiang, and M. Ohtsu, "Highly Controllable Fabrication of Fiber Probe for Photon Scanning Tunneling Microscope", Scanning, Vol.16, No.6, Dec. 1994, pp.362-367

[pp.44 - 49]

[7] M. Ohtsu, "Photon Scanning Tunneling Microscope", Parity, Vol.9, No.11, Nov. 1994, pp.60-65 (Review paper, in Japanese)

[pp.50 - 55]

(b) International Conferences

[1] R. Uma Maheswari, M. Ohtsu, H. Tatsumi, Y. Katayama, "High resolution imaging of subsellular structures of neurons by an illumination mode photon scanning tunneling microscope", Technical Digest, Conference on Lasers and Electro-Optics/Pacific Rim'95, pp.125 - 126, July 1995, Makuhari, Chiba

[pp.56 - 57]

[2] M. Ohtsu, "Photon scanning tunneling microscopy: from imaging to fabrication and manipulation", Technical Digest, Conference on Lasers and Electro-Optics/Pacific Rim'95, p.144, July 1995, Makuhari, Chiba (Tutorial)

[p.58]

[3] Y. Toda, M. Kouroggi, Y. Nagamine, Y. Arakawa, M. Ohtsu, "Near-field optical properties of GaAs quantum dot structures measured by photon scanning tunneling microscope", Technical Digest, Conference on Lasers and Electro-Optics/Pacific Rim'95, pp.165-166, July 1995, Makuhari, Chiba

[pp.59 -60]

[4] W. Jhe and M. Ohtsu, "High-resolution photon scanning tunneling microscopy and its quantum optical aspects", Twelfth International Conference on Laser Spectroscopy, June 1995, Island of Capri, Italy (Invited)

[pp.61 - 65]

[5] T. Saiki, S. Mononobe, and M. Ohtsu, "Nanometric integrating tip: enhanced sensitivity of fluorescence detection in photon STM", Technical Digest, Quantum Electronics and Laser Science Conference, pp.84-85, May 1995, Baltimore, MA

[pp.66 - 67]

[6] H. Ito, K. Sakaki, T. Nakata, W. Jhe, and M. Ohtsu, "Atomic waveguide using evanescent waves in a hollow fiber", Technical Digest, Quantum Electronics and Laser Science Conference, pp.155 - 156, May 1995, Baltimore, MA

[pp.68 - 69]

[7] M. Naya, R. Uma Maheswari, R. Micheletto, S. Mononobe, and M. Ohtsu, "High resolution imaging of bio-samples by a photon scanning tunneling microscope with an apertured probe", The Third Int. Conf. on Near Field Optics and Related Technol., European Opt. Soc., Topical Meeting Digest Series, Vol.8, pp.67-68, May 1995, Brno, Czech

[pp.70 - 71]

[8] S. Mononobe, M. Naya, R. Uma Maheswari, T. Saiki, and M. Ohtsu, "Fabrication technique of pencil-type fiber probes and nanometric apertures for photon scanning tunneling microscope", The Third Int. Conf. on Near Field Optics and Related Technol., European Opt. Soc., Technical Meeting Digest Series, Vol.8, pp.105 -106, May 1995, Brno, Czech

[pp.72 - 73]

[9] T. Matsumoto and M. Ohtsu, "Three dimensional nanophotolithography for fabricating a nano-apertured probe and a

nanometric super cup", The Third Int. Conf. on Near Field Optics and Related Technol., European Opt. Soc., Technical Meeting Digest Series, Vol.8, pp.107-108, May 1995, Brno, Czech

[pp.74 - 75]

[10] T. Saiki, S. Mononobe, and M. Ohtsu, "High-resolution fluorescence imaging with enhanced sensitivity due to short-range electromagnetic interaction in photon STM", The Third Int. Conf. on Near Field Optics and Related Technol., European Opt. Soc., Technical Digest Series, Vol.8, pp.127-128, May 1995, Brno, Czech

[pp.76 - 77]

[11] H. Ito, K. Sakaki, T. Nakata, W. Jhe, and M. Ohtsu, "Optical guidance of neutral atoms using evanescent waves in a cylindrical-core hollow fiber", The Third Int. Conf. on Near Field Optics and Related Technol., European Opt. Soc., Technical Digest Series, Vol.8, pp.161-162, May 1995, Brno, Czech

[pp.78 - 79]

[12] M. Ohtsu, "High resolution photon scanning tunneling microscopy due to nanometric fiber probe", Abstracts of International Symposium on Ultra Materials for Picotransfer, p.90, March 1995, Makuhari, Chiba (Invited)

[p.80]

[13] R. Uma Maheswari, M. Naya, M. Ohtsu, H. Tatsumi, and Y. Katayama, "A high resolution photon scanning tunneling microscope for observation of sub cellular structures of neurons", Abstracts of the Second Hamamatsu Int. Symp. on Biomolecular Mechanisms and Photonics: Cell-cell Communication, p.1, Feb. 1995, Hamamatsu, Shizuoka

[p.81]

[14] M. Ohtsu, "Progress of nanometric resolution photon scanning tunneling microscopy", Abstracts of the Second Hamamatsu Int. Symp. on Biomolecular Mechanisms and Photonics: Cell-cell Communication, p.13, Feb. 1995, Hamamatsu, Shizuoka (Invited)

[p.82]

[15] M. Naya, S. Mononobe, R. Uma Maheswari, T. Saiki, M. Ohtsu, "Imaging experiments of bio-samples by a photon scanning tunneling microscope with an apertured probe", Proceedings of SPIE, Vol. 2384, Scanning Probe Microscopies III, Feb. 1995, San Jose, CA

[pp.83 - 90]

[16] M. Ohtsu, "Progress of high resolution photon scanning tunneling microscope with a nanometric fiber probe", Conf. Proceedings, The Tenth Optical Fibre Sensor Conference, pp.203-210, Oct. 1994, Glasgow, Scotland (Invited)

[pp.91 - 98]

[17] Y. Toda and M. Ohtsu, "Photon-scanning tunneling microscopy for diagnosing propagating characteristics of optical waveguides", Opt. Soc. Am. Annual Meeting, paper number TuS5, Oct. 1994, Dallas, Texas

[p.99]

[18] R. Uma Maheswari, S. Mononobe, M. Naya, T. Saiki, and M. Ohtsu, "Fabrication of a fiber probe with nano-aperture for photon scanning tunneling microscope(PSTM)", Opt. Soc. Am. Annual Meeting, paper number ThEEE2, Oct. 1994, Dallas, Texas

[p.100]

[2] PHOTON CONTROL IN THE FREQUENCY DOMAIN

(a) Journal Papers

[1] W. Wang and M. Ohtsu, "Generation of Frequency-Tunable Light and Frequency Reference Grids Using Diode Lasers for One-Petahertz Optical Frequency Sweep Generator", IEEE J. Quantum Electron., Vol.31, No.3, March, pp.456-467

[pp.101 - 112]

[2] M. de Labachellerie, K. Nakawaga, Y. Awaji, and M. Ohtsu, "High-frequency-stability laser at 1.5 um using Doppler-free molecular lines", Opt. Lett., Vol.20, No.6, March 1995, pp.572-574

[pp.113 - 115]

[3] T. Saito, M. Kouroggi, and M. Ohtsu, "A Waveguide-Type Optical-Frequency Comb Generator", IEEE Photonics Technol. Lett., Vol.7, No.2, Feb. 1995, pp.197-199

[pp.116 - 118]

[4] K. Nakagawa, M. de Labachellerie, Y. Awaji, M. Kouroggi, T. Enami, and M. Ohtsu, "Highly precise 1-THz optical frequency-difference measurement of 1.5-um molecular absorption lines", Opt. Lett., Vol.20, No.4, Feb. 1995, pp.410-412

[pp.119 - 121]

[5] A.M. Akulshin, K. Nakagawa, and M. Ohtsu, "Frequency Chain Towards the Ca Intercombination Line Based on Laser Diodes: First Step", Appl. Phys. Vol.B58, 1994, pp.529-532

[pp.122 - 125]

[6] M. Kouroggi and M. Ohtsu, "A frequency-comb generator in

optical region", Oyo Buturi (A monthly publication of The Japan Soc. Appl. Phys.), Vol.63, No.9, Sept. 1994, pp.915-918 (Review paper, in Japanese)

[pp.126 - 129]

[7] K. Nakagawa, A.S. Shelkovnikov, T. Katsuda, and M. Ohtsu, "Absolute frequency stability of a diode-laser-pumped Nd:YAG laser stabilized to a high-finesse optical cavity", Appl. Opt., Vol.33, No.27, Sept. 1994, pp.6383-6386

[pp.130 - 133]

[8] M. Ohtsu, "Frequency Control of Semiconductor Lasers", Rev. of Laser Eng., Vol.22, No.8, Aug. 1994, pp.610-616 (Review paper, in Japanese)

[pp.134 - 140]

[9] A. M. Akul'shin and M. Ohtsu, "Pulling of the emission frequency of an injection laser by Doppler-free absorption resonances in an intracavity cell", Quantum Electronics, Vol.24, No.7, 1994, pp.613-614

[pp.141 - 142]

(b) International Conferences

[1] T. Fujii, T. Nayuki, K. Nemoto, M. Kouroggi, and M. Ohtsu, "Sideband-locked stabilized semiconductor laser for accurate frequency tunability", Technical Digest, Conference on Lasers and Electro-Optics/Paricic Rim'95, pp.215-216, July 1995, Makuhari, Chiba

[pp.143 - 144]

[2] T. Saitoh, E. Durand, M. Kouroggi, and M. Ohtsu, "A frequency

resettable semiconductor laser system for 1.2 THz frequency span at 1.5 micron wavelength", Technical Digest, Conference on Lasers and Electro-Optics/Pacific Rim'95, p.255, July 1995, Makuhari, Chiba

[p.145]

[3] M. Kouroggi, M. Ohsu, and T. Saito, "Nonlinear frequency conversion and comb generation for stable reference grids in the visible and near-infrared region", Technical Digest, Conference on Lasers and Electro-Optics, p.404, May 1995, Baltimore, MA (Invited)

[p.146]

[4] T. Saitoh, E. Durand, M. Kouroggi, and M. Ohtsu, "Waveguide type optical frequency grid generator", Proceedings of SPIE, Vol.2378, Laser Frequency Stabilization and Noise Reduction, Feb. 1995, San Jose, CA

[pp.147 - 156]

[5] M. Ohtsu, "An optical-frequency comb generator for stable frequency reference grids and accurate frequency counting", Opt. Soc. Am., Annual Meeting, paper number TuJ1, Oct. 1994, Dallas, Texas (Invited)

[p.157]

[6] M. de Labachellerie, K. Nakagawa, H. Sasada, M. Ohtsu, "1.5-um laser diode optical-frequency standards using sub-megahertz molecular saturated-absorption line", Opt. Soc. Am., Annual Meeting, paper number TuJ2, Oct. 1994, Dallas, Texas (Invited)

[p.157]

PUBLISHED BOOKS

- [1] M. Ohtsu, Modern Optical Science, Vol.I (214 pages),
Asakura Shoten Publ., Tokyo, Oct. 1994 (in Japanese)
- [2] M. Ohtsu, Modern Optical Science, Vol.II (191 pages),
Asakura Shoten Publ., Tokyo, Dec. 1994 (in Japanese)

COOPERATION PROGRAMS

The following three programs were supported by JRDC (Research Development Corporation of Japan) :

- [1] Development of a commercial "Passive Ring Resonator-Type Fiber Gyroscope" based on Ohtsu's patent, with Tokyo Koku Keiki, Co. Ltd. (1991 - 1994)
- [2] Development of a commercial "LD-pumped Rubidium Atomic Clock" based on Ohtsu's patent, with Anritsu Co. Ltd. (1991 - 1994)
- [3] Pre-research program on "Atomic Scale Electron/Photon Systems", (Dec. 1994 - March 1995)

[1]

PHOTON CONTROL IN THE SPATIAL DOMAIN



Progress of High-Resolution Photon Scanning Tunneling Microscopy Due to a Nanometric Fiber Probe

Motoichi Ohtsu, *Senior Member, IEEE*

(Invited Paper)

Abstract—The present status of a photon scanning tunneling microscope (PSTM) and its application are reviewed. In order to realize a nanometric apertured fiber probe, a highly reproducible chemical etching process was developed to realize a sharpened fiber with the cone angle and tip diameter as small as 14° and 3 nm, respectively. The possibility of tailoring the shapes of the sharpened fibers was presented. Chemical etching and nanometric photolithography were developed to fabricate a metallic aperture with a diameter of 30 nm (or even smaller) on the sharpened fiber tip. Imaging experiments with biological specimens were carried out by operating the PSTM in the collection mode and illumination mode geometries. Dependencies of these images on the polarization state of the incident light were found, and a resolution of 10 nm or even smaller was achieved. Nondestructive inspection of dielectric optical waveguides with subwavelength resolution was proposed by presenting the diagnosed results of a proton-exchanged LiTaO₃ waveguide. Possibilities of diagnosing nanometric active photonic devices were also demonstrated through imaging experiments of semiconductor quantum dots. Experiments on fluorescence detection from dye-doped nanometric polystyrene spheres confirmed the enhanced efficiency of coupling of the fluorescence to the fiber tip, and this was attributed to the spatially inhomogeneous spontaneous emission due to the short-range electromagnetic interaction between the sphere and probe tip. To demonstrate the possibilities of nanometric fabrication, high density optical storage, especially the photon-mode storage, was demonstrated to realize a stored circular pit of 100 nm diameter on an organic thin film. As an ultimate goal of fabrication to explore the future technology of atomic-level material processing, an atom guide using a hollow fiber and atom trapping by the illumination mode PSTM were proposed to control the thermal motion of freely flying atoms in vacuum. The concept of a virtual photon based on an intuitive modeling of the localized evanescent light was introduced to provide a semiclassical theory of the PSTM. Transfer functions of the PSTM were calculated by using this model, which agreed qualitatively with the experimental results.

I. INTRODUCTION

DESPITE the common use of optical microscopes for diagnosing photonic and electronic devices, rapid progress of their high integration requires drastic improvements in the performance of the optical microscope. A photon scanning tunneling microscope (PSTM) has been developed recently

Manuscript received December 24, 1994.

The author is with the Interdisciplinary Graduate School of Science and Engineering, Tokyo Institute of Technology, Yokohama 226, Japan, and the "Photon Control" Project, Kanagawa Academy of Science and Technology, Kawasaki 213, Japan.

IEEE Log Number 9412276.

to break through this diffraction-limit of the resolution of the conventional optical microscopes in order to achieve nanometric resolution.

The PSTM can be considered as one member of the scanning probe microscope (SPM) family because a scanning probe is used to scatter or generate an evanescent light. One may think that the principle of operation of a PSTM is different from that of other SPM's, such as a scanning tunneling microscope (STM) and an atomic force microscope (AFM) because the PSTM measures the evanescent light while, e.g., STM and AFM measure the tunneled electrons and atomic forces, respectively. However, as will be described in Section VII, the principle of operation of the PSTM can be described in the common framework of other SPM's.

The PSTM has several advantages, such as operation capabilities in different environments (including air, liquid, etc.); possibilities of observing nonconductive materials and of measuring optical spectral properties; and so on. Furthermore, it can also be used for nanometric fabrication and manipulation. Because of these advantages, studies on the PSTM have been progressing rapidly in recent years.

Since the proposal of PSTM about 60 years ago [1], experiments have been carried out by using microwaves [2]. Experiments in the optical region started in the 1980's by several groups including the author's [3]. Theoretical investigations based on the electromagnetic theory have also been developed [4]. The principal reason for the success in the optical region after a half-century delay could be the development of the nanometric probe fabrication technologies. Thus, the PSTM study could be characterized as a novel field of optics and photonics which is supported by nanofabrication technology. Additional reasons could be the techniques used for scanning the probe and of processing the images which were transferred from those of other SPM's developed in the 1980's.

The PSTM can be considered as one of the applications of the optical fiber sensor-based systems because the most reliable PSTM probe is fabricated from an optical fiber. However, it can also be considered as an exotic fiber sensor because it deals with the nonpropagating evanescent light while conventional fiber sensors deal with propagating lights. Even though the PSTM is an exotic fiber sensor, it can introduce a new field of fiber sensors because future technologies require high resolution in measurement and fabrication.

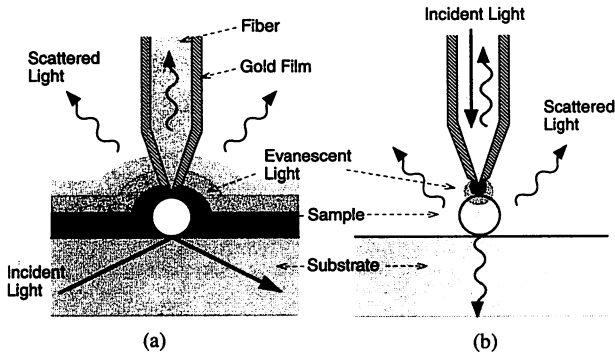


Fig. 1. Configurations of the two modes of operation of the photon scanning tunneling microscope (PSTM): (a) collection mode (C-mode); (b) illumination mode (I-mode).

Listed below are possibly the most essential problems to be solved for the growing field of PSTM study, which are especially indispensable for contribution to optical fiber sensors, photonics, and quantum optics.

- 1) Fabrication of high-performance probes, and improvement in the resolution of imaging by using these probes.
- 2) Studies of novel physical phenomena, e.g., quantum optical phenomena, which can be found by improving the resolution of imaging experiments.
- 3) Atom manipulation.
- 4) Processing and fabrication of nanometric photonic devices, and exploration of novel materials for these devices.
- 5) Development of theory.

This paper reviews the current status, and presents a future outlook of the PSTM study by describing mainly the results of recent studies related to above-mentioned problems. The next section describes the principle of operation of the PSTM. Section III reviews the fabrication technologies of probe. Section IV describes the PSTM system, and demonstrates the results of imaging experiments, in which the observations of quantum optical phenomena are included. Section V reviews the experimental results of high-density optical storage—an apt example of nanometric fabrication. In Section VI, the control of thermal motion of gaseous atoms in vacuum is proposed, and calculated results will be given. A novel theoretical model of the PSTM will be presented in Section VII. Section VIII gives the summary and future outlook.

II. PRINCIPLE OF OPERATION

The basic parts of the PSTM are shown in Fig. 1(a) and (b). Fig. 1(a) represents the configuration of the collection mode (C-mode), in which a nanometric sample is irradiated by a propagating light to generate an evanescent light whose power is localized on the surfaces of the sample and the substrate. Although the evanescent light is generated irrespective of the incident angle of the propagating light [5], it is most convenient if the light is incident into the substrate surface under the condition of total reflection because the evanescent light is selectively generated suppressing the transmitted and scattered lights. Generated evanescent light is then scattered by the probe, and the detected power of the scattered light is displayed as a function of the position of the scanned

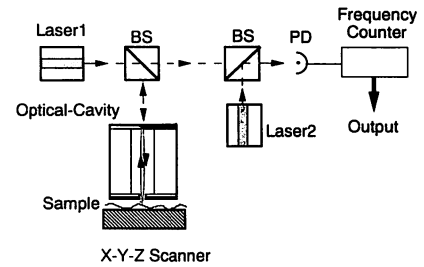


Fig. 2. The schematic explanation of the reflection-resonance-type PSTM, in which the magnitude of frequency shift, due to the phase change of the optical cavity with a subwavelength aperture used as a probe, is measured by the heterodyne detection method. Laser 1: Reference laser. Laser 2: The laser which is phase-locked to the optical cavity.

probe to represent a three-dimensional distribution of the evanescent light power, which provides information about three-dimensional characteristics of the sample. Since the resolution is limited by the volume of the scattered light, i.e., the size and shape of the probe tip, a high-resolution beyond the diffraction-limited value can be realized when the probe tip is smaller than the optical wavelength.

Fig. 1(b) represents the configuration of the illumination mode (I-mode), where the evanescent light is generated from the subwavelength aperture at the probe tip to shine the sample. The evanescent light is then scattered by the sample to be detected and displayed as the function of the position of the scanned probe. The resolution is also determined by the size and shape of the probe tip.

The advantages of the C-mode are that the polarization state of the incident propagating light can be adjusted, and the rapid decrease of the evanescent light power normal to the surface can be used to control the sample-probe separation by maintaining the detected light power constant (see Figs. 18 and 20).

The advantages of the I-mode are that the sample can be selectively illuminated to realize the high contrast of imaging of the sample, and that it can be used for nanometric fabrication and atom manipulation (refer to Sections V and VI, respectively). However, the problems are: the polarization state of the evanescent light depends on the aperture structure in a complicated manner, and an additional auxiliary servo-control loop is required to control the sample-probe separation (refer to Section IV-A).

It should be noted that the detected light power is low and decreases with decreasing the size of the probe tip, which means that the detection sensitivity is not compatible with the resolution. In order to improve the detection sensitivity, a method of measuring the phase change of the lightwave has been proposed instead of measuring the light power. Fig. 2 explains schematically the principle of operation, which is called a reflection-resonance-type PSTM [6]. Here, the evanescent light generated from the subwavelength aperture on a small optical cavity facet is scattered by the sample. Due to this scattering, the complex optical impedance of the cavity facet varies slightly, which shifts the cavity resonance frequency. Even though this frequency shift is small, it can be measured by the heterodyne detection method between a reference laser and the laser which is phase-locked to the

cavity. The magnitude of the frequency shift obtained as the function of the position of the scanned optical cavity represents the three-dimensional image of the sample surface. Since frequency shift as low as 4×10^{-4} Hz has been detected by the heterodyne-type phase locking technique [7], this method could be more sensitive than the power detection method. Theoretical estimation confirmed that the shot-noise-limited lateral resolution of 1/400 times the wavelength can be expected, and preliminary experiments for confirming the cavity resonant frequency shift has been carried out [6], [8].

A similar experiment has also been carried out in the microwave frequency region by using an interferometer to achieve a resolution of 1/4000 times the wavelength [9]. A future problem to be solved is to fabricate high finesse cavities with subwavelength aperture.

The PSTM has also been called a scanning near-field optical microscope (SNOM) because the probe is scanned in the near-field region of the sample surface to scatter the evanescent light. However, this microscope is called a PSTM in this paper because physically essential features of the PSTM can be understood by discussing it in the same framework of other SPM's as will be claimed in Section VII.

III. FABRICATION OF PROBES

Several methods have been proposed to fabricate the probe, which is the most essential device of the PSTM. The fabrication methods are, for example, pulling heated glass capillaries [10] and sharpening quartz rods or optical fibers by chemical etching [11], [12]. However, they have not yet achieved sufficiently high reproducibility and, moreover, the tip diameter of the fabricated probe has not been small enough for resolving the nanometric-scale structure of the sample. To solve these problems, a selective etching method widely used in semiconductor VLSI chip fabrication was applied to sharpen a single-mode fiber by using a buffered hydrofluoric (HF) acid as an etching solution [13]. Subsections A and B describe the processes of sharpening the fiber and forming a subwavelength aperture, respectively. Subsection C reviews fabrication and performance of other novel fiber probes.

A. Sharpening the Fiber

A fiber can be sharpened by utilizing the difference in the etching rates between the core and cladding in a selective etching solution of a buffered HF acid. Advantages of this method are high reproducibility, mass production, capability of tailoring the shape of the resulting fiber by controlling etching condition, and so on—and are hence compatible to industrialization.

A buffered HF acid with composition of 40% (weight%) NH_4F , 50% HF, and H_2O was used for etching. Here, NH_4F was used to decrease the dissolution rate of the GeO_2 -doped core, which is explained as follows: the chemical reaction of SiO_2 in the cladding with HF in water solution produces H_2SiF_6 , and that of GeO_2 in the core produces H_2GeF_6 . As the next step, they react with NH_3 , ionized from NH_4F to produce $(\text{NF}_4)_2\text{SiF}_6$ and $(\text{NH}_4)_2\text{GeF}_6$, respectively. The difference in the solubility of the $(\text{NH}_4)_2\text{SiF}_6$ and $(\text{NH}_4)_2\text{GeF}_6$ generated

in the etching solution leads to the difference in the etching rate between the core and cladding. Therefore, by adjusting the composition of the etching solution, doping ratio of GeO_2 , and the etching time, sharpened fibers with various cone angles and tip diameters can be realized.

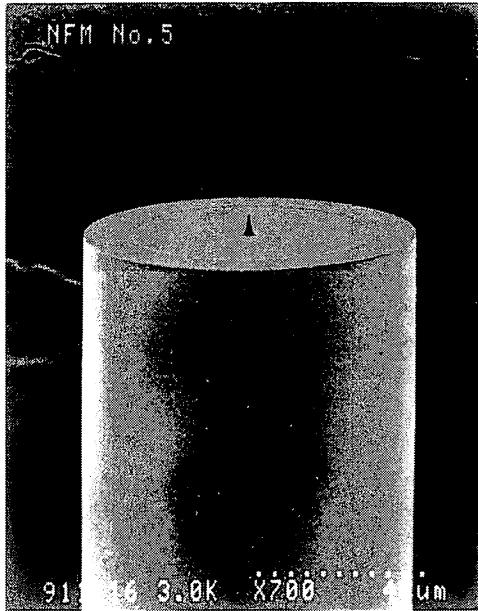
Although the above discussion attributed the reason for sharpening the fiber only to the difference in etching rates between the GeO_2 -doped silica core and the pure silica cladding, it is still uncertain why the fiber with uniformly GeO_2 -doped core was sharpened and nanometric tip diameter was realized. One of the other reasons may be the existence of a binding energy distribution of the Si–O–Ge network along the core radius, resulting from the residual stress which is generated by the rapid cooling during the fiber fabrication processes [14]. During this etching process, polar materials such as H_2O could change the dissolution rate along the core radius. However, since it has not yet been made clear whether the nanometric silica maintains characteristics of amorphous (see Subsection A-3-b), more intensive studies on properties of nanometric silica could be required.

Several experimental results are reviewed below (details have been reported in [15] and [16]).

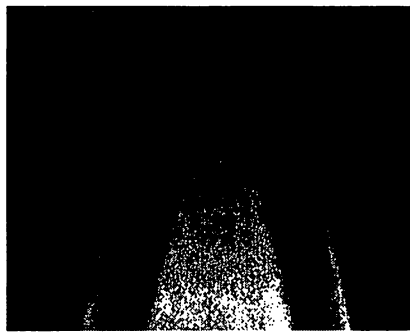
1) *One-step etching*: Since the buffering condition was controlled by varying the volume ratio X of NH_4F , the composition of the used etching solution will be identified by the value of X in this paper, while maintaining the volume ratio of HF to H_2O at 1 : 1. The solution temperature was maintained at $22 \pm 1^\circ\text{C}$. By introducing the fiber into this solution, the core was selectively sharpened. A typical SEM (scanning electron microscope) micrograph of a fiber having 23 mol% GeO_2 -doped core after etching in $X = 10$ for a duration of 120 min is shown by Fig. 3(a). The tip diameter, i.e., the curvature diameter of the fiber tip can be estimated to be around 3 nm from Fig. 3(b), which is even smaller than that of the conventional pyramid tips attached to cantilevers used in the AFM; and the cone angle is around 20° . Although it has been reported that the cone angle θ_1 depended only on the doping ratio [17], we found that θ_1 depended also on X , especially in the case of the fiber with the highly GeO_2 -doped core. This dependency is shown by Fig. 4 for several fibers of different doping ratios. It should be noted that the values of θ_1 for curves A, C, and D can be larger than 180° for $X < 1.6$. This means that the core is etched at a rate faster than that of the cladding, resulting in a fiber with concave facets. However, with increasing value of X , θ_1 decreases, and for $X > 4$, θ_1 is almost constant and it is independent of slight fluctuations in the composition of solution as θ_1 will be determined by doping ratio. The minimum of θ_1 , as small as 14° , was realized for the case of curve E. In the following discussions, the core of our fibers has a doping ratio around 23 mol%.

Finally, it is worth mentioning that we have succeeded in realizing identical nanometric tips (see [16], Fig. 2) by etching a dual-core fiber, i.e., two cores in a common cladding.

2) *Two-step etching*: As seen from Fig. 3(a), the cladding face has a diameter of $90 \mu\text{m}$, in contrast to the length of sharpened core of about $10 \mu\text{m}$. Due to this large difference, in practical situations of scanning a sample with this probe, there are chances for the sample to be hit by the large cladding face,



(a)



(b)

Fig. 3. (a) An SEM micrograph of the fiber sharpened by the one-step etching with cladding diameter of $90\ \mu\text{m}$. (b) A magnified SEM micrograph of the fiber tip. The original tip with the diameter of $3\ \text{nm}$, coated with 7-nm -thick Pt/Pd, is covered by contamination C_t with the thickness of $22\ \text{nm}$.

and hence damage caused to the sample. In order to overcome this difficulty, a two-step etching process was proposed: in the first step, the cladding diameter is reduced; in the second step, the core is sharpened by the method discussed above. In the first step, an etching solution, with X being 1.7 , was used in order to have equal etching rates for the cladding and the core. It was found that the reduction rate of the cladding diameter was $0.95\ \mu\text{m}/\text{min}$ for the fiber with $23\ \text{mol}\%$ GeO_2 -doped core.

The second step involves the sharpening of the core by the one-step etching method described in Subsection A-1, with values of X being greater than 3 . Due to this step, an additional decrease of the cladding diameter by about $20\ \mu\text{m}$ was introduced, with fluctuations of final cladding diameters etched under the same condition being as small as $1.5\ \mu\text{m}$. Fig. 5 shows the SEM micrograph of the sharpened fiber with a cladding diameter of $7.9\ \mu\text{m}$, which was reduced from the original value of $125\ \mu\text{m}$. However, when reducing the diameter of cladding, one should remember to maintain the

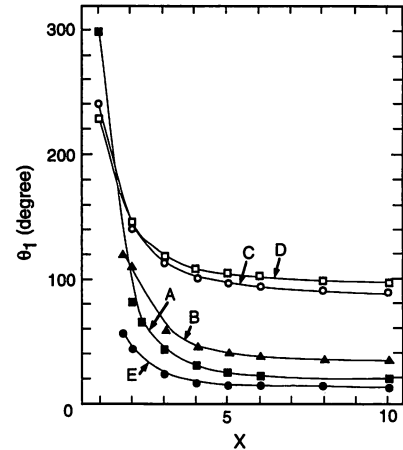


Fig. 4. Dependence of cone angle θ_1 of the sharpened fiber on the volume ratio X of NH_4F . Curves A, B, C, and D are the results for fibers with a GeO_2 -doped silica cores with ratios of 23 , 14 , 8.5 , and $3.6\ \text{mol}\%$, respectively. Curve E represents the result for the fiber with $22\ \text{mol}\%$ GeO_2 -doped silica core and $2.1\ \text{mol}\%$ F-doped silica cladding.

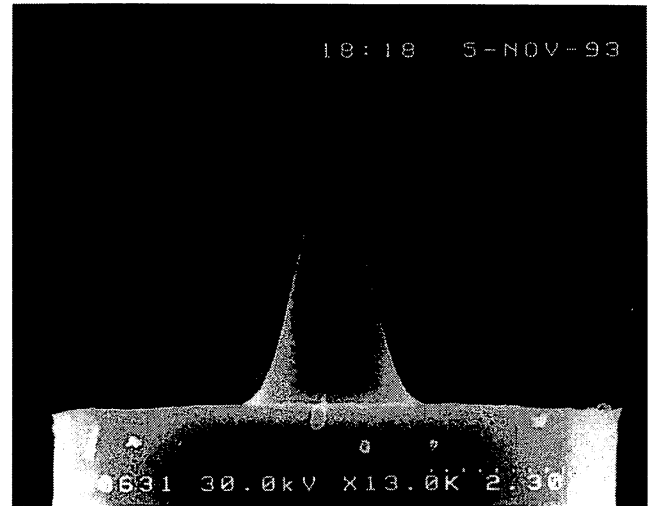


Fig. 5. An SEM image of the fiber sharpened by the two-step etching. The cladding diameter has been decreased to $7.9\ \mu\text{m}$.

optical transmission loss at a minimum; the cladding diameter has to be at least twice the core diameter.

Apart from solving practical problems while scanning, the two-step etching makes the fiber flexible due to the reduced cladding diameter, and hence it can be very easily used as a cantilever in AFM, which is used in the I-mode PSTM for servo-control.

3) *Fabrication of other sharpened fibers:* Next, fabrication processes of a pencil-type fiber and a flattened-top fiber are reviewed.

a) *A pencil-type fiber:* The sharpened fibers described in Sections I-A-1 and I-A-2 have a discontinuous step at the boundary between the core and cladding. This could lead to the problem of improper coating of metallic film around this boundary when used for fabricating subwavelength apertures (refer to Section III-B).

In order to solve this, a pencil-type fiber has been fabricated by a four-step etching, explained schematically in Fig. 6 [18]. In this process, the first step tapers off the cladding. Here,

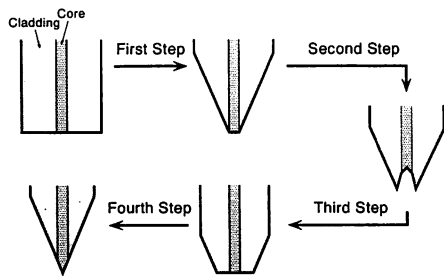
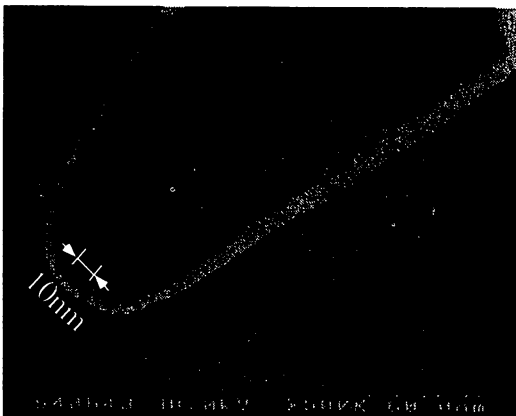


Fig. 6. Schematic explanation of the four-step etching process for fabricating a pencil-type fiber.



(a)



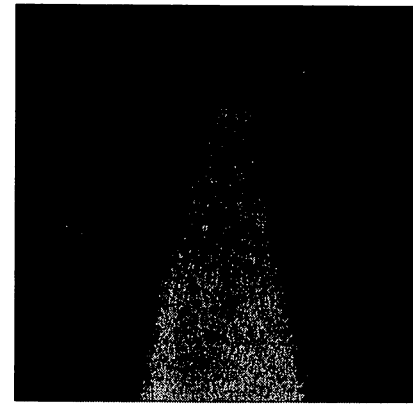
(b)

Fig. 7. (a) An SEM micrograph of the pencil type fiber. (b) A magnified SEM micrograph of (a).

to avoid etching of the cladding by the vapor of the etching solution, a layer of silicon oil was spread over the etching solution. In the next step, by etching in HF acid alone, the core is etched faster, with the result of a dip in the core. The third step simultaneously makes the ends of core and tapered cladding flat. Here, the value of X need not be accurately adjusted, as the requirement is only to etch away the cladding peaks on either sides of the core valley. The fourth step sharpens the core by the same process as in Section A-1.

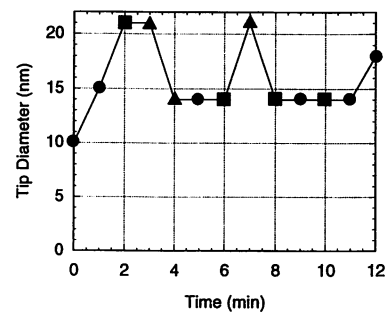
Fig. 7(a) and (b) shows the SEM image of the pencil-type fiber and its magnified image, respectively. Here, the tip diameter is smaller than 10 nm.

b) A flattened-top fiber: Next, we discuss the fabrication of a fiber with a nanometric flat top by a three-step etching



60nm

(a)



(b)

Fig. 8. (a) An SEM micrograph of a flattened-top fiber. (b) Variation of tip diameter and shape as a function of etching time. Closed circles, squares, and triangles represent rounded, flattened, and intermediate shapes of the fiber tips, respectively.

method. Although this type of fiber has been previously fabricated by the heating and pulling method [19], the present etching method can realize higher reproducibility and smaller size.

This is fabricated by a further etching of a sharpened fiber fabricated by two-step etching as discussed in Subsection A-2 for about 2 min in 10 times diluted solution of $X = 10$. The result is shown in Fig. 8(a), and it has a trapezoidal top in contrast to Figs. 3(b) or 7(b) which have a triangular top. By this method, a trapezoidal cross section as small as 15–20 nm could be realized [20]. The flattened-top fibers could be advantageously used for fabricating a subwavelength aperture by coating a gold film on sides of the trapezoid and for fixing dye molecules on the top to realize a super-tip (refer to Section III-C).

It has been found that the cross-sectional shape of the top of the fiber varied between trapezoidal and triangular shapes almost cyclically, and this variation is shown in Fig. 8(b). The origin of such a pseudoperiodic variation is not found straightforwardly from the knowledge of the etching process of bulky amorphous silica glass. Since the nanometric top of the fiber core is composed only of several hundreds of atoms, it may have different properties from that of bulk amorphous material, and further studies of nanometric properties of glass are required.

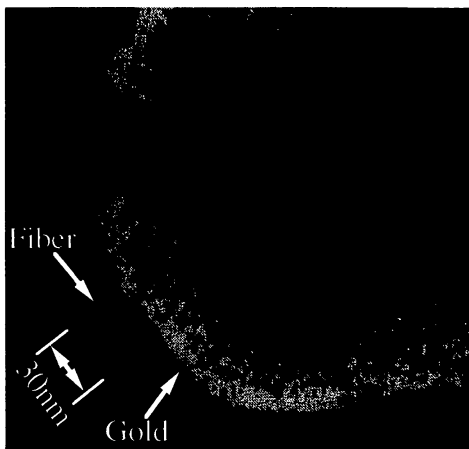


Fig. 9. An SEM micrograph of the gold-coated probe with the protruded fiber tip.

Apart from the success in the development of etching techniques for fabricating sharpened fibers of various shapes out of a special expensive fiber with high GeO_2 -doped core, we have recently succeeded in developing modified etching techniques suitable for commercially available multimode fibers having relatively low GeO_2 -doped core. Furthermore, we have found that our etching technique (Section I-A) can be successfully applied also to sharpen Er^+ -doped fibers used as optical amplifiers, and hence this can be expected to be used as a functional probe with optical gain.

B. Fabrication of a Subwavelength Aperture

A subwavelength aperture must be fabricated at the top of the sharpened fiber developed by techniques in Section III-A in order to suppress scattering (C-mode) or generation (I-mode) of low spatial-Fourier frequency components of the evanescent light. In this subsection, we discuss two methods of fabrication of such subwavelength apertures at the top of the sharpened fiber. In either method, the initial common step is that of coating the sharpened fiber with a metallic film of sufficient thickness to block unwanted light. We used a skin-thick layer of gold for optical attenuation of 30 nm, and the thickness of the coat was around 150 nm. For stronger adhesion of the coated gold film to the fiber, it is necessary to coat a chromium film of several nanometer thickness prior to the coating of the gold film. The second common step involves coating of a guard layer, such as a coat of acryl resin or photoresist discussed in Subsections B-1 and B-2, respectively

1) *Chemical etching by KI/I_2 solution:* In this method, first, the metal-coated fiber was dipped into an acryl resin solution having low viscosity so that the topmost portion of the fiber is free of resin coat with only gold film exposed. When this fiber is next etched in an etching solution to etch gold, only the top of the fiber could protrude out of the gold film as shown in the SEM micrograph of Fig. 9. The etching is done by commonly used KI/I_2 solution, which is a 50–200 times diluted form of the solution with the weight fraction of $\text{KI} : \text{I}_2 : \text{H}_2\text{O} = 20 : 1 : 400$ and the etching times varied between a few minutes and 15 min at room temperature. Although, as seen from Fig. 9, the diameter at the foot of

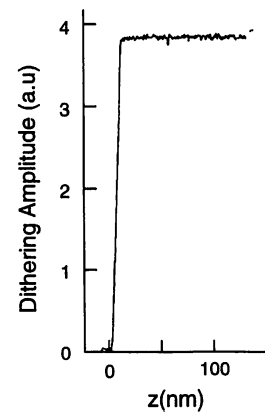


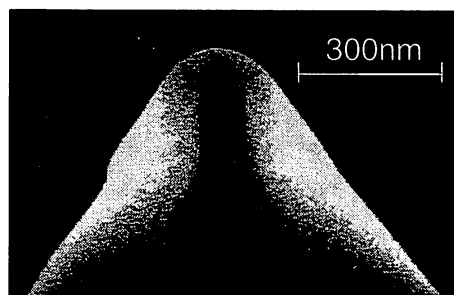
Fig. 10. The relation between the fiber–prism separation z and the measured dithering amplitude, which represents the magnitude of the shearing force.

the protruded fiber is found to be 30 nm, its real value could be even smaller as it is buried in the contamination at the stage of SEM observation. The effective aperture diameter governing the resolution can be even smaller because the high spatial-Fourier frequency components of the evanescent light are preferably scattered (C-mode) or generated (I-mode) at the protruded fiber tip.

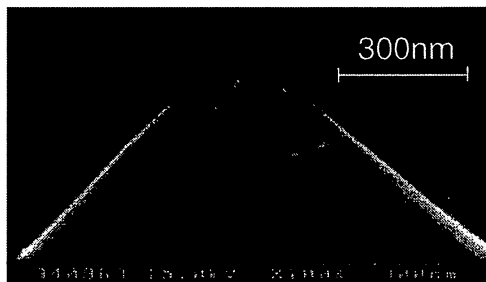
2) *Nanometric photolithography:* This method is based on photolithography, and it consists of four steps: 1) coating of photoresist on a gold-coated fiber; 2) removal of photoresist from only the top of the fiber by exposure to evanescent light and development; 3) removal of gold film by KI/I_2 etching method described above; and 4) removal of remaining photoresist film (refer to Figs. 11 and 12, which give results of the second and fourth steps). Although this method of fabricating a nanoaperture seems to be a little elaborate compared to that of Section III-B-1, this is the first demonstration of the possibility of performing three-dimensional nanometric photolithography, and it is also possible to control accurately the protruded region having a gold coat.

Next, we will describe the first and second steps in detail, as they were developed especially for performing three-dimensional nanometric photolithography. In the first step, a droplet of the photoresist generated at the top of a syringe was made to touch the top of the gold-coated fiber. When the syringe was lifted up, leaving the droplet on the top, a bell-shaped layer of photoresist following the contour of sharpened fiber or just a block of photoresist is formed depending on the cladding diameter. In order to realize a proper bell shape, it is essential to have an optimum cladding diameter of around 25 μm , which could be easily fabricated by the two-step etching. The thickness of the coated photoresist was about 100 nm (reproducibility was confirmed to be sufficiently high).

Next, to selectively expose the top of the sharpened fiber with a bell-shaped photoresist layer, an evanescent light was employed. The evanescent light was generated on the flat surface of a prism by irradiating the He–Cd laser light of wavelength 422 nm under the condition of total reflection. Here, it was essential to control accurately the separation between the top of the fiber and the prism surface for achieving high reproducibility of the size of exposed volume. A shearing force was monitored by the method described in Section



(a)



(b)

Fig. 11. SEM micrographs of the photoresist (a) before and (b) after the exposure/development.

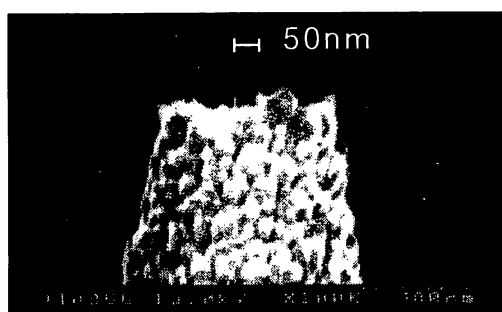


Fig. 12. An SEM micrograph of the probe fabricated by the method of nanometric photolithography.

IV-A, and was used for this control. Fig. 10 shows the relation between the fiber-prism separation and the measured magnitude of the shearing force, from which it is found that a magnitude of the shearing force changes rapidly when the fiber-prism separation is smaller than 10 nm. The separation was fixed to be 5 nm by using this rapid decrease for high-gain servo-control of the position of the fiber. The He-Cd laser power incident into the prism was 25 mW, and exposure time was 130 ms.

Fig. 11(a) and (b) represents the SEM micrographs of the surface of the photoresist before and after the exposure/development, respectively. Comparison between the two views shows that the area with a diameter smaller than 200 nm was selectively exposed. Fig. 12 shows the SEM micrograph of the final result, showing the root of the protruded fiber to have a diameter smaller than 50 nm.

This novel photolithography could be significant in the sense that nanometric fabrication is possible by inducing photochemical reaction of a few tens of molecules of photoresist confined in the three-dimensionally nanometric dimension even if the evanescent light is two-dimensional. Thus, it can be claimed

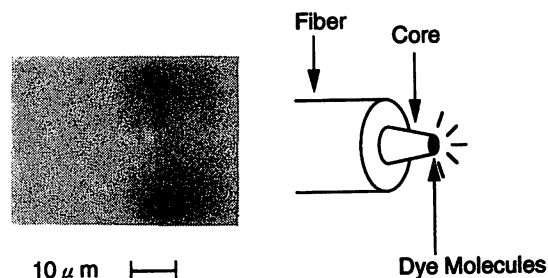


Fig. 13. An optical microscopic image of the fluorescence from the Rhodamine 6G dye droplet fixed on the flattened-top fiber (left) and its schematic explanation (right).

that this method demonstrated the possibility of fabricating optically the three-dimensional nanometric materials, and can be used for future fabrication technology of nanometric devices.

Finally, considering the minimum diameter fabricated by either of these methods, the governing principal factor could be the clustering of gold atoms at the stage of coating. Although the diameters of these clustered grains were about 10 and 30 nm for the cases of a conventional vacuum evaporation unit (Fig. 9) and sputter (Fig. 12), respectively, this diameter can be decreased to several nanometer if, e.g., more advanced vapor deposition techniques are used. However, it should be noted that the aperture diameter observed by the SEM gives only an auxiliary measure to estimate an near-field optically effective diameter of the aperture. For accurate estimation of the effective diameter, one should measure the spatial distribution of the evanescent light power generated at the top of the sharpened fiber.

C. Other Novel Probes

Several varieties of novel probes have been proposed by other groups. Some of them have been called "super-tip" because they can convert optical signal to other physical signals or vice versa [21]. As a first example, a cleaved edge of a GaAs crystal was used for a light-emitting probe by forming a Schottky contact consisting of GaAs as the semiconductor and aluminum as the metallic contact on the two adjacent cleaved faces [22]. Its advantage is that the opto-electronic conversion can be integrated into the probe itself. The second example is a pH sensor fabricated by incorporating fluoresceinamine into an acrylamide-methylenebis (acrylamide) copolymer which was attached covalently to a silanized fiber tip surface by photoinitiated polymerization [23]. Its advantage is short response time of around several milliseconds due to the small size. Further developments in fabrication technologies are still required as the former is still two-dimensional in its shape, while the latter is about 1 μm in size. Hence, it is necessary to improve the spatial resolution by reducing the sizes of these probes.

As an example of such a super-tip, Fig. 13 shows the optical microscopic image of the fluorescence from the Rhodamine 6G dye droplet fixed on the flattened-top fiber with the 1- μm diameter of the upper side of the cross-sectional trapezoid. Although the size of this preliminary super-tip is still as large as optical wavelength, further reduction in the size can be expected, which can be used as a nanometric light source to

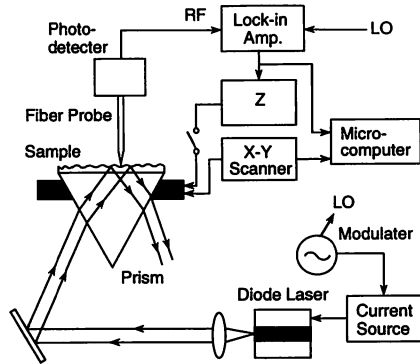


Fig. 14. The experimental setup of the C-mode PSTM.

study, e.g., the cavity quantum electrodynamic phenomena to be described in Section IV-B-2.

In another variation of novel probes, a small particle suspended in a solution trapped by a focused laser beam can act as a probe [24]. It can be advantageously used to observe, e.g., biological samples in water without damaging their surfaces because the optical force pressing the particle to the sample surface is even smaller than the atomic force. However, an essential disadvantage is that control of the particle position becomes more difficult with decreasing the size of the particle, because it is trapped by using conventional far-field optics which is not compatible with the near-field optical microscope.

IV. IMAGING EXPERIMENTS

A. System

Generally, a typical C-mode PSTM system is as shown in Fig. 14, with a light source which in this case is a semiconductor laser of wavelength 780 nm and a maximum output power of 30 mW for the possibility of doing amplitude modulation and hence conduct phase sensitive detection. Either the sample mounted on the prism or the sharpened fiber probe is placed on an XYZ piezo-scanner. The picked up light reaches a photodetector to be converted to an electrical signal, and the remaining scanning control and the image processing unit are the same as that for an SPM.

Fig. 15 shows the variation of detected power as a function of z for different cone angles of the probe plotted in a semi-log scale, from which it is found that the typical detected light power is several picowatts because the prism-probe separation is usually fixed to be about 10 nm. Curve A of Fig. 16 shows the power spectral density of the relative intensity noise associated with such a low optical power detection by the C-mode PSTM, where the laser power incident into the prism was 10 mW. The line B is the reference level representing the relative intensity noise of -40 dB, which corresponds to the error variance of $1 \text{ nm}^2/\text{Hz}$ for measuring the prism-probe separation, i.e., normal resolution of 1 nm at 1 Hz bandwidth of the measurement. It was confirmed that magnitudes of electric noises and laser power fluctuations were lower than the value of curve A.

On the other hand, line C represents the estimated shot noise level of photodetection, which corresponds to the normal

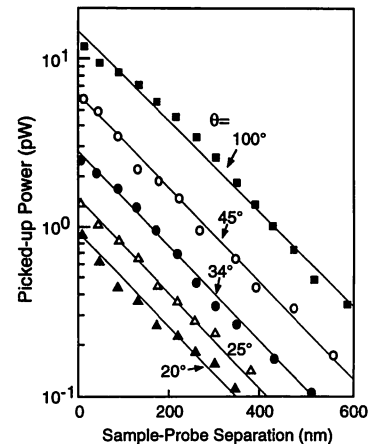


Fig. 15. The detected evanescent light powers as a function of the prism-probe separation. A semiconductor laser of 780 nm wavelength and of 30 mW output power was used as a light source. Five families of results were obtained by using fibers sharpened by one-step etching without coating the metallic film. Their cone angles are 100° (A), 45° (B), 34° (C), 25° (D), and 20° (E).

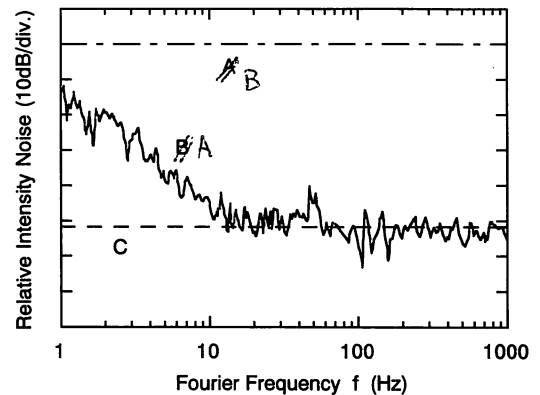


Fig. 16. The power spectral density of the relative intensity noise associated with the C-mode PSTM, where the laser power incident into the prism was 10 mW. A: Measured value. B: Reference level representing the relative intensity noise of -40 dB, which corresponds to the error variance of $1 \text{ nm}^2/\text{Hz}$ for measuring the prism/probe separation. C: Estimated shot noise level.

resolution of $3 \times 10^{-3} \text{ nm}$ at 1 Hz bandwidth by referring to curve B. Although it is assumed that the photon energy of the evanescent light is equal to that of the conventional propagating light for estimating the shot noise level, it may not be sufficient to consider only the zero-point fluctuations of the light field for this estimation. Instead, the magnitude of zero-point fluctuations of a small number of elementary excitations should be estimated because the shot noise is generated at the point where the evanescent light field and the optically induced polarizations couple between each other at the sample surface. In this sense, it should be noted that the specific noise is included in the evanescent light detection, which is different from the noise properties of detecting the conventional propagating light.

It is found (by comparing curves A and C) that the principal noise source at the Fourier frequency f lower than 10 Hz was the acoustic vibration and thermal drift of the fiber, while that for $f > 10$ Hz is the shot noise. Curve A shows that the acoustic vibration and thermal drift limited the normal

resolution at $f = 1$ Hz to be 0.1 nm at 1 Hz bandwidth. Careful acoustic shield and temperature control are required to improve the normal resolution.

The sample should be carefully fixed on the substrate to avoid unwanted scattered light sources. Although one of the advantageous properties of the PSTM is the capability of observing the sample in air, one should carefully avoid attractive force due to the electric charges on dielectric surfaces, water capillary effect due to water molecules in the gap between the sample and probe, and so on. Processes of fixing biological samples on the substrate could be almost the same as the ones used for the AFM measurements. Although the PSTM can also be operated in water, positioning of the probe should be carefully controlled, otherwise it will be disturbed by surface tension of the water and Brownian motions of water molecules.

In the case of the C-mode operation, sample-probe separation can be controlled by utilizing the rapid decrease of the detected evanescent light power. However, such an optoelectric servo-control is not possible in the I-mode. In order to overcome this difficulty, an auxiliary method of controlling the sample-probe separation has been used in the I-mode by monitoring the shearing force, i.e., a lateral atomic force between the sample and the probe [25]. In order to do this, the probe is dithered laterally at its resonant frequency, and the dither vibrations are detected by shining laser light on the probe, and measuring the scattered light power through synchronous detection. When the sample-probe separation is made to be smaller than 10 nm, the dithering amplitude decreases rapidly as shown in Fig. 10. Thus, the sample-probe separation can be controlled accurately for maintaining the shearing force constant.

An alternative method of detecting the atomic force between the sample and probe is required when imaging fragile samples such as biological specimens, as they could be easily damaged by the laterally dithered probe. One such method is shown in Fig. 17(a), that is, the probe fabricated by the two-step etching is scanned by tilting its axis as small as 5° . The magnitude of deflection of the tilted probe due to the atomic force can be easily measured by detecting the scattered laser power. The reason for this tilted probe being sensitive to the atomic force is due to its decreased cladding diameter, which causes it to bend easily. Fig. 17(b) shows the dependence of measured atomic force on the sample-probe separation. Since this force exists in the vicinity of the sample surface, very high gain can be obtained for servo-control. One problem is the coupling between the X - and Y -components of deflection characteristics due to axially symmetric shape and spring constant of the fiber, resulting in fluctuations of the probe along the Y -axis, while it is scanned along the X -axis of the sample surface.

B. Experimental Results

1) *Biological specimens*: Biology could be the field in which optical microscopes have been popularly used for a long time. Among the most significant biological specimens, thicknesses of cell walls, sizes of functional polymers such as ion channels, sizes of intracellular connecting elements,

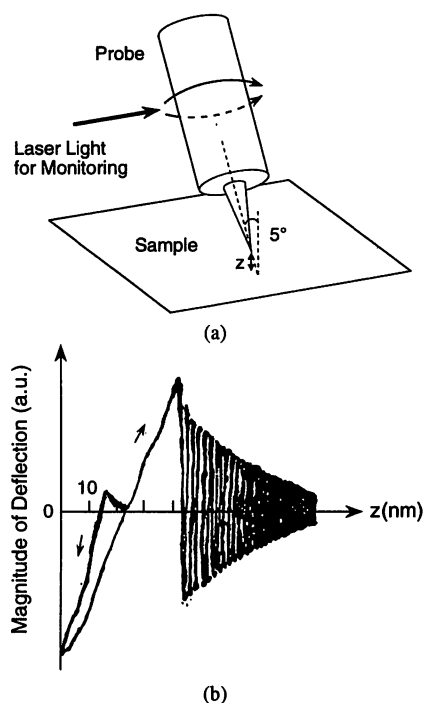


Fig. 17. (a) Schematic explanation of detecting an atomic force between the sample surface and fiber probe tip with decreased cladding diameter, whose axis was tilted about 5° . (b) Dependence of measured atomic force on the sample-probe separation z .

diameters of actin filaments, and so on are in the order of nanometers and have been preliminarily observed by using a differential contrast video microscope, SEM or TEM, and AFM. Since observations by optical methods could provide unique information about these specimens, it is significant to obtain the images of several nanometric biological specimens by the PSTM. As a first step, we have obtained the images of bacteriophage T4 with a spherical head of 100 nm diameter and cylindrical tail of 10 nm diameter [26]. As a second step, we used the following two biological specimens as samples for more advanced imaging experiments of the C-mode and I-mode PSTM, respectively.

a) *Flagellar filaments of salmonella*: This has been known as a representative example of a molecular motor. Fig. 18(a) shows the transmission electron micrograph of stretched straight filaments [27]. From this figure, the diameter of the filament can be found to be 25 nm. In order to do the imaging by the C-mode PSTM, the filaments were fixed on a glass plate. A fiber sharpened by the two-step etching, having a subwavelength aperture fabricated by the method of Section III-B, was used as a probe. Although the aperture diameter observed by SEM was 30 nm, it should be smaller than this value because of the effect of the contamination on the surface of the protruded fiber. The sample-probe separation was fixed at 15 nm. Fig. 18(b) and (c) shows the images taken by the C-mode PSTM of the same filaments randomly oriented on the glass substrate for s - and p -polarizations of the incident laser beam of wavelength 488 nm, respectively. In the two views, the direction of laser beam propagation was from the upper left to the lower right, and it can be seen that the

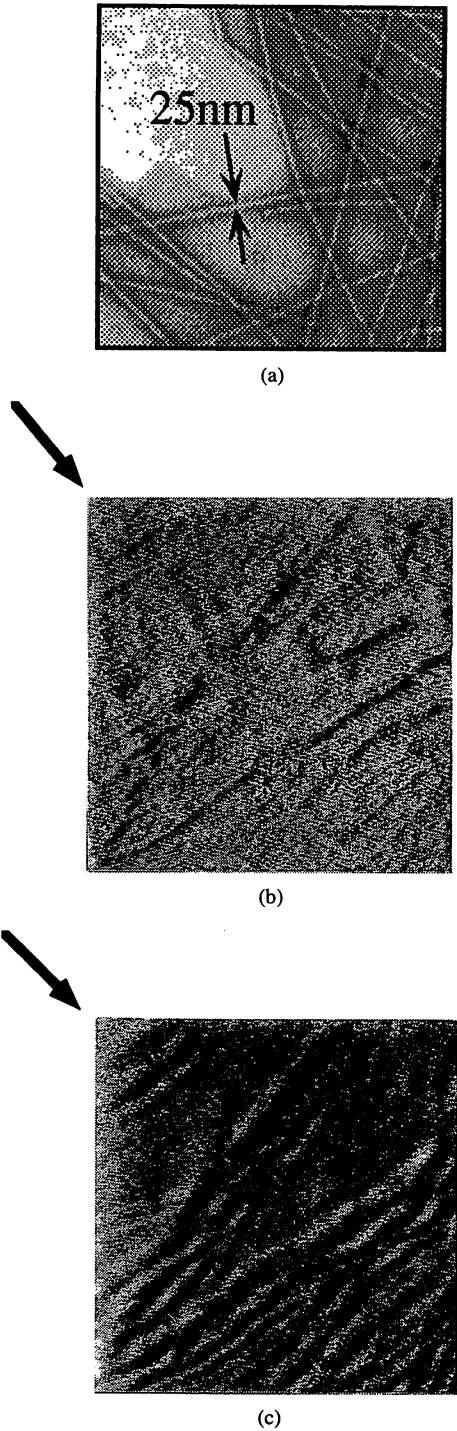


Fig. 18. (a) Image of linear flagellar filament of *salmonella* taken by a transmission electron microscope. Gray-scale optical images of the same filaments taken by the C-mode PSTM under the irradiation of (b) *s*- and (c) *p*-polarized lights. Scanning areas are $5 \mu\text{m} \times 5 \mu\text{m}$. Arrows represent the directions of propagation of the incident light used to irradiate the sample.

filaments oriented perpendicular to this direction are seen with higher contrast. Furthermore, a comparison between these two figures shows that higher resolution was obtained for the case of *s*-polarized light.

The reason for this dependency of resolution of imaging on the state of polarization of incident light can be explained with the help of the schematic shown in Fig. 19(a) and (b). Here, the evanescent light is interpreted or considered as the field

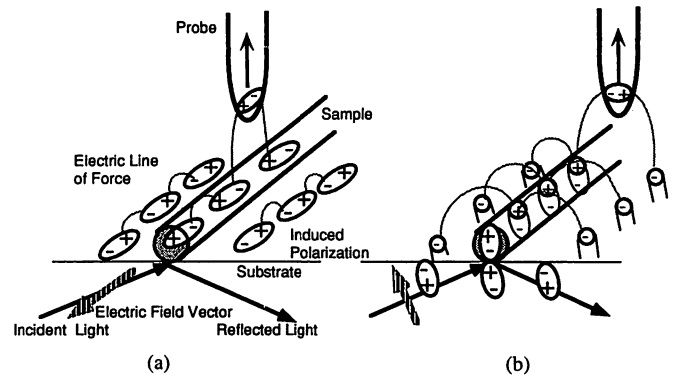


Fig. 19. Schematic explanation of directions of polarizations induced by the incident light. The broken curves represent the electric lines of force of the evanescent light. (a) *s*-polarization. (b) *p*-polarization.

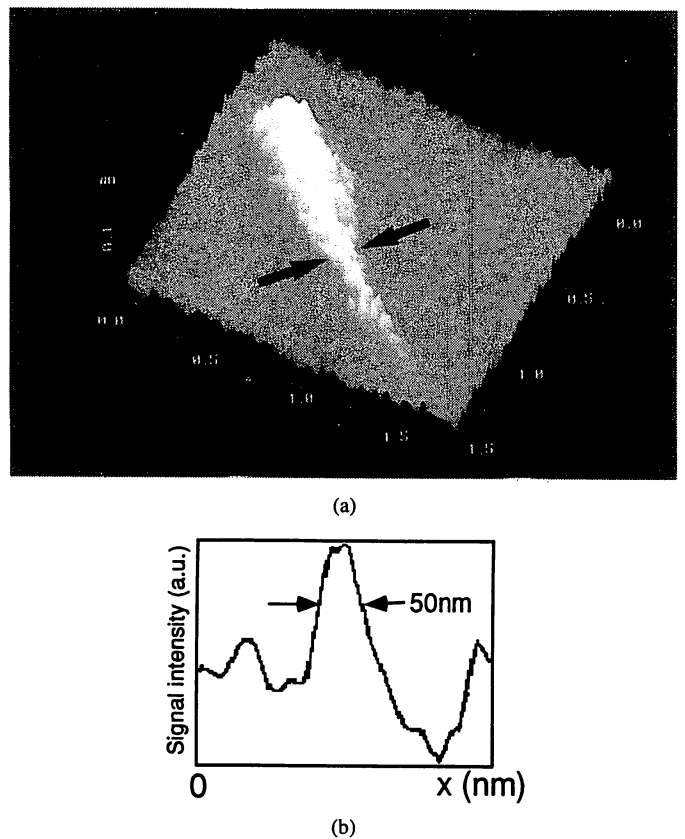


Fig. 20. (a) Magnified gray-scale optical image of a part of the filament by scanning the probe tip with 20 nm incremental step. (b) Cross-sectional profile of the detected signal intensity across the line indicated by arrows in (a).

mediating the short-range electromagnetic interaction between the polarizations which are induced by the incident light on the surface. In the case of *s*-polarization, the direction of the induced polarizations are parallel to that of the filament axis, as shown by Fig. 19(a), because the direction of the electric field vector is parallel to the filament axis. Then the electric lines of forces of the evanescent light bridging the neighborhood polarizations are also parallel to the filament axis. Thus, when the probe tip is scanned perpendicular to the filament axis, these electric lines of forces can be reoriented to the probe tip mainly from the filament. On the other hand, Fig. 19(b)

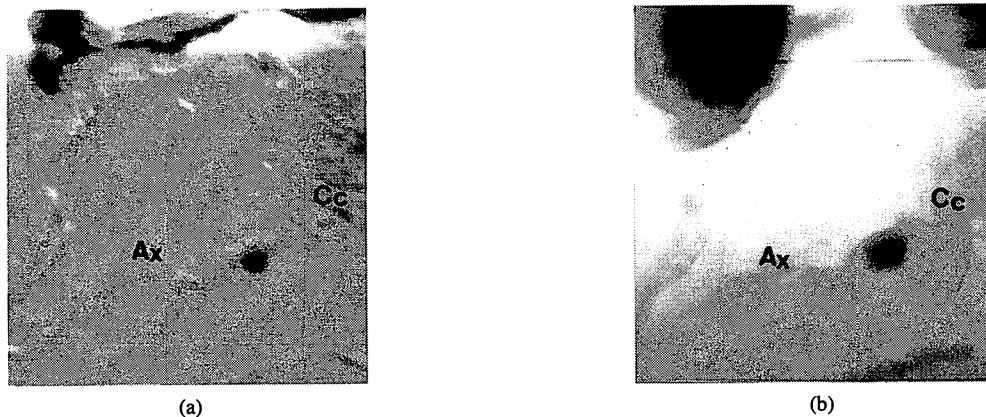


Fig. 21. Gray-scale optical images of neuron cells and branching axons taken simultaneously by the (a) I-mode PSTM and (b) the shearing force microscope, respectively. Scanning areas are $50\ \mu\text{m} \times 50\ \mu\text{m}$. The symbols *Cc* and *Ax* represent the section of neuron cell and branching axon, respectively.

shows that the electric field of the *p*-polarized incident light can induce the polarizations which are not parallel to the filament axis. As a result, the electric lines of forces can be reoriented to the probe tip not only from the filament but also from its vicinity. Hence, due to this difference in the spatial distributions of reoriented electric lines of force of the evanescent light, the *s*-polarization could realize higher resolution.

Fig. 20(a) shows the magnified image of the part of a filament with a cross-sectional profile of the detected signal intensity across the line shown in this figure. The width at half-maximum of this profile is found to be 50 nm. Here, the increment during scanning was 20 nm. By considering these numerical values, a comparison to the width of the filament found from Fig. 18(a) could give a rough estimation of resolution to be smaller than 10 nm, which is smaller than the aperture diameter estimated using the SEM. The origin of such a high resolution could be that the evanescent light was preferably scattered at the top of the protruded fiber, as was pointed out in Section III-B.

Furthermore, it has been found that the resolution deteriorated with increasing the sample-probe separation and increasing aperture dimension. These dependencies agree qualitatively with the characteristics of transfer function of the detection efficiency of the evanescent light, i.e., the dependency of the detection efficiency on the spatial-Fourier frequency, estimated by using a virtual photon model to be discussed in Section VII.

One of the major significances of this imaging is that the resolution as high as 10 nm (or even smaller) was achieved by using only a narrow-bandwidth opto-electrical servo-control of the sample-probe separation without using an auxiliary method such as shearing force. The principal reason for this success is due to the use of an aperture as small as 30 nm (or even smaller) fabricated on the sharpened fiber in a very reproducible manner. Such a high resolution has never been reported, to the author's knowledge, in the literature published previously for the C-mode PSTM. Although it has not been straightforward to observe this specimen by using an AFM without injuring its fragile surface, a clear image was obtained by using the C-mode PSTM.

b) Subcellular structures of neurons: We have imaged subcellular structures of neurons obtained from the hippocampus region of the brain of a wistar rat [29] by I-mode PSTM employing aperture fabricated from metal-coated flattened-top fiber (Section III-A-3) operated with shear force feedback control (Section III-B-2). The neuron samples have been nonspecifically labeled with tracing blue and gold colloid particles of diameter 23 nm, and the illumination wavelength was 488 nm.

Fig. 21(a) and (b) shows the respective PSTM and topographic images observed simultaneously, with *Cc* showing a section of neuron cell and *Ax* indicating branching axon. In spite of the correspondence of structures in (a) and (b), the resolution and contrast of topographic image is very poor due to larger tip diameter resulting from metal coat and larger thickness of the biological sample. Furthermore, labeling of the sample with dye has very much enhanced the contrast of PSTM images.

Fig. 22(a) shows a magnified image of a branching axon shown by Fig. 21(a). Bundles of microtubules can be seen that lie parallel to each other. From a cross-sectional profile of the detected signal intensity shown by Fig. 22(b), at the narrowest part, the width at half-maximum was found to be 25 nm. This value is almost the same as the diameter of the microtubules estimated from SEM or TEM observation of extracted microtubules from branching axon. In our observations, the probe was scanned with 12-nm incremental steps. An origin of such a very high resolution could be attributed to the edge effect of the circular boundary between the flattened top of the fiber and the coated gold film, as has been pointed out qualitatively [29]. One of the major significances of this imaging was the capability of high resolution, as high as that of AFM, in imaging the microtubules lying under the protein sheath of the branching axon, without removing the sheaths as has been done for making observations by AFM or TEM.

2) Photonic devices and related materials: High-resolution diagnostic techniques for photonic devices could be of more demand in the future because of their growing compact sizes and improved performances. Results of diagnosing photonic devices and their related materials are reviewed in the following subsections.

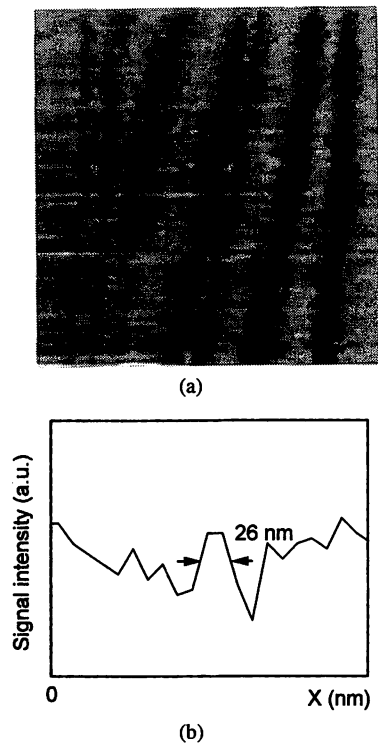


Fig. 22. (a) Magnified gray-scale optical image of a branching axon of Fig. 21(a), in which several microtubules can be seen. Scanning area is $1 \mu\text{m} \times 1 \mu\text{m}$. (b) Cross-sectional profile of the detected signal intensity across the central part of the microtubules indicated by arrows in (a).

a) A Dielectric optical waveguide: This is a representative example of passive photonic devices. For their material analyses, mass spectroscopy using secondary ion-mass spectroscopy (SIMS) has been popularly used. For evaluating the propagation loss, a cutback method, a scattering method, an interferometric method, and a method using a TV camera have been conventionally employed [30]. The problems of these methods are that the resolution could not go beyond the diffraction-limit even though the maximum measurable size could be as large as several centimeters (or even larger). Furthermore, the diagnostics using SIMS and the cutback method are destructive inspections. The C-mode PSTM can realize a nondestructive and high-resolution inspection if the evanescent light generated on the waveguide surface is picked up while guiding the light through the waveguide. A preliminary experiment has been reported by Tsai *et al.* [31].

Fig. 23(a) shows the profile of the guided mode of a Y-branched single-mode waveguide with the stripe width of $3.8 \mu\text{m}$ made of a proton-exchanged LiTaO₃ crystal, which was observed by the C-mode PSTM by guiding light of wavelength 680 nm [32]. The probe with relatively large aperture could be used for these measurements because such a waveguide is much larger than the optical wavelength. However, the problem was that the probe was attracted toward the sample surface and thus deformed due to the attractive force induced by the electric charges stored on the ferroelectric LiTaO₃ surface. In order to reduce the effect of this attraction, the probe was dithered laterally as was the case for detecting the shearing force. By this operation, a small elliptic bright spot of diameter 500 nm along the major axis of the ellipse

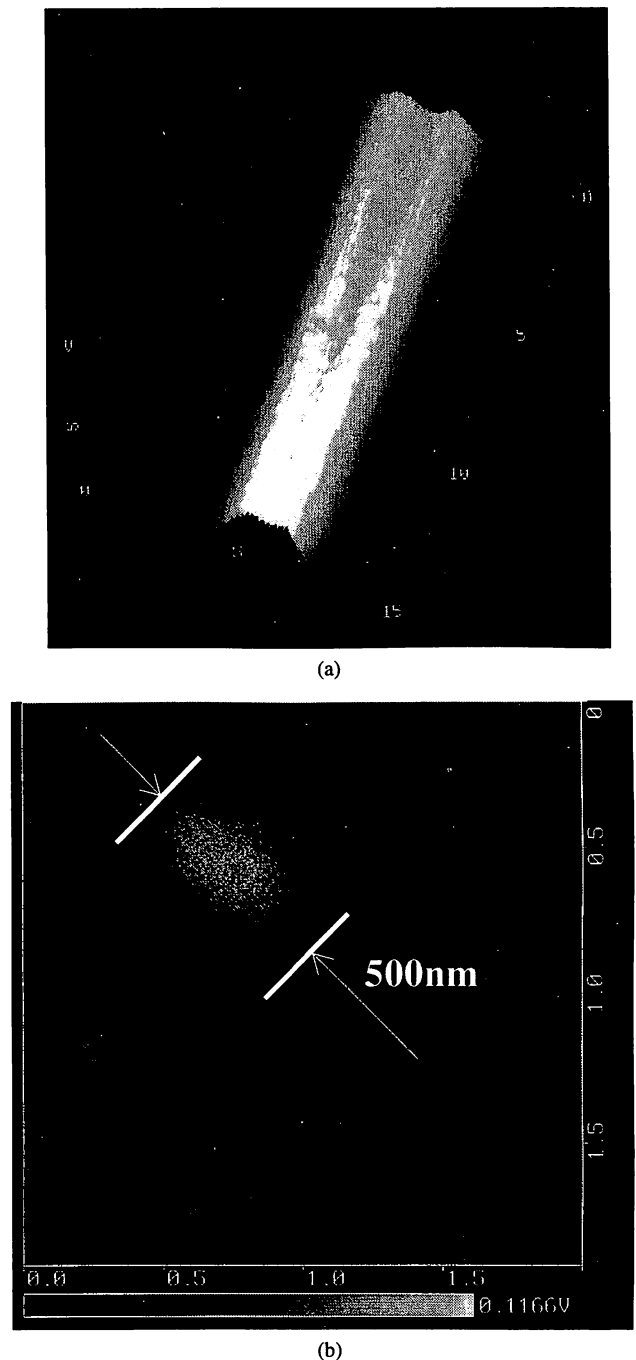


Fig. 23. (a) Gray-scale optical image of the profile of the guided mode of a proton-exchanged Y-branched LiTaO₃ single-mode waveguide with the stripe width of $3.8 \mu\text{m}$, which was observed by the C-mode PSTM. (b) Gray-scale optical image of the measured elliptic bright spot of diameter 500 nm along the major axis of the ellipse, which was attributed to the scattered guided light in the vicinity of surface.

was found in the near-field region, as is shown by Fig. 23(b). This can be attributed to the scattering of the guided light in the vicinity of the surface which could be originating from the spatial inhomogeneity of the exchanged proton density or contamination on the surface. Thus, the capability of finding subwavelength scattering sources can improve the accuracy in designing the mask for forming the guiding layer so that the guiding loss of the waveguides can be decreased.

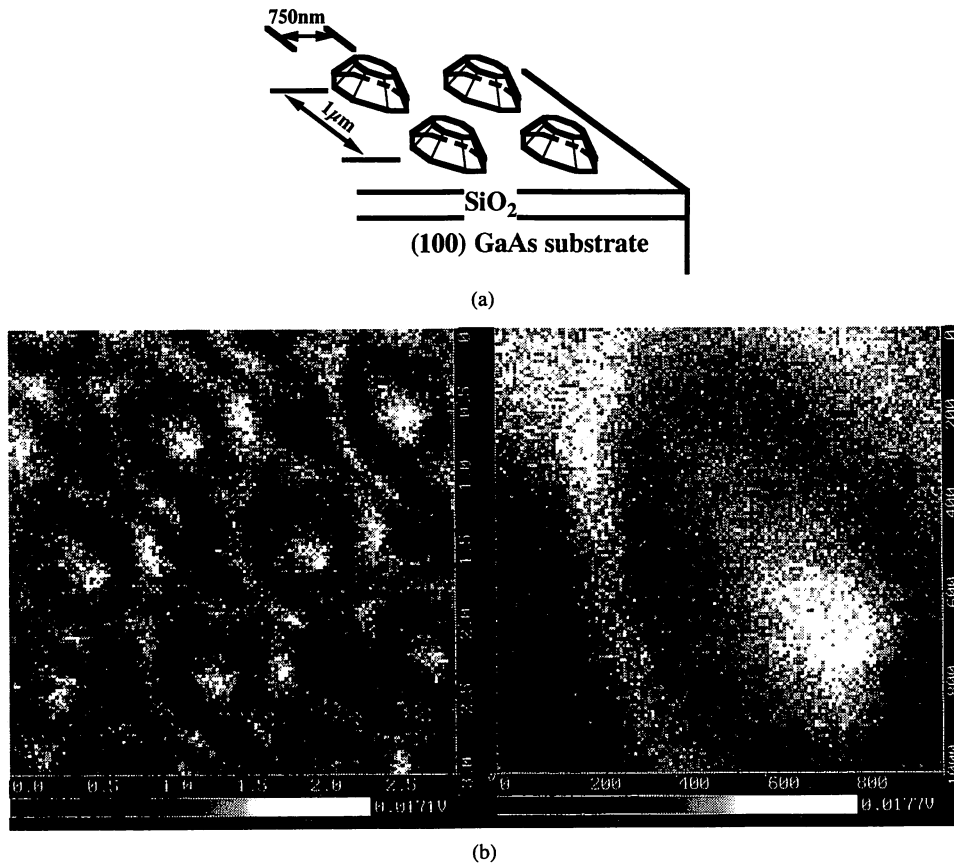


Fig. 24. (a) Schematic illustration of the shape of two-dimensional array of GaAs quantum dots with the base diameter of 750 nm grown on an SiO₂/GaAs substrate. (b) Gray-scale optical image of quantum dots measured by the I-mode PSTM (left: scanning area is 3 μm × 3 μm) and its magnified image (right: scanning area is 1 μm × 1 μm).

Guided power variation along the waveguide axis was also measured at the Y-branching region, and the variation rate was estimated as -1.2×10^{-1} dB/μm, which agreed with the calculated result using the beam propagation method (BPM) by assuming steplike lateral profile of refractive index of the guided layer. This measurement could be significant for the possibility of obtaining experimental results of the high resolution of conducting two-dimensional nondestructive inspection for the first time.

b) A semiconductor quantum dot: This is an example of a submicron device used for fabricating active photonic devices such as semiconductor lasers [33]. Fig. 24(a) shows a schematic illustration of the shape of two-dimensional array of GaAs quantum dots with the base diameter of 750 nm grown on an SiO₂/GaAs substrate. Since the size of each dot is of subwavelength dimension, only the optical spectral properties integrated over several dots have been measured so far, which could average out the quantum size properties of an individual dot. However, it can be expected that a high-resolution measurement by the PSTM will overcome this difficulty.

Fig. 24(b) shows the image of quantum dots measured by the I-mode PSTM, with simultaneous use of shear force to control the sample-probe separation. Because of the large size of the quantum dot, an aperture as large as 100 nm could be used to obtain an individual image of the dot. Since the sample is opaque at 680 nm wavelength of the light source, the light

reflected from the sample surface was detected. Here, a high contrast was obtained due to the difference in reflectivities between GaAs and SiO₂. For this reflection measurement, the evanescent light illuminating the sample got scattered on its surface and was picked up again by the apertured probe. The light power transmitted through the aperture was measured at the end of the fiber by using a fiber-beam splitter. Here, the transmission occurring through the aperture twice could be advantageous in the sense that the contribution of the low spatial-Fourier frequency components of the detected light are reduced effectively; hence, images with higher contrast could be obtained as compared to that from a single transmission through the aperture.

The next step could be to measure the photoluminescence spectral profile from each quantum dot. For this, the sample should be cooled down in order to avoid the spectral broadening or decrease of quantum efficiency. Although this measurement has never been carried out, spectral profiles emitted from excitons in the GaAs/AlGaAs single quantum well with 2.3 nm thickness have been observed at a temperature of 2K [34]. The sample was irradiated by pumping the light through the aperture with the diameter as large as 100 nm, and the sharp emission spectral profiles from different emission sites with different potential energies were separately measured. Furthermore, the diffusion length of the exciton and the fluctuation magnitude of the quantum well thickness were

estimated. As a related experiment, emission from the quantum wire has been detected at low temperature [35].

c) *Fluorescence detection from dye molecules:* Fluorescence from dye molecules has also been detected. Especially, the fluorescence from a single dye molecule was detected, and molecular orientation was estimated by irradiating the pumping light through the aperture with the diameter as large as 100 nm [36]. The quenching process of this fluorescence and reversible variation of fluorescence intensity with time interval of several tens of seconds were also measured. Furthermore, the effect of metallic film coated around the aperture on the fluorescence lifetime was also studied with the time scale of several nanoseconds [37], [38].

It can be expected that the fluorescence spectroscopy of a single dye molecule by the PSTM described above is widely applied, such as labeling biological samples. This is because the fluorescence spectral profiles, the lifetimes, and the quantum efficiencies of the dye molecules depend strongly on their surroundings. However, the principal problem in fluorescence detection from the single dye molecule could be its sensitivity. A solution to this problem could be the development of a novel probe for the I-mode operation that has high efficiency of guiding the light to the aperture while suppressing the heat induced by thermal dissipation.

On the other hand, increase in detection sensitivity can be expected by considering the coupling between the sample and probe due to the short-range electromagnetic interaction. From the viewpoint of such a coupling, an experiment was carried out to study the increase in detection efficiency, which is schematically explained by Fig. 25(a). Polystyrene spheres doped with Rhodamine dye molecules of 110 nm diameter were used as the sample. An argon ion laser (wavelength 488 nm) was used for excitation, and the fluorescence emitted from the sphere at the wavelength of 560 nm was detected by the C-mode PSTM using a sharpened fiber fabricated by two-step etching [39]. As shown by Fig. 25(b), an image of the fluorescence intensity distribution with the diameter of 180 nm was obtained. Such a subwavelength resolution has not been obtained by conventional far-field detection with a fluorescent microscope in which the fluorescence was emitted homogeneously into the free space.

The origin of such a high resolution could be attributed to the short-range electromagnetic interaction between the sphere and the probe. As a result of this interaction, the spatial mode for emitting the fluorescence can be considered to be modified from that of the free space. As a consequence of this, the emitted fluorescence becomes spatially inhomogeneous so as to be coupled to the probe with higher efficiency. In order to confirm this selective coupling to the probe, the experimentally realized coupling efficiency was estimated by using experimental parameters such as the power density of the argon ion laser, quantum efficiencies of emission from the dye molecules and of the photomultiplier, and was found to be $(2-5) \times 10^{-3}$. On the other hand, the efficiency calculated by considering the geometrical solid angle of the probe with respect to the sphere was $0.1/4\pi$, assuming the spontaneous emission to be spatially homogeneous. Thus, total calculated coupling efficiency is given by $(0.1/4\pi)\gamma$, where γ represents the coupling efficiency

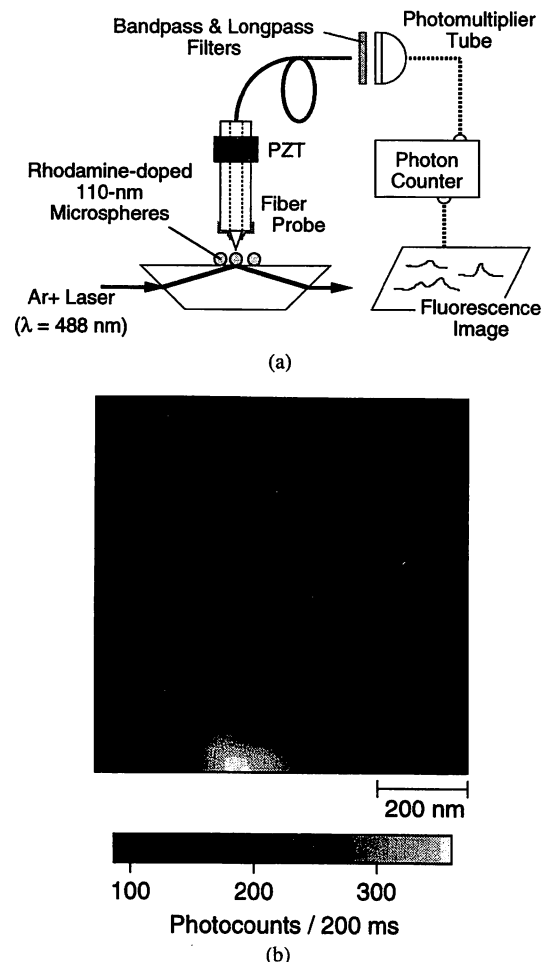


Fig. 25. (a) Experimental setup of the C-mode PSTM for detecting the fluorescence from dye-doped spheres of 110 nm diameter. (b) Gray-scale optical image of fluorescence intensity distribution.

of the homogeneously propagating fluorescent light to the fiber with nanometric tip, i.e., to a cutoff optical waveguide. Since the value of γ is much smaller than unity, this geometrically calculated efficiency is much smaller than the experimentally estimated efficiency. This large difference in efficiency can prove the modification of spatial mode, and also explain the realization of subwavelength resolution.

Modification of spontaneous emission probability, similar to the presently observed phenomenon, has been observed in a closed optical cavity with the size of optical wavelength. As compared to such a study of cavity quantum electrodynamics, the present experiment corresponds to the observation of the quantum optical phenomenon with subwavelength dimension.

As other examples of spectroscopy of condensed matters, emission spectrum of a ruby under the condition of applying the mechanical stress [40] and Raman spectrum of diamond [41] have been observed. Furthermore, detection of surface plasmon propagation on a metallic film [42], and improvement of resolution by utilizing the surface plasmon [43], have also been reported.

V. NANOMETRIC FABRICATION

As an example of realizing photonic devices with nanometric dimension, experiments on high density optical storage by

utilizing the surface on structural changes of the medium under illumination by evanescent light in I-mode PSTM have been carried out.

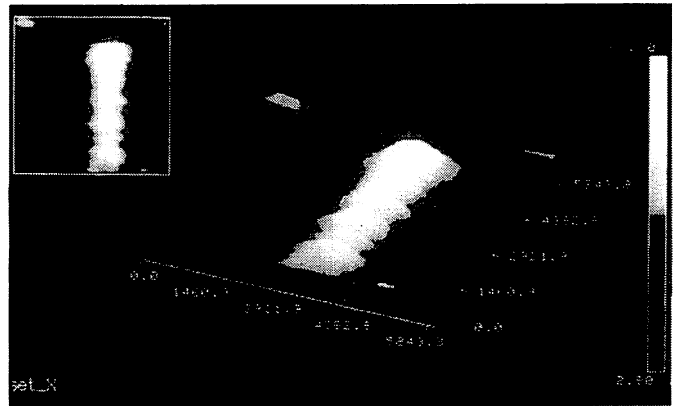
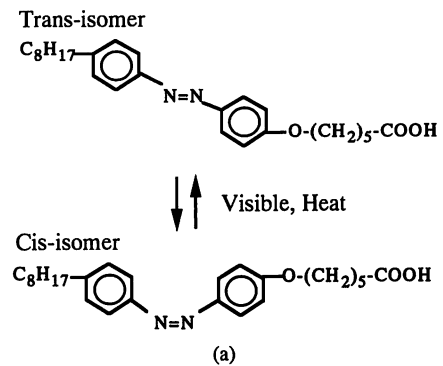
Thermal-mode optical storage has already been carried out for magneto-optical storage medium of Pt/Co by heating its surface by the evanescent light from the probe [44]. A pit diameter of 60 nm was obtained. It corresponded to a storage density of 45 Gb/in², which is about 20 times that of the conventional optical memory.

In our experiments, photon-mode optical storage on the Langmuir-Blodgett (LB) film of amphiphilic azobenzene derivative has been carried out by local photochemical reaction with the evanescent light in order to transform its molecular structure [45]. In this case, as is shown by Fig. 26(a), the trans-isomer of this molecule is transformed into the cis-isomer under irradiation of the ultraviolet light, and this photochemical transformation corresponds to formation of optical memory. This is an erasable memory because the cis-isomer can be transformed back to the trans-isomer by heating or irradiating with visible light. Since the optical absorption at wavelength 360 nm of the cis-isomer is about half that for the trans-isomer, measurement of the difference in absorption by the PSTM corresponds to reading the memory.

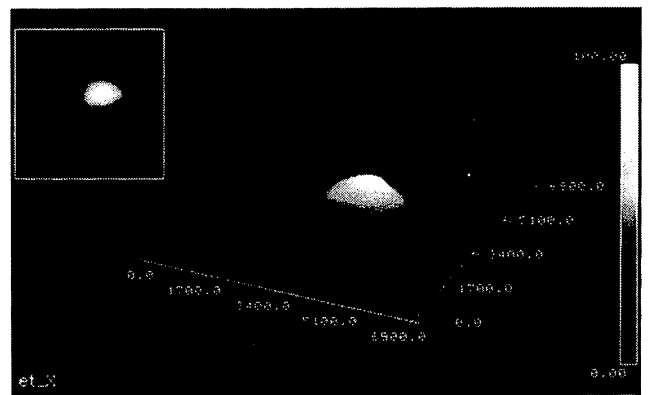
An argon laser of wavelength 360 nm was used for writing and reading. The I-mode PSTM was used for reading the stored memory by measuring the evanescent light power transmitted through the thin film. The thickness of the film was 180 nm, and the evanescent light power used for storage was 30 nW. The difference in the evanescent light powers absorbed by the trans- and cis-isomers was 0.3 nW, and was measured while reading the written memory. Fig. 26(b) shows the image of the stored circular pit with 100 nm diameter read by the I-mode PSTM. Further, Fig. 26(c) shows the image of a stripe with 100 nm width which was stored by scanning the probe along one direction. This result implies that the present method of storage can also be used for fabricating a nanometric fine grating. Further significance of this method is that it demonstrated the possibility of inducing nanometric photochemical reaction by the evanescent light.

A problem with this material is its low sensitivity of photochemical reaction, and hence that a writing time longer than that of the thermal-mode storage was required. It limited the minimum size of the pit due to thermal drift of the probe. In order to decrease this size, it becomes necessary to develop a novel probe tip which is less sensitive to the optical damage by the high power laser light and has high throughput efficiency of generating evanescent light. Furthermore, it is necessary to find more sensitive storage media or to develop methods for more sensitive detection of absorption difference.

As will be described in Section VII-B, the evanescent light emitted from the subwavelength aperture couples most efficiently when the sample dimensions are equivalent to the aperture size, which corresponds to momentum conservation in the exchange of evanescent photon. Thus, it is most effective for decreasing the storage time to use a granular storage medium with a smaller grain size. Since the surface of the LB film is homogeneous, it is rather difficult to expect such an



(b)



(c)

Fig. 26. (a) Molecular structures of amphiphilic azobenzene derivative. (b) Gray-scale optical image of stored circular pit. The circle at the center of this figure represents the part of cis-isomer with the diameter of 100 nm. (c) Gray-scale optical image of stored stripe with width 100 nm.

efficient coupling of the evanescent light. In order to improve this coupling, a preliminary layer of polystyrene spheres of 42 nm diameter was closely packed on a glass plate to form a two-dimensional array as shown by the SEM micrograph in Fig. 27. The deposition was done by a temperature/humidity-controlled evaporation method. The evanescent light from the aperture of the probe tip can be coupled more efficiently to the LB film formed on the array, and hence promises an optical storage with increased sensitivity and higher density.

Although the technology of the high-density optical storage by the PSTM is still at the initial stage, a very high density (as high as about 1 Tb/in²) can be expected in the future, with due improvements in the size of the probe tip and new storage media.

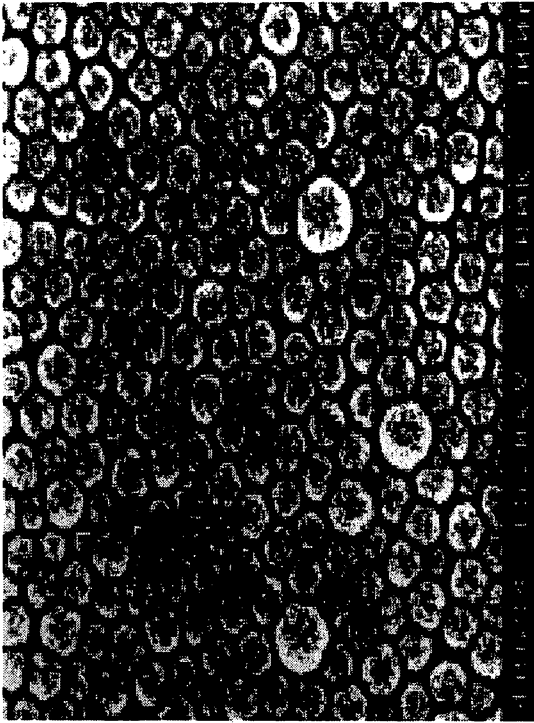


Fig. 27. The SEM micrograph of a two-dimensional array of polystyrene spheres of 42 nm diameter, which were fixed on a glass plate by the temperature/humidity-controlled evaporation method.

VI. MANIPULATION AND TRAPPING OF ATOMS

One of the ultimate goals of the nanometric fabrication technique described in Section V could be the handling of atoms. By using light pressure of evanescent light, it is possible to control thermal motions of atoms which fly freely in vacuum. An atomic mirror used for the experiments of atom optics to reflect atomic beam has been proposed by using two-dimensional evanescent light on a glass substrate [46]. Trapping of atoms has also been proposed by using the evanescent light on the surface of a small spherical optical cavity in order to realize the atomic gallery around the cavity [47].

For improving the spatial accuracy of trapping and controlling atoms, it is essential to decrease the degrees of freedom of the thermal motion of atoms. To do this, the spatially tailored evanescent lights are required and we have proposed an atom guide using a hollow fiber shown schematically in Fig. 28(a) [48]. In this case, a cylindrical potential barrier can be formed by the gradient force of the evanescent light generated on the inner wall of the hollow fiber. By this potential barrier, the atoms incident into the hollow fiber can be guided through it without getting attached to the inner wall. Although the use of a glass capillary with homogeneous distribution of refractive index has been proposed [49], [50], it is more effective to use a bundle of eccentric-core fibers in order to concentrate the power density of the guided light and thus, to realize a sufficiently high potential barrier [51]. Furthermore, it is found to be more effective to use a hollow fiber with a doughnut-shaped core due to its technical readiness of fabrication [48].

As an example of the atom guide using this hollow fiber with a doughnut-shaped core, we consider the case of rubidium

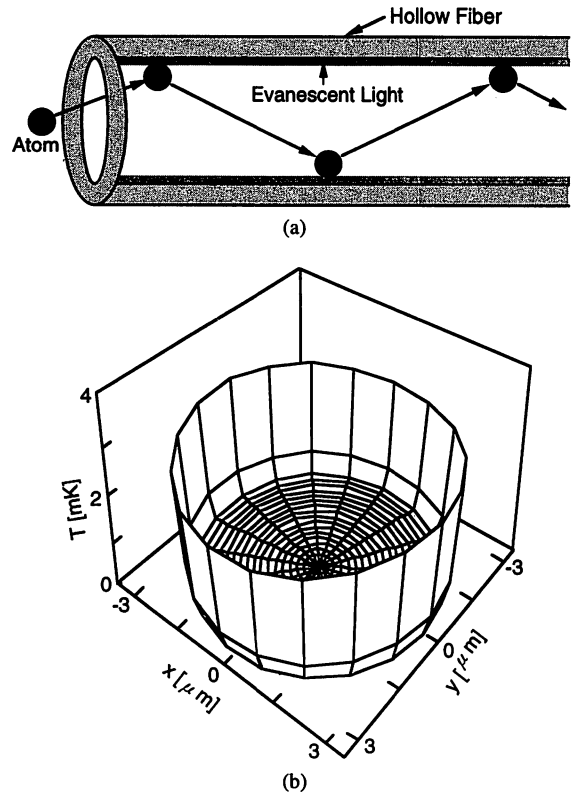


Fig. 28. (a) Schematic explanation of guiding atoms through a hollow fiber by using the gradient force of the evanescent light on the inner wall. (b) Profile of the potential barrier to guide rubidium(Rb) atoms by the evanescent light of wavelength 780 nm. It was assumed that the laser power incident into the doughnut-shaped core of the fiber was 1 mW and the blue-detuning of the laser from the Rb resonance frequency was fixed to be three times that of the natural linewidth of the Rb.

(Rb) atoms being guided by its resonant light with 780 nm wavelength which can be obtained from a GaAs laser, and calculated the potential barrier. Here, the inner diameter and core thickness of the hollow fiber were assumed to be 7 and 3.8 μm , respectively, to realize sufficiently high potential barrier. The LP_{01} mode is the guided mode of the lowest-order for this hollow fiber, and two more higher-order modes (LP_{11} and LP_{22} modes) can be also guided. A calculated profile of the potential barrier is shown by Fig. 28(b), where it was assumed that the principal contribution to this barrier is from the LP_{01} mode, and that the laser power incident into the doughnut-shaped core was 1 mW. It was also assumed that the blue-detuning of the laser from the Rb resonance frequency was optimized, i.e., fixed to be three times the natural linewidth of the Rb. It is seen from this figure that the potential barrier is several mK, which is represented by the equivalent temperature of kinetic energy of atomic thermal motion in vacuum. Since this barrier is sufficiently high to trap the atoms in a collimated atomic beam or the cold atoms in a magneto-optical trap [52], it is expected that one-dimensional control of atomic motion is possible.

To further decrease the degrees of freedom of the trapped atomic motion, use of evanescent light from the probe tip of the I-mode PSTM has been proposed [53], that is, the resonance interaction of an atom with localized evanescent light can

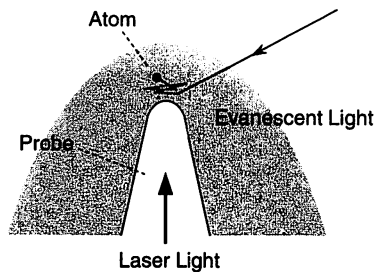


Fig. 29. Schematic explanation of trapping atoms by using the evanescent light at the fiber tip of the I-mode PSTM.

exhibit several specific features which cannot be obtained by using ordinary propagating light. First, an atom scattering an evanescent photon into a propagating photon via resonance absorption and spontaneous emission receives extremely large recoil momentum parallel to the probe surface. Second, the atom feels strong gradient force normal to the probe surface due to the rapid decrease of the field intensity in the near-field region. These features result in a mechanical interaction between the atom and the probe, which is analogous to the interatomic van der Waals force. A novel technique of trapping atoms can be thus realized by using the localized evanescent light on the probe tip of the I-mode PSTM.

As a simple consideration of the possibility of trapping atoms, let us assume that the evanescent light at the probe tip is red-tuned from the atomic resonance, as is shown in Fig. 29. An atom coming into the evanescent light resonantly absorbs the counterpropagating photon due to positive Doppler shift against the red-detuning, and spontaneously emits a propagating photon. By this process, the atom is recoiled strongly in the direction parallel to the probe surface according to the Heisenberg's uncertainty principle, since the momentum of the absorbed evanescent photon is much larger than the momentum of the emitted propagating photon. This acts as a cooling force until the momentum of the atom becomes comparable to the recoil momentum. Because of the spatial variation of the field momentum along the curvature of the probe, the cooling force accompanies the centrifugal component, which could be compensated for by the strong gradient force [54] in the near-field region where the field intensity decreases exponentially. The balance of the centrifugal component of scattering force and gradient attractive force produces a potential valley along the probe surface. The atom will move back and forth in this potential valley like a pinball in the optical standing wave. The trapping condition will be achieved when the cooled atomic motion is reversed by each recoil, and such scattering occurs several times per passage at the proximity of the probe tip. This condition determines the optimum curvature diameter of the probe tip and equivalent temperature of the trapped atoms.

As an example, for the case of the Rb, the trapping condition is satisfied by a probe tip with the curvature diameter of about 30 nm, and the equivalent temperature of the trapped atom will be about 80 μ K, where the red-detuning was fixed to be the optimized value, i.e., 10 MHz. The atoms cooled by the technique of laser cooling are sufficiently cold so that they can be trapped by this trapping method. As a preliminary experiment of confirming large momentum

transfer from evanescent light to atoms, Doppler-free pump-probe laser spectroscopy of Rb has been carried out [55].

This trapping corresponds to realizing the atomic quantum dot because of the zero degree of freedom of the trapped atomic motion. As an alternative method of realizing the atomic quantum dot, the trapping by the evanescent light generated on a nanometric dip on the dielectric surface has been also proposed [56].

This section demonstrated the possibilities of decreasing the degree of freedom of atomic thermal motion to one or zero. If such a controlled atom is transferred to the surface of a cold crystal, it can be fixed on certain positions of the crystal surface, by which novel methods of an atomic-level crystal growth and fabrication of an atomic-level memory devices are expected. For applications to crystal growth and device fabrication, it is advantageous to increase the number of atomic species that can be trapped by the present method. This is possible if one can prepare coherent light resonant to relevant atom, e.g., the wavelengths of the lights required for trapping Si, Ga, and Pb are 252 nm, 403 nm, and 368 nm, respectively. This in turn implies that the coherent lights of visible and ultraviolet regions are required, which can be realized by nonlinear optical frequency conversions of compact semiconductor lasers [57].

VII. THEORETICAL APPROACH

A. Virtual Photon Model

The theories of near-field optics are concerned with mesoscopic phenomena in which electromagnetic fields are coupled strongly to their sources. Thus, a major problem to be solved is how to find the source distribution as well as how to solve the field equations. In fact, difficulties in solving Maxwell's equation as a boundary problem for a nanometric sample-probe system of PSTM have been discussed, and electromagnetic theories based on a self-consistent approach have been developed [58], [59]. In general, theoretical models based on experimental results play important roles in the theory of mesoscopic phenomena, since complicated many-body interactions are involved. Based on these backgrounds, we have proposed an intuitive model describing the evanescent light localized on the sample surface instead of solving Maxwell's equation [53]. In this section, we review a qualitative analysis of near-field optics and a semiquantitative theory based on the intuitive model of localized evanescent light.

To start the discussion, it is assumed that the fundamental process of PSTM is described in terms of quasi-static short-range interaction between nanometric objects irradiated by propagating light. This assumption leads to a local theory describing the evanescent light by reducing the whole system to a simple model.

Now, in order to construct the simplest model, we introduce the concept of virtual photons with a nanometric Compton wavelength described in terms of Yukawa function [53]. The Compton wavelength, or the effective mass of virtual photons, is the essential parameter characterizing the interaction, and is

determined by the size of the nanometric particle which is the source of the evanescent light.

The virtual photons exhibit the characteristics of quasi-particles, which helps us understand how the PSTM process is similar to other SPM's such as STM and AFM. Among them, the surface plasmon near-field microscope (SPNM) [43], [60] has been a representative example of quasi-particle near-field picture with the localized electromagnetic interaction described in terms of surface plasmon. In contrast the SPNM, in which energy is really transferred to the plasmon mode due to resonance, the photon-surface coupling in PSTM occurs instantaneously; and, e.g., in the case of the C-mode PSTM, the energy is transferred into reflected or transmitted photons. Thus, the assumed quasi-particle is virtual in the sense that the coupling process is out of dispersion relations and no real resonance occurs.

Realization of nanometric resolution demonstrated in Section IV-B-1. confirms that the sample-probe interaction has a much smaller range of action than the optical wavelength. This implies that the interaction is considered to be mediated by a highly localized evanescent light according to the Heisenberg's uncertainty principle. That is, an electromagnetic field with extraordinarily large wave vector is involved in the PSTM since the resolution is determined by the shortest wavelength available in the measurement.

It is natural to describe the near-field optical problem in terms of the quasi-static short-range interaction via evanescent photons. Here, the term "quasi-static" is used in the sense that the propagation or retardation effects can be neglected because the sample-probe separations are much smaller than the wavelength of the propagating light. It is well known that such quasi-static short-range interaction is simply described by using a Yukawa function, $\phi(r) \propto \exp(-r/\lambda_c)/r$, where λ_c is the Compton wavelength characterizing the interaction range. Here, it is proposed that the localized evanescent light is described by the Yukawa function. This implies that the theory is based on the modified Helmholtz equation, $\{\nabla^2 - (1/\lambda_c)^2\}\phi = 0$, which is the spatial reduction of the Klein-Gordon equation describing the field of particles with the mass of $m = \hbar/c\lambda_c$, where \hbar and c are the Planck's constant divided by 2π and the speed of light in vacuum, respectively. This mass can be considered as the effective mass of the virtual photons resulting from the coupling between the electromagnetic field and the excitation on the sample surface.

In order to demonstrate the validity of the virtual photon model, it was applied to a calculation of evanescent light behind a subwavelength metallic circular aperture irradiated by the propagating light with the wavelength λ , as schematically explained by Fig. 30(a). By assuming the Compton wavelength of the virtual photons equal to the aperture radius, the intensity distribution in the near-field region was estimated as a Hamiltonian obtained by integrating the Yukawa function over the aperture. Fig. 30(b) shows the calculated profile of the intensity distribution, which agrees well with the numerical results given by Leviatan based on the boundary problem (Fig. 11 of [61]). The peaks at the edges of the aperture and the bump at the center in this distribution originated from the gradient term $|\nabla\psi|^2$ and mass term $|\psi|^2/\lambda_c^2$ of the integrated

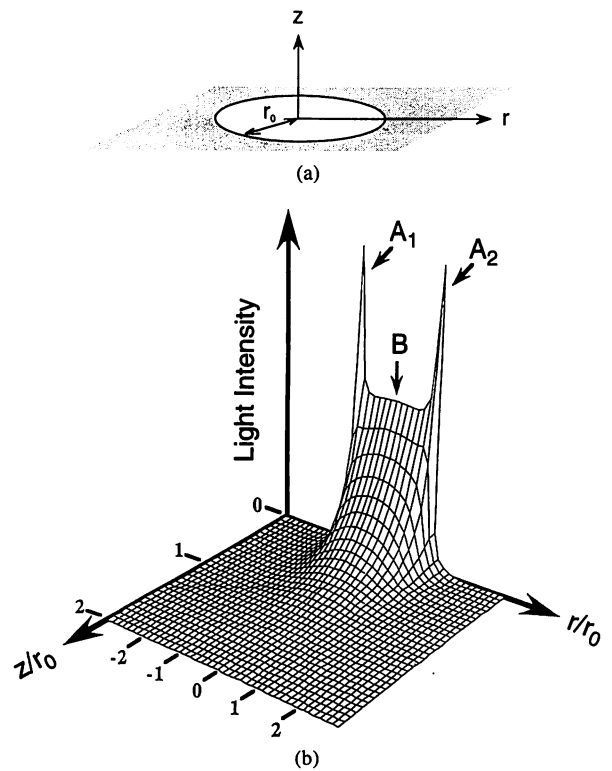


Fig. 30. Application of the Yukawa function model for calculating the intensity distribution of the evanescent light generated behind the metallic subwavelength aperture with the radius r_0 , which is irradiated by the propagating light with the wavelength $\lambda_0 = \lambda/150$. (a) Schematic explanation of the coordinate system on the aperture with the radius r_0 . (b) Calculated profile of intensity distribution of the evanescent light. Two peaks (A_1 and A_2), and a bump (B) on this profile originated from the gradient term and mass term of the integrated Yukawa function, respectively.

Yukawa function ψ , respectively. It should be noted that these features are very similar to the field distribution obtained by the electromagnetic theory for the TM and TE incident lights, respectively.

The origin of the difficulty in dealing with near-field optical problems is due to the fact that the interaction, or the source, of electromagnetic field is of fundamental importance. There are several ways of avoiding explicit use of interactions in the electromagnetic theory, otherwise one has to solve complicated inhomogeneous differential equations. In the conventional theory based on the macroscopic Maxwell's equation, interactions, except for magnetic interaction, are replaced by dielectric constant in a medium and by boundary condition on a surface. On the other hand, the concept of effective mass has been popular in the field theory which simplifies complicated interactions of particles with the medium.

The identity of nanometric evanescent light can be considered as a quasi-static or Coulomb-like interaction between electric polarizations induced on the sample surface by the incident or the reflected propagating light. In this sense, the evanescent light correlates a pair of incident and reflected lightwaves at one position on the surface with that at the other position. This implies that the evanescent light represents the propagator similar to the two particle-Green's function, which integrates the many-body interaction on the surface. This picture is consistent with the quantum theory of the

evanescent electromagnetic field near a flat dielectric surface, developed by Carniglia and Mandel [62].

B. Theoretical Model of a Photon Scanning Tunneling Microscope

Based on the consideration given in Subsection A, the fundamental process of PSTM can be modeled as a localized interaction via evanescent photons between two closely spaced small dielectric spheres coupled to incoming and outgoing propagating photons. This requires us to extend the description of near-field optical propagator to the case of closely spaced disconnected surfaces, i.e., the propagator connecting electric polarizations of two closely spaced dielectric spheres. In this sense, the interaction in PSTM has a close relation to the van der Waals force which is described by an exchange of two virtual photons connecting polarizations of two closely spaced dielectric objects. The difference is that the range of the PSTM interaction is greater than that of the van der Waals force because the electric polarization is enhanced by the incidence of propagating light. It should be noted that it might be difficult to solve Maxwell's equation under such a disconnected boundary condition.

In order to describe the interaction of a nanometric sample-probe system, the model, together with the virtual photon picture, makes it possible to interpret the PSTM process as a particle tunneling through an effective potential barrier. Similar to the resonant tunneling effect, multiple scattering processes between two nanometric objects are essential to produce a considerable increase of the tunneling probability. This implies that the PSTM process is basically a destructive measurement of the evanescent light. In the model of the localized evanescent light using a Yukawa function, such a many-body interaction is reduced to the effective mass or Compton wavelength of tunneling photons determined by the size of the interacting bodies. As a natural consequence of the reduced many-body interaction, the idea of resonance in the sample-probe interaction can be introduced; that is, the evanescent lights on the two objects couple to each other if their Compton wavelengths are equal. This is due to the momentum conservation in the exchange of evanescent photons between the sample and probe tip.

The optical near-field of the nanometric sample-probe system can be approximated as a sum of evanescent lights with several different Compton wavelengths, which may correspond to spatial-Fourier expansion of optical near-field. This is also equivalent to approximating the sample-probe system by a set of small spheres having several different radii. This simple picture of PSTM leads to natural definitions of the resolution and pick-up efficiency of evanescent light. As shown by Fig. 31(a) for the C-mode PSTM, let us consider a small dielectric sphere of radius r_0 as a sample placed on a substrate surface. The surface is described by dielectric spheres whose radii are equal to the wavelength $\lambda (\gg r_0)$ of incident propagating light because the evanescent light at total internal reflection angle is characterized by a decay length of the order of λ . On the other hand, consider a probe tip described by a set of dielectric spheres approximating its conical shape, as

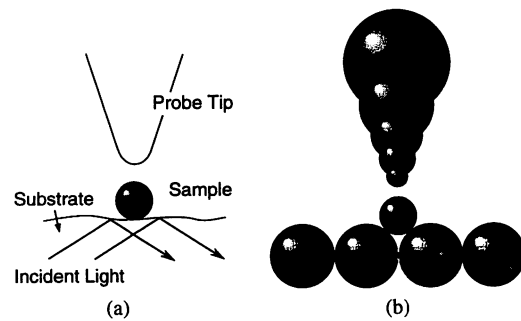


Fig. 31. Model of sample-probe interaction in PSTM. Nanometric sample, probe tip, and substrate shown in (a) are approximated as sets of dielectric spheres, as shown in (b), around which spatial-Fourier components of the evanescent lights are localized.

shown by Fig. 31(b). According to the resonance assumption described above, the resolution of the PSTM depends on the radius of the sphere at the extremity of the probe tip. In determining the resolution, the most important point is considered to be the filtering characteristic of the evanescent light generated on the substrate surface. Consider the case that the sample-probe separation is equal to the curvature radius r_0 of the probe tip. Then, the tunneling probability of the evanescent light with Compton wavelength of r_0 is e^{-1} , and the evanescent lights with shorter Compton wavelengths due to small bumps on the sample surface are filtered out since their interaction ranges are much shorter than the sample-probe separation.

When the probe tip has an obtuse profile with a large cone angle, the evanescent lights having Compton wavelengths larger than r_0 have a relatively large tunneling probability, and consequently these evanescent lights give considerable contributions to the total evanescent light picked up by the probe. On the other hand, when the probe tip has an acute profile with a small cone angle, the evanescent lights with Compton wavelengths larger than r_0 are filtered out because the corresponding spheres recede more rapidly than the increase in their radius. Thus, these evanescent lights could give minor contributions to the total evanescent light picked up by the probe. As a consequence, the PSTM process can be viewed as a kind of spatial filtering of the optical near-field. Therefore, the curvature radius and cone angle of the probe tip and, furthermore, the sample-probe separation could determine the resolution and the dependency of the pick-up efficiency on the spatial-Fourier frequency, i.e., the characteristics of the transfer function of the PSTM system.

In order to estimate the transfer function of the C-mode PSTM, the tunneling photon current was derived by calculating the overlap integral of the evanescent lights described by the Yukawa function, according to the resonance tunneling picture or the tunneling current descriptions. Since the present model of PSTM is based on the modified Helmholtz equation, the calculation is almost similar to those in STM [63].

Fig. 32 shows the calculated results of the transfer function for several values of curvature radii, cone angles, and sample-probe separations. These curves exhibit the characteristics of a bandpass filtering, and the high-frequency cutoff is determined by the curvature radius of the probe tip (see,

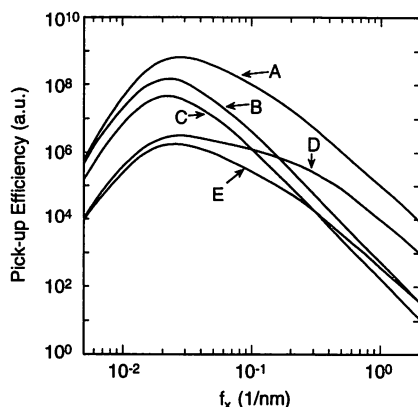


Fig. 32. Calculated results of the transfer function of the PSTM system with vertical axis being pick-up efficiency. The horizontal axis represents the spatial Fourier frequency f_x . The curvature radius r_0 and cone angle θ of the probe tip, and the sample-probe separation d are $r_0 = 5$ nm, $\theta = 100^\circ$, $d = 1$ nm (A); $r_0 = 100$ nm, $\theta = 100^\circ$, $d = 1$ nm (B); $r_0 = 100$ nm, $\theta = 20^\circ$, $d = 1$ nm (C); $r_0 = 5$ nm, $\theta = 20^\circ$, $d = 1$ nm (D); and $r_0 = 5$ nm, $\theta = 20^\circ$, $d = 10$ nm (E), respectively.

for example, curve D) which gives the resolution of the PSTM. However, it is found by comparing curves A and D that such cutoff characteristics are not seen clearly in the case of a larger cone angle. Furthermore, it is also found by comparing curves D and E that the efficiency decreases with increasing sample-probe separation, especially at the high spatial-Fourier frequency region. These characteristics of the transfer functions give quantitative descriptions of the discussion given above. Furthermore, it should be noted that characteristics of the images obtained experimentally, e.g., the results reviewed in Section IV-B-1 agree qualitatively with those described by the transfer functions derived here. Thus, in order to analyze the characteristics of the observed image, it is essential to find the transfer function of the PSTM system, which could be more important than paying attention only to the resolution.

As shown by the example given here, it is straightforward to calculate the transfer function which in turn corresponds to the calculation of the tunneling photon current or pick-up efficiency, since the model describes the interaction between nanometric objects characterized by a Compton wavelength determined by their sizes. This fact allows us to calculate the pick-up efficiency for a sample and probe tip of arbitrary shapes in the same manner, using spatial-Fourier expansion. This is an essential feature of the local theory we proposed. A direct quantitative comparison of the Yukawa function model to the electromagnetic field theory based on the self-consistent approach given by Labani *et al.* [58] and Vigoureux *et al.* [59] is now in progress.

VIII. SUMMARY

We have reviewed the present status of the PSTM and its application, with the main focus on tackling the most essential problems including fabrication of nanometer-sized fiber probes and apertures. To realize a nanometric apertured fiber probe for the PSTM, highly reproducible chemical etching process was developed to sharpen a fiber with the minimum cone

angle of 14° and curvature diameter of the fiber tip of 3 nm. Furthermore, by etching, the possibility of controlling the tip shape of the resulting fibers was also presented. In the process of fabricating a flattened-top fiber tip, peculiar etching properties were discovered, which were very different from those of bulk silica glasses, and we believe this may help in understanding the fundamental process of sharpening the fiber to nanometric dimension. In order to fabricate a metallic aperture at the top of the sharpened fiber, chemical etching process and three-dimensional nanometric photolithography were developed to realize aperture diameters as small as 30 nm (or even smaller).

Imaging experiments on biological specimens by the collection and illumination mode geometries were reviewed. Especially, in the case of the collection mode, dependencies of the observed images on the polarization state of the incident light were found, and these were attributed to the difference in the distribution of electric lines of force of the evanescent light. From these experimental results, the estimated resolution was about 10 nm (or even smaller). This value was smaller than the aperture diameter of the probe tip, because the evanescent light was preferably scattered at the top of the probe tip protruding from the metallic film. In the case of the experiments on illumination mode PSTM using a metal-coated fiber probe having a flattened top, high-resolution results were obtained. Such a high resolution was attributed to the edge effect of the probe tip at the boundary between the glass surface and the rim of the metallic film.

Possibilities of nondestructively inspecting guiding characteristics of a dielectric optical waveguide were demonstrated with subwavelength resolution. Furthermore, possibilities of evaluating the characteristics of the nanometric active photonic devices were demonstrated through imaging experiments of semiconductor quantum dots. In experiments of fluorescence detection from dye-doped polystyrene spheres with the collection mode PSTM, high-sensitivity and high-resolution results were obtained. Such results could be explained in terms of a short-range electromagnetic interaction between the sphere and probe tip.

In order to demonstrate the possibilities of nanometric fabrication, high-density optical storage by the illumination mode PSTM was reviewed. In the case of the photon-mode storage, a circular pit of diameter 100 nm and a stripe of width 100 nm were stored on an organic thin film. A method of increasing the storage density was also proposed. As an ultimate goal of fabrication, controlling thermal motion of freely flying atoms in vacuum through interaction with the evanescent light was reviewed to explore the future technology of the atomic level material processing. As the promising methods of such control, an atom guide using a hollow fiber and atom trapping by the probe under the illumination-mode PSTM were proposed.

To investigate the principle of PSTM and to analyze the experimental results, the concept of the virtual photon was introduced. The proposed concept provides us with a semiclassical theory based on the intuitive modeling of the localized evanescent light. Calculated results obtained using this model were presented, and these agreed with those obtained from the

boundary problems based on the conventional electromagnetic theories. Transfer functions for characterizing the PSTM were also derived, which agreed qualitatively with the results of imaging experiments.

It should be noted that the principle of operation and application of the PSTM are relevant to a wide range of fields, such as surface physics, quantum optics, photonics, bioscience and technology, and chemistry. It can be expected that the PSTM, as one member of fiber sensors, can be used not only for a variety of photonic sensing with high spatial resolution but also opens up the possibility of using it as a nanometric fabrication tool to produce novel photonic materials and nanometric devices in the future.

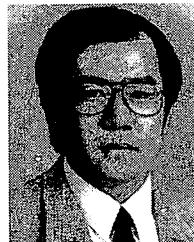
ACKNOWLEDGMENT

The author would like to thank Prof. A. Ikai, Prof. M. Fujihira (Tokyo Institute of Technology), Prof. Y. Arakawa (University of Tokyo), Prof. S. Aizawa (Teikyo University), and Prof. H. Tatsumi (Tokyo Medical and Dental University) for providing him with organic, semiconductor, and biological specimens. He also acknowledges Prof. H. Hori (Yamanashi University) for his collaboration in conducting theoretical investigation. His thanks also to Dr. H. Tanaka and Dr. T. Gozen (Mitsubishi Cable Industries) and Dr. S. Miyamoto (Fujikura Ltd.) for their useful comments on fibers. He is also indebted to Dr. T. Saiki, Dr. R. Uma Maheswari, Dr. S. Mononobe, Dr. M. Naya, Dr. H. Ito, Dr. K. Kurihara, Dr. R. Micheletto (Kanagawa Academy of Science and Technology), Dr. S. Jiang, M. Kourogi, Y. Toda, T. Matsumoto, and K. Imai (Tokyo Institute of Technology) for providing him with figures. He expresses special thanks to Dr. R. Uma Maheswari for her critical reading and comments on the manuscript.

REFERENCES

- [1] E. H. Syngé, "A suggested method for extending microscopic resolution into ultra-microscopic resolution," *Phil. Mag.*, vol. 6, pp. 356–362, 1928.
- [2] E. A. Ash and G. Nicholls, "Super-resolution aperture scanning microscope," *Nature*, vol. 237, pp. 510–512, June 1972.
- [3] D. W. Pohl, "Some remarks on the history on near-field optics," in *Near Field Optics*, D. W. Pohl and D. Courjon, Eds. Dordrecht: Kluwer, 1993, pp. 1–5.
- [4] J. M. Vigoureux, C. Girard, and D. Courjon, "General principles of scanning tunneling optical microscopy," *Opt. Lett.*, vol. 14, pp. 1039–1041, Oct. 1989.
- [5] E. Wolf and M. Nieto-Vesperinas, "Analyticity of the angular spectrum amplitude of scattered fields and some of its consequences," *J. Opt. Soc. Amer.*, vol. 2, pp. 886–889, June 1985.
- [6] S. Jiang, K. Nakagawa, and M. Ohtsu, "Reflection-resonance-type photon scanning tunneling microscope," *Japan. J. Appl. Phys.*, vol. 33, pp. L55–L58, Jan. 1994.
- [7] C.-H. Shin and M. Ohtsu, "Heterodyne optical phase-locked loop by confocal Fabry–Perot cavity coupled AlGaAs lasers," *IEEE Photon. Technol. Lett.*, vol. 2, pp. 297–300, Apr. 1990.
- [8] E. Betzig, S. G. Grubb, R. J. Chichester, D. J. DiGiovanni, and J. S. Weiner, "Fiber laser probe for near-field scanning optical microscopy," *Appl. Phys. Lett.*, vol. 63, pp. 3550–3552, Dec. 1993.
- [9] M. Fee, S. Chu, and T. W. Hansch, "Scanning electromagnetic transmission line microscope with sub-wavelength resolution," *Opt. Commun.*, vol. 69, pp. 219–224, Jan. 1989.
- [10] K. Liberman, S. Harush, A. Lewis, and R. Kopelman, "A light source smaller than the optical wavelength," *Science*, vol. 247, pp. 59–61, Jan. 1990.
- [11] D. W. Pohl, W. Denk, and M. Lanz, "Optical stethoscopy: Image recording with resolution $\lambda/20$," *Appl. Phys. Lett.*, vol. 44, pp. 651–653, Apr. 1984.
- [12] H. Pagnia, J. Radojewski, and N. Sotnik, "Operation conditions of an optical STM," *Optik*, vol. 86, pp. 87–90, Mar. 1990.
- [13] T. Pangaribuan, K. Yamada, S. Jiang, H. Ohsawa, and M. Ohtsu, "Reproducible fabrication technique of nanometric tip diameter fiber probe for photon scanning tunneling microscope," *Japan. J. Appl. Phys.*, vol. 31, pp. L1302–L1304, Sept. 1992.
- [14] F. L. Galeener, "Planar rings in vitreous silica," *J. Non-Crystalline Solids*, vol. 49, pp. 53–62, 1982.
- [15] T. Pangaribuan, S. Jiang, and M. Ohtsu, "Two-step etching method for fabrication of fibre probe for photon scanning tunneling microscope," *Electron. Lett.*, vol. 29, pp. 1978–1979, Oct. 1993.
- [16] T. Pangaribuan, S. Jiang, and M. Ohtsu, "Highly controllable fabrication of fiber probe for photon scanning tunneling microscope," *Scanning*, vol. 16, pp. 362–367, Dec. 1994.
- [17] M. Kawachi, T. Edahiro, and H. Toba, "Microlens formation on VAD single-mode fiber ends," *Electron. Lett.*, vol. 17, pp. 71–72, Jan. 1982.
- [18] S. Mononobe, M. Naya, R. Uma Maheswari, T. Saiki, and M. Ohtsu, "Fabrication technique of pencil-type fiber probes and nanometric apertures for a photon scanning tunneling microscope," *Int. Conf. Near Field Opt. Related Technol.*, Bruno, Czech, May 1995, paper NPR-P03.
- [19] E. Betzig, A. Lewis, A. Harootunian, M. Isaacson, and E. Kratschmer, "Near-field scanning optical microscopy (NSOM): Development and biological applications," *Biophys. J.*, vol. 49, pp. 269–279, Jan. 1986.
- [20] R. Uma Maheswari, S. Mononobe, M. Naya, T. Saiki, and M. Ohtsu, "Fabrication of a fiber probe with nano-aperture for photon scanning tunneling microscope," presented at the OSA Ann. Meet. Dallas, TX, Oct. 1994, paper ThEEE2.
- [21] R. Kopelman, W. Tan, Z.-Y. Shi, and D. Birnbaum, "Near field optical and exciton imaging, spectroscopy and chemical sensors," in *Near Field Optics*, D. W. Pohl and D. Courjon, Eds. Dordrecht: Kluwer, 1993, pp. 17–24.
- [22] H.-U. Danzebrink and U. C. Fischer, "The concept of an optoelectronic probe for near field microscopy," in *Near Field Optics*, D. W. Pohl and D. Courjon, Eds. Dordrecht: Kluwer, 1993, pp. 303–308.
- [23] W. Tan, Z.-Y. Shi, and R. Kopelman, "Development of submicron chemical fiber optic sensors," *Anal. Chem.*, vol. 64, pp. 2985–2990, Dec. 1992.
- [24] S. Kawata, Y. Inoue, and T. Sugiura, "Near-field scanning optical microscope with a laser trapped probe," *Japan. J. Appl. Phys.*, vol. 33, pp. L1725–L1727, Dec. 1994.
- [25] E. Betzig, P. L. Finn, and J. S. Weiner, "Combined shear force and near-field scanning optical microscopy," *Appl. Phys. Lett.*, vol. 60, pp. 2484–2486, May 1992.
- [26] S. Jiang, H. Ohsawa, K. Yamada, T. Pangaribuan, M. Ohtsu, K. Imai, and A. Ikai, "Nanometric biosample observation using a photon scanning tunneling microscope," *Japan. J. Appl. Phys.*, vol. 31, pp. 2282–2287, July 1992.
- [27] T. Hirano, S. Yamaguchi, K. Oosawa, and S. Aizawa, "Roles of FliK and FlhB in determination of flagellar hook length in *salmonella typhimurium*," *J. Biotechnol.*, vol. 176, pp. 5439–5449, Sept. 1994.
- [28] S. Okabe and N. Hirokawa, "Microtubule dynamics in nerve cells: Analysis using microinjection of biotinylated tubulin into PC12 cells," *J. Cell Biol.*, vol. 107, pp. 651–664, Aug. 1988.
- [29] G. P. Collins, "Near-field optical microscopes take a close look at individual molecules," *Phys. Today*, vol. 47, pp. 17–20, May 1994.
- [30] A. Miki, Y. Okamura, and S. Yamamoto, "Optical waveguide directional coupler measurements using a microcomputer-assisted TV camera system," *J. Lightwave Technol.*, vol. 7, pp. 1912–1918, Dec. 1989.
- [31] D. P. Tsai, H. E. Jackson, R. C. Reddick, S. H. Sharp, and R. J. Warmack, "Photon scanning tunneling microscope study on optical waveguide," *Appl. Phys. Lett.*, vol. 56, pp. 1515–1517, Apr. 1990.
- [32] Y. Toda and M. Ohtsu, "High spatial resolution diagnostics of optical waveguides using a photon scanning tunneling microscope," *IEEE Photon. Technol. Lett.*, vol. 7, pp. 84–86, 1995.
- [33] S. Tukamoto, Y. Nagamune, M. Nishioka, and Y. Arakawa, "Fabrication of GaAs quantum wires (–10 nm) by metalorganic chemical vapor selective deposition growth," *Appl. Phys. Lett.*, vol. 63, pp. 355–357, July 1993.
- [34] H. F. Hess, E. Betzig, T. D. Harris, L. N. Pfeiffer, and K. W. West, "Near-field spectroscopy of the quantum constituents of a luminescent system," *Science*, vol. 264, pp. 1740–1745, June 1994.
- [35] R. D. Grober, T. D. Harris, J. K. Trautman, E. Betzig, W. Wegscheider, L. Pfeiffer, and K. West, "Optical spectroscopy of a GaAs/AlGaAs quantum wire structure using near-field scanning optical microscopy," *Appl. Phys. Lett.*, vol. 64, pp. 1421–1423, Mar. 1994.
- [36] J. K. Trautman, J. J. Macklin, L. E. Brus, and E. Betzig, "Near-field spectroscopy of single molecules at room temperature," *Nature*, vol. 369, pp. 40–42, May 1994.

- [37] W. P. Ambrose, P. M. Goodwin, J. C. Martin, and R. A. Keller, "Single molecule detection and photochemistry on a surface using near-field optical excitation," *Phys. Rev. Lett.*, vol. 72, pp. 160-163, Jan. 1994.
- [38] X. S. Xie and R. C. Dunn, "Probing single molecule dynamics," *Science*, vol. 265, pp. 361-364, July 1994.
- [39] T. Saiki, S. Mononobe, and M. Ohtsu, "Nanometric integration tip: Enhanced sensitivity of fluorescence detection in Photon STM," in *Quantum Electron. Laser Sci. Conf.*, 1995 OSA Tech. Dig. Series, vol. 4 (Opt. Soc. Amer., Washington, DC, 1995), paper QTuJ3.
- [40] P. J. Moyer, C. L. Jahncke, M. A. Paesler, R. C. Reddick, and R. J. Warmack, "Spectroscopy in the evanescent field with an analytical photon scanning tunneling microscope," *Phys. Lett. A*, vol. 145, pp. 343-347, Apr. 1990.
- [41] D. P. Tsai, A. Othonos, M. Woskivits, and D. Uttamachandani, "Raman spectroscopy using a fiber optic probe with subwavelength aperture," *Appl. Phys. Lett.*, vol. 64, pp. 1768-1770, Apr. 1994.
- [42] P. Dawson, F. de Fornel, and J.-P. Goudonnet, "Imaging of surface plasmon propagation and edge interaction using a photon scanning tunneling microscope," *Phys. Rev. Lett.*, vol. 72, May 1994.
- [43] M. Specht, J. D. Pedarnig, W. M. Heckel, and T. W. Hansch, "Scanning plasmon near-field microscope," *Phys. Rev. Lett.*, vol. 68, pp. 476-479, Jan. 1992.
- [44] E. Betzig, J. K. Tautman, R. Wolfe, E. M. Gyorgy, P. L. Finn, M. H. Kryder, and C.-H. Chang, "Near-field magneto-optics and high density data storage," *Appl. Phys. Lett.*, vol. 61, pp. 142-144, July 1992.
- [45] S. Jiang, J. Ichihashi, H. Monobe, M. Fujihira, and M. Ohtsu, "Highly localized photochemical processes in LB films of photochromic material by using a photon scanning tunneling microscope," *Opt. Commun.*, vol. 106, pp. 173-177, Mar. 1994.
- [46] V. I. Balykin and V. S. Letokhov, "Laser optics of neutral atomic beams," *Phys. Today*, vol. 42, Apr. 1989.
- [47] H. Mabuchi and H. J. Kimble, "Atomic galleries for whispering atoms: Binding atoms in stable orbits around an optical resonator," *Opt. Lett.*, vol. 19, pp. 749-751, May 1994.
- [48] M. A. Ol'Shannii, Yu. B. Ovchinnikov, and V. S. Letokhov, "Laser guiding of atoms in a hollow optical fiber," *Opt. Commun.*, vol. 98, pp. 77-79, Apr. 1993.
- [49] S. Marksteiner, C. M. Savage, and P. Zoller, "Coherent atomic waveguides from hollow optical fibers: Quantized atomic motion," *Phys. Rev. A*, vol. 50, pp. 2680-2690, Sept. 1994.
- [50] W. Jhe, M. Ohtsu, H. Flori, and R. Freiberg, "Atomic waveguide using evanescent waves near optical fibers," *Japan. J. Appl. Phys.*, vol. 33, pp. L1680-L1682, Dec. 1994.
- [51] H. Ito, K. Sakaki, T. Nakata, W. Jhe, and M. Ohtsu, "Optical potential for atom guidance in a cylindrical-core hollow fiber," *Opt. Commun.*, vol. 113, 1995, pp. 57-64.
- [52] C. Monroe, W. Swann, H. Robinson, and C. Wieman, "Very cold trapped atoms in a vapor cell," *Phys. Rev. Lett.*, vol. 65, pp. 1571-1574, Sept. 1990.
- [53] H. Hori, S. Jiang, M. Ohtsu, and H. Ohsawa, "A nanometer-resolution photon scanning tunneling microscope and proposal of single atom manipulation," in *Tech. Dig. 18th Int. Quantum Electron. Conf.*, Vienna, June 1992, pp. 48-49.
- [54] J. P. Gordon and A. Ashkin, "Motion of atoms in a radiation trap," *Phys. Rev. A*, vol. 21, pp. 1606-1617, May 1980.
- [55] M. Kozuma, S. Jiang, T. Pangaribuan, M. Ohtsu, and H. Hori, "Analysis and experimental evaluation of a localized evanescent field by using Yukawa potential," in *Tech. Dig. Quantum Electron. Laser Sci.*, Baltimore, May 1993, pp. 227-228.
- [56] J. P. Dowling and J. Gea-Banacloche, "Atomic quantum dots," in *Int. Quantum Electron. Conf.*, vol. 9, 1994 OSA Tech. Dig. Series (Opt. Soc. Amer., Washington DC, May 1994), pp. 185-186.
- [57] M. Ohtsu, K. Nakagawa, M. Kourogi, and W. Wang, "Frequency control of semiconductor lasers," *J. Appl. Phys.*, vol. 73, pp. R1-R17, June 1993.
- [58] B. Labani, C. Girard, D. Courjon, and D. Van Lebeke, "Optical interaction between a dielectric tip and a nanometric lattice: Implications for near-field microscopy," *J. Opt. Soc. Amer. B*, vol. 7, pp. 936-943, June 1990.
- [59] J. M. Vigoureaux, F. Depasse, and C. Girard, "Superresolution of near-field optical microscopy defined from properties of confined electromagnetic waves," *Appl. Opt.*, vol. 31, pp. 3036-3045, June 1992.
- [60] U. Ch. Fischer and D. W. Pohl, "Observation of single-particle plasmons of near field optical microscopy," *Phys. Rev. Lett.*, vol. 62, pp. 458-461, Jan. 1989.
- [61] Y. Leviatan, "Study of near-zone fields of a small aperture," *J. Appl. Phys.*, vol. 60, pp. 1577-1583, Sept. 1986.
- [62] C. K. Carniglia and L. Mandel, "Quantization of evanescent electromagnetic waves," *Phys. Rev. D*, vol. 3, pp. 280-296, Jan. 1971.
- [63] C. J. Chen, "Tunneling matrix elements in three-dimensional space: The derivative rule and the sum rule," *Phys. Rev. B*, vol. 42, pp. 8841-8857, Nov. 1990.



Motoichi Ohtsu (M'88-SM'90) was born in Kanagawa, Japan, on October 5, 1950. He received the B.E., M.E., and Dr.E. degrees in electronics engineering from the Tokyo Institute of Technology, Tokyo, Japan, in 1973, 1975, and 1978, respectively.

In 1978 he was appointed a Research Associate, and in 1982 he became Associate Professor at the Tokyo Institute of Technology. From 1986 to 1987, while on leave from Tokyo Institute of Technology, he joined the Crawford Hill Laboratory, AT&T Bell Laboratories, Holmdel, NJ. In 1991 he became a Professor at the Tokyo Institute of Technology. Since April 1993, he has been concurrently the leader of the "Photon Control" project of Kanagawa Academy of Science and Technology, Kanagawa, Japan. His main fields of interest are photon scanning tunneling microscopy, its application to nano-scale photonics and quantum optics, and laser frequency control. He has written over 130 papers, and has received a number of patents. He is the author and coauthor of thirteen books, including two in English, entitled *Highly Coherent Semiconductor Lasers* (Boston, MA: Artech House, 1992) and *Coherent Quantum Optics and Technology* (Dordrecht: Kluwer, 1993). He has been a tutorial lecturer of the SPIE and OSA.

Dr. Ohtsu has been awarded eight prizes from academic institutions, including the Issac Koga Gold Medal of URSI in 1984, Japan IBM Science Award in 1988, and two awards of the Japan Society of Applied Physics in 1982 and 1990. He is a member of the Institute of Electronics, Information and Communication Engineers of Japan, the Institute of Electrical Engineering of Japan, the Japan Society of Applied Physics, and the Optical Society of America.

Optical potential for atom guidance in a cylindrical-core hollow fiber

Haruhiko Ito^a, Keiji Sakaki^b, Takeshi Nakata^b, Wonho Jhe^c, Motoichi Ohtsu^{a,b}

^a *Kanagawa Academy of Science and Technology, KSP East, 3-2-1 Sakado, Takatsu-ku, Kawasaki 213, Japan*

^b *Interdisciplinary Graduate School of Science and Engineering, Tokyo Institute of Technology,
4259, Nagatsuta-cho, Midori-ku, Yokohama 226, Japan*

^c *Department of Physics, Seoul National University, Seoul 151-742, South Korea*

Received 30 August 1994; revised version received 12 December 1994

Abstract

We describe a practical atomic waveguide using a cylindrical-core hollow fiber. Theoretical analyses of propagating field modes are presented for a multimode fiber. An evanescent wave leaked out to the hollow region is shown to produce a deep optical potential enough to guide atoms with low coupling laser power under an optimal blue-detuning determined by fiber parameters, exciting mode and azimuthal angle. The excitation of an HE_{11} mode required for stable atomic guidance in the multimode hollow fiber is experimentally realized with the power-coupling efficiency of more than 10%.

1. Introduction

Atomic waveguides using evanescent waves have been proposed by two groups; one with a hollow fiber [1] and the other with a combination of eccentric-core fibers [2]. Contrary to the previous proposal using a Gaussian laser beam propagating inside a hollow fiber to guide atoms [3], these types of atomic waveguide can reduce strong heating effects on atoms suffered from a copropagating intense laser beam [3], because the evanescent waves are employed to produce an optical potential for atomic guidance: the evanescent waves leaked out within one wavelength from the inner core-surface repel the approaching atoms. The realization of atomic waveguides will promote interesting studies in atom optics, near-field optics and cavity QED. One of our goals is the nano-scale crystal growth using atom manipulation techniques with lasers [4]. Atomic waveguides are expected to be useful tools for our purpose. In contrast to the traditional thermal or chemical methods involving a process treating a large number of atoms at once, the mechanical one using atomic waveguides enables one even to handle a single atom.

In this paper, we describe a hollow fiber with a thin cylindrical core appropriate for the atomic waveguide using the evanescent wave. The optimal conditions for atomic guidance are clarified through the quantitative analyses of the optical potential due to the evanescent wave near the inner surface of the hollow fiber assuming the classical motion of atoms. At first, we analytically write down the dispersion equations for the cylindrical-core hollow fiber. The light propagation modes are derived from the numerical solutions of the dispersion equations, featuring a multimode fiber with practical parameters. Since a multimode hollow fiber generally has

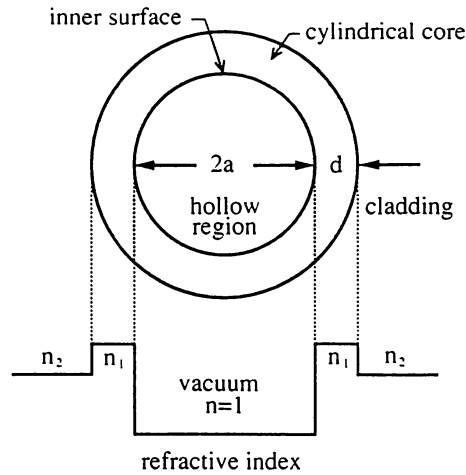


Fig. 1. The diagram of the cylindrical-core hollow fiber. The diameter of the hollow region and the thickness of the cylindrical core (hatched area) are $2a$ and d , respectively. The cladding can be taken to be infinite. The refractive indices stepwise change as 1, n_1 and n_2 in order from inside.

a large hollow region and a large numerical aperture so that it can facilitate the coupling of atoms and laser beams to the fiber, the use of the multimode fiber is convenient for a demonstration of the atomic waveguide. Secondly, we discuss the repulsive optical potential to guide Rb atoms in the case of the excitation of an HE_{11} mode which is the fundamental one for the hollow fiber. The dependences of the potential barrier on coupling power, frequency detuning and azimuthal angle are investigated. Lastly, we show laser excitation of the several propagating modes for the multimode hollow fiber. The selected excitations of the modes are carried out by adjusting the incident angle.

The evanescent wave yields the intense gradient force due to the exponential decay of the field. The depth of the optical potential originating from the gradient force depends on the field intensity. The core thickness of the present hollow fiber is only a few μm and the power density in the core is dense with several mW coupling power, with the result that the optical potential can be deep enough to overcome comparative atomic transverse kinetic energy. A well-collimated atomic beam is appropriate as the source of the atoms injected into the proposed atomic waveguide. The attachment of a funneled device will be useful for pouring atoms into the facet of the hollow fiber [5].

2. Light propagation characteristics of a cylindrical-core hollow fiber

The light propagation modes of the cylindrical-core hollow fiber are analyzed similarly to that of a concentric-core fiber based on Maxwell equations expressed in terms of the cylindrical coordinate system (r, θ, z) . Fig. 1 shows the step-index hollow fiber. The diameter of the vacuum hollow region and the thickness of the cylindrical core are $2a$ and d , respectively. We assume that the cladding is much thicker than both the hollow region and the cylindrical core. The refractive indices of the cylindrical core and the cladding are n_1 and n_2 , respectively.

We consider the electromagnetic field propagating along the z -axis in the cylindrical core.

$$E(r, \theta, z, t) = E_0(r, \theta) \exp(i\omega t - i\beta z), \quad (1)$$

$$H(r, \theta, z, t) = H_0(r, \theta) \exp(i\omega t - i\beta z), \quad (2)$$

where ω and β are the angular frequency and the propagation constant, respectively, $E_0 = (E_r, E_\theta, E_z)$ and $H_0 = (H_r, H_\theta, H_z)$. The longitudinal component E_z follows the Maxwell equation [6],

$$\frac{\partial^2 E_z}{\partial r^2} + \frac{1}{r} \frac{\partial E_z}{\partial r} + \frac{1}{r^2} \frac{\partial^2 E_z}{\partial \theta^2} + (k^2 n^2 - \beta^2) E_z = 0, \quad (3)$$

where k and n are the wave number and the refractive index, respectively. The similar equation is written for H_z . The solution satisfying Eq. (3) is given by

$$\begin{aligned} E_z(r, \theta) &= AI_m(ur) \sin(m\theta + \phi) \quad (r < a), \\ &= [BJ_m(ur) + CN_m(ur)] \sin(m\theta + \phi) \quad (a \leq r \leq b), \\ &= DK_m(wr) \sin(m\theta + \phi) \quad (r > b), \end{aligned} \quad (4)$$

where J_m and N_m are the Bessel functions of the first and the second kind of order m , respectively, I_m and K_m are the modified Bessel functions of the first and the second kind of order m , respectively, ϕ is an arbitrary phase constant and $b = a + d$. The constants A , B , C and D should be determined by the continuous conditions for the tangential components E_θ , E_z , H_θ and H_z at the boundaries $r = a$ and b . The quantity $u = \sqrt{k^2 n_1^2 - \beta^2}$ is a transverse propagation constant, while $v = \sqrt{\beta^2 - k^2}$ and $w = \sqrt{\beta^2 - k^2 n_2^2}$ are transverse attenuation constants. We obtain the similar solution of the longitudinal magnetic component H_z by replacing $\sin(m\theta + \phi)$ by $\cos(m\theta + \phi)$ in Eq. (4). The other components E_r , E_θ , H_r and H_θ are derived from the longitudinal ones E_z and H_z [6].

We derive the dispersion equations describing the light propagation modes of the cylindrical-core hollow fiber from the secular equation, which is obtained by applying the boundary conditions to the tangential components E_z , E_θ , H_z and H_θ [6]. After the long but straightforward calculations, we get the next equation;

$$\begin{aligned} [\text{TE}][\text{TM}] &+ \left[\frac{1}{ab} \left(\frac{\beta m}{k} \right)^2 \left(\frac{1}{u^2} + \frac{1}{v^2} \right) \left(\frac{1}{u^2} + \frac{1}{w^2} \right) [J_m(ua) N_m(ub) - J_m(ub) N_m(ua)] \right]^2 \\ &+ \frac{1}{ab} \left(\frac{\beta m}{k} \right)^2 \left\{ \frac{2n_1^2}{u^2} \left(\frac{1}{u^2} + \frac{1}{v^2} \right) \left(\frac{1}{u^2} + \frac{1}{w^2} \right) \right. \\ &\times [J_m(ua) N_m'(ua) - J_m'(ua) N_m(ua)] [J_m(ub) N_m'(ub) - J_m'(ub) N_m(ub)] \\ &- \frac{a}{b} \left(\frac{1}{u^2} + \frac{1}{w^2} \right)^2 \left[\left(\frac{1}{u} N_m'(ua) + \frac{1}{v} \frac{I_m'(va)}{I_m(va)} N_m(ua) \right) J_m(ub) \right. \\ &- \left. \left(\frac{1}{u} J_m'(ua) + \frac{1}{v} \frac{I_m'(va)}{I_m(va)} J_m(ua) \right) N_m(ub) \right] \\ &\times \left[\left(\frac{n_1^2}{u} N_m'(ua) + \frac{1}{v} \frac{I_m'(va)}{I_m(va)} N_m(ua) \right) J_m(ub) - \left(\frac{n_1^2}{u} J_m'(ua) + \frac{1}{v} \frac{I_m'(va)}{I_m(va)} J_m(ua) \right) N_m(ub) \right] \\ &- \frac{b}{a} \left(\frac{1}{u^2} + \frac{1}{v^2} \right)^2 \left[\left(\frac{1}{u} N_m'(ub) + \frac{1}{w} \frac{K_m'(wb)}{K_m(wb)} N_m(ub) \right) J_m(ua) \right. \\ &- \left. \left(\frac{1}{u} J_m'(ub) + \frac{1}{w} \frac{K_m'(wb)}{K_m(wb)} J_m(ub) \right) N_m(ua) \right] \\ &\times \left[\left(\frac{n_1^2}{u} N_m'(ub) + \frac{n_2^2}{w} \frac{K_m'(wb)}{K_m(wb)} N_m(ub) \right) J_m(ua) \right. \\ &- \left. \left(\frac{n_1^2}{u} J_m'(ua) + \frac{n_2^2}{w} \frac{K_m'(wb)}{K_m(wb)} J_m(ub) \right) N_m(ua) \right] \left. \right\} = 0, \end{aligned} \quad (5)$$

where prime signs express the differentiation with respect to r . The factors [TE] and [TM] are written as

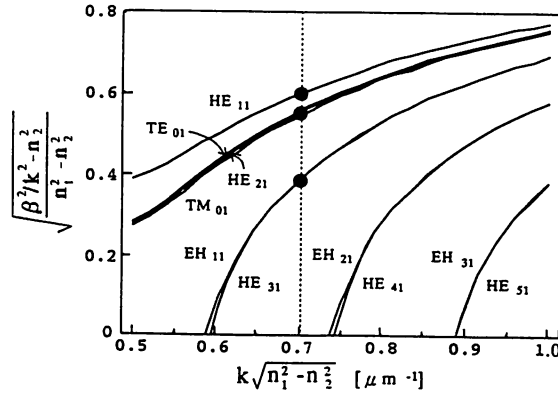


Fig. 2. The dispersion curves of the light propagation modes of low orders for $\lambda = 780$ nm in a cylindrical-core hollow fiber with $2a=7$ μm , $d=3.8$ μm and $\Delta n=0.18\%$. The normalized propagation constant $\sqrt{(\beta^2 k^2 - n_2^2)/(n_1^2 - n_2^2)}$ is shown as a function of the normalized wave number $k\sqrt{n_1^2 - n_2^2}$. The broken line shows the normalized wave number in the present case ($n_2 = 1.45$ for a silica fiber). The coupling modes are indicated by the solid circles; HE₁₁, TE₀₁, TM₀₁, HE₂₁, EH₁₁ and HE₃₁. The cutoffs arise at the points where the normalized propagation constants become zero, namely on the horizontal axis.

$$\begin{aligned}
 [\text{TE}] = & \left[\frac{1}{u} J_m'(ua) + \frac{1}{v} \frac{I_m'(va)}{I_m(va)} J_m(ua) \right] \left[\frac{1}{u} N_m'(ub) + \frac{1}{w} \frac{K_m'(wb)}{K_m(wb)} N_m(ub) \right] \\
 & - \left[\frac{1}{u} N_m'(ua) + \frac{1}{v} \frac{I_m'(va)}{I_m(va)} N_m(ua) \right] \left[\frac{1}{u} J_m'(ub) + \frac{1}{w} \frac{K_m'(wb)}{K_m(wb)} J_m(ub) \right], \quad (6)
 \end{aligned}$$

$$\begin{aligned}
 [\text{TM}] = & \left[\frac{n_1^2}{u} J_m'(ua) + \frac{1}{v} \frac{I_m'(va)}{I_m(va)} J_m(ua) \right] \left[\frac{n_2^2}{u} N_m'(ub) + \frac{n_2^2}{w} \frac{K_m'(wb)}{K_m(wb)} N_m(ub) \right] \\
 & - \left[\frac{n_1^2}{u} N_m'(ua) + \frac{1}{v} \frac{I_m'(va)}{I_m(va)} N_m(ua) \right] \left[\frac{n_2^2}{u} J_m'(ub) + \frac{n_2^2}{w} \frac{K_m'(wb)}{K_m(wb)} J_m(ub) \right]. \quad (7)
 \end{aligned}$$

The equations $[\text{TE}]=0$ and $[\text{TM}]=0$ determine TE and TM modes of the zeroth-order. Fig. 2 shows some dispersion curves of low orders for the silica fiber ($n_2=1.45$) with $2a=7$ μm , $d=3.8$ μm and the relative refractive index difference $\Delta n = (n_1^2 - n_2^2)/(2n_1^2) = 0.18\%$. We designed the fiber in order to get the sufficiently deep optical potential for the guidance of Rb atoms with low-power diode lasers (see the next section). For the wavelength $\lambda = 780$ nm of Rb D₂ line, it becomes multimode and the lowest mode is HE₁₁ similarly to a concentric-core fiber [6]. The solid circles in Fig. 2 show the light propagation modes in the present case. We derive the cutoff frequencies of the propagation modes from the equation

$$\begin{aligned}
 & \left[\left(\frac{1}{u} N_m'(ua) + \frac{1}{v} \frac{I_m'(va)}{I_m(va)} N_m(ua) \right) J_m(ub) - \left(\frac{1}{u} J_m'(ua) + \frac{1}{v} \frac{I_m'(va)}{I_m(va)} J_m(ua) \right) N_m(ub) \right] \\
 & \times \left[\left(\frac{n_1^2}{u} N_m'(ub) + \frac{1}{v} \frac{I_m'(va)}{I_m(va)} N_m(ua) \right) J_m(ub) - \left(\frac{n_2^2}{u} J_m'(ua) + \frac{1}{v} \frac{I_m'(va)}{I_m(va)} J_m(ua) \right) N_m(ub) \right] \\
 & = \frac{1}{a^2} \left(\frac{\beta m}{k} \right)^2 \left(\frac{1}{u^2} + \frac{1}{v^2} \right)^2 [J_m(ua) N_m(ub) - J_m(ub) N_m(ua)]^2. \quad (8)
 \end{aligned}$$

Incidentally, the equations obtained by setting zero on the first and the second terms of the left-hand side of Eq. (8) give the cutoff frequencies of TE and TM modes, respectively. Such cutoffs arise on the horizontal axis in Fig. 2. For single-mode operation, it is necessary to take smaller values of the parameters a , d and Δn .

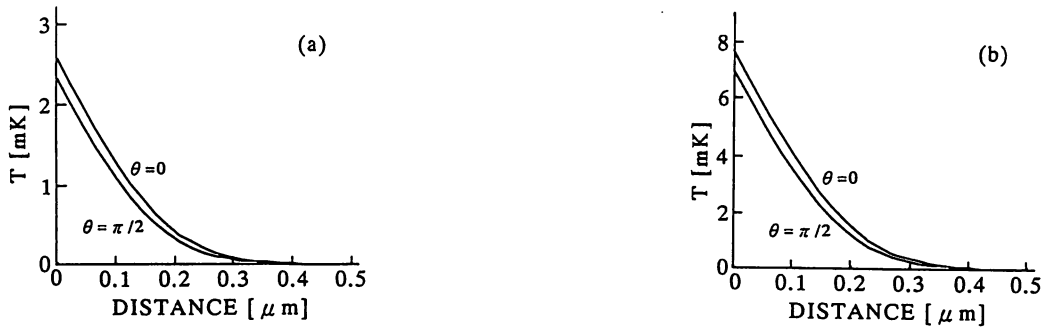


Fig. 3. The cross-sectional change of the optical potential produced by the evanescent wave for ^{85}Rb atoms under the excitation of the HE_{11} mode with $\lambda = 780$ nm. The potential barrier is shown as a function of the distance from the inner surface in terms of temperature representing one-dimensional kinetic energy: the coupling power and the blue-detuning are (a) 1 mW and 3Γ ; (b) 10 mW and 8Γ , respectively. The upper and the lower curves of each figure are obtained for $\theta = 0$ and $\pi/2$ in the case of $\phi = 0$, respectively.

3. Optical potential for the guidance of Rb atoms

Next, we consider the optical potential to guide Rb atoms. The atoms approaching the inner surface undergo the intense gradient force from the evanescent wave. The detuning of the laser frequency above an atomic resonance, namely the blue-detuning, results in a repulsive force. For two-level atoms, the potential $U(r)$ due to the gradient force is known as [3]

$$U(r) = \frac{1}{2}\hbar\Delta \ln\left(1 + \frac{I(r)/I_0}{1 + 4\Delta^2/\Gamma^2}\right), \quad (9)$$

where $\Delta = \omega - \omega_0$ is the detuning of the laser frequency ω from the atomic resonance frequency ω_0 and $I(r)$ is the field intensity. The saturation intensity I_0 and the natural linewidth Γ are 1.6 mW/cm^2 and 6.1 MHz for ^{85}Rb D_2 line, respectively [7]. We evaluate the intensity $I(r)$ by calculating the z component of the time-averaged Poynting vector \overline{S}_z defined as [8]

$$\overline{S}_z = \frac{1}{2}(\mathbf{E} \times \mathbf{H}^*) \cdot \mathbf{e}_z = \frac{1}{2}(E_r H_\theta^* - E_\theta H_r^*), \quad (10)$$

where \mathbf{e}_z is the unit vector in the z direction.

Fig. 3 shows the cross-sectional change of the optical potential expressed in terms of temperature for ^{85}Rb atoms in the case of the excitation of the HE_{11} mode with 1 or 10 mW coupling power under each optimal blue-detuning. We set zero on the arbitrary phase constant ϕ . In the present case, the components E_r , E_z and H_θ become zero at $\theta = 0$ and maximum at $\theta = \pi/2$. The optical potential produced by the evanescent wave exponentially decreases and hence the effective interaction region is several hundred nanometers from the inner surface as shown in Fig. 3. Heating effects on atoms, which will prevent the clear-cut observation of guided atoms, can be minimized owing to the wide empty region free from intense laser light. The small index difference between the core and the cladding results in the large leakage of the laser power to the cladding, while the large index difference between the core and the vacuum results in the slight leakage to the hollow region. Provided that the blue-detuning is optimal, however, the millikelvin potential well is produced even with 1 mW coupling power. The θ dependence of the optical potential shown in Fig. 3 will be discussed later.

4. Results and discussion

We give consideration to the optimal blue-detuning for guiding atoms and the feasibility of the experiment using a thermal atomic beam. The blue-detuning affects both the range and the height of the potential barrier.

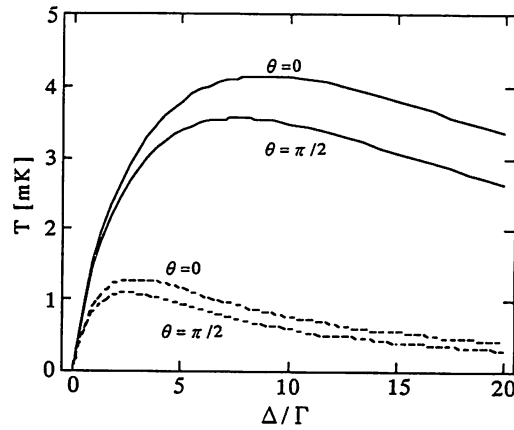


Fig. 4. The blue-detuning dependence of the optical potential under the excitation of the HE_{11} mode with $\lambda = 780$ nm at the distance 100 nm from the inner surface. The horizontal axis is labeled by the blue-detuning Δ divided by the natural linewidth Γ . The solid and the broken curves are obtained for 10 and 1 mW coupling powers, respectively. The upper and the lower curves of each case are obtained for $\theta = 0$ and $\pi/2$ in the case of $\phi = 0$, respectively.

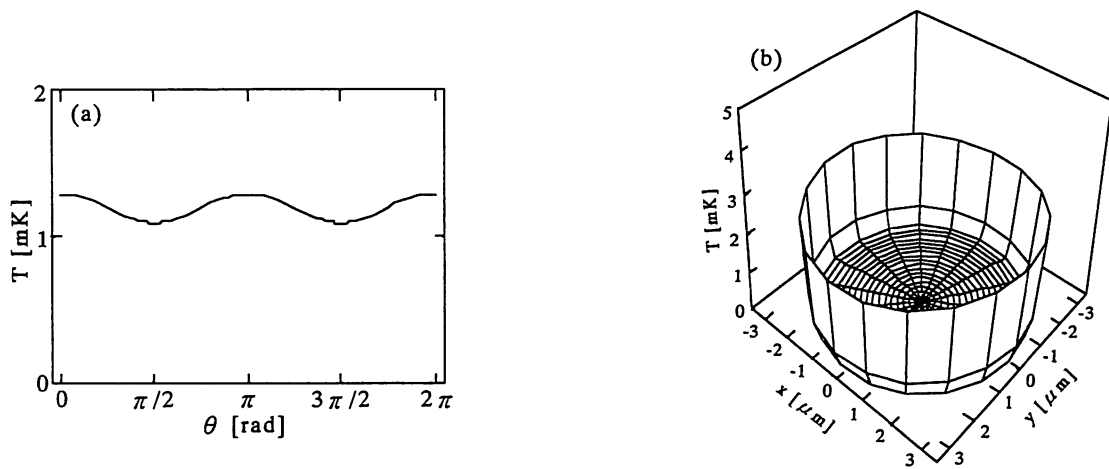


Fig. 5. The azimuthal change of the potential barrier under the excitation of the HE_{11} mode with $\lambda = 780$ nm in the case of the 1 mW coupling power and $\Delta = 3\Gamma$: (a) the periodic change as a function of θ at 100 nm away from the inner surface; (b) the spatial distribution in the hollow region. The x - y plane is taken as the x -axis corresponds to the direction of $\theta = 0$.

For a given mode intensity $I(r)$ at the distance r from the inner surface, the height of the barrier becomes maximum at $\Delta \simeq \frac{1}{4}\Gamma\sqrt{I(r)/I_0}$. Since the intensity of the evanescent wave exponentially decreases within several hundred nanometers, it is important to adjust the detuning to the coupled mode power at an appropriate position inside the hollow region. Unsuitable detunings shorten and lower the potential barrier. Fig. 4 shows the optical potential at $r=100$ nm as a function of the blue-detuning Δ normalized by the natural linewidth Γ under the excitation of the HE_{11} mode with 1 or 10 mW coupling power. For 1 mW excitation, the optical potential becomes maximum at $\Delta \sim 3\Gamma$. In this case, as shown in Fig. 3a, the depth of the potential is approximately 1 mK, which corresponds to the atomic velocity of 30 cm/s. It is possible to make a well-collimated atomic beam having transverse atomic velocities and transverse velocity distribution less than 5 cm/s such that Doppler-shift effects can be neglected on the interaction with the evanescent wave. The atomic flux to the hollow fiber with 7 μm diameter are estimated as 10^3 atom/s [9]. With a 10 cm length fiber, atoms bounce several times on the inner surface so that it causes trivial heating on atoms.

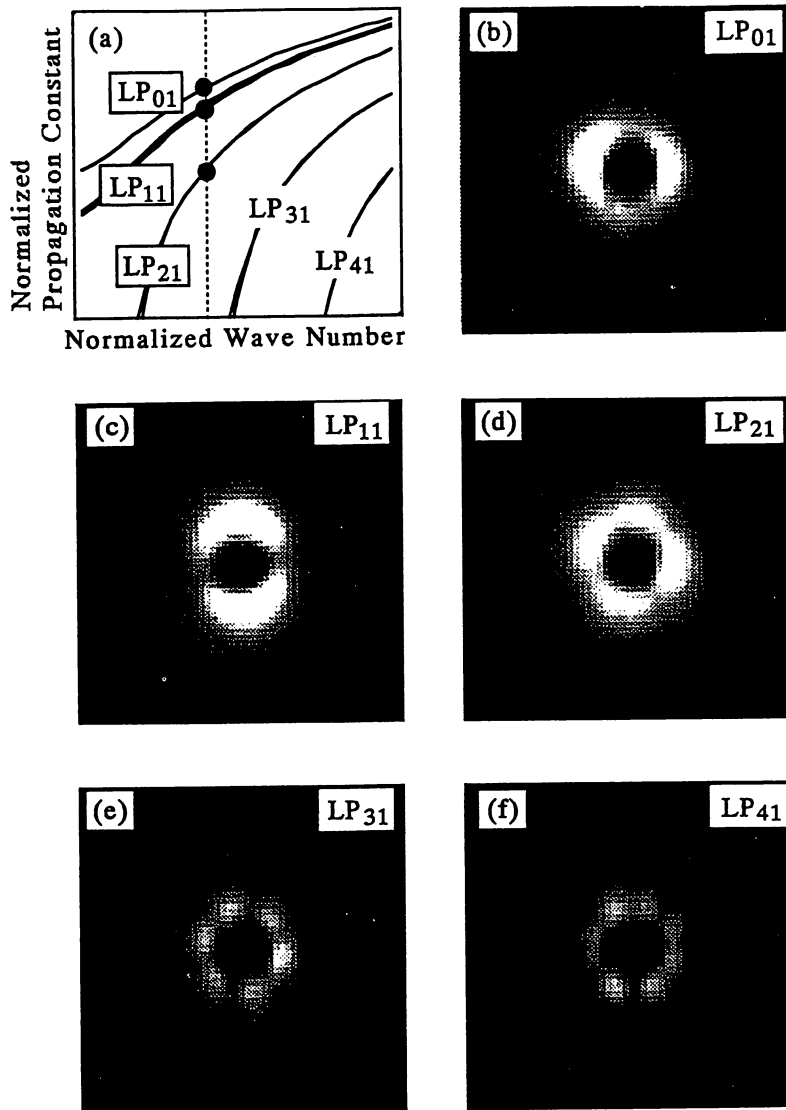


Fig. 6. The excitation mode patterns in the multimode hollow fiber. The vector modes are grouped into LP modes as shown in (a). By using a diode laser with $\lambda = 780$ nm, three LP modes are excited: (b) LP₀₁ made up of HE₁₁; (c) LP₁₁ made up of TE₀₁, TM₀₁ and HE₂₁; (d) LP₂₁ made up of EH₁₁ and HE₃₁. More two LP modes are excited by a HeNe laser with $\lambda = 633$ nm: (e) LP₃₁ made up of EH₂₁ and HE₄₁; (f) LP₄₁ made up of EH₃₁ and HE₅₁.

The HE₁₁ mode approximately has linear polarization in a concentric-core fiber, on the other hand, the distortion appears as an inhomogeneous field in the hollow fiber in spite of the small relative refractive index difference possible to apply the weakly-guiding approximation which leads to linearly polarized modes (LP modes, see Ref. [8]). As a result, the optical potential periodically changes as a function of the azimuthal angle θ as shown in Figs. 3 and 4. In the present case, the potential barrier for the HE₁₁ excitation becomes minimum at $\theta = \pi/2$ and maximum at $\theta = 0$. Fig. 5a shows the θ dependence of the optical potential at the distance 100 nm from the inner surface under 1 mW coupling power and the optimal blue-detuning. Fig. 5b shows the spatial distribution of the optical potential inside the hollow region. The optimal blue-detuning should be determined such that the potential is maintained to be sufficiently deep for all the value of θ .

The present hollow fiber has six vector modes for the 780 nm wavelength as shown in Fig. 2. The six vector

modes are rearranged to three LP modes; HE_{11} to LP_{01} ; TE_{01} , TM_{01} and HE_{21} to LP_{11} ; EH_{11} and HE_{31} to LP_{21} . Fig. 6 shows the mode patterns of these three LP modes excited by a diode laser, including LP_{31} and LP_{41} modes excited by a HeNe laser (633 nm). The LP_{11} and the LP_{21} modes have one and two node-lines, respectively, while the LP_{01} mode has no node-line so that it can form the stable potential well with no gap. Therefore the LP_{01} mode, namely the HE_{11} mode, is suitable for the atomic guidance. We have gained the laser coupling efficiency of more than 10% to the hollow fiber, which is sufficient to produce the millikelvin barrier with commercial diode lasers.

In summary, we showed the production of the deep optical potential due to the evanescent wave in the cylindrical-core hollow fiber. The experiment using an atomic beam can be carried out with low-power lasers. For the efficient atomic guidance, the HE_{11} mode should be excited.

References

- [1] S. Marksteiner, C.M. Savage and P. Zoller, *Phys. Rev. A* 50 (1994) 2680.
- [2] W. Jhe, M. Ohtsu, H. Hori and S.R. Friberg, *Jpn. J. Appl. Phys.* 33 (1994) L1680.
- [3] M.A. Ol'Shanii, Yu. B. Ovchinnikov and V.S. Letokhov, *Optics Comm.* 98 (1993) 77.
- [4] H. Hori, S. Jiang, M. Ohtsu and H. Ohsawa, *Int. Quantum Electronics Conference*, Vol. 8, 1992 OSA Technical Digest Series (Optical Society of America, Washington, D.C., 1992) pp. 48-49.
- [5] E. Riis, D.S. Weiss, K.A. Moler and S. Chu, *Phys. Rev. Lett.* 64 (1990) 1658.
- [6] D. Marcuse, *Light Transmission Optics*, 2nd Ed. (Robert E. Krieger, Malabar, 1989).
- [7] W. Happer, *Rev. Mod. Phys.* 44 (1972) 169.
- [8] D. Marcuse, *Theory of Dielectric Optical Waveguides*, 2nd Ed. (Academic Press, New York, 1991).
- [9] N.F. Ramsey, *Molecular Beams*, (Oxford University Press, London, 1956).

High Spatial Resolution Diagnostics of Optical Waveguides Using a Photon-Scanning Tunneling Microscope

Yasunori Toda and Motoichi Ohtsu, *Senior Member, IEEE*

Abstract—We propose a high-resolution diagnostics technique for optical waveguides using a photon-scanning tunneling microscope (P-STM). This technique has the advantageous capabilities of nondestructive measurement and informative analysis of guided mode. The capability of this technique was evaluated by measuring the characteristics of an LiTaO₃ waveguide. Scattered light spot of 500-nm diameter caused by defects was measured, and a normalized width was estimated to be 3.7 μm. Moreover, we obtained the power dispersion in Y-branch waveguides, which were in good agreement with the theoretical plots calculated by the beam propagation method (BPM).

I. INTRODUCTION

WITH the development of optical communication and information processing systems using optical waveguides, designs of functional and miniature components are required for a variety of applications such as local area network, optical computing and so on. So far, several testing methods for diagnosing these waveguides, e.g., OADR, HSD, and TV camera methods have been reported [1]–[4]. For future devices with higher integration, the method with higher resolution should become indispensable.

A method using a photon scanning tunneling microscope (P-STM method) [5], which has the advantage of high spatial resolution by picking up the evanescent field on the waveguide surface, enables us to diagnose the waveguide nondestructively. The following features which are important for the design and fabrication process of the waveguide can be characterized by the P-STM method: 1) scattering caused by deformation and defect of the surface and inhomogeneity of the composition, 2) intensity profile of a guided mode, and 3) comparison between numerical calculation and measured results to map the profile of refractive index. In this letter, we demonstrate the P-STM method with the view of these three features.

In the case of the waveguide whose upper cladding layer is air, it is possible to monitor the evanescent field of the guided mode leaked through the upper boundary layer, i.e., the guided mode profile can be monitored through the interaction between the waveguide and the fiber tip via evanescent field.

Manuscript received July 1, 1994; revised September 12, 1994.

Y. Toda is with the Interdisciplinary Graduate School of Science and Engineering, Tokyo Institute of Technology, 4259 Nagatsuta, Midori-ku, Yokohama, Kanagawa 227, Japan.

M. Ohtsu is with the Kanagawa Academy of Science and Technology, KSP East Rm 408, 3-2-1 Sakado, Takatsu-ku, Kawasaki 213, Japan.

IEEE Log Number 9407092.

Because the size of the fiber tip is much smaller than that of the object, it can be regarded as a nondestructive measurement. Both pick-up efficiency of the evanescent photons and the spatial resolution are determined by the size and the refractive index of fiber tip [6]. By using the fiber tip with a curvature radius less than 10 nm which we have fabricated by a chemical etching method [7], [8], sufficiently high spatial resolution is expected for diagnosing the waveguides.

II. EXPERIMENTAL SETUP

The experimental setup for P-STM method is shown in Fig. 1. The light from a diode laser (LD) at 680 nm wavelength is coupled by a lens (*L*) to a waveguide (WG). The waveguide under test is a proton-exchanged Z-cut LiTaO₃ waveguide whose normalized cross-sectional area is $3.8 \times 2.7 \mu\text{m}^2$ and operates as a single-mode waveguide for 633 nm wavelength. The propagation loss measured by the cut-back method is 0.7 dB/cm. Only a transverse magnetic (TM) mode was excited in the waveguide. The evanescent field in the guide layer can be picked up by the fiber tip and detected by a photomultiplier (PM). A piezoelectric transducer (PZT) is used for scanning the fiber tip.

The dependence of pick up power on the surface-probe separation is shown in the inset of Fig. 1. Here, the coupled power to the waveguide is about 1 mW. Since the waveguide is made of a ferroelectric material, electric charges are induced on the surface. Thus, a Coulomb force is induced between the surface of the waveguide and probe, by which the probe is pulled and deformed. In order to prevent the pulling and the deformation, the distance between probe and surface is modulated by dithering PZT. The modulation amplitude and frequency are 50 nm (peak-to-peak) and 800 Hz, respectively. A lock-in amplifier (LIA) is used to detect the picked up light power by synchronising to the modulation signal.

III. EXPERIMENTAL RESULTS

Guided light is scattered due to the deformation and inhomogeneity at the proximity of the surface of the waveguide [9]. These scatterings offer some information about the loss mechanism of the waveguide. Fig. 2(a) shows the measured profile of a linear waveguide with scanned area of $15 \times 15 \mu\text{m}^2$. Fig. 2(b) is the magnified image corresponding to one of these scattering points which is indicated by the white square in Fig. 2(a), and the scan area is $1 \times 1 \mu\text{m}^2$. The full width at

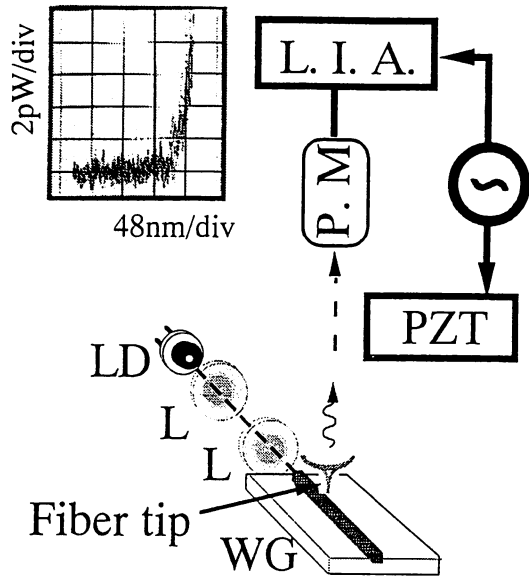


Fig. 1. Experimental setup for P-STM method (LD: diode laser; WG: waveguide; PZT: piezoelectric transducer; P.M.: photomultiplier; L: confocal lens L.I.A.: lock-in amplifier). Inset: The dependence of pick up power on surface-probe separation while dithering the probe over the core with the LD power of 1 mW.

half maximum (FWHM) of the power distribution in Fig. 2(b) is 500 nm, which is the subwavelength value.

To examine the flatness of the surface, we observed the waveguide by a scanning electron microscope (SEM) and an atomic force microscope (AFM). As a result, surface variation was sufficiently small, and we interpret these scatterings mainly due to the dust particles in the air and the inhomogeneity of the composition. In order to investigate the scattering, we compare the image between the near field and the far field. Fig. 3(a) and (b) show the measured profiles for which the surface-probe separations z are $z < 50$ nm and $z > 500$ nm, respectively. In the regions A and B in Fig. 3(a), there are some bright spots. In the region A' in Fig. 3(b) corresponding to the region A, some bright spots are also observed due to the scatterings. On the other hand, no bright spots are seen in Fig. 3(b) corresponding to the region B. This may imply that the intensity of the observed scattering depends on the solid angular distribution of the light-induced dipoles, which is determined by the size and the composition at the proximity of the surface of the waveguide.

One of the important parameters for evaluating the waveguide is the normalized width of the waveguide, which can be estimated from the spatial profile of the guided mode. Fig. 4(a) shows the measured spatial profile of the guided mode in the waveguide. The transverse profile of TM mode is shown in Fig. 4(b) which is obtained by averaging 256 times at every 60 nm along the longitudinal direction (z -axis in Fig. 4(a)). By approximating parabolic profile of the refractive index, the evanescent field amplitude can be expressed by a Gaussian function $\exp(-x^2/2\sigma^2) + A$, where σ is standard deviation [4] and A is a noise magnitude of evanescent field detection by the P-STM that is evaluated by the dependence of the detected power on surface-probe separation. The solid curve in Fig. 4(b) is Gaussian being least-square-fitted to the measured

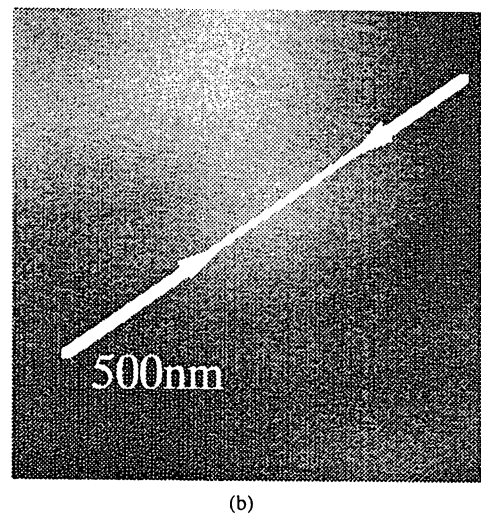
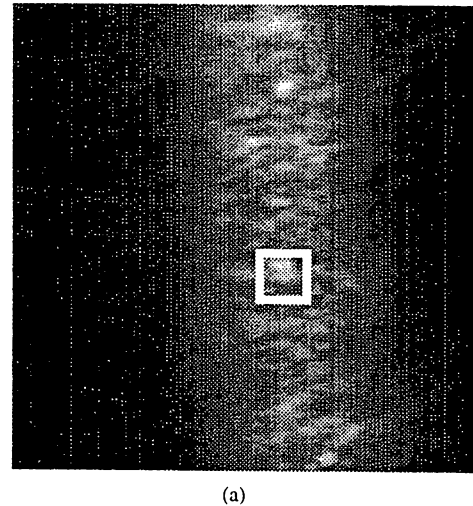


Fig. 2. Measured profile of the waveguide. (a) P-STM image with the scanned area of $15 \times 15 \mu\text{m}^2$. One of the scatterings is indicated by the white square. (b) Magnified image with the scanned area of $1 \times 1 \mu\text{m}^2$.

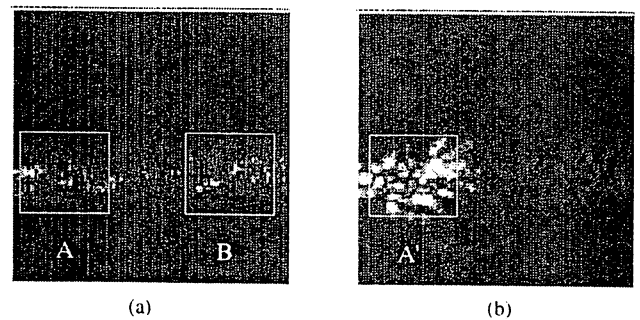


Fig. 3. Scanning profile of propagation mode on the waveguide involved scattering ($15 \times 15 \mu\text{m}^2$). (a) Near field image (probe-surface separation $z < 50$ nm). (b) Far field image ($z > 500$ nm).

value, and from this fitting, the normalized width which is expressed by the $1/e$ of the intensity ($2\sqrt{2}\sigma$) is evaluated to be $3.7 \mu\text{m}$ which is good agreement with the value of $3.8 \mu\text{m}$ expected at the stage of designing the device. Although the normalized width can be obtained by various methods, here we estimate them by the near-field optical sensing method using the fiber tip, to our knowledge, for the first time. This also

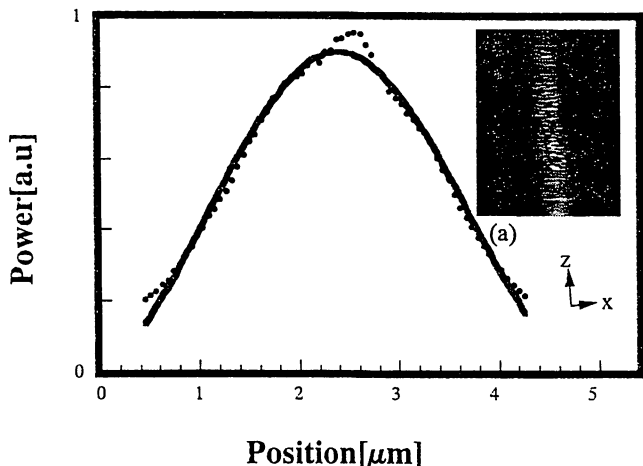


Fig. 4. (a) Scanning profile of propagation mode ($10 \times 15 \mu\text{m}^2$). (b) Transverse intensity profile in (a).

indicates that the P-STM method enable us to investigate the propagation constant at the desirable points nondestructively.

One of the advantages of P-STM method is the capability of two-dimensional imaging of the intensity profile of the guided mode, which is particularly useful for planar integrated optical devices (i.e., directional coupler, Y-coupler, etc.). To demonstrate this capability, we measured another Y-branch proton-exchanged LiTaO₃ waveguide and compared the results with the numerical calculations to map the refractive index profile. The beam propagation method (BPM) [11] which is one of the most powerful methods for the modelling and simulation of optical waveguide devices is used for the calculation. Fig. 5 shows the measured value on the line A-A' line in the inset of this figure, which shows the measured spatial profile of three continuous regions of Y-branch. The experimental values were fitted to the exponential function by the least-square method and the power variation rate is estimated to be $-1.2 \times 10^{-1} \text{ dB}/\mu\text{m}$. For the calculation by BPM, the models of refractive index distribution were approximated as a) step-like and b) Gaussian profiles. Both attenuation curves can be least-square-fitted by the exponential function, and each power variation rate is estimated to be a) $-1.2 \times 10^{-1} \text{ dB}/\mu\text{m}$ b) $-0.30 \times 10^{-1} \text{ dB}/\mu\text{m}$, respectively. Compared with the measured power variation rate, the approximation using the step-like profile is more accurate than using the Gaussian profile in the regions around the branch of this sample. These comparisons have shown that the P-STM method can be employed to evaluate the profile of refractive index.

IV. CONCLUSION

By using the high resolution P-STM method, LiTaO₃-waveguide are evaluated by measuring the propagation mode profile. The measured profile gives us the information about

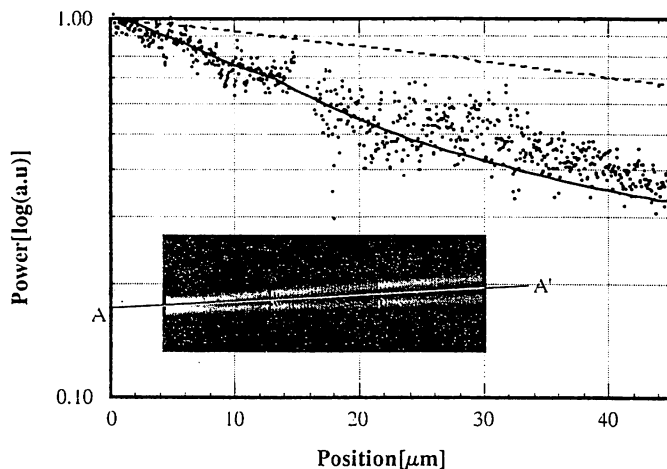


Fig. 5. Normalized power variation on the A-A' line in the inset of this figure. The solid and broken curves are the calculated power variation by the approximation as step-like and Gaussian, respectively. Inset: Image profile of Y-branch waveguide with the area of $15 \times 45 \mu\text{m}^2$ for the numerical analysis.

the scattering source and refractive index profile. Some scattering caused by defects are observed with a spatial resolution higher than 500 nm. From the transverse intensity profile of guided mode, the normalized width of $3.7 \mu\text{m}$ was obtained. Compared with the numerical calculation method, this technique enables us to map the distribution of refractive index for the calculation. The present technique is more advantageous for integrated devices with more complicated structures, and P-STM method is expected to be widely used for various applications in the future.

ACKNOWLEDGMENT

The authors would like to thank Y. Kokubun (Yokohama National University) for his theoretical comments, and also thank Y. Yokoo, and S. Takano (HOYA. Co., Ltd.) for supplying the waveguide and useful discussion.

REFERENCES

- [1] Y. Kokubun, T. Kuroiwa, and A. Yamato, in *MOC/GRIN '93*, C-5, 1993.
- [2] R. C. Youngquist, S. Carr, and D. E. N. Davis, *Opt. Lett.*, vol. 12, pp. 158-160, 1987.
- [3] A. Kohlhaas, C. Fromchen, and E. Brinkmeyer, *J. Lightwave Technol.*, vol. 9 pp. 1493-1502, 1991.
- [4] A. Miki, Y. Okamura, and S. Yamamoto, *J. Lightwave Technol.*, vol. 7, pp. 1912-1918, 1989.
- [5] S. Jiang, H. Ohsawa, K. Yamada, T. Pangaribuan, M. Ohtsu, K. Imai, and A. Ikai, *Jpn. J. Appl. Phys.*, vol. 31, p. 2282, 1992.
- [6] H. C. Van de Hulst, *Light Scattering by Small Particles*. New York: Wiley, 1957, pp. 85-102.
- [7] T. Pangaribuan, K. Yamada, S. Jiang, H. Ohsawa, and M. Ohtsu, *Jpn. J. Appl. Phys.*, vol. 31, L1302, 1992.
- [8] T. Pangaribuan, S. Jiang, and M. Ohtsu, *Electron. Lett.*, vol. 29, p. 1978, 1993.
- [9] K. Tada, T. Nakabayashi, T. Iwashima, and T. Ishikawa, *Jpn. J. Appl. Phys.*, vol. 26, p. 503, 1987.



フォトン走査トンネル顕微鏡

大津 元一

東京工業大学総合理工学研究科 〒226 横浜市緑区長津田 4259
 神奈川科学技術アカデミー・大津「フォトン制御」プロジェクト
 〒213 川崎市高津区坂戸 3-2-1, KSP 東棟 408

(1994年8月5日受理)

Photon Scanning Tunneling Microscopes

Motoichi OHTSU

Interdisciplinary Graduate School of Science and Engineering, Tokyo Institute of Technology,
 4259, Nagatsuta, Midori-ku, Yokohama 226

Ohtsu "Photon Control" Project, Kanagawa Academy of Science and Technology,
 408 KSP East, 3-2-1, Sakado, Takatsu-ku, Kawasaki 213

1. ま え が き

従来取り扱われている光は自由空間または波長にくらべ大きな領域を伝搬している。この光を用いた光学顕微鏡の分解能は回折効果により決定される。しかし物質表面にしみ出たエバネッセント光を用いると回折限界を越える分解能をもつ光学顕微鏡が可能となる。これはフォトン走査トンネル顕微鏡(フォトン STM)と呼ばれる。エバネッセント光は物質表面に近接した領域にある場であることからフォトン STM および関連する光学現象に関する研究分野は近接場光学(near field optics)と呼ばれる。フォトン STM の原理と提案は60年前にさかのぼるが¹⁾、その実験は1980年代に入ってから開始された²⁾。しかしここ数年その研究開発が急激に活発化している。その理由は近接場光学の基礎となる科学技術、さらに応用可能分野が図1に示すようにきわめて広い分野、特に将来の科学技術に関わる分野と密接に関わっているからである。

フォトン STM については過去に本誌で紹介させていただいているので³⁾、本稿ではその後の国内外の研究の進展のようす、さらに微細加工技術の一つである超高密度光記録の試みについてご紹介する。

2. 原理と構成

物体に光を照射するとその表面では光は反射、透過

し、伝搬していく。そのとき同時に物体表面にはエバネッセント光が発生している。エバネッセント光は光照射により物体中に生じた分極の間の局所的相互作用を光として表現したものに他ならない。したがって上記の反射光、透過光と異なり、遠方へ伝搬せず、分極近傍に局在している。すなわち、エバネッセント光とはこのような電磁的相互作用が物質表面に露出したものである³⁾。

図2にフォトン STM の基本的構成を示す。先端の鋭いプローブを試料表面付近で走査しながらこのエバネッセント光を散乱して伝搬光に変換し、そのパワーを検出してプローブの位置の関数として図示すれば試料表面の三次元的像が表示できる。このとき像の分解能はプローブ先端の鋭さによって決まるので、通常の光学顕微鏡とは異なり光の回折限界を越えることができる。

光子(フォトン)は電磁相互作用を媒介する光の量子である。従来の光学や光エレクトロニクスでは真空中や光ファイバなどの媒質中を伝搬しエネルギーや情報の伝達を担う光学がもっぱら興味の対象となってきた。しかし、近距離での電磁相互作用(例えばイオン間のクーロン力や近接原子間の振動電気双極子相互作用など)も光子を通じて媒介されると考えられる。フォトン STM とはこのようなきわめて近距離での電磁相互作用を光子のトンネリングと考え、外部に伝搬する実光子を情報の担い手として用いてこの相互作用を観測する装置といえる。

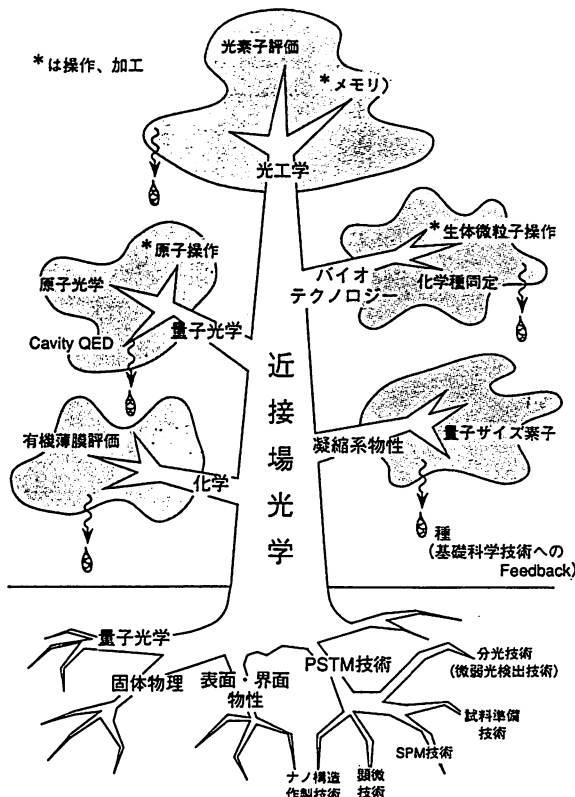


図1 近接場光学とその基礎分野、応用分野の関係

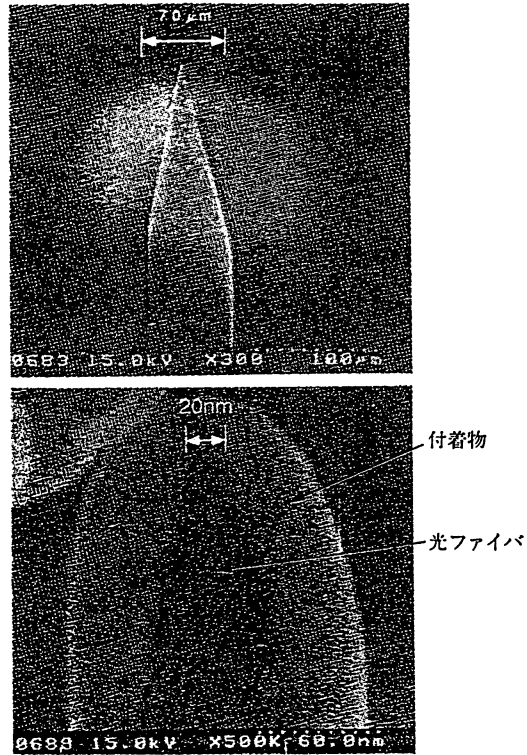


図3 ペンシル形プローブの電子顕微鏡写真(上)とその先端部拡大図(下)^{9,10)}。下図の最外部は電子顕微鏡による観測時に附着した汚れ、内部が金属膜の蒸着された先鋭化光ファイバ。

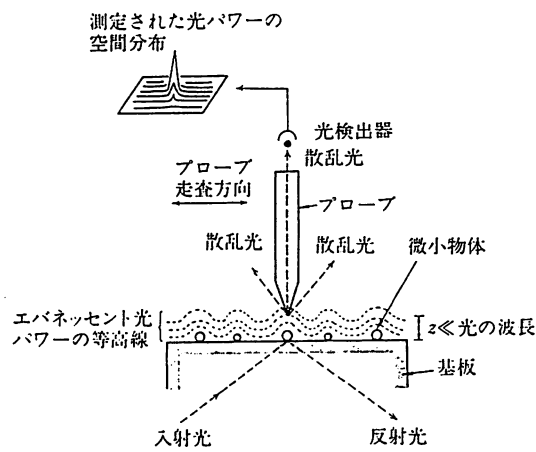


図2 フォトンSTMの基本的構成

3. 顕微鏡システムの性能

3.1 プロープ

フォトンSTMの分解能を決めるものはプローブ先端形状である。従来、ガラス性のマイクロピペットを加熱して引き伸ばしたもの⁴⁾、光ファイバを加熱して引き伸ばしたもの⁵⁾、さらには微小球を用いるもの⁶⁾、などがプローブとして用いられてきた。われわれは製作の際の高い再現性、先端曲率半径を10nm以下にすること、高

い集光効率を得ること、などを旨として、光伝送用のファイバを緩衝フッ酸溶液で選択化学エッチングし先鋭化することを試みている⁷⁾。NH₄Fの体積比を調節することによりコア部のみを先鋭化し、さらには二段階エッチングによりクラッド部を細径化すること⁸⁾、四段階エッチングによりクラッド部の角のないペンシル形にすること^{9,10)}、などが可能である。先端形状の電子顕微鏡写真を図3に示すが、10nm以内の先端曲率半径が実現している。また、先鋭角の最小値は15度になる。

選択化学エッチングで先鋭化できる理由については反応生成物のエッチング液への溶解速度の差、ファイバ線引きの際に生じたコア・クラッド境界の残留応力などによると解釈されているが、まだその理由は明らかにされていない。また先端が数nmの形状になったガラスファイバのアモファス性が保存されているか否かについても明確ではない。このようにナノ構造をもつプローブの物性そのものにも多くの興味深い問題がある¹¹⁾。

先鋭化したプローブの根元に金属膜をコーティングし、先端部分の金属膜をKI溶液により除去してファイバ先端部を露出させ、開口を形成することが試みられている。先端部の電子顕微鏡写真を図4に示すが、開口径30nmが実現している¹⁰⁾。

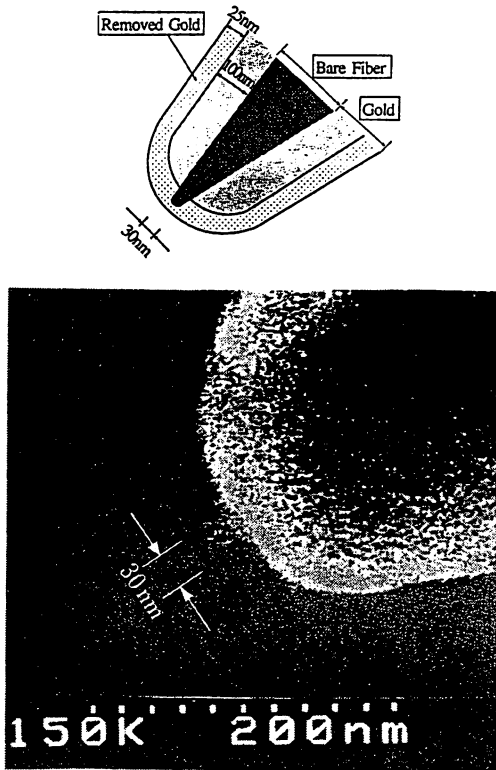


図 4 金属膜を除去しファイバ先端部が露出したプローブの断面説明図(上)とその電子顕微鏡写真(下)¹⁰⁾

3.2 装置の構成

(1) プローブ位置制御: 図2のように光を試料裏面から全反射角で入射させ、発生したエバネッセント光をプローブでピックアップする方法のほかに、プローブ先端にエバネッセント光をしみ出させ、これを試料により散乱光に変換して測定する方法などがあるが、フォトンSTMの装置で重要なのはプローブの位置制御である。そのためにプローブと試料との間のせん断応力をモニターする方法が考案されている¹²⁾。このほかに上記の二段階エッチングによりクラッド部が細径化されたプローブをわずかに傾けて試料に近づけ、試料との間の原子間力によるたわみをモニターしてプローブ位置を制御する方法もある¹³⁾。これらの方法を使うとプローブと試料との間隔を制御することができるのみでなく、フォトンSTM像と同時にAFM像が測定できる利点を有する。

(2) 検出系の雑音: 検出される光パワーは数 pW~数 nW なので低雑音の測定環境を準備する必要がある。フォトンSTM独自の雑音源は光検出の際のショット雑音である。われわれの雑音のパワースペクトル密度測定結果の例では、フーリエ周波数 10 Hz 以上ではショット雑音が支配的であり、対応する縦方向分解能は $3\text{ pm}/\sqrt{\text{Hz}}$ であった。10 Hz 以下では音響振動の影響により

雑音レベルが大きく、フーリエ周波数 1 Hz では対応する縦分解能は 0.1 nm であった。

上記の光パワー直接検出方式の他に共振形プローブを用いたヘテロダイン検出法も提案されているが¹⁴⁾、その場合微小開口をもつQ値の高い微小共振器を作成することが課題である。

なお、フォトンSTMのショット雑音として、光の場の0点揺らぎのみを考えるのでは不十分であると思われる。すなわち、雑音の発生源は物質表面の分極とエバネッセント光の場とが結合した箇所であるので、少数個の素励起の0点揺らぎの大きさを評価する必要がある。このような意味でエバネッセント光の検出には通常の実光子の検出とは異なる雑音が含まれている。

(3) 測定試料の準備: 一辺 1 μm 以下の視野で像を観測するために、試料を基板に固定するには注意が必要である。すなわち、試料固定時に散乱光発生源を作らないこと、などである。生体試料の基板への固定にはAFM像観察用試料に対する手法が使われている。フォトンSTMの特長の一つは大気中での観察が可能なことであるが、そのときは試料とプローブとの間の水分子の存在、誘電体試料表面の帯電荷などに注意する必要がある。

3.3 測定例

(1) 形状観測: フォトンSTMの分解能を評価するために各種の微粒子が観測されている。誘電体のラテックス球¹⁵⁾、バクテリオファージ T4¹⁶⁾などが観測されている。さらに図5に示すのは直径 25 nm のサルモネラ菌の鞭毛の測定例である。分解能は数 nm に達している。今後、システム性能の向上により高分解能化が進むであろう。

(2) 光素子評価: フォトニクス用微小素子の評価が行われている。図6はプロトン交換 LiTaO₃ 導波路の

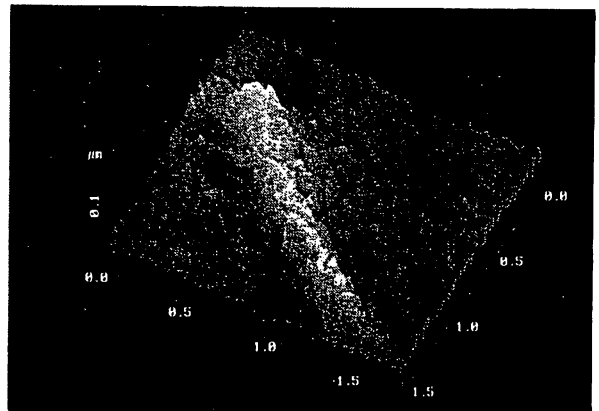


図 5 サルモネラ菌の直径 25 nm の鞭毛の観測像

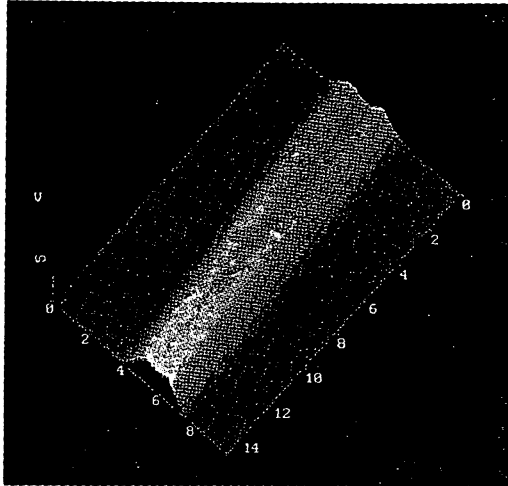


図6 プロトン交換 LiTaO_3 製のY分岐光導波路の導波モードの観測像^{17,18)}

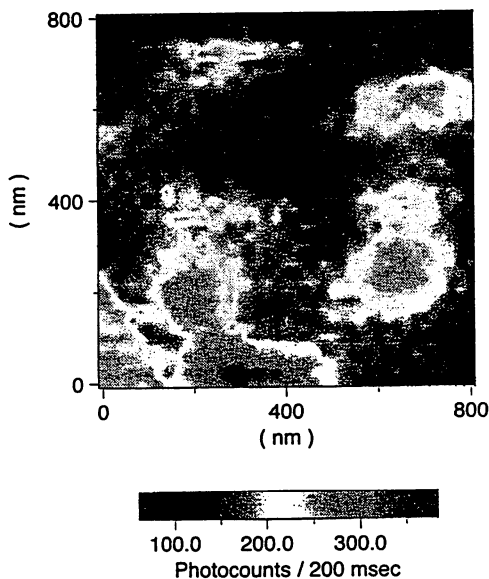


図7 色素ドーパされた直径 100 nm の複数のラテックス球からの蛍光測定結果²⁰⁾。図下部の色素示は測定時間 200 ms 間に測定されたフォトン数を表す。

導波モードの測定結果であるが、これより波長以下の寸法をもつ散乱源の同定、ビーム伝搬法による計算結果との比較などがなされ、光導波路の非破壊・高分解能評価法を提示している^{17,18)}。一方、半導体の量子細線の形状測定なども試みられている¹⁹⁾。

(3) 蛍光測定と分光実験：他の走査プローブ顕微鏡と異なり、フォトン STM では入射光により励起された試料からの蛍光を局所的に測定することが可能である。ただしこの場合、光子計数法などの微弱光検出技術を組み合わせる必要がある。一例として、図7に色素がドーパされたラテックス球からの蛍光像を示す²⁰⁾。

さらにフォトン STM の特長として入射光の波長を掃引することにより試料の局所的な光学スペクトルが観測可能である。これにより試料形状のみでなく、試料構造、特に生体試料の場合には局所的な化学種の同定が可能となる。今までに応力下のルビーの蛍光スペクトル²¹⁾、ダイヤモンドのラマンスペクトル²²⁾、さらには単一色素分子からの蛍光スペクトル²³⁾が測定されており、またプローブが近づいたときの蛍光クエンチングが検出されている²⁴⁾。これは cavity quantum electrodynamics に関連する現象として興味深い。また、上記の半導体量子細線の蛍光スペクトルが低温にて測定されている¹⁹⁾。これらの分光実験では空間的分解能は 100 nm 程度であり、まだ予備実験の段階といえる。最近は分解能は低い、低温技術、超短光パルスによる励起²⁵⁾、などの技術を組み合わせる分光法の開発が盛んになっている。

(4) その他の関連する実験：金属試料の場合には入射光により表面プラズモンが励起され、測定感度、分解能が向上する。この古くから知られている技術を利用して、数 nm の分解能を達成した実験²⁶⁾、半導体プローブをガラス基板表面に近づけたときに生ずる光励起表面電圧による引力を利用したエバネッセント光検出の実験²⁷⁾など、複合システムが提案されている。

4. 微細加工機としての使用

微細加工の一例としてプローブからエバネッセント光をしみ出させ、その光パワーを用いて光メモリ材料に記録する試みが報告されている。記録寸法はプローブ先端寸法によって決まるので、従来の光記録とは異なり、回折限界を越えた記録が可能になる。光磁気メモリ材料の Co/Pt にアルゴンレーザーを用いて熱モードで記録し、記録寸法約 100 nm、記録密度 45 Gb/inch² を得ている²⁸⁾。読み出しもフォトン STM を用いている。記録装置寸法を小型化するために同じ記録を半導体レーザーにより行う試みも報告されている²⁹⁾。

なおこの方法では光の偏光を利用しているが、光波長以下の微小開口からのエバネッセント光の偏光状態は入射光の偏光を保存しないので今後の高密度化の際に問題となる。この点を解決するためにフォトンモードによる記録が試みられている³⁰⁾。

図8にフォトンモードによる記録、再生の原理を示す。すなわち：

〔記録〕 フォトン STM 用プローブ先端にエバネッセント光をしみ出させ、プローブとメモリ用媒体との距離を光波長以下（すなわち近接場の領域）に保ったまま掃

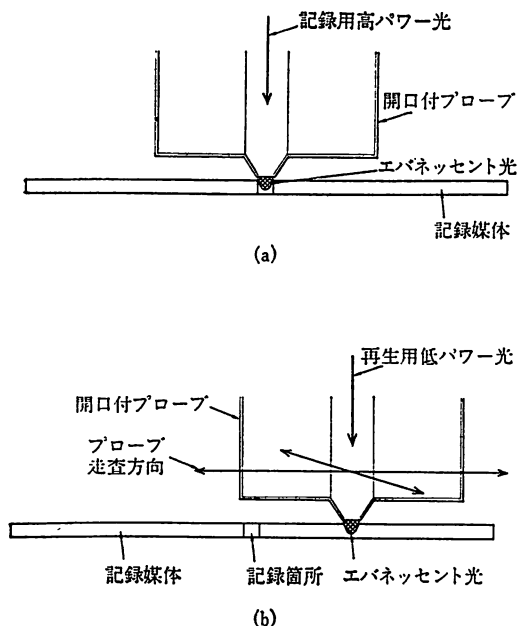


図 8 フォトンモードの光記録(a), 再生(b)の装置の基本構成

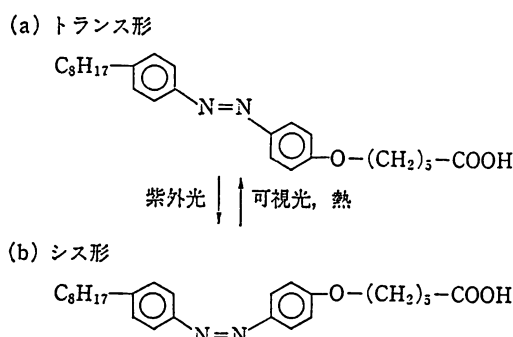


図 9 記録媒体の分子構造

引する。このときエバネッセント光のエネルギーにより媒体表面の構造変化を誘起させる。

【再生】 顕微鏡としてのフォトン STM で上記の記録過程での変形, または構造変化を測定する。

フォトクロミック材料であるジアゾベンゼン誘導体の LB 膜 (60 層) が記録媒体として使われている³⁰⁾。図 9 に示すように波長 350 nm の紫外光により記録媒体をトランス形異性体からシス形異性体へと変化させることにより記録を行う。上記の紫外光は出力パワー 60 mW のアルゴンレーザーから得た。なお、実際の記録の際のエバネッセント光パワーは約 30 nW であった。

再生にも同じ光源を用いたが、出力パワーを 0.6 mW まで減少させている。波長 350 nm における吸光度はトランス形異性体では 0.31, シス形異性体では 0.16 であること、すなわちその差が 0.15 と大きく異なることを

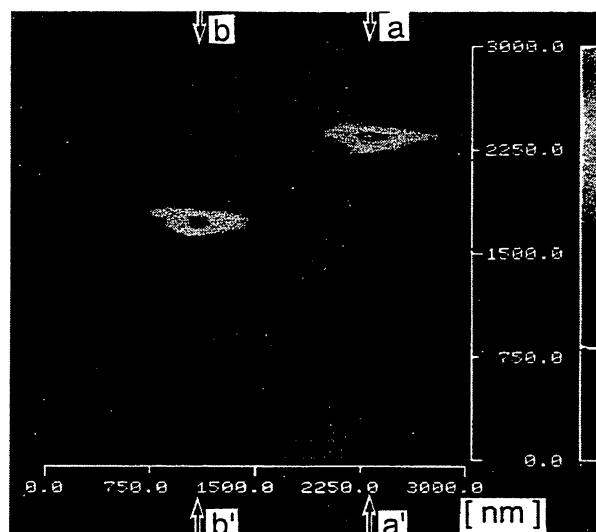


図 10 光記録されたピットの再生像³⁰⁾
a-a', b-b' に沿った楕円形状のピットの短軸は約 130 nm。図の一辺は 3 μm に相当。

利用し、再生には同じ装置をフォトン STM として用い、記録媒体の透過率の面内での局所変化を測定することにより行った。このとき両異性体を透過するエバネッセント光パワーの差は 0.3 nW であった。図 10 には再生結果の例を示す。二つの楕円状スポットがシス形異性体に構造変化している箇所であり、ピットに相当する。ピットと背景部との透過率の差は 0.08 であり、上記の値 (0.15) とは異なる。この理由としては微小光パワー領域での吸光度の減少 (すなわち光パワーに対する吸光度の非線形性) が挙げられる。

なお、この図ではそれらの直径は約 130 nm であり、記録時の光波長以下の値になっている。これらの直径の値は記録中のプローブ位置の横方向揺らぎに依存する。長期変動は周囲温度揺らぎによるドリフトであった。

ドリフトを除去するためにはプローブ位置制御が有効である。われわれは二段階エッチングによってファイバ・クラッド先端部を細径化したものをわずかに傾けて記録媒体表面上で走査し、記録媒体との間の原子間力によるプローブのたわみをモニターし、プローブ位置を制御した。この結果、プローブの縦方向位置の揺らぎは 0.1 nm 以下に抑圧することができた。横方向揺らぎについては未だ十分に定量的な評価をしていないが、非制御時にくらべ明らかに減少している。

ここで示した近接場光学による光記録・再生方式はまだ研究開発の初期段階であり、さらに進展させるには下記の基本的な問題を解決する必要がある。

(1) 最適記録媒体の探索

- (2) プロープへの入力可能レーザー光パワーの上限とプロープ熱破壊限界の推定
- (3) 再生の際の光検出雑音の評価と記録密度上限、再生速度上限の推定

しかし記録できるピット径は最終的にはプロープ先端曲率半径により制限される値まで小さくすることが期待され、数 nm となり得る。この意味で本方法は超高密度の光記録実現のための有望な方法といえる。また、ここで示したフォトンモードの光記録は見方を変えれば局所的な光化学反応の実験と考えることができる。したがって熱モードによる方法もあわせ考えれば光記録のみならず、将来はその他の極微加工、すなわち、レーザートリミング、レーザーアニーリング、マニピュレーションなどへの発展も期待できる。

ところで極限的な微細加工の方向を示す研究として、最近では三次元構造をもつエバネッセント光を用いた原子操作が活発になっている。たとえば、微小リング共振器の whispering gallery mode から共振器外周にしみ出すエバネッセント光による原子の周回³¹⁾、さらに中空ファイバ中にしみ出したエバネッセント光による原子導波路³²⁾、さらには凹状先端をもつファイバからのエバネッセント光中による原子の捕獲³³⁾、などの提案がなされている。われわれもすでにプロープ先端にしみ出すエバネッセント光により真空中に浮遊する原子を一つずつ捕獲する方法を提案している^{34,35)}。これらの操作、捕獲のためのポテンシャルの深さは原子の熱運動等価温度にして数十 μK ~ 数 mK であることが多いが、すでにレーザー光を用いた原子冷却法により 1 μK 以下が実現しているので³⁶⁾、この原子冷却法を用いれば操作、捕獲のために十分な低エネルギー原子群が準備でき、実験技術に関して本質的な問題はない。

以上の原子操作は小数個の原子と光子との相互作用の研究に対する興味のみでなく、捕獲された原子を冷却結晶基板の上に一つずつ固定して単原子レベルの結晶成長を行うことにも応用が期待される。

5. おわりに

近接場光学を応用した装置であるフォトン STM は高分解能の光学顕微鏡のみでなく、加工機、操作機として利用可能である。また、その素過程は物理学の基本的問題にも深く関わっており、さらに応用分野は広い。このような事情からフォトン STM は将来の重要な光学の研究課題と思われる。

最近ではフォトン STM 装置の市販品も現れ、ユーザー

数も増えている。研究人口も増加し、既に過去二回の国際会議が開催されている^{37,38)}。第三回目は来春チェコのブルノ市で開催されることが決まっている。また、日本でも研究人口が活発化し、応用物理学会・日本光学会により近接場研究グループが発足している。今後は凝縮系物理、表面・界面物理、量子光学、などの分野を融合した新しい光学の研究分野として発展することを期待したい。

実験結果の写真をご提供いただいた神奈川科学技術アカデミー、物部秀二氏 (図 3, 4)、納谷昌之氏 (図 5)、齋木敏治氏 (図 7) に感謝します。

文 献

- 1) E. H. Synge: "A suggested method for extending microscopic resolution into ultra-microscopic resolution," *Phil. Mag.*, **6** (1928) 356-362.
- 2) E. Betzig and J. K. Trautman: "Near-field optics: microscopy, spectroscopy, and surface modification," *Science*, **257** (1992) 189-195.
- 3) 大津元一, 堀 裕和: "フォトン STM の実験と理論", *光学*, **21** (1992) 780-788.
- 4) E. Betzig, M. Issacson, H. Barshatzky, A. Lewis and K. Lin: "Near-field scanning optical microscopy (NSOM)," *Proc. SPIE*, **897** (1988) 91-99.
- 5) U. Durig, D. Pohl and F. Rohner: "Near-field optical scanning microscopy with tunnel-distance regulation," *IBM J. Res. Dev.*, **30** (1986) 478-483.
- 6) 片岡俊彦, 高田和政, 遠藤勝義, 井上晴行, 森 勇蔵, 穂垣耕司: "走査型近接場光学顕微鏡 (SNOM) の開発 IV", 第 41 回応用物理学関係連合講演会, 28 aC 4 (1994).
- 7) T. Pangaribuan, K. Yamada, S. Jiang, H. Ohsawa and M. Ohtsu: "Reproducible fabrication technique of nanometric tip diameter fiber probe for photon scanning tunneling microscope," *Jpn. J. Appl. Phys.*, **31** (1992) L1302-L1304.
- 8) T. Pangaribuan, S. Jiang and M. Ohtsu: "Two-step etching method for fabrication of fibre probe for photon scanning tunneling microscope," *Electron. Lett.*, **29** (1993) 1978-1979.
- 9) 物部秀二, R. ウママヘスワリ, 齋木敏治, 納谷昌之, 大津元一: "フォトン走査トンネル顕微鏡用ペンシル形ファイバプローブの作成", 第 41 回応用物理学関係連合講演会, 28 pD 1 (1994).
- 10) 物部秀二, 納谷昌之, R. ウママヘスワリ, 齋木敏治, 大津元一: "フォトン走査トンネル顕微鏡用ペンシル用ファイバプローブと微小開口の作製法", 第 13 回光波センシング技術研究会, LST 13-13 (1994).
- 11) R. ウママヘスワリ, 物部秀二, 納谷昌之, 齋木敏治, 大津元一: "フォトン走査トンネル顕微鏡用ファイバプローブ先端へのナノ開口", 第 41 回応用物理学関係連合講演会, 28 pD 2 (1994).
- 12) E. Betzig, P. L. Finn and J. S. Weiner: "Combined shear force and near-field scanning optical microscopy," *Appl. Phys. Lett.*, **60** (1992) 2484-2486.
- 13) 今井一宏, 興昭元伸, 蔭 晴東, 大津元一: "AFM 同時動作可能なフォトン走査トンネル顕微鏡", 第 41 回応用物理学関係連合講演会, 28 pD 4 (1994).
- 14) S. Jiang, K. Nakagawa and M. Ohtsu: "Reflection-

- resonance-type photon scanning tunneling microscope," *Jpn. J. Appl. Phys.*, **33** (1994) L55-L58.
- 15) S. Jiang, N. Tomita, H. Ohsawa and M. Ohtsu: "A photon scanning tunneling microscope using an AlGaAs laser," *Jpn. J. Appl. Phys.*, **30** (1991) 2107-2111.
 - 16) S. Jiang, H. Ohsawa, K. Yamada, T. Pangaribuan, M. Ohtsu, K. Imai and A. Ikai: "Nanometric scale biosample observation using a photon scanning tunneling microscope," *Jpn. J. Appl. Phys.*, **31** (1992) 2282-2287.
 - 17) 戸田泰則, 大津元一: "フォトン走査トンネル顕微鏡による LiTaO₃ 導波路の導波モード観測", 第 41 回応用物理学関係連合講演会, 30 pG 12 (1994).
 - 18) 戸田泰則, 大津元一: "フォトン走査トンネル顕微鏡による光導波路の高分解能評価", 第 13 回光波センシング技術研究会, LST 13-15 (1994).
 - 19) R. D. Grober, T. D. Harris, J. K. Trautman, E. Betzig, W. Wegscheider, L. Pfeiffer and K. West: "Optical spectroscopy of GaAs/AlGaAs quantum wire structure using near-field scanning optical microscopy," *Appl. Phys. Lett.*, **64** (1994) 1421-1423.
 - 20) 斎木敏治, 納谷昌之, R. ウママヘスワリ, 物部秀二, 大津元一: "先鋭化光ファイバ・プローブの分光への応用", 日本物理学会第 49 回年会, 29 aD 2 (1994).
 - 21) P. J. Moyer, C. L. Jahncke, M. A. Paesler, R. C. Reddic and R. J. Warmack: "Spectroscopy in the evanescent field with an analytical photon scanning tunneling microscopy," *Phys. Lett. A*, **145** (1990) 343-347.
 - 22) D. P. Tsai, A. Othonos, M. Woskivits and D. Utamachandani: "Raman spectroscopy using a fiber optic probe with subwavelength aperture," *Appl. Phys. Lett.*, **64** (1994) 1768-1770.
 - 23) W. P. Ambrose, P. M. Goodwin, J. C. Martin and R. A. Keller: "Single molecule detection and photochemistry on a surface using near-field optical excitation," *Phys. Rev. Lett.*, **72** (1994) 160-163.
 - 24) R. C. Dunn, G. R. Holton and X. S. Xie: "Fluorescence spectroscopy on a single molecule basis with a near-field spectrometer," *Tech. Digest of Int. Quantum Electron. Conf. 94*, Anaheim (1994), pp. 2-3.
 - 25) S. Smith, B. G. Orr, R. Kopelman and T. Norris: "Femtosecond near-field scanning optical microscope," *Tech. Digest of Conference on Lasers and Electro-Optics*, Anaheim (1994), pp. 147-148.
 - 26) M. Specht, J. D. Pedarnig, W. M. Heckel and T. W. Hänsch: "Scanning plasmon Near-field microscope," *Phys. Rev. Lett.*, **68** (1992) 476-479.
 - 27) J. Mertz, M. Hipp, J. Mlynek and O. Marti: "Optical near-field imaging with a semiconductor probe tip," *Appl. Phys. Lett.*, **64** (1994) 2338-2340.
 - 28) E. Betzig, J. K. Trautman, R. Wolfe, E. M. Gyorgy, P. L. Finn, M. H. Kryder and C.-H. Chang: "Near-field magneto-optics and high density data storage," *Appl. Phys. Lett.*, **61** (1992) 142-144.
 - 29) 新谷俊通, 中村公夫, 丸山洋治, 保坂純男, 井村 亮: "半導体レーザを用いた SNOM の試作", 第 41 回応用物理学関係連合講演会, 31 aMC 7 (1994).
 - 30) S. Jiang, J. Ichihashi, H. Monobe, M. Fujihira and M. Ohtsu: "Highly localized photochemical processes in LB films of photochromatic material by using a photon scanning tunneling microscope," *Opt. Commun.*, **106** (1994) 173-177.
 - 31) H. Mabuchi and H. J. Kimble: "Atom galleries for whispering atoms: binding atoms in stable orbits around an optical resonator," *Opt. Lett.*, **19** (1994) 749-751.
 - 32) M. A. Ol'Shanii, Yu. B. Ovchinnikov and V. S. Letokhov: "Laser guiding of atoms in a hollow optical fiber," *Opt. Commun.*, **98** (1993) 77-79.
 - 33) J. P. Dowling and J. Gea-Balacloche: "Atomic quantum dot," *Tech. Digest of Int. Quantum Electron. Conf. 94*, Anaheim (1994), pp. 185-186.
 - 34) 大津元一: "フォトン STM(V)一単原子レベル結晶成長", 第 51 回応用物理学学会学術講演会, 27 aL 79 (1990).
 - 35) H. Hori, S. Jiang, M. Ohtsu and H. Ohsawa: "A nanometer-resolution photon scanning tunneling microscope and proposal of single atom manipulation," *Tech. Digest of the 18th Int. Quantum Electron. Conf.*, Vienna (1992), pp. 48-49.
 - 36) P. S. Jessen, A. Kastberg, W. D. Phillips, S. L. Rolston and R. J. C. Spreeuw: "Sub- μ K temperatures by adiabatic cooling in a 3D optical lattice," *Tech. Digest of Int. Quantum Electron. Conf. 94*, Anaheim (1994), pp. 236-237.
 - 37) 大津元一, 堀 裕和: "近視野光学ワークショップ報告", 応用物理, **62** (1993) 292.
 - 38) 大津元一: "第 2 回近接場光学国際会議報告", 応用物理, **63** (1994) 77.

Atomic Waveguide Using Evanescent Waves near Optical Fibers

W. JHE, M. OHTSU^{1,2}, H. HORI³ and S. R. FRIBERG⁴

Department of Physics, Seoul National University, Seoul 151-742, Korea

¹*Interdisciplinary Graduate School of Science and Engineering, T.I.T., Yokohama*

²*Kanagawa Academy of Science and Technology, Kanagawa*

³*Faculty of Engineering, Yamanashi University, Yamanashi 400*

⁴*NTT Basic Research Laboratories, Atsugi-shi, Kanagawa 243-01*

(Received October 3, 1994; accepted for publication November 7, 1994)

We discuss an atomic waveguide that guides atoms in a similar way a quadrupole mass spectrometer guides charged particles. A two dimensional guiding potential barrier is produced by repulsive optical dipole forces caused by evanescent waves from optical fibers. A realization of this new atom optical element is proposed.

KEYWORDS: atomic waveguide, evanescent wave, fiber, atom optics, dipole force

There has been much interest and activity in the manipulation of atoms with laser light¹⁾ and its application to atom optics.²⁾ Some recent demonstrations of atom optical elements include atomic mirror, atomic lens, atomic diffraction grating, and atomic zone plate. In many cases, the optical dipole force due to the intensity gradient of near-resonant radiation is employed. An excellent radiation source with a spatial gradient is provided by an evanescent wave, since it provides a short-range repulsive potential that minimizes perturbing effects of the guiding radiation.^{3,4)}

It would be interesting and useful to guide atoms in an arbitrary direction, much as an optical fiber guides laser radiation. A method of guiding atoms through a hollow optical fiber in the presence of a copropagating Gaussian laser beam has recently been proposed.⁵⁾ Also, the possibility of guiding thermal atoms along a glass surface via specular reflection at grazing incidence has been demonstrated with³⁾ and without⁶⁾ evanescent waves produced by total internal reflection. However, these methods have both drawbacks and limitations as discussed below.

In this paper, we address the possibility of a new optical device for atoms—an atomic waveguide—that uses the evanescent waves present near optical fibers. Specifically, we consider a waveguide fabricated from specially prepared optical fibers [Fig. 1(a)] arranged to provide a quadrupole geometry [Fig. 1(b)] similar to that of a commercial quadrupole mass spectrometer that guides charged particles.⁷⁾ For atoms, a two-dimensional guiding potential may be produced by the superposition of short-range repulsive optical potentials due to the evanescent waves near the optical fibers. The proposed method would offer a versatile tool for guiding atoms. It may also overcome practical difficulties associated with the Gaussian beam/hollow fiber guide,⁵⁾ such as the fragility of hollow fibers and dipole heating effects due to the guiding laser beam. It therefore allows an arbitrary guiding geometry, increased atomic guidance times and distances, decreased minimum radii of curvature, and inherently small collimation angles.

When laser light is focused and coupled to the cores of the optical fibers,⁸⁾ evanescent waves with exponentially decaying intensities are produced in the guiding

region adjacent to the core. If the laser frequency is detuned to the blue of the atomic resonance line, atoms will be subject to repulsive optical dipole forces. As a result, they will be pushed away from the high-intensity region near the core of each fiber towards the low-intensity central region of the waveguide. Consequently, atoms tend to travel through a field-free region, minimizing heating effects due to radiation forces. Note that the quadrupole-type atomic

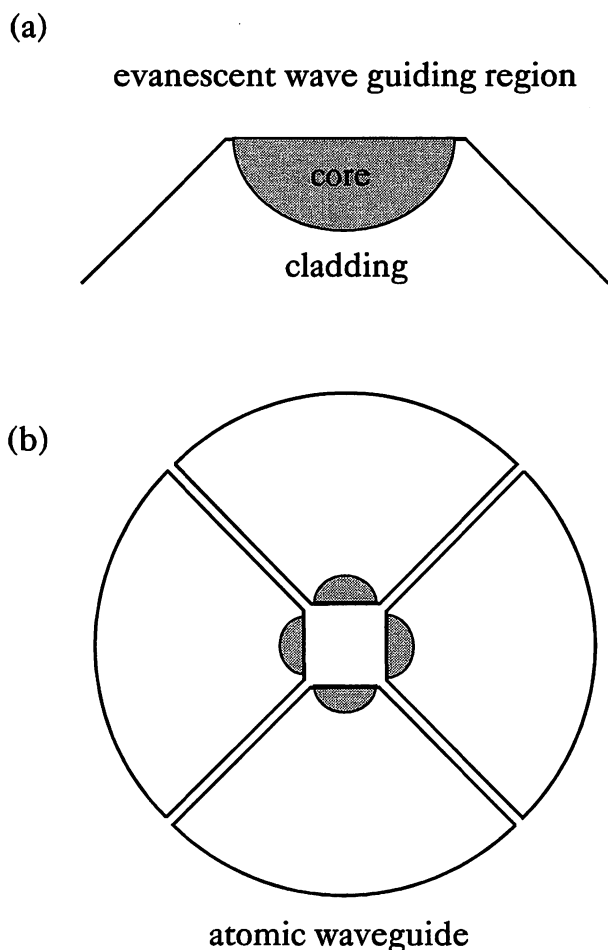


Fig. 1. (a) For an optical fiber with a core adjacent to its surface, an evanescent field extends several hundred nanometers out into space. (b) A combination of such fibers in a quadrupole geometry may be used as an atomic waveguide.

waveguide of Fig. 1 is similar to a quadrupole mass analyzer guiding charged particles along its center axis in the sense that the latter provides repulsive electric potentials (although instantaneous and time-varying) around each cylindrical electrode. However, unlike the case of a mass analyzer, the optical potential for an atomic waveguide is not quadratic. Rather, it is exponential and localized to the vicinity of each fiber and therefore vanishes near the waveguide center.

Let us now consider the spatial field distribution of the evanescent waves in the guiding region next to the core of one of the fibers. Since the calculation of the exact spatial distribution for arbitrary core geometries is not possible, we will use a simple model for qualitative analysis. We assume that the core can be approximated by a rectangular dielectric waveguide, and estimate the field distribution using the standard methods.^{9,10} We obtain good estimates for optical modes far from cutoff, as the fields are then confined to the center of the core reducing the dependence on the core geometry.

A realistic example is diagrammed in Fig. 2(a), where we assume a core 6 μm wide and 3 μm deep. Using typical optical fiber refractive index values at wavelengths near 800 nm (1.455 and 1.45 for the core and cladding), we find that the maximum evanescent field amplitudes are about 14% of the peak core amplitudes. The evanescent wave amplitudes roll off only near the core edges, where they are reduced to 6%. The numerical results of the amplitude contours of the evanescent fields around a rectangular core are presented in Fig. 2(b). The transverse field-distribution inside the atomic waveguide is then obtained by simply adding the fields from each fiber shown in Fig. 2(b). For a quadrupole geometry as in Fig. 1(b), the evanescent field amplitude is largest near the cores and smallest near the corners between fibers, vanishing in the central region.

The motion of a two-level atom inside the atomic waveguide can be determined in the following way. In a steady state condition, the optical potential energy for an induced atomic dipole is given by,¹¹

$$U(\mathbf{r}) = \frac{\hbar\Delta}{2} \ln \left(1 + \frac{S(\mathbf{r})}{1 + 4\Delta^2/\Gamma^2} \right), \quad (1)$$

where $\Delta = \omega - \omega_0 - kv_z$ is the effective detuning of the laser frequency ω with respect to the atomic resonance frequency ω_0 and includes the Doppler shift kv_z , with k the wave vector of the laser light in the fiber and v_z the longitudinal component of the atomic velocity. $S(\mathbf{r}) = I(\mathbf{r})/I_{\text{sat}}$ is the saturation parameter, with $I(\mathbf{r})$ the evanescent wave intensity at position \mathbf{r} and I_{sat} the transition saturation intensity. Γ is the spontaneous decay rate of the excited state. As can be seen in eq. (1), the potential is repulsive (attractive) near fibers provided that $\Delta > 0$ ($\Delta < 0$).

Let the laser frequency be blue-detuned, i.e., $\Delta > 0$. Then, the evanescent fields near the fibers will produce a two-dimensional potential barrier with a functional form similar to the field distribution in Fig. 2(b). This allows atoms to be guided by successive (specular)

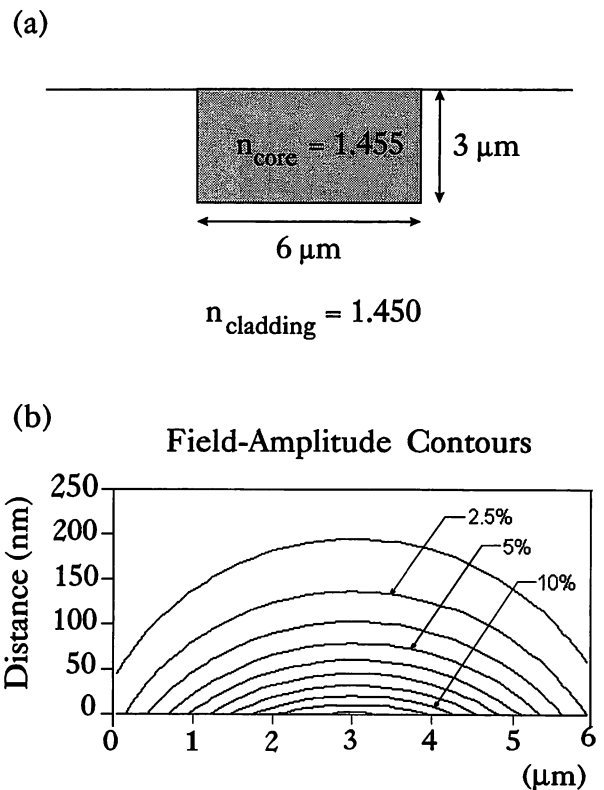


Fig. 2. (a) A simple example of a rectangular core geometry with typical refractive index values at 800 nm. (b) The numerical field-amplitude contours of the evanescent wave. The distance is normal to the core surface.

reflections from the optical potential barriers. Therefore, an atomic beam can be entrapped in the central field-free region, and can cover great distances with little broadening and small loss. Moreover, by bending the atomic waveguide, one may force the atoms to follow complex and arbitrary trajectories.

Now let us estimate the optical guiding potential of the waveguide. As is clear from Fig. 2(b), the minimum height of the potential barrier near the corners will determine the maximum possible temperature of the lateral atomic motion. For rubidium atoms with $I_{\text{sat}} \approx 1.8 \text{ mW/cm}^2$, we estimate that 100 mW cw power from a semiconductor laser can produce a maximum saturation parameter of $S(b) = 5 \times 10^6$ close to the core and a minimum of about 10^6 near the corners.⁷⁾ The optimum laser frequency detuning is $\Delta \approx \Gamma(S)^{1/2} \approx 10^3\Gamma$. Then the evanescent field induced optical potential barriers can guide atoms with a maximum transverse motion temperature of $T = U/k_B \approx 100 \text{ mK}$, which is higher than that determined by the collimation angle ($\geq 10^{-5}$ rad) for a thermal atomic beam (300 K) in the waveguide itself (1 m long). A computational simulation of the atomic trajectories in the waveguide is presented in Fig. 3, which shows the atomic motion along the waveguide axis projected on a plane normal to the axis.

A useful waveguide parameter is the minimum radius of curvature R_{min} for which atoms can avoid colliding with the fiber surfaces and remain inside a curved waveguide. This can be determined by the

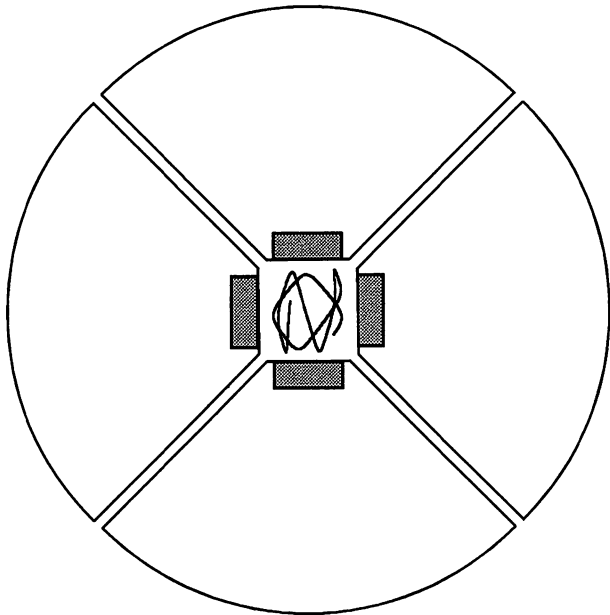


Fig. 3. A typical atomic trajectory inside the waveguide made of fibers in Fig. 2(a), projected on the plane normal to the guiding axis, is shown for Rb atoms with experimental parameters as given in the text.

balance between the average optical gradient force $\langle F_0 \rangle \approx U/\lambda$ (λ is the atomic transition wavelength) and the centrifugal force $F_c = Mv^2/R$,

$$R_{\min} \approx \lambda M v^2 / U. \quad (2)$$

Due to the increased flexibility of our waveguide, the minimum radius of curvature is much smaller than for guiding in hollow fibers,⁵⁾ and is limited only by the longitudinal temperature of the atoms. For example, thermal Rb atoms with $\lambda = 780$ nm and $v = 400$ m/s give $R_{\min} \approx 3$ cm. Using precooled atoms, the radius of curvature can be made even smaller.

Another important parameter is the atomic momentum-diffusion coefficient due to quantum fluctuations caused by interactions between atoms and photons. However, as mentioned earlier, our waveguide employs short-range evanescent wave barriers, so that the perturbing effects of radiation can be minimized and rendered insignificant. For example, atoms bounce off the optical potential barriers only several times while being guided along a 1 m path. The atom-field interaction time becomes of the order $10 \mu\text{s}$, whereas it is a few ns for a hollow fiber case,⁵⁾ so that the momentum-diffusion can be negligible. Therefore, in principle, atomic

guidance times can be made much longer, for example, by increasing the laser frequency detuning or by using precooled atoms. To summarize, our estimates show that an atomic waveguide using evanescent waves near optical fibers may transmit atoms without substantial losses over long distances and guide them through arbitrary trajectories. The waveguide provides the possibility of a versatile and compact mechanical/optical transporter for (cold) atoms that offers precise delivery to a target. This may be applied, for example, to microfabrication using single atoms. Note that another interesting method of manipulation of single atoms using localized evanescent waves near a Photon Scanning Tunneling Microscope (PSTM) fiber tip has recently been proposed,¹²⁾ which offers similar advantages. The possibility of arbitrary manipulation of atomic trajectories may be used for demonstrating Berry's phase in a screwed geometry (atomic coil). The proposed atomic waveguide may also serve as a high-density atomic bottle for studies of collective effects⁴⁾ in a U-shaped geometry (atomic hose) where extremely cold atoms could be guided and localized by gravity.

Realization of the proposed atomic waveguide is currently under progress.

WJ is grateful to S. Eah for his assistance in computer simulation and to KOSEF for its support.

- 1) See, for instance, special volume in J. Opt. Soc. Am. B **6** (November, 1989).
- 2) See, for instance, special volume in Appl. Phys. B **54** (May, 1992).
- 3) V. I. Balykin, V. S. Letokhov, Yu. B. Ovchinnikov and A. I. Sidorov: Phys. Rev. Lett. **60** (1988) 2137.
- 4) M. A. Kasevich, D. S. Weiss and S. Chu: Opt. Lett. **15** (1990) 607.
- 5) M. A. Ol'Shanii, Yu. B. Ovchinnikov and V. S. Letokhov: Opt. Commun. **98** (1993) 77.
- 6) A. Anderson, S. Haroche, E. A. Hinds, W. Jhe, D. Meschede and L. Moi: Phys. Rev. A **34** (1986) 3513.
- 7) One may design an atomic waveguide in a triangle geometry. In this case, a smaller guiding area but higher evanescent wave intensity near each corner can be obtained with respect to the quadrupole case.
- 8) In practice, one may couple the laser beam to each core using a single fiber.
- 9) E. A. J. Marcatili: Bell Syst. Tech. J. **48** (1969) 2071.
- 10) D. Marcuse: Theory of Dielectric Optical Waveguides (Academic, New York, 1974).
- 11) R. J. Cook and R. K. Hill: Opt. Commun. **43** (1982) 258.
- 12) H. Hori, S. Jiang, M. Ohtsu and H. Ohsawa: *Technical Digest of the 18th Int. Quantum Electronics Conf.*, eds. G. Magerl (Institute fur Nachrichtentechnik der TU Wien, Vienna, 1992) p. 48.

Highly Controllable Fabrication of Fiber Probe for Photon Scanning Tunneling Microscope

TOGAR PANGARIBUAN,* SHUDONG JIANG,* MOTOICHI OHTSU*†

*Interdisciplinary Graduate School of Science and Engineering, Tokyo Institute of Technology, Yokohama, Kanagawa; †Kanagawa Academy of Science and Technology, Kawasaki, Japan

Summary: A selective chemical etching was used to fabricate fiber probes for the photon scanning tunneling microscope (PSTM). The cladding diameter of the fiber probe was controlled by varying the first-step etching time. The cone angle of the fiber probe tip was controlled by varying the doping ratio of the fiber and the composition of the etching solution. A cladding diameter of 8 μm and a tip diameter of about 3 nm were fabricated. The smallest cone angle was 14°.

Key words: photon, scanning tunneling microscope, optical fiber, etching

Introduction

Advances in technology for the fabrication of submicrometer size objects have led to the realization of a photon scanning tunneling microscope (PSTM) with image subwavelength structures in a sample surface (Jiang *et al.* 1991, Jiang *et al.* 1992, Lieberman *et al.* 1990, Pagnia *et al.* 1990, Pohl *et al.* 1984, Reddick *et al.* 1989). Because the image of the sample surface is obtained by picking up the spatially localized evanescent field which is generated under the total internal reflection and modulated by the sample, the resolution of the PSTM is limited by the probe tip diameter and the separation between the probe and the sample. A reproducible and efficient fabrication of the probe, therefore, becomes very important for PSTM. Some fabrication methods (Lieberman *et al.* 1990, Pagnia *et al.* 1990, Pohl *et al.* 1984) have been reported, but sufficiently high reproducibility and detection efficiency have not yet been achieved and the tip diameter of the fabricated probe has not

been small enough for resolving the nanometric scale structure of the sample. To solve these problems, a selective etching method using a buffered hydrofluoric (HF) acid as an etching solution has been applied to a single-mode fiber, fabricated by the vapor-phase axial deposition (VAD) method for fabricating the fiber probes (Jiang *et al.* 1991; Pangaribuan *et al.* 1992, 1993). Based on this method, we present in this paper a highly controllable fabrication of fiber probes with nanometric tip diameters. The fiber probe with the smallest cone angle and a cladding diameter of 14° and 8 μm , respectively, has been fabricated with high reproducibility.

Principles of Selective Etching

Selective chemical etching using a buffered HF acid has been widely used in processing dielectric materials. An etching solution with composition 40% (weight %) NH_4F , 50% HF, and H_2O was used to sharpen a fiber with pure silica cladding and GeO_2 -doped silica core to fabricate the fiber probe. The sharpening process of such a fiber can be explained by the following chemical reactions. The chemical reaction of SiO_2 with HF in water solution can be expressed as (Burns *et al.* 1980):



while for GeO_2 it is expressed as (Rochow 1973)



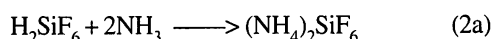
Comparing the preliminary experimental results of the dissolution rate of GeO_2 -doped silica core and pure silica cladding, it was found that the dissolution rate of the core was faster than that of the cladding and the end of the fiber core became concave (similar to the shape shown by Fig. 3b in Pangaribuan *et al.* 1992). To obtain a lower dissolution rate of the

Part of this work was supported by a Grant-in-Aid for Scientific Research (Grant No.03452089) of the Ministry of Education, Science and Culture of Japan, the Kajima Foundation, and the International Communication Foundation.

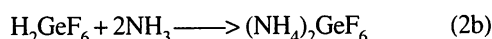
Address for reprints:

Motoichi Ohtsu
Interdisciplinary Graduate School of Science and Engineering
Tokyo Institute of Technology
4259 Nagatsuta, Midori-ku
Yokohama, Kanagawa 227, Japan

GeO₂-doped core, NH₄F is added to HF as a buffer solution. In this case, the resultant H₂SiF₆ and H₂GeF₆ [see Eqs.(1c) and (1f)] react with NH₃, ionized from NH₄F, as follows:



and



The difference in the solubility of the generated (NH₄)₂SiF₆ and (NH₄)₂GeF₆ in the etching solution leads to the difference in the etching rate between core and cladding. Therefore, by adjusting the composition of the etching solution, that is, the volume ratio of NH₄F and the doping ratio of GeO₂, fiber probes with various cone angles and tip diameters can be fabricated.

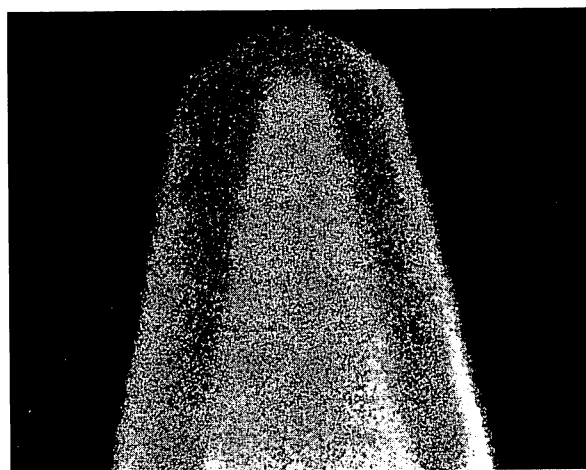
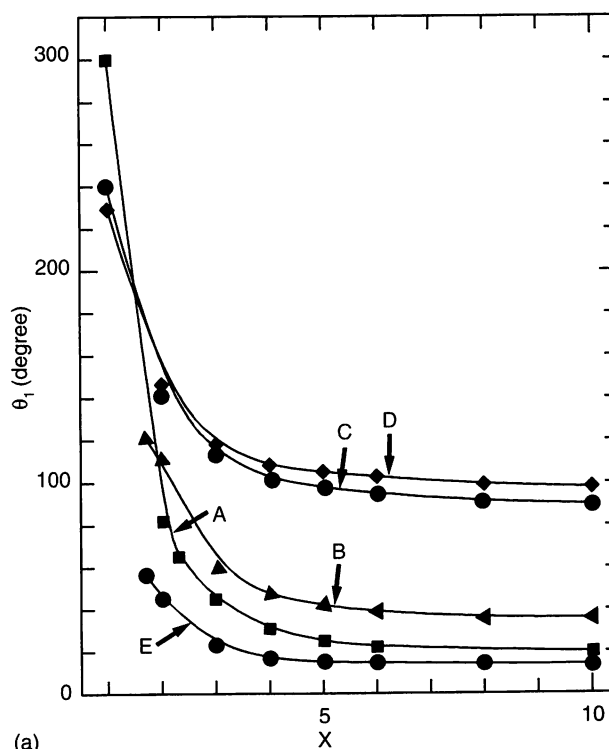
Experimental Results and Discussions

One-Step Etching for Fiber Sharpening

Based on the above-mentioned process, the sharpness of the fiber probe (denoted by the cone angle θ_1) was investigated by etching five kinds of fibers. The first four fibers have pure silica claddings and GeO₂-doped cores with doping ratios of 3.6, 8.5, 14, and 23 mol% (which correspond to the relative refractive-index differences of 0.36, 0.85, 1.4, and 2.3%), respectively. The fifth fiber has a silica cladding doped with 2.1 mol% F and a silica core doped with 22 mol% GeO₂. The etching solution was composed of 40% (weight %) NH₄F, 50% HF and H₂O. The buffering condition was controlled by varying the volume ratio of NH₄F, denoted as X, and the volume ratio of HF to H₂O was maintained at 1:1. Hereafter, the composition of the used etching solution will be identified by the value of X. To avoid the high-temperature operation of HF and to save etching time, all the experiments were carried out at the etching solution temperature of (22±1)°C.

The dependence of cone angle θ_1 on X is shown in Figure 1a. Curves A, B, C, and D are the results for the first four fibers, while curve E is the result for the fifth fiber. It can be seen that the cone angle θ_1 became smaller with increasing values of X and doping ratios, and the sharpest fiber probe with a cone angle of 14° was obtained by etching the fifth fiber with value of X=5 in 40 min. Using the etching solution with X=1, instead of sharpening the fiber even gives a “negative cone angle,” which is expressed by the cone angles larger than 180° in curves A, C, and D. In these cases, the etching rate of the core became larger than that of the cladding. Although it was reported that the difference in etching rate of core and cladding and θ_1 is dependent only on the doping ratio of GeO₂ in the core (Kawachi *et al.* 1982), we found that θ_1 is dependent also on X, especially in the case of the fiber with a high GeO₂ doping ratio (Pangaribuan *et al.* 1992). Moreover, in the case of the fifth fiber, the presence of F in the cladding leads to an increased etching rate and a decreased cone angle.

To estimate the tip diameter of the fiber probe, we observed the fiber probe with a cone angle of 20° (coated with 7 nm-thick Pt-Pd) with a scanning electron microscope (SEM) (Hitachi S-4500) with magnification of 5×10⁵. The SEM image of this tip is shown in Figure 1b. The image of the original coated tip is the inside part: we suppose that the outside part with thickness C_i is due to contamination from the SEM chamber during



(b) → / C_i / ←

FIG. 1 (a) The dependence of cone angle θ_1 of the fiber probes on X. Curves A, B, C, and D are the results for fibers with GeO₂-doped silica cores with ratios of 23, 14, 8.5, and 3.6 mol%, respectively. The fiber used for curve E has 2.1 mol% F-doped silica cladding and 22 mol% GeO₂-doped silica core. (b) SEM image of the tip. The original tip with the diameter of about 3 nm, coated with 7 nm thick Pt-Pd, is covered by contamination C_i with a thickness of 22 nm.

observation, because the extension of bombardment time of the electron beam on the tip did not change the size of the inside part, whereas C_1 was gradually enlarged. From such a result, the tip diameter is estimated to be about 3 nm, considering that the coating thickness was 7 nm. As the probe for PSTM, this is, to the authors' knowledge, the smallest tip diameter ever reported.

To confirm the reproducibility of our method, a series of experiments with an identical etching procedure was carried out and the results have shown that the standard deviation of the cone angle ($=\Delta\theta_1$) was $<0.5^\circ$. Reproducibility in space homogeneity was also evaluated by etching a dual-core fiber with GeO_2 doping ratio of 3.6 mol%. The experimental result is shown in an SEM image in Figure 2. Comparing the two etched tips, the cone angle and the differences in height between tip 1 and tip 2 are within 1° and 20 nm, respectively.

We also investigated the minimum etching time for sharpening to avoid the degradation on the tip sharpness because of over-etching. A single-mode fiber with pure silica cladding and GeO_2 -doping core ratio of 23 mol% was used. The relation between the cone angle (θ_1), the necessary minimum etching time (T_m), and the corresponding value of X is shown in Figure 3.

Two-Step Etching for Reducing the Cladding Diameter

A side view of the fiber probe and the sample is shown in Figure 4. Here, h is the length of the tip which varies from 2–6 μm depending on its cone angle, d of about 90 μm is the cladding diameter, and s is the separation between tip and sample during scanning. This separation should be kept in the range of 10–100 nm in order to pick up the exponentially decreased evanescent field and to achieve a nanometer resolution in the measurement. However, in the practical systems, the end surface of the fiber cannot be perfectly parallel to the sample surface. It would be tilted at an angle α (see the end surface of the fiber represented by line CD). With such a large ratio of d to h (i.e., $d/h > 15$), a tilt angle α of about 5° should bring the

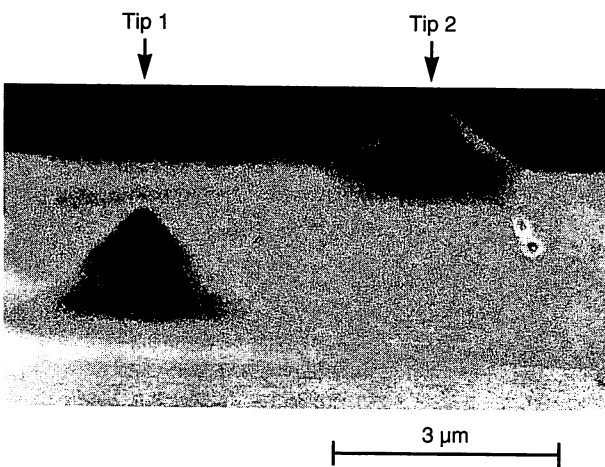


FIG. 2 SEM image of the tips produced on a dual-core fiber. GeO_2 -core doping ratio is 3.6 mol%.

cladding edge into collision with the sample surface. To solve this problem, a two-step etching method was proposed (Panaribuan *et al.* 1993).

A diagram of the two-step etching method is shown in Figure 5. The original cladding diameter of the fiber is $d_0=125 \mu\text{m}$ and the fiber core diameter is $d_c=3.4 \mu\text{m}$. Process I, first-step etching, is used to reduce the cladding diameter d_0 to d_1 , while Process II, the second-step etching, is used to sharpen the fiber end, where the cladding diameter becomes d_2 and the sharpness is denoted by θ_2 .

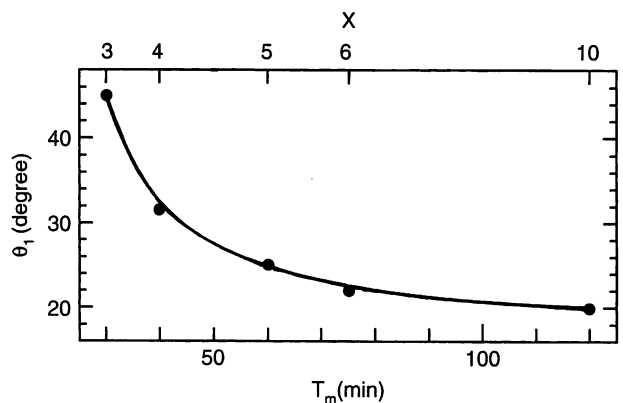


FIG. 3 Relation between the cone angle θ_1 , the volume ratio of NH_4FX , and the minimum etching time T_m for sharpening. GeO_2 -core doping ratio is 23 mol%.

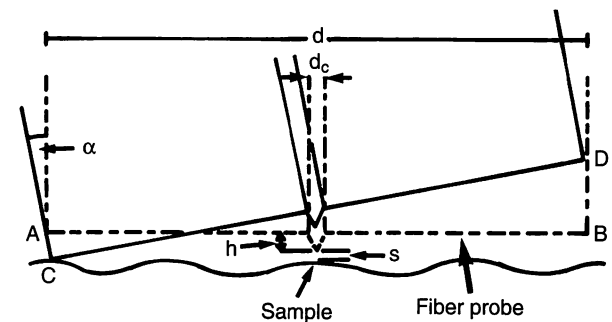


FIG. 4 Side view of the fiber probe and sample. Fiber core $d_c = 3.4 \mu\text{m}$, cladding diameter $d = 90 \mu\text{m}$, length of the tip $h = 2\text{--}6 \mu\text{m}$, tip-sample separation $s = 10\text{--}100 \text{ nm}$, and α is the tilt angle.

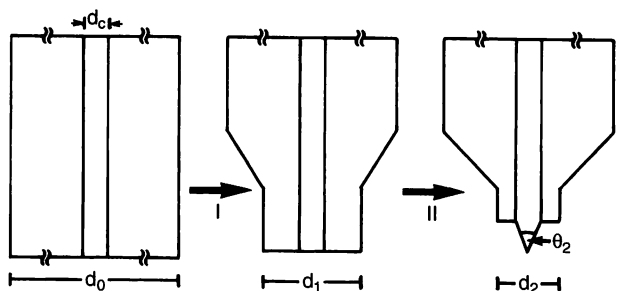


FIG. 5 Diagram of the two-step etching method. The first step (I) reduces the cladding diameter from d_0 to d_1 . The second step (II) gives fiber sharpening after applying the minimum etching time. The cladding diameter and the cone angle after two-step etching are d_2 and θ_2 , respectively.

First-step etching: To optimize the first-step etching process, we first investigated the rate of reduction of the cladding diameter during first-step etching. The relation between cladding diameter d_1 and first-step etching time t_1 is shown in Figure 6a. Lines A to H show cases in which etching solutions with values of X ranging from 1.6 to 10 to a fiber of 23 mol% GeO_2 -core doping ratio were used and show that the cladding diameter decreased linearly with increasing etching time, and that, for the same d_1 , a longer etching time is necessary with increasing X . We also found from these experiments that an etching solution with a value of $X < 3$ produced an almost flat fiber end and that the etching process mainly acted by reducing the cladding diameter. Furthermore, since the fiber end was concave when etching with $X < 1.7$, an etching solution with a

value of $X=1.7$ was used in first-step etching: in such a solution, it was found that the rate of reduction of the cladding diameter can be expressed by $v = -0.95 \mu\text{m}/\text{min}$ (see line B). Figure 6b shows an SEM picture of an example of a fiber end etched with this solution, where the etching time was 102 min and the cladding diameter d_1 was reduced to $29 \mu\text{m}$. Although the fiber end after the first-step etching was not exactly flat, we found that it had no significant effect on the sharpness of the fiber probe tip after the fiber sharpening in the second-step etching.

Although the cladding diameter can be reduced to nearly zero by increasing the etching time, the minimum cladding diameter should be found considering the optical propagation loss in the fiber cladding. From our preliminary results on the light transmission through the fibers with reduced cladding diameter, it was found that the minimum cladding diameter $d_{2,\text{min}}$ should be twice the core diameter d_c for negligible transmission loss, in agreement with calculated values (Ainslie *et al.* 1982). In the first-step etching, the value of d_1 is therefore adjusted to $d_1 > 2d_c + \delta_x$. Here δ_x is the cladding diameter reduced with the minimum etching time for each value of X . The examples of δ_x are shown in Table I, and these δ_x do not change when the temperature of the etching solution is constant.

Second-step etching: The desired cone angle of the fiber probe is obtained by using an etching solution with a value of $X=3$ or larger in the second-step etching. It was found that the relation between cone angle and X and the associated minimum etching time for each value of X used in a one-step etching method does not change when the temperature is constant (Pangaribuan *et al.* 1993). The sharpening process in the second-step etching was carried out by utilizing this relation as explained in a previous section.

Combining the rate of reduction of cladding diameter when $X=1.7$ with δ_x as shown in Table I, the cladding diameter d_2 limited by $d_1 - \delta_x > d_2 > 2d_c$ obtained after two-step etching can be empirically expressed as

$$d_2 = d_0 - 0.95 t_1 - \delta_x. \quad (3)$$

By adjusting the first-step etching time and following the above-mentioned second-step etching, a fiber probe with the desired cone angle and cladding diameter can therefore be obtained.

TABLE I The relation between the reduced cladding diameter during sharpening with the minimum etching time and the cone angle for various volume ratios of NH_4F in the etching solution. A fiber with pure silica cladding and 23 mol% GeO_2 -doped silica core was used.

Cone angle, θ_1 (degree)	Volume ratio of NH_4F , X	Minimum etching time, T_m (min)	Reduced cladding diameter, δ_x (μm)
45	3	30	19.6
31	4	45	20.4
25	5	60	20.9
22	6	75	21.2
20	10	120	21.3

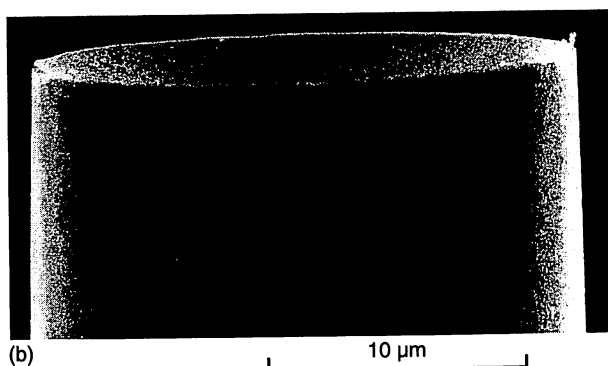
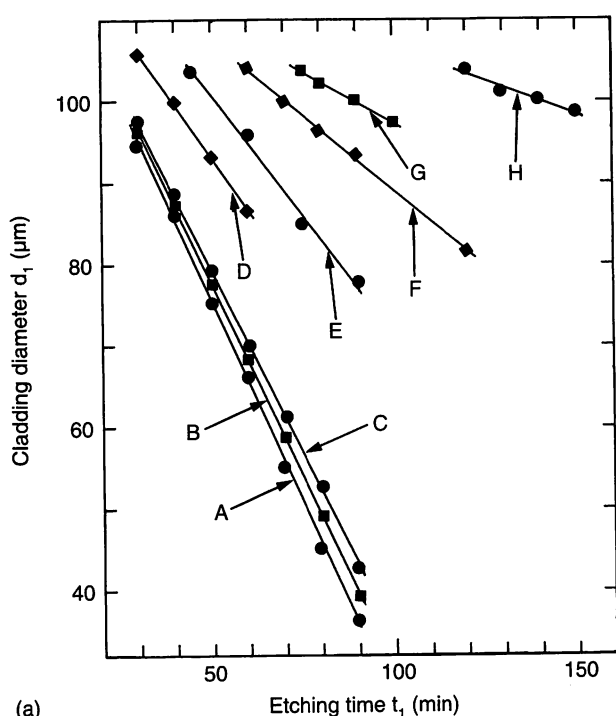


FIG. 6 (a) Dependence of the cladding diameter d_1 on etching time of the first-step t_1 . The etching solutions with X of 1.6, 1.7, 1.8, 3, 4, 5, 6, and 10 were used in curves A, B, C, D, E, F, G, and H, respectively. (b) SEM image of a fiber end after first-step etching with $X = 1.7$. GeO_2 -core doping ratio is 23 mol%.

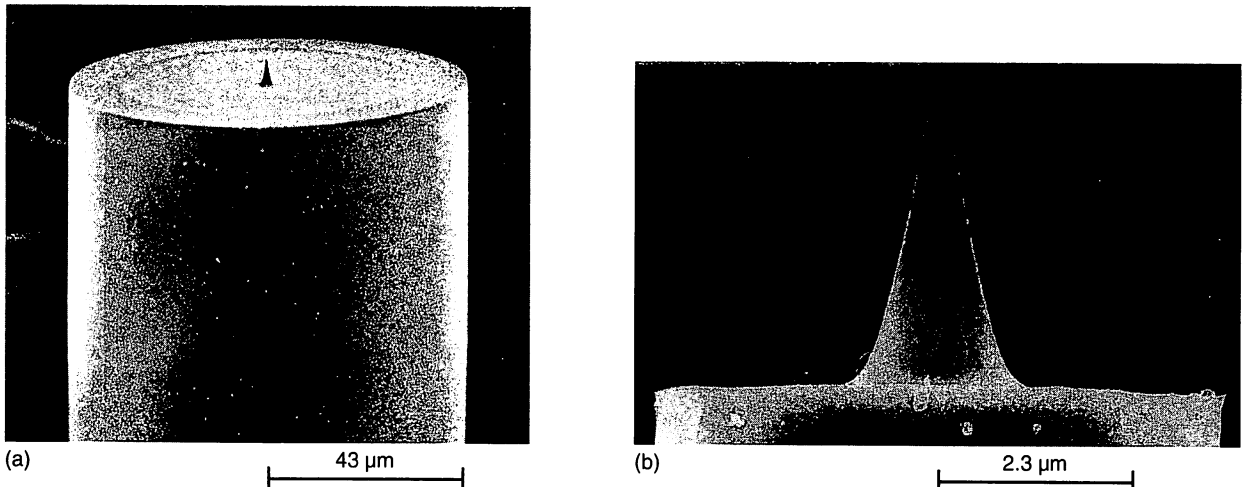


FIG. 7 (a) SEM image of fiber probe fabricated by one-step etching. (b) SEM image of fiber probe fabricated by two-step etching. For both (a) and (b), GeO_2 -core doping ratio is 23 mol%.

Figures 7a and 7b are SEM images of fiber probes fabricated by one-step and two-step etching, respectively. The etching solution with a value of $X=10$ was used in Figure 7a, while in Figure 7b etching solutions with value of $X=1.7$ and $X=10$ were used in first-step and second-step etchings, respectively. Here, the first-step etching time was 102 min. The cone angles for both fiber probes are 20° and the cladding diameter of fiber probes in Figures 7a and 7b are $90\ \mu\text{m}$ and $8\ \mu\text{m}$, respectively. Comparing these two figures, it is clear that the cladding diameter has been reduced by more than one order. Furthermore, the value of $d_2 > d_c$ is well maintained and the cone angle θ_2 produced by two-step etching is guaranteed equal to the cone angle θ_1 produced by one-step etching. From a series of experimental results for a fiber with 23 mol% GeO_2 core-doping ratio, it was found that the relative difference of the cone angles defined by $(\theta_1 - \theta_2)/\theta_1$ was $< 2\%$.

Because a tilt angle α up to 45° is permissible when $d_2 = 8\ \mu\text{m}$, collision of the cladding edge with the sample surface is easily avoided. However, a fiber probe with such small cladding diameter tends to be flexible and its use leads to some degradation of the mechanical stability of the PSTM system. To estimate the mechanical stability of the fiber probe in a practical PSTM system (Jiang *et al.* 1991), we estimated the relative deflection due to external mechanical forces. Figure 8a shows an optical microscope image of our fiber probe. The cone-like cladding part with a length of $l_1 = 300\ \mu\text{m}$ was due to surface tension effect etching. The $90\ \mu\text{m}$ length of the fiber with reduced cladding diameter d_2 was determined by the length of the fiber dipped into the etching solution and the effect of surface tension etching. Because the part of the fiber with cladding diameter d_2 etched by the surface tension effect cannot be reduced to $< 70\ \mu\text{m}$, the available minimum value of l is about $80\ \mu\text{m}$. Since the length of the fiber clamped to the rigid fiber probe holder is about 5 mm, l_1 can be neglected, and the approximation model shown in Figure 8b was used for estimation. The relative deflection y/y_0 of the free fiber end with

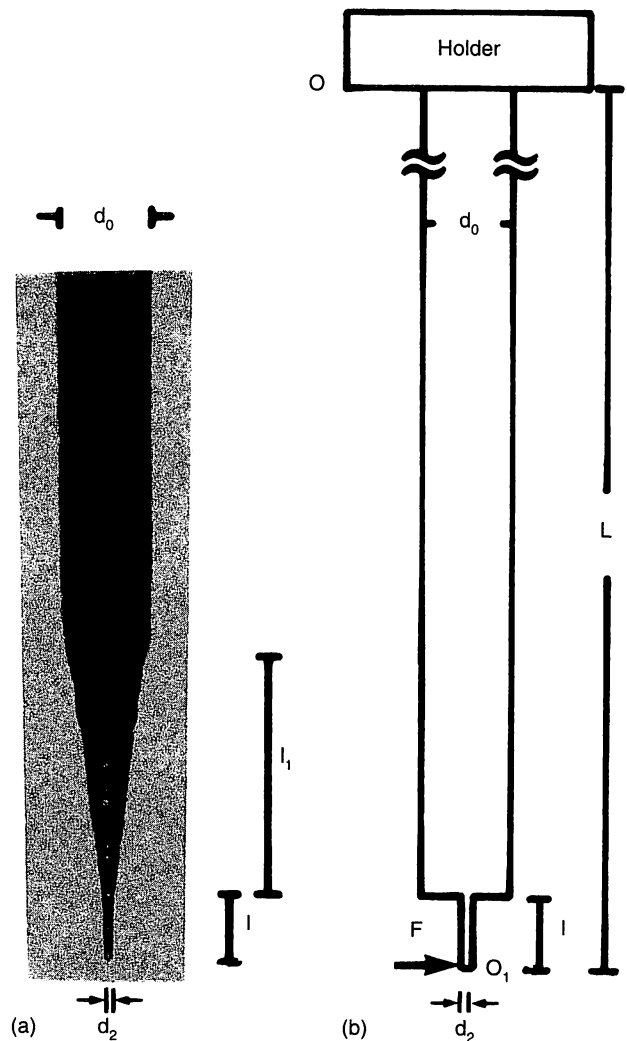


FIG. 8 (a) Optical microscope image of the fiber probe. Magnification = 100, $l_1 = 300\ \mu\text{m}$, $l = 90\ \mu\text{m}$, and $d_2 = 8\ \mu\text{m}$. (b) Approximation model for stability estimation. F is the external force loaded at free end O_1 , $L = 5\ \text{mm}$.

the external force loaded perpendicularly to O_1 can be expressed as:

$$y/y_0 = \{d_0^{-4}(l^3/6 + L^3/3 - L^2l/2) + d_2^{-4}(l^3/3)\}/(d_0^{-4}L^3/3), \quad (4)$$

where y_0 is the deflection of an unetched fiber, that is, the fiber is a uniform rod with cladding diameter d_0 due to the same external force.

Calculated results of y/y_0 as a function of d_2/d_c for various values of l are shown in Figure 9. Curves A, B, C, D, E, and F show the relative deflections corresponding to the values of l equal to 50, 90, 100, 150, 200, and 250 μm , respectively. It can be seen that the value of l of a fiber probe with $d_2=2d_c$ should be $< 90 \mu\text{m}$ to maintain mechanical instability within 10 times that of a fiber with unreduced cladding diameter (see curve B).

On the other hand, because the deflection of such a fiber probe can be estimated by $y = (64F/\pi E) \{d_0^{-4}(l^3/6 + L^3/3 - L^2l/2) + d_2^{-4}(l^3/3)\}$, the force constant, defined as F/y , can be calculated. Here, F is the external force and $E=5 \times 10^9 \text{ N/m}^2$ (Zwick *et al.* 1985) is the modulus elasticity of the fiber. It has been determined that, for $250 > l > 100 \mu\text{m}$ and $d_2=2d_c$, F/y is in the order of 0.1–1 N/m, comparable to the force constant of the cantilever used in AFM (Rugar and Hansma 1990). Such a fiber probe can be employed for combined shear force-NSOM

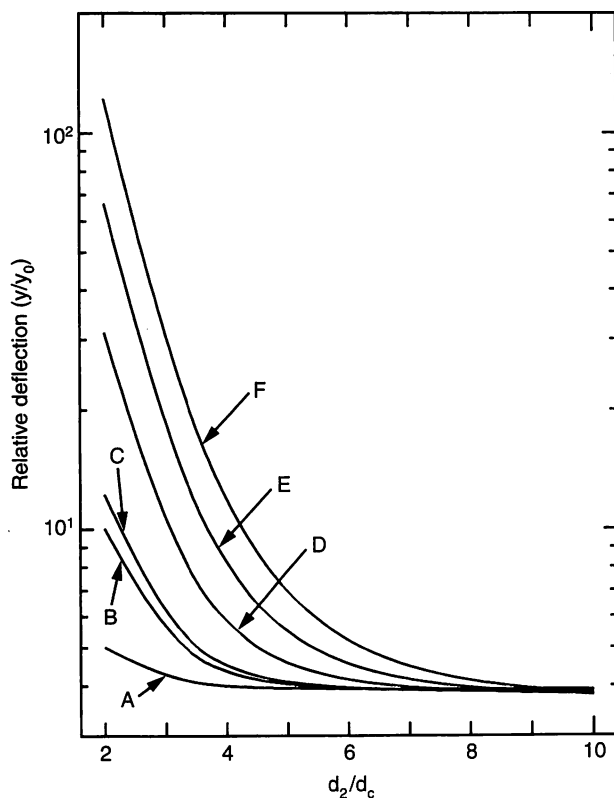


FIG. 9 Calculation result of relative deflection versus d_2/d_c with values l of 50, 90, 100, 150, 200, and 250 μm for curves A, B, C, D, E, and F, respectively.

(Betzig *et al.* 1992) because of the high relative deflection; that is, it is highly sensitive to a small value of external force.

Conclusion

Selective chemical etching methods were used to fabricate fiber probes for PSTM with various cone angles with high reproducibility, not only by varying the doping ratios of the fiber core and fiber cladding but also by varying the composition of the etching solution. The smallest cone angle of 14° , a tip diameter of about 3 nm, and the cladding diameter of 8 μm were obtained. The relative difference between cone angles produced by one-step and two-step etching was kept $< 2\%$. By two-step etching, the cladding diameter has been reduced to one order smaller than that of the one-step etching process.

Acknowledgment

The authors thank Dr. S. Miyamoto (Fujikura) and Professor H. Kawazoe (Tokyo Institute of Technology) for discussions on optical fibers, and Mr. K. Yamada (Tokyo Institute of Technology) for his help in the experiment.

References

- Ainslie BJ, Beales KJ, Day CR, Rush JD: The design and fabrication of monomode optical fiber. *IEEE Trans Microwave Theory Tech*, MT-30, 360–369 (1982)
- Betzig E, Finn PL, Weiner JS: Combined shear force and near-field scanning optical microscopy. *Appl Phys Lett* 60, 2484–2486 (1992)
- Burns DT, Townshend A, Catchpole AG: *Inorganic Reaction Chemistry: Systematic Chemical Separation* (1st ed.). Ellis Horwood Ltd., West Sussex, England (1980)
- Jiang S, Ohsawa H, Yamada K, Pangaribuan T, Ohtsu M, Imai K, Ikai A: Nanometric scale biosample observation using a photon scanning tunneling microscope. *Jpn J Appl Phys* 31, 2282–2287 (1992)
- Jiang S, Tomita N, Ohsawa H, Ohtsu M: A photon scanning tunneling microscope using an AlGaAs laser. *Jpn J Appl Phys* 30, 2107–2111 (1991)
- Kawachi M, Edahiro T, Toba H: Microlens formation on VAD single-mode fiber ends. *Electron Lett* 17, 71–72 (1982)
- Lieberman K, Harush S, Lewis A, Kopelman R: A light source smaller than the optical wavelength. *Science* 247, 59–61 (1990)
- Pagnia H, Radojewski J, Sotnik N: Operation conditions of an optical STM. *Optik* 86, 87–90 (1990)
- Pangaribuan T, Jiang S, Ohtsu M: Two-step etching method for fabrication of fiber probe for photon scanning tunneling microscope. *Electron Lett* 29, 1978–1979 (1993)
- Pangaribuan T, Yamada K, Jiang S, Ohsawa H, Ohtsu M: Reproducible fabrication technique of nanometric tip diameter fiber probe for photon scanning tunneling microscope. *Jpn J Appl Phys* 31, L1302–L1304 (1992)
- Pohl DW, Denk W, Lanz M: Optical stethoscopy: Image recording with resolution $\lambda/20$. *Appl Phys Lett* 44, 651–653 (1984)
- Reddick RC, Warmack RJ, Ferrel TL: New form of scanning optical microscopy. *Phys Rev B*, 39, 767–770 (1989)
- Rochow EG: In *Comprehensive Inorganic Chemistry*, Vol. 2 (1st ed.) (Ed. Bailar JC). Pergamon Press Ltd., Headington Hill Hall-Oxford, England (1973)
- Rugar D, Hansma P: Atomic force microscopy. *Physics Today* October, 23–30 (1990)
- Zwick U, Freidinger R, Wittmann M: Fiber with high tensile strength. *SPIE* 584, 88–92 (1985)

フトン走査トンネル顕微鏡

大津元一

近代科学の基本的な道具として古くから使われてきた光学顕微鏡の分解能は光の回折効果により制限される。すなわち、試料により散乱された光をレンズで集め、結像させようとする光がわずかに広がり、像がぼけてしまう。そのぼけの大きさは光の波長程度であるので、光学顕微鏡では光の波長(可視光の波長は約390~760ナノメートル)以下の寸法の試料は観察できない。より小さな試料を見るために電子顕微鏡が発明され、さらには原子像の見える走査トンネル顕微鏡(STM)や原子間力顕微鏡(AFM)などの走査プローブ顕微鏡が発明されている。これらの顕微鏡により分解能は向上したが、光により観測することにより得られるいく

つかの特長は失われている。

しかし、最近になってフトン走査トンネル顕微鏡(フトンSTM)と呼ばれ、上記の回折限界を打破する光学顕微鏡が出現した。

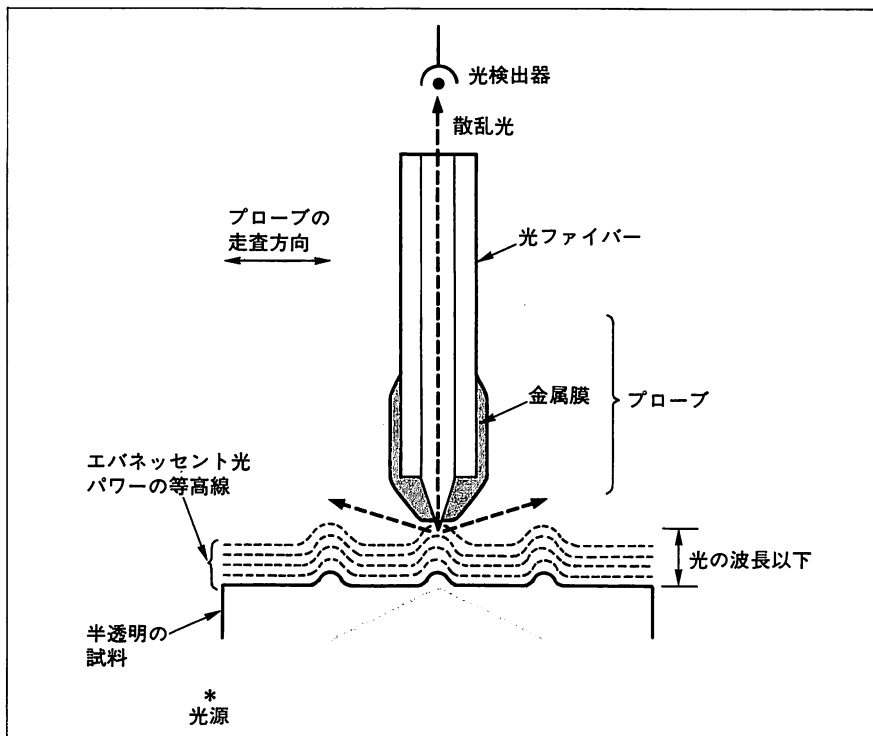
フトンSTMではエバネッセント光を使う。光学の教科書によるとエバネッセント光は試料表面で光が全反射するとき、表面の近く(表面から光の波長程度以内の“近接場”とよばれる領域)に発生する表面波である。それは表面に沿って伝搬し、そのパワーは表面から離れるにつれ急激に減少する。

ところで、表面にわずかな凹凸がある場合にも表面に沿ってエバネッセント光は存在する。実際には全反射の場合のみでなく、どんな方向から表面に

光を照射しても、通常の反射光、透過光、散乱光と同時に表面近傍にはエバネッセント光が発生することがわかっている。そしてエバネッセント光のパワー分布は物体表面の形状や構造を反映している。そこで、このパワー分布を測定するために<図1>に示すようにエバネッセント光を先端の鋭いプローブ(針)で散乱させ、物体表面でプローブを走査する。この微弱な散乱光のパワーを測定し、プローブの位置の関数として図示すれば物体の像が得られる。この測定の分解能はいかに小さな領域のエバネッセント光を散乱させるかにより決まる。すなわちプローブ先端の寸法によって決まるので、これが光の波長以下であれば従来の光学顕微鏡の回折限界を打破することができる。

以上がフトンSTMの動作原理である。原理は簡単にみえるが、これは従来の光学の教科書には書かれていない。なぜなら、物体表面の凹凸の寸法が光の波長以下であるとき、その場所の屈折率の値はなにか、どこが表面か、プローブが近づいたときエバネッセント光の分布はどのように変化し、どのように散乱されるか、などを簡単に表わしにくいからである。特にフトンSTMにより観察された像が物体に関するどのような情報を与えているか、などについて知るためには物質と光との局所的な相互作用を調べる必要がある。フトンSTMに関するこれらの問題を取り扱う物理学である“近接光学”の今後の発展が待たれる。

フトンSTMの提案は1928年であるが¹⁾、その実験が開始されたのは1984年頃からである。この半世紀におよぶ空白は先端の鋭いプローブがつく



<図1> 半透明試料に対するフトンSTMの基本構成

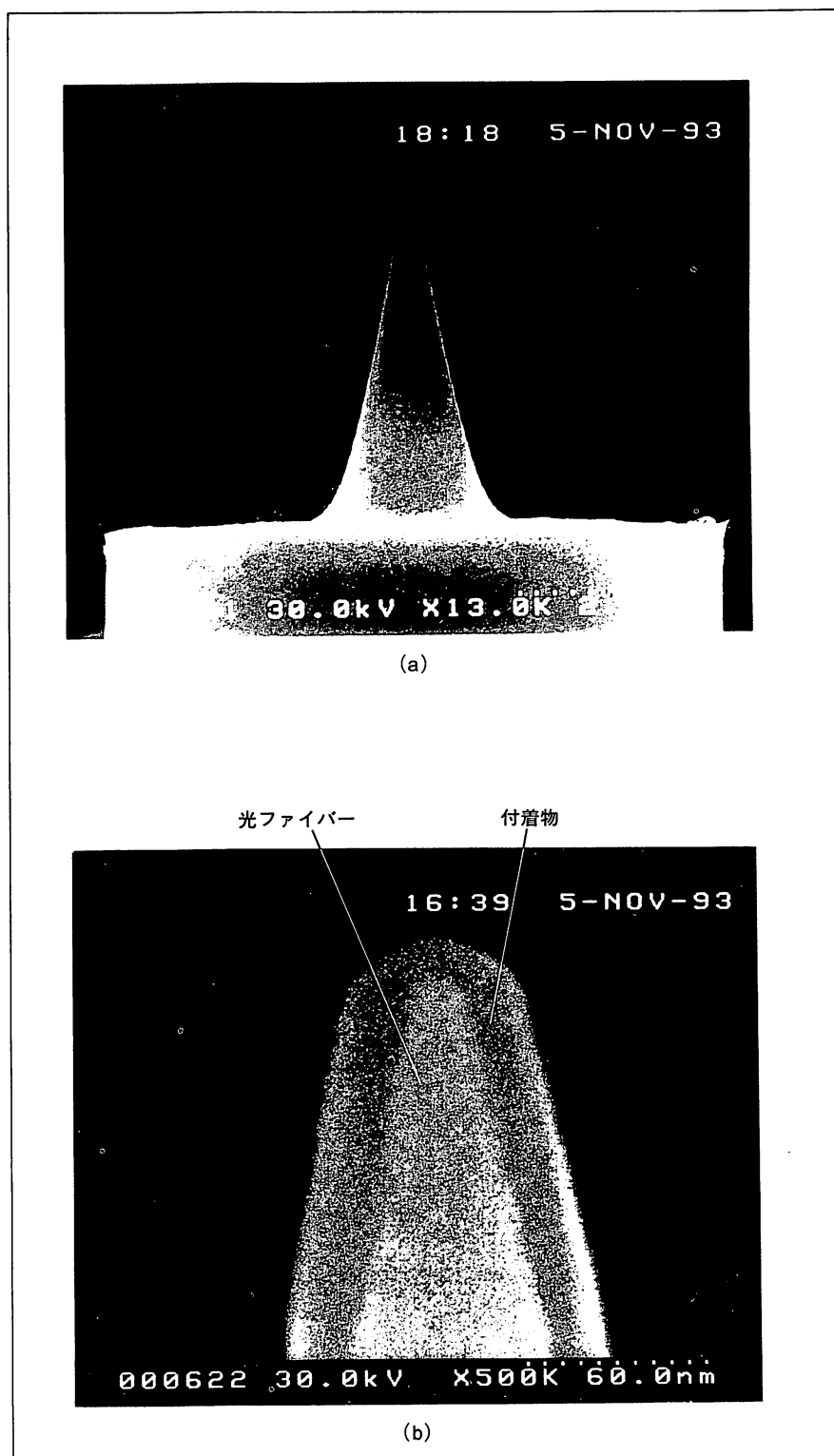
不透明試料に対してはプローブ末端からレーザー光を入射させ、先端の微小開口からエバネッセント光をしみ出させる。それを試料にあて、散乱光のパワーを測定する。

れなかったことに起因する。このことから近接場光学はナノメートル寸法をもつプローブ作製という微小素子作成技術に立脚した科学であるといえる。

プローブ作成については従来より多くの方法が試みられてきた。そのなかでわれわれは散乱光を効率よく集めて検出するためには光ファイバーを用いることが有利で、その先端を尖らすためにはフッ酸溶液による化学エッチングの方法が優れていることを見いだした。〈図 2a〉には加工後の光ファイバーの端面の電子顕微鏡写真を示す。中心の光を通る部分(コア)が先鋭化され、まわりのクラッド部が除去されていることがわかる。コアの尖り角はコアに入っている GeO_2 の濃度に依存するが最小の値として 14 度が実現している²⁾。〈図 2b〉にはコア先端部の拡大写真を示す。先端部の曲率半径は 10 ナノメートル以下であり、これは AFM のプローブの先端曲率半径より小さく、同寸法のタングステン針より硬いことがわかっている。

このように先鋭化できる理由はコアとクラッドの境界面に存在する応力の効果、エッチングの際の種々の生成物が溶液に溶ける速度が異なること、などとされているが、明らかではない。寸法が数ナノメートルの先端には原子が 100 個程度しか並んでおらず、光ファイバーの材料であるガラス(これは従来はアモルファス材料と考えられている)がこのような小さな寸法のときどのような物質構造になっているのか不明である。先鋭化の理由を明らかにするにはナノメートル寸法の物質の性質に関する研究の発展を待たざるを得ない。

光ファイバーを先鋭化した後、金の

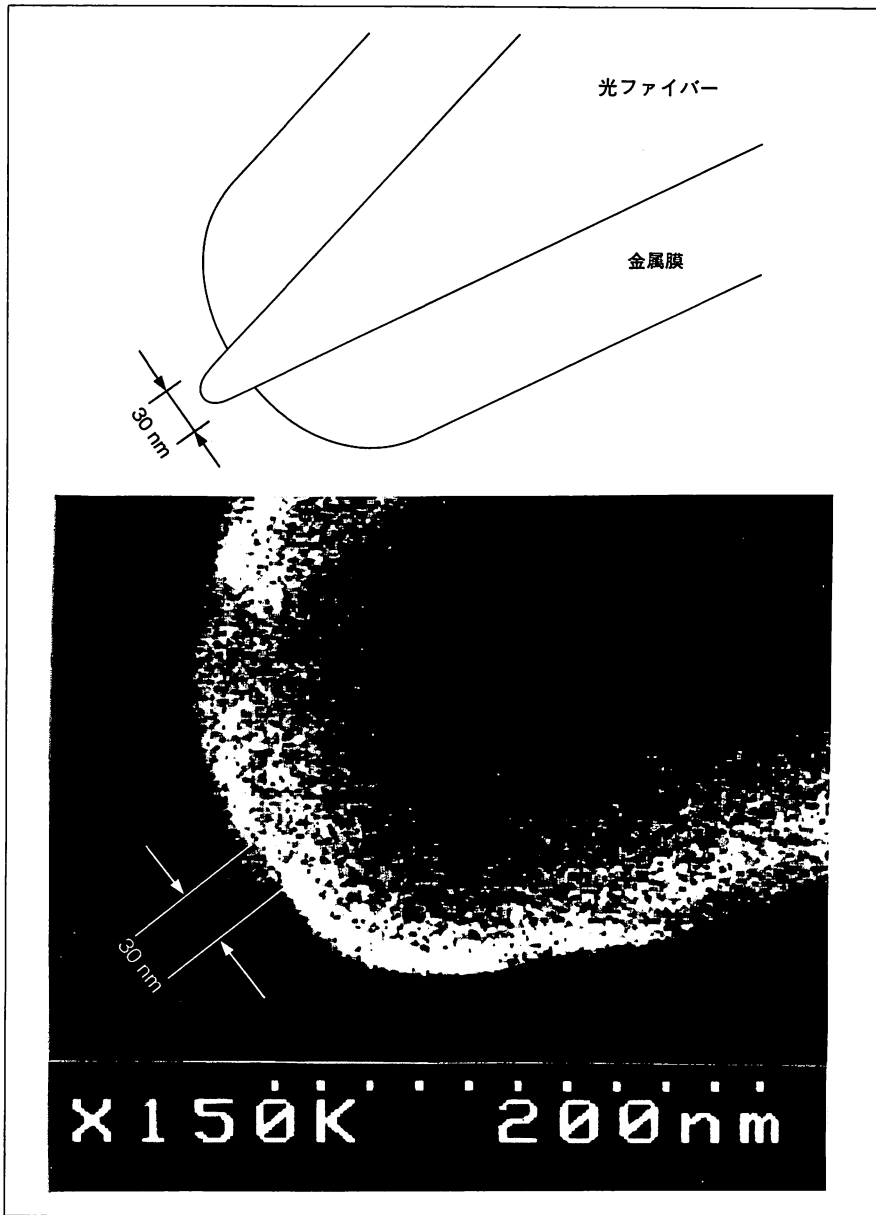


膜を蒸着し、ヨウ化カリウム溶液に浸すと〈図 3〉のように光ファイバー先端のみが露出する。これにより微小な開口がつかれるようになった。

〈図 1〉の装置において、プローブを走査したり画像を表示する部分は他の走査プローブ顕微鏡の装置と同じである。レーザー光源を使うこと、プローブが光ファイバーからなることのみが

〈図 2〉

(a)加工された光ファイバー端の電子顕微鏡写真。光ファイバー外径は 8 マイクロメートル。(b)先端部の拡大図。最外部は電子顕微鏡による観測時に付着した汚れ。内部が金属膜の蒸着された先鋭化光ファイバー。



〈図3〉 光ファイバー先端部の金属膜を除去してつくった微小開口の説明図と電子顕微鏡写真
(神奈川科学技術アカデミー、物部秀二氏による。)

異なっている。

いくつかの測定例を示そう。電子顕微鏡やSTMと異なり、フォトンSTMは空気中で使え、試料表面は非金属でもよいので微小な生体試料などが観察できる。今までにバクテリオファージT4の像などが観測されている²⁾。また、最近では〈図4〉に示すよう

に分子モーター⁴⁾の一種であるサルモネラ菌の直径25ナノメートルの鞭毛の像が見えるようになった。フォトンSTMを溶液中で動作させることは原理的には可能で、実際そうなればバイオテクノロジーの分野で広く応用されるようになるだろう。

このほか、単に試料形状を観察するだけでなく、光源の波長を掃引してスペクトルを測定することができる。これはSTM、AFMにはない特長であり、この測定は物体の局所的構造を調べるのに役立つ。たとえば、〈図5〉に示すように色素分子が入った微小誘電体球からの微弱な蛍光の観察とそのスペクトル測定、さらには色素分子1個からの蛍光測定も報告されている⁵⁾。また、ルビーの蛍光スペクトル、ダイヤモンドのラマンスペクトルなども観測されている。

とくに量子井戸構造をもつ微小半導体の発光スペクトル測定が最近始まっている。まだ分解能はそれほど高くないが、フォトンSTMを液体ヘリウム温度で動作させて測定したり、フェムト秒の光パルスで励起したりするなど、多様な技術と組み合わせて微小半導体の光物性を評価する試みが盛んになっている。

プローブの末端からレーザー光を照射させて先端の微小開口からエバネッセント光をしみ出させると、そのパワーは小さいが、単位断面積あたりのパワー密度は大きい。この光を利用すれば物質表面に穴をあけたり、構造を変化させること、さらには物質を他の場所へ移動することができる。すなわち、光の波長にくらべ小さな寸法の微細な加工や操作が可能になる。

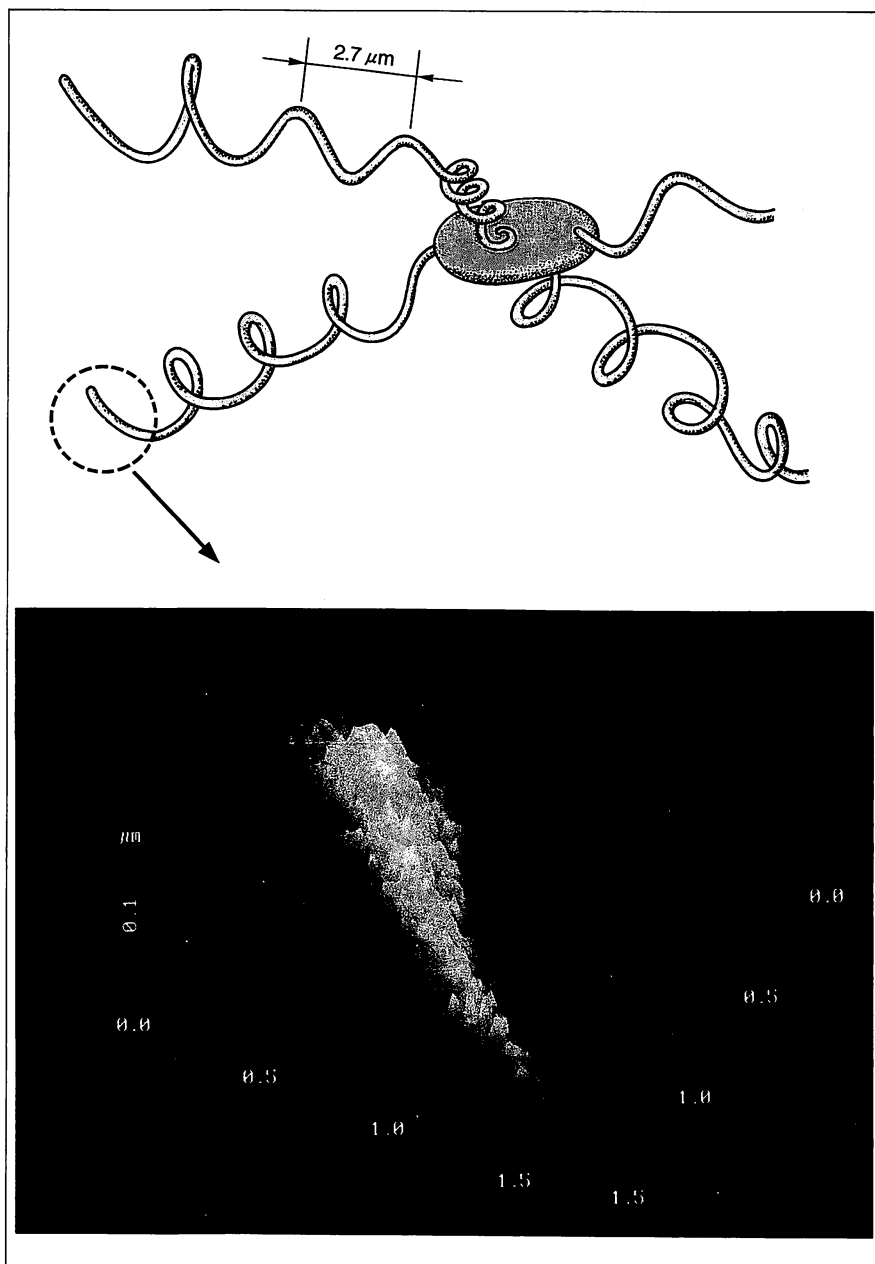
微細加工の例として光磁気記録材料

である白金コバルト膜表面をエバネッセント光により局所的に加熱して高密度光メモリーがつくられている⁶⁾。メモリーの1ビットの寸法は直径100ナノメートル程度であり、従来のコンパクトディスクの約100倍の記録密度が達成されている。

一方、微小開口からのエバネッセント光により有機超薄膜の構造を局所的に変化させて光メモリーをつくる方法もある。この場合は記録後に別の波長の光を当てたり、加熱すればもとの構造に戻すことができるのでメモリーを消去できる利点を有する。〈図6〉は記録された2つのビットの像である。楕円形状をしているが長軸の長さが約100ナノメートルであり、上記の光磁気記録の場合と同程度の大きさである⁷⁾。記録中のプローブ位置のゆらぎをさらに抑圧するなどして装置の性能を向上させ、プローブの先端曲率半径程度の寸法のビットが記録できればさらに20倍の記録密度の増加が期待される。

微細な操作の極限的な例を示そう。それは真空中に浮遊する原子の運動の制御である。すなわち、小さなガラス球のまわりにしみ出したエバネッセント光のエネルギーを利用して真空中の原子をガラス球のまわりに周回させたり⁸⁾、プローブ先端からしみ出すエバネッセント光の中に原子を捕獲する提案がなされている⁹⁾。とくに後者は光による原子のピンセットとして使い、捕獲した原子を結晶基板の上に1つずつ固定して新しい微小物質や微小デバイスをつくる基礎技術となりそうである。

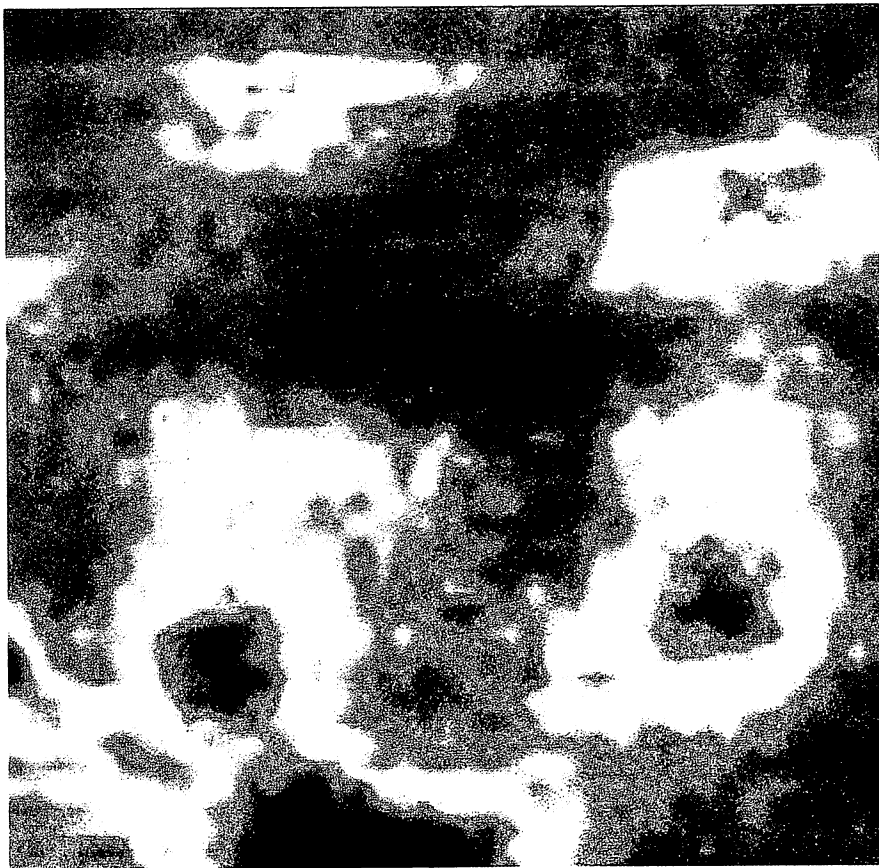
STMでは電子のトンネル効果、すなわちポテンシャル障壁を越えて電子



〈図4〉 サルモネラ菌の形状の説明図とその直径25ナノメートルの鞭毛のフォトンSTMによる観測像
(神奈川科学技術アカデミー・富士写真フィルム㈱, 納谷昌之氏による。)

の波動関数がしみ出すことを利用している。一方、フォトンSTMでは波動としての光のしみ出しであるエバネッセント光を利用している。この類似性からエバネッセント光は光のトンネル現象と表現できる。

さらに考えをすすめると、エバネッセント光は物質表面に光を照射したときに生ずる分極の間の電磁相互作用を媒介する量子とみなすことができる。すなわち表面プラズモン、ポラリトンなどの素励起と同様の解釈ができるが、この素励起を“フォトン”とよぶことができるので、ここで説明した超高倍率の光学顕微鏡を“フォトン”



〈図5〉 色素分子の入った直径100ナノメートルの誘電体球からの蛍光をフォトンSTMにより測定した結果

赤い部分は球からの強い蛍光を表す。図の面積は $0.8\mu\text{m} \times 0.8\mu\text{m}$ 。(神奈川科学技術アカデミー、齊木敏治氏による。)

STMとよんでいる。このように考えるとフォトンSTMは光学顕微鏡と考えるよりは、STM、AFMなどの走査プローブ顕微鏡の一形態と考えた方が自然な場合があり、この考え方に基づいて新しい理論をつくらうとする試みもある¹⁰⁾。この理論は量子光学、表面物理学などとも深く関係があり、今後の発展が期待される。

フォトンSTMは単に光の波長以下

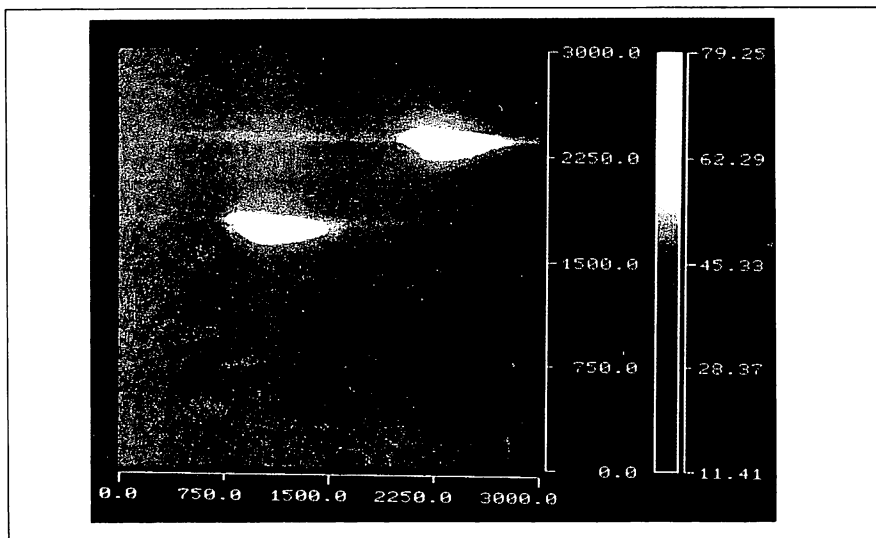
の寸法の物体像やその構造を観察する測定機としてのみでなく、新しい物質をつくり出すナノメートル寸法の微細加工機、操作機としての機能も持っている。この特徴こそが微小半導体デバイス、光メモリー、さらにはバイオテクノロジーなどの広い分野で最近注目を集めている理由である。また、その動作原理の基礎も奥深く、従来の光学ではカバーしきれない内容を含む。すなわち〈図7〉に示すようにフォトンSTMを扱う“近接場光学”の基礎と応用はきわめて多岐にわたる。

今年に入り、国内では応用物理学会の研究グループが発足している。また、すでに2年前から国際会議も開かれている。そこで関心を集めているのはファイバー製造技術などをはじめとする日本の誇る光エレクトロニクスの研究成果である。フォトンSTM、近接場光学の起源は古いが、その発展はきわめて新しい。材料開発も含め、実験と理論の今後に期待したい。

★ ★ ★

〈図6〉 記録された2つのビット像

フォトンSTMのプローブからしき出したエバネッセント光によりジアゾベンゼン誘導体の有機超薄膜の構造を局所的に変化させた結果。この像は変化させた部分を同じフォトンSTMにより観察して得られた像を示している。図の面積は $3\mu\text{m} \times 3\mu\text{m}$ 。

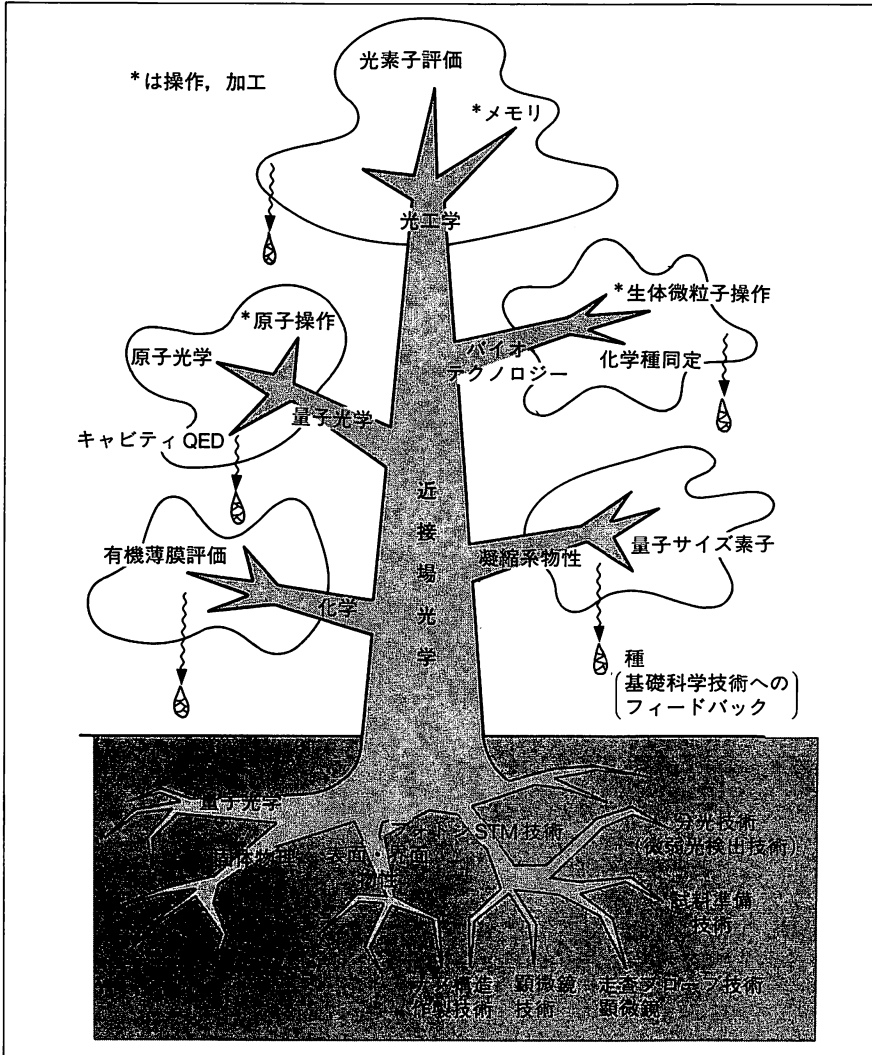
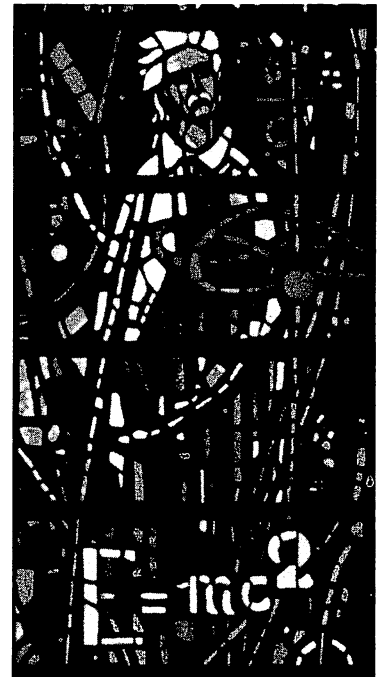


アインシュタイン 博物館

館長 杉元賢治

A4変形/180p. 定価 4,944円

アインシュタインの足跡を知られざるエピソードと600余枚の絵画、銅像、手紙、原論文、切手で綴る写真伝記。アインシュタインをめぐる科学者や家族の姿も同時に浮き彫りにし、彼らの生きた“物理学の黄金時代”を振り返る。



〈図7〉 フォトンSTMを扱う近接場光学が関わる基礎と応用の各分野

サルモネラ菌の鞭毛試料をご提供いただいた、帝京大学相沢慎一先生に感謝致します。

参考文献

- 1) E. H. Syngé: Phil. Mag., 6, 356(1928).
- 2) T. Pangaribuan, S. Jiang and M. Ohtsu: Electron. Lett. 29, 1978(1994).
- 3) S. Jiang, H. Ohsawa, K. Yamada, T. Pangaribuan, M. Ohtsu, K. Imai and A. Ikai: Jpn. J. Appl. Phys. 31, 2282(1992).
- 4) 久堀智子, 相沢慎一: 細胞 24, 520(1992).
- 5) W. P. Ambrose, P. M. Goodwin, J. C. Martin and R. A. Keller: Phys. Rev. Lett., 72, 160(1994).
- 6) E. Betzig, J. K. Trautman, R. Wolfe, E. M. Gyorgy, P. L. Finn, M. H. Kryder and C. -H. Chang: Appl. Phys. Lett. 61, 142(1992).
- 7) S. Jiang, J. Ichihashi, H. Monobe, M. Fujihira and M. Ohtsu: Opt. Commun., 106, 173(1994).
- 8) H. Mabuchi and H. J. Kimble: Opt. Lett. 19, 749(1994).
- 9) 大津元一: 第51回応用物理学会学術講演会, 1990年秋季, 講演番号 27aL9.
- 10) 大津元一, 堀裕和: 光学 21, 780(1992).

- Floor1 ウルム市の偉大な息子
- Floor2 夢想家
- Floor3 物理学の幸せな時代
- Floor4 Bird of Passage—渡り鳥
- Floor5 ベルリン—科学の殿堂
- Floor6 アインシュタインの功罪
- Floor7 芸術の中のアインシュタイン

定価は税込み

丸善 (出版事業部)

〒113 東京都文京区本郷2-38-3 本郷KM弓町ビル
営業(03)5684-5571

ThF2

915

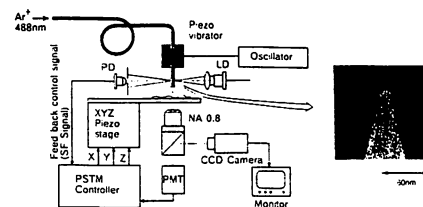
High resolution imaging of subcellular structures of neurons by an illumination mode photon scanning tunneling microscope

R. Uma Maheswari, Motoichi Ohtsu,*
Hitoshi Tatsumi, Yoshifumi Katayama,**
Kanagawa Academy of Science and
Technology, KSP East Block, Rm 408, 3-2-1
Sakado, Tatatsu Ku, Kawasaki, Kanagawa 213,
Japan

Photon Scanning Tunneling Microscope (PSTM) or near-field scanning microscope has been getting popularity over conventional optical microscope in the field of biology and medicine for the possibility of attaining high resolution beyond diffraction limit introduced by the wave length of light. In this work, we present results of high contrast imaging of subcellular structures of neurons by an illumination mode PSTM.

In our PSTM system, the nano-aperture has been fabricated by metal coating of sharpened fiber probes with flattened tip made by chemical etching technique¹ and has got a diameter of less than 30 nm. The neuron samples fixed on a glass substrate were taken from the hippocampus region of brain of a wistar rat and are labelled with racing blue and gold colloid of 23 nm. The sample mounted on a xyz piezo stage was illuminated by argon ion laser light (wave length is 488 nm) through the nano aperture and the scattered light was collected by an objective lens of high numerical aperture (0.8). While scanning the sample, the probe-sample separation was controlled to be around 10 nm by monitoring the shear force (Shear Force Microscope or SFM) originating between them.² Figure 1 shows a schematic of the experimental system for simultaneous recording PSTM and topographic (SFM) images with an inset of the fiber probe.

Figure 2 shows the PSTM image obtained over a scan area of $50 \times 50 \mu\text{m}^2$. In this figure, a part of the neuron cell (Cc) with branching axon (Ax) connecting other neuron cell is seen. Figures 3(a) and (b) show the magnified PSTM and topographic images of a section of the axon shown in Fig. 2. Bundles of microtubulins present inside the axon lying under protein sheaths can be imaged very well with high contrast by PSTM while in the corresponding topographic image, only a constant field has been observed. Moreover, from the intensity variation across the marked line of Fig. 3(a), the full width at half maximum was estimated to be 26 nm and this value agrees very well with diameter of 24 nm of tubulin measured after removing the overlying sheaths. Thus, the resolution of our system could be estimated to be around several nanometers and to our knowledge, this is one of the highest resolutions to be reported concerning imaging of biological samples. The capability of our system in resolving details



ThF2 Fig. 1. Experimental system for simultaneous recording of PSTM and topographic images (SFM) with an inset of the chemically etched fiber probe prior to metal coating.



ThF2 Fig. 2. Recorded PSTM image of neurons with Cc being a part of the cell and Ax being the branching axon extending from the cell. Scanning area is $50 \times 50 \mu\text{m}^2$.



ThF2 Fig. 3. Magnified PSTM (left) and SFM (right) images of a section of axon shown in Fig. 2. Note the microtubules lying under sheaths being observed in PSTM image. Full width at half maximum of the marked tube is around 26 nm. Scanning area is $1 \times 1 \mu\text{m}^2$.

smaller than the diameter of the aperture is believed to be arising out of the aperture edges existing at the boundary between the sharpened silica fiber and the metal coating covering this fiber probe.³ In our presentation, we will discuss further about the mechanisms behind the contrast enhancement and the effect of dye in imaging by comparing with undyed samples.

*Interdisciplinary Graduate School of Science and Engineering, Tokyo Institute of Technology, Nagatsuda, Midori-ku, Yokohama, Kanagawa - 226, Japan

**Department of autonomic physiology, Tokyo medical and dental university, Chiyoda Ku, Tokyo 101, Japan

1. R. Uma Maheswari, *et al.*, OSA Annual meeting digest, 179 (1994).
2. E. Betzig, *et al.*, *Science*, 257, 189 (1992).
3. M. Issacson, *et al.*, *Ultramicroscopy* 47, 15 (1992).

TutG 1130–1230
Room 304

**Tutorial: Photon Scanning
Tunneling Microscopy: From
Imaging to Fabrication and
Manipulation**

S. Kawata, *Osaka University, Osaka, Japan,
Presider*

TutG 1130

**Photon scanning tunneling microscopy:
from imaging to fabrication and
manipulation**

Motoichi Ohtsu, *Tokyo Institute of
Technology, Tokyo, Japan*

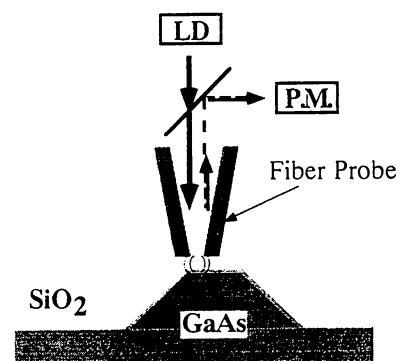
This tutorial describes the rapidly growing field of near-field optics, especially photon scanning tunneling microscopy (or, scanning near field optical microscopy) and its application to nano-scale photonics and quantum optics. Principle of the nano-metric resolution photon STM, fabrication technology of probe tip including functional super-tip, and control system for data acquisition are reviewed. Results of imaging experiments on photonic devices as well as biological samples are demonstrated. Novel quantum optical phenomena originating from short-range electromagnetic interactions observed in the fluorescence detection are presented. As an application to nano-scale photonics, possibility of high density optical storage is discussed. Furthermore, in order to explore the new field of atom manipulation, control of thermal motion of atoms in vacuum, e.g., an atom guide, are discussed. Finally a future outlook of the relevant near-field optics will be given.

Near-field optical properties of GaAs quantum dot structures measured by photon scanning tunnelling microscope

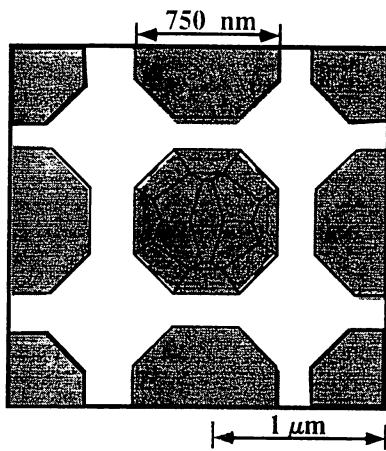
Yasunori Toda, Motonobu Kourogi,*
Yasushi Nagamune,** Yasuhiko Arakawa,**
Motoichi Ohtsu,* *Interdisciplinary Graduate
School of Science and Engineering, Tokyo
Institute of Technology, 4259 Nagatsuda,
Midori-ku, Yokohama, Kanagawa 227, Japan*

Nowadays requirements of study of photonic devices, i.e., superlattice, nanoclu-star, etc. are generally met by optical measurements of conventional far-field technique. However, optical studies of these structures beyond the sub-wavelength resolution have already been a subject of near-field optics. Recently, a photon scanning tunnelling microscope (P-STM) has become a powerful and indispensable tool for providing the information on optical properties with sub-wavelength resolution. Basic principle of the P-STM is a photon tunnelling between a sharpened nanometric fiber probe with a small aperture and a specimen's surface in the presence of evanescent light. It enable us not only to obtain high spatial resolution but also to evaluate near-field mesoscopic properties as well. We have recently demonstrated feasibility of P-STM technique for measurements of near-field optical properties of the optical waveguide, which is an example of passive photonic devices, and obtained optical information on scattering sources as well as the guided mode properties with sub-wavelength resolution.¹ For application to the evaluating the active devices, we present P-STM measurements of the optical properties of GaAs quantum dot-structure.

A schematic of the experimental setup is shown in Fig. 1. In order to obtain the scattering and reflection of the evanescent light on the GaAs surface, a probe tip is used not only to generate the evanescent light for illuminating the specimen but also to collect the scattered light, therefore the detected light comes through the aperture two times. In this configuration, the image contrast of the mesoscopic area is enhanced due to that light coming from the far-field patterns



FA3 Fig. 1. A schematic of the experimental apparatus. The fiber probe tip (cone angle of 30°) is fabricated by chemical etching method and is coated by 200 nm Au (curvature radius smaller than 100 nm). The sample and the fiber tip portions are drawn to scale.



FA3 Fig. 2. Schematic illustration of the GaAs dot-structure.³ The window of the SiO₂ mask is presented by a broken line.

1. Y. Toda, M. Ohtsu, Photo. Tech. Lett. to be published (1995).
2. M. Naya, S. Mononobe, R. Uma Maheswari, T. Saiki, M. Ohtsu, SPIE Photonics West '95 in California USA.
3. Y. Nagamune, S. Tsukamoto, M. Nishioka, Y. Arakawa, J. Crystal Growth, 126, 707 (1993).



FA3 Fig. 3. Gray-scale images of GaAs quantum dots. (a) SFM image scanned over a $3 \times 3 \mu\text{m}^2$. (b) Simultaneously obtained P-STIM image.

are effectively suppressed. The fiber tip is fabricated by chemical etching method. Metal coating is used for making an aperture.² The sample is GaAs quantum dots which were fabricated by the selective epitaxial growth on SiO₂-masked GaAs substrate as shown in Fig. 2.³ In addition, shear force microscope (SFM) is employed to measure the sample structure and to map the near-field image by using the common sharpened fiber as a probe. Besides, SFM is used to control the position of the fiber tip.

Figure 3(a) is a measured profile of SFM, and (b) is simultaneously detected P-STIM image by using a laser diode of wavelength 680 nm. The scanning area is $3 \mu\text{m} \times 3 \mu\text{m}$ with a pixel size of 23 nm. In Fig. 3(a), the region A and B represent to the area of GaAs and SiO₂ respectively and each dot is clearly resolved. Compared to A, the detected light intensity in B is lower. It is due to the difference between the reflectivities of GaAs and SiO₂. In A, the signal is constant except for the center with the diameter of about 200 nm, which implies that there exists the difference of structures or optical properties on the top of dot. We have started at the spectroscopic measurements of the quantum dots at the low temperature region in order to investigate this difference.

* Kanagawa Academy of Science and Technology, KSP East Rm 408, 3-2-1 Sakado, Takatsu-ku, Kawasaki, 213, Japan

** Institute of Industrial Science, University of Tokyo, 7-22-1 Roppongi Minato-ku, Tokyo 106, Japan

HIGH-RESOLUTION PHOTON SCANNING TUNNELING MICROSCOPY AND ITS QUANTUM OPTICAL ASPECTS

W. JHE

Department of Physics, Seoul National University, Seoul, Korea

and

M. OHTSU

*Interdisciplinary Graduate School, Tokyo Institute of Technology and
Kanagawa Academy of Science and Technology, Kanagawa, Japan*

ABSTRACT

We describe a high-resolution Photon Scanning Tunneling Microscopy (PSTM) and its nanometric images. We also provide several quantum optical aspects of the PSTM.

1. Introduction

Photon Scanning Tunneling Microscope (PSTM) provides high-resolution images beyond the diffraction limit, which is based on the short-range electromagnetic interaction between a small dielectric probe and a sample [1]. The PSTM is commonly operated in the collection mode (c-mode) where a nanometric dielectric probe tip is used as a light collector. When the tip is introduced in the evanescent field near the sample surface produced by the incident light under the total internal reflection (TIR) condition, the non-radiative evanescent light is converted into the scattered light which is guided to the detection optics.

Here we present high-resolution imaging by c-mode PSTM with a nano-apertured probe, whose resolution is quantitatively studied. We also consider several quantum optical aspects of the PSTM.

2. High-Resolution PSTM

2.1. Experiments

In the c-mode PSTM [2], an intensity-modulated Ar⁺ laser (488 nm) was used as an incident light source. The evanescent wave (EW) generated near the sample was picked up by a small fiber probe, which is scanned in the XYZ-direction. The sample/probe separation was maintained constant by electrical feedback and no auxiliary scheme such as STM or AFM was needed in our experiment. To selectively detect the strongly localized near-field, or the high spatial-Fourier frequency component of the EW, to obtain high resolution images, a nanometer-apertured probe is essential. For fabrication of such a tip, an optical fiber was sharpened to 10 nm of its apex curvature by selective two-step chemical etching [3]. The fiber, coated with 150-nm thick Au, was then dipped

in KI/I_2 solution to remove the gold only from the top of the tip to realize a sub-wavelength aperture. The aperture size was measured less than 30 nm by a SEM (Scanning Electron Microscope). As a well-calibrated nanometric standard sample, we used a straight-type flagellar filaments of salmonella (FFS). A TEM (Transmission Electron Microscope) image showed a cylindrical-rod shape with the diameter of 25 nm, which was about the same size as the probe tip.

2.2. High-Resolution Images

Fig. (1a) is a PSTM image of the FFS for the s-polarized incident light. Scanning area is $5 \mu\text{m} \times 5 \mu\text{m}$, one pixel size was about 20 nm and the sample/probe separation was maintained at about 15 nm. We find that the FFS lying perpendicular to the direction of the incident beam was well imaged with high contrast. The width of the bright line due to the FFS was 50 nm and the dark region on both sides of the FFS correspond to the shadow formed by the filament. Comparing the PSTM image with the nominal TEM image, we estimate the resolution to be better than the aperture diameter of about 30 nm. Fig. (1b) shows an image similar to Fig. (1a), except a larger sample/probe separation of 65 nm. A lower resolution was achieved, the width of the FFS being about 150 nm. This dependency of resolution on the sample/probe distance can be understood as due to the localization of the high spatial-frequency components of the EW near a small sample. Therefore, for efficient pick-up, the probe must be brought close to the sample. Fig. (1c) shows the PSTM image of the same sample taken with a larger apertured probe of 100 nm. The poor resolution is due to the fact that the EW having high spatial-Fourier frequency is picked up most efficiently by a probe with the same size as the sample. Therefore a probe with larger aperture picks up rather lower frequency components and hence the resolution deteriorates.

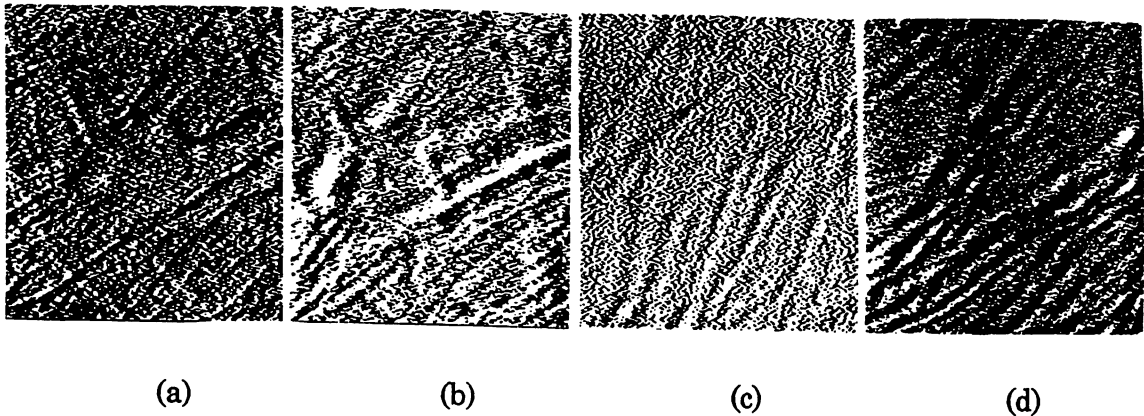


Fig. 1. (a) A PSTM image of a FFS for a s-polarized light, (b) same as (a) except larger sample/probe distance of 65 nm, (c) same as (a) except larger aperture of 100 nm, and (d) same as (a) except p-polarization.

Fig. (1d) presents a PSTM image of the same FFS for the p-polarized incident light, showing a two-peak structure in contrast to the case of Fig. (1a). The dependence on the polarization states may be qualitatively understood by the image dipole model of cavity QED. Moreover, the FFS lying perpendicular to the incident beam could be observed with a resolution relatively lower than that obtained in Fig. (1a), which is in conflict with the predictions of the recent field-propagator theory [4].

3. Quantum Optical Aspects

3.1. Cavity QED: Image Dipole Model

The polarization dependence can be qualitatively understood by simple cavity QED consideration of the image dipole model. It has been found [5] that the radiative properties of an atomic dipole near a dielectric sphere can be approximated by the dipole-image dipole interaction both in the nonretarded- and retarded-regime. In the PSTM, the apertured fiber-probe is modeled as a dielectric sphere. Let us consider a small sample on a glass substrate under the TIR condition. When the exciting laser is s- (p-) polarized, the sample can be considered as an induced dipole polarized parallel (normal) to the substrate plane. The probe tip approaching the sample can then be replaced by an image dipole whose direction of polarization depends on its lateral position relative to the sample. Let us first consider the s-polarization case. When the tip is right above the sample, the equivalent image dipole is also polarized in the substrate plane. Then the detected light intensity, radiated by the tip and transmitted through the optical fiber, becomes maximum. As the tip is scanned over the sample in the lateral direction, the orientation of the image dipole should rotate to meet the boundary conditions and as a result the measured power decreases. We thus expect a single peak mimicking the topology of the sample object. Now let us consider the p-polarization case. When the tip is above the sample dipole, the probe becomes also p-polarized and the radiated power through the fiber is minimum. When the tip is scanned laterally, the orientation of the image dipole rotates so that the detected power increases. It will however decrease quickly due to the localized distribution of the EW near the sample. We thus expect an image having a double-peak structure. These results agree well with the high-resolution PSTM images described in section 2.2. The strong point of the simple cavity QED model given here is that it includes not only the effects of the probe tip itself but those of the specific configuration of the guiding optical fiber. This method is a good approximation for the case of a small tip and a small sample where the effects of the higher-multipole terms can be neglected [5,6].

3.2. Near-Field Distribution of a 3-D Object

Leviatan [7] has calculated the intensity profile of the EW near a subwavelength-sized circular metallic-aperture and found that it extends about the radius of the aperture. Here, we consider a small dielectric sphere as a

typical three-dimensional (3-D) object and calculate its near-field intensity profile by using the Mie scattering theory. Let us consider a small dielectric sphere on a dielectric prism under the TIR condition. In this case, the inhomogeneous but plane evanescent wave, produced near the prism surface, is scattered by the dielectric sphere. The calculated near-field intensity distribution is presented in Fig. 2. As can be seen, the EW's extend over about the radius (a) of the sphere and the characteristic decay length is independent of the wavelength of the illuminating laser. In other words, the EW's of a 3-D object are localized within the object size, having the high spatial-frequency components. Now when one considers a second dielectric sphere (the tip) which scatters the near field of the first sphere (the sample), one can obtain the transfer function which determines the resolution of the PSTM. The effects of the tip-size, the sample/probe distance, and the sample-size can also be understood quantitatively. One may also consider a metallic circular aperture as a simple model for the probe-tip, instead of the dielectric sphere. Note that an intuitive Yukawa potential model [8] has been proposed to calculate the transfer function as well as the near-field intensity profile.

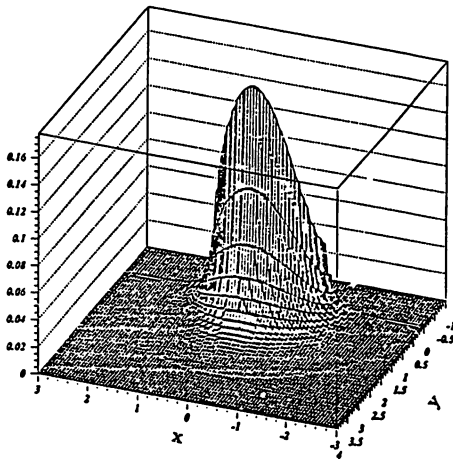


Fig. 2 Near-field intensity distribution of a dielectric sphere. $ka = 0.5$.

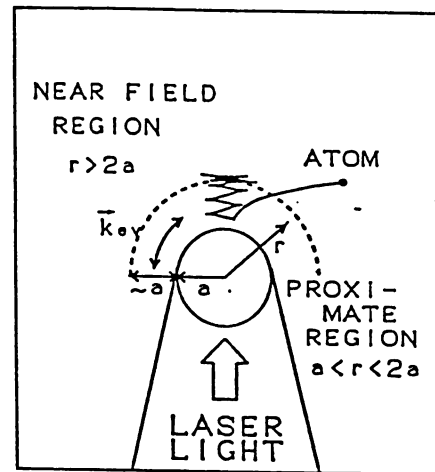


Fig. 3 Single atom trapping

3.3. Atom Manipulation

When the laser is illuminated from the opposite end of the fiber tip, the EW's produced near the tip may be used for optical manipulation of nearby single atoms [8]. When an atom approaches the fiber probe-tip where a localized EW is produced, it may be trapped near the tip due to the optical gradient forces and scattering forces. In other words, due to the interaction of the localized EW and an atom, a stable optically-bound system may be formed (Fig. 3). Since the separation is on the order of the radius of curvature of the tip,

which is more than 10 times larger than the distance for the van der Waals interaction minima, the atom is not attracted to the tip surface and lost. In fact, the optical binding can be achieved only for red-detuned laser frequencies with respect to the atomic resonance frequency. When blue-detuned, however, the atom is repelled by the EW and escapes from the fiber tip. Using the frequency-dependent optical forces, one can trap, move, and deposit the atoms on a cold substrate for crystal growth on an atomic scale. For example, one needs a coherent laser source of 252 nm wavelength to manipulate silicon atoms and the equivalent temperature of the trapping potential for 10 nm radius of curvature of the tip is about 3 mK. This low temperature can be easily obtained for room-temperature atoms in a typical laser trap such as the magneto-optical trap. The pre-cooled atoms can then be trapped and controlled by the fiber tip. In this case, the cavity QED effects of the fiber tip, which can be approximated as a dielectric sphere, may also be important for the atom-radiation interaction [5]. The quantum optical aspects of the PSTM and the realization of the optical binding are currently under cooperative research between the authors.

We are grateful to Dr. M. Naya of KAST for the high-resolution images and Mr. K. Jang of SNU for the numerical calculation of the near-field distribution.

4. References

1. *Near Field Optics*, edited by D.W. Pohl and D. Courjon (Kluwer Academic Publishers, 1992); M. Ohtsu, *IEEE J. Lightwave Technol.* Vol. 13, No. 7, in press (July, 1995).
2. M. Naya, S. Mononobe, R. Uma Maheswari, T. Saiki, and M. Ohtsu, *Proceed. of SPIE Symposium on Scanning Probe Microscopes III*, Vol. 2384 (Feb, 1995).
3. T. Pangaribuan, K. Yamada, S. Jiang, H. Ohsawa and M. Ohtsu, *Jpn. J. Appl. Phys.* 31, (1992) L1302.
4. O. J. Martin, C. Girard, and A. Dereux, *Phys. Rev. Lett.* 74 (1995) 526.
5. W. Jhe and J. W. Kim, *Phys. Rev. A* 51, (1995); *ibid*, *Phys. Lett. A* 197, 192 (1995).
6. D. Barchiesi and D. Van Labeke, *J. Mod. Opt.* 40 (1993) 1239.
7. Y. Leviatan, *J. Appl. Phys.* 60 (1986) 1577.
8. H. Hori, S. Jiang, M. Ohtsu and H. Ohsawa, *Tech. Digest of the 18th Int'l Quant. Electron. Conf.* (June 1992, Vienna) pp.48.

QTuJ3

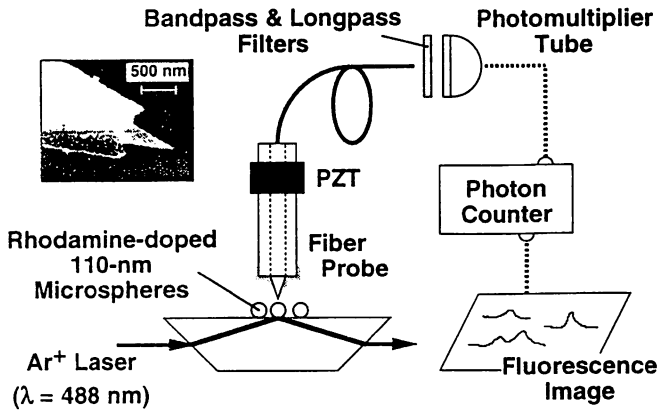
3:15 pm

Nanometric integrating tip: enhanced sensitivity of fluorescence detection in photon STM

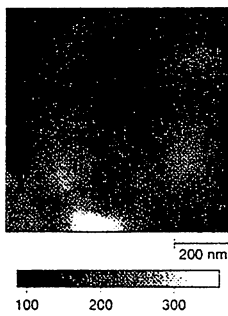
T. Saiki, S. Mononobe, M. Ohtsu,*
Kanagawa Academy of Science and Technology, 3-2-1 Sakado, Takatsu-ku, Kawasaki, Kanagawa 213, Japan

Fluorescence detection with subwavelength resolution is important in biological applications¹ such as the observation of a membrane selectively labeled with dye molecules. Photon scanning tunneling microscopy (PSTM), which is also called scanning near-field optical microscopy (SNOM),² enables us to detect fluorescence with the resolution determined by the tip diameter at the apex of the fiber probe. In comparison with the illumination mode in PSTM, the most favorable quality of the collection mode is that probe-sample distance can be controlled by all-optical means without a feedback mechanism based on shear force, which may damage samples. It is, therefore, essential to estimate the resolution and the sensitivity of PSTM as fluorescence microscopy. Also, local detection of fluorescence with a fiber tip is an attractive subject in quantum optics. The approach of the tip to a fluorescent material in the near-field region will largely modify its radiation modes. This modification leads to a change of its radiation pattern and of its lifetime, which offers the possibility of highly effective collection of fluorescence. From these viewpoints, we here report the fluorescence imaging of dye-doped 110-nm microspheres, and we estimate the pickup efficiency, which demonstrates that the fiber tip acts as something like a nanometric integrating tip in collecting fluorescence.

Our experimental setup is shown in Fig. 1. As a sample, rhodamine-doped polystyrene microspheres of 110-nm diameter are dispersed on a silica substrate. The sharpened fiber probe with a 20-nm tip diameter is fabricated by chemical etching.³ A part of the tip is coated with gold to eliminate background fluorescence [a practical coating scheme is shown in Fig. 3(a)]. Fluorescence from the rhodamine molecules is picked up by the fiber tip and is measured by a photon-counting method. Figure 2 shows a near-field fluorescence image of microspheres. A sample-probe separation of ~ 20 nm is kept during scanning. The image size of the spheres is estimated as ~ 180 nm full width at half maximum, beyond the diffraction limit.



QTuJ3 Fig. 1. Experimental scheme of fluorescence detection with the PSTM system. Inset shows SEM image of a fiber tip.

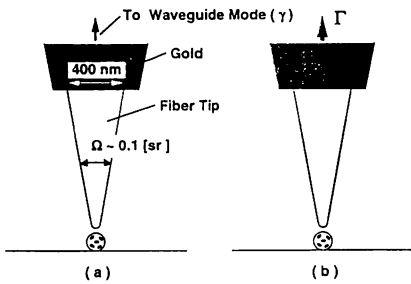


QTuJ3 Fig. 2. Near-field fluorescence image of dye-doped 110-nm microspheres.

is induced by the modification of radiation modes due to the strong coupling between the fiber tip and the sphere in the near-field region [Fig. 3(b)]. That is, the fiber probe works as a nanometric integrating tip in the collection of fluorescence.

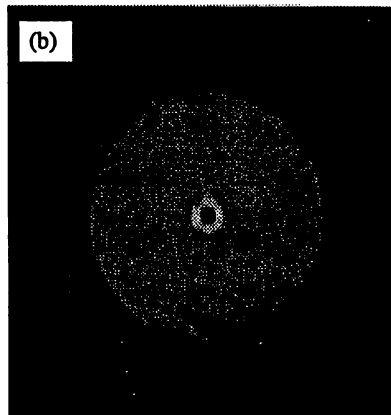
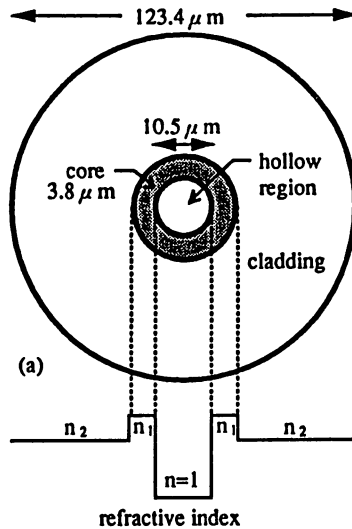
* Also with *Interdisciplinary Graduate School of Science and Engineering, Tokyo Institute of Technology, 4259 Nagatsuta-cho, Midori-ku, Yokohama, Kanagawa 226, Japan*

1. R. C. Dunn, G. R. Holtom, L. Mets, and X. S. Xie, *J. Chem. Phys.* **98**, 3094 (1994).
2. E. Betzig and R. Chichester, *Science* **262**, 1422 (1993).
3. T. Pangaribuan, S. Jiang, and M. Ohtsu, *Electron. Lett.* **29**, 1978 (1993).



QTuJ3 Fig. 3. (a) Pickup efficiency determined by the solid angle at the aperture plane from the sample (Ω) and coupling coefficient to waveguide mode (γ). (b) Enhanced pickup efficiency (Γ) due to near-field coupling between the tip and the sample.

To clarify the mechanism of fluorescence detection with high resolution, we estimate the pickup efficiency Γ (defined as the ratio of fluorescence intensity finally coupled to the waveguide mode of the fiber probe to the total fluorescence intensity). (By applying the parameters of the dye molecules and detection systems, a Γ of 2×10^{-3} to 5×10^{-3} is obtained. If the radiation pattern of the dye molecules is isotropic, even when the probe approaches the sphere to a distance of less than 20 nm, the pickup efficiency is estimated as $(0.1/4\pi)\gamma$, where $\gamma (\ll 1)$ is the coupling coefficient to the waveguide mode [Fig. 3(a)]. By comparing these two values, it is confirmed that the enhanced sensitivity of Γ



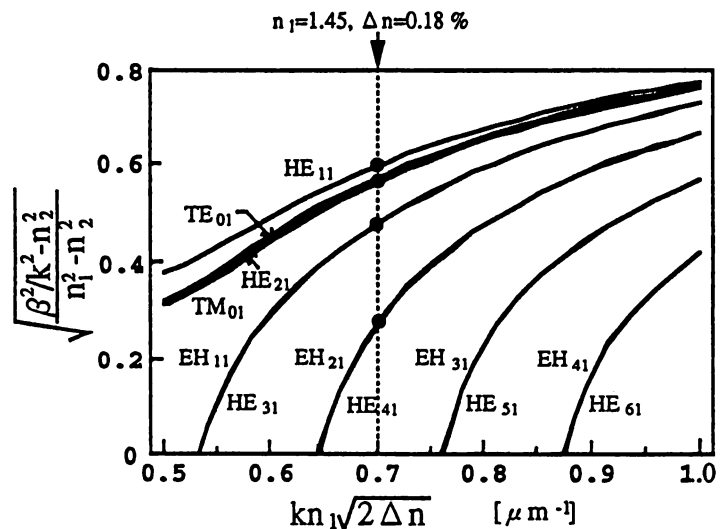
QW11 Fig. 1. (a) Configuration of the hollow silica fiber with a thin cylindrical core. The refractive indices of the core and the cladding are n_1 and n_2 , respectively. The relative refractive-index difference Δn is 0.18%. (b) Cross-sectional view for demonstrating the hollow-fiber configuration and cylindrical beam propagation. A He-Ne laser was used.

ular, one can avoid laser-light perturbations of guided atoms due to heating effects. Evanescent waves have an effective thickness less than one wavelength and therefore interact only with atoms approaching the inner surface of the hollow fiber.

Figure 1 shows the configuration of the cylindrical-core hollow fiber fabricated on the basis of our design and a view of the cross section when a He-Ne laser beam was directed into the fiber. Figure 2 shows the dispersion curves for a wavelength of 780 nm, for which eight propagation modes are folded. Note that the fundamental mode is HE_{11} , as in the case of the conventional homogeneous-core fibers for optical transmission.

The atoms in the hollow region are kicked back by the strong gradient force due to the evanescent wave near the inner surface under blue-detuning conditions. The optical potential is evaluated by calculating the time-averaged Poynting vector. Figure 3(a) shows the optical potential for ^{85}Rb atoms in terms of the temperature representing thermal kinetic energy as a function of the distance from the inner surface. For simplicity, we supposed that the HE_{11} mode gives the principal contribution to the optical potential. Provided that the optimal blue-detuning Δ is chosen, an optical potential deeper than 1 mK is produced with a laser power of a few milliwatts, which is sufficient to guide atoms injected into the hollow fiber from an atomic beam or a magneto-optical trap. The optimal blue detuning changes according to the coupled laser power. Moreover, as shown in Fig. 3(b), the axial dependence of the HE_{11} mode is periodic, so that the produced optical potential depends on the azimuth angle θ . The optimal detuning ought, therefore, to be determined such that the optical potential is sufficiently deep for all values of θ .

We will report our experiments using an atomic beam, including laser-beam tailoring for efficient coupling to the hollow fiber. We also touch on an atomic funnel for pouring atoms into the hollow fiber.



QW11 Fig. 2. Dispersion curves of low-order modes in the cylindrical-core hollow fiber shown in Fig. 1(a), where β and k are the propagation constant and the wave number, respectively. Filled circles indicate the propagation modes of the hollow fiber for a wavelength of 780 nm. The vertical axis is the normalized propagation constant, and the horizontal axis is proportional to the normalized frequency.

QWI 4:30 pm
Hyatt B

Atom Optics

William Daniel Phillips, National Institute of Standards and Technology, Presider

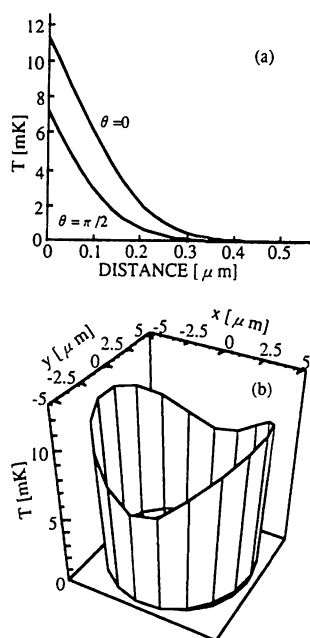
QWI1 4:30 pm

Atomic waveguide using evanescent waves in a hollow fiber

Haruhiko Ito, Keiji Sakaki,*
Takeshi Nakata,* Wonho Jhe,**
Motoichi Ohtsu, † Kanagawa Academy of Science and Technology, KSP East, 3-2-1 Sakado, Takatsu-ku, Kawasaki 213, Japan

The realization of atomic waveguides, which have been proposed by a few research groups,¹⁻³ is an important subject in atom optics. Atomic waveguides are expected to apply even to nanoscale crystal growth, by combination with the laser manipulation of atoms.⁴ For this application, atomic waveguides are used for one-dimensional manipulation to carry atoms to a specified point on a substrate.

Our proposed atomic waveguide is composed of a hollow silica fiber with a thin cylindrical core. This type of atomic waveguide is advantageous because evanescent waves are used to produce the optical potential for guiding atoms. In partic-



QW11 Fig. 3. Optical potential produced by the evanescent wave (HE_{11}) for 10 mW of laser power. The blue-detuning Δ is taken to be 12 times as large as the natural linewidth Γ , which is almost optimal. The potentials are expressed by a temperature representing one-dimensional thermal kinetic energy: (a) cross-sectional profile as a function of the distance from the inner surface and (b) three-dimensional distribution. The azimuth angle θ is chosen such that the potential becomes maximum at $\theta = 0$ and minimum at $\theta = \pi/2$.

*Interdisciplinary Graduate School of Science and Engineering, Tokyo Institute of Technology, 4259, Nagatsuta, Midori-ku, Yokohama 226, Japan

**Department of Physics, Seoul National University, Seoul 151-742, Korea

†Also with Interdisciplinary Graduate School of Science and Engineering, Tokyo Institute of Technology, 4259, Nagatsuta, Midori-ku, Yokohama 226, Japan

1. M. A. Ol'Shanii, Yu. B. Ovchinnikov, and V. S. Letokhov, *Opt. Commun.* **98**, 77 (1993).
2. S. Marksteiner, C. M. Savage, P. Zoller, and S. L. Rolston, *Phys. Rev. A* **50**, 2680 (1994).
3. W. Jhe, M. Ohtsu, H. Hori, and S. R. Friberg, *Jpn. J. Appl. Phys.*, in press.
4. H. Hori, S. Jiang, M. Ohtsu, and H. Ohsawa, in *Proc. International Quantum Electronics Conference, 1992*, Vienna, p. 48.

HIGH RESOLUTION IMAGING OF BIO-SAMPLES BY A PHOTON SCANNING TUNNELING MICROSCOPE WITH AN APERTURED PROBE

Masayuki Naya¹⁾²⁾, R. Uma Maheswari¹⁾, Ruggero Micheletto¹⁾, Shuji Mononobe¹⁾, Motoichi Ohtsu¹⁾

1) Kanagawa Academy of Science and Technology

Address : KSP East, 3-2-1 Sakado, Takatsu-ku, Kawasaki 213, Japan

Phone: +81-44-819-2071, Fax: +81-44-819-2072

e-mail: KFH02563@niftyserve.or.jp

2) Fuji Photo Film Co., Ltd.

KEY WORDS; PSTM, c-mode, nano-apertured probe, bio-samples, flagellar filaments of salmonella

1. INTRODUCTION

We demonstrate high resolution imaging by collection mode photon scanning tunneling microscope (c-mode PSTM) with a nano-apertured probe we have developed. To evaluate the resolution and properties, we used flagellar filaments of salmonella (FFS) with diameter of 25 nm [1], as a standard sample.

2. EXPERIMENT

Figure 1 shows our experimental system of the c-mode PSTM. To realize high resolution detection, a probe with nanometric sized fiber tip protruding out from Gold film was used (Inset of Fig.1). A minimum aperture diameter at the foot of the protruded fiber was about 30 nm. As the samples, flagellar filaments of salmonella (FFS) with a diameter of 25nm, fixed on a hydrophilized glass plate were imaged with a collection mode PSTM.

3. RESULTS

High resolution imaging was realized by using c-mode PSTM (Fig.2). The full width at half maximum (FWHM) of the image of filaments obtained were 50nm. Such a high resolution was caused by the fact that the high spatial Fourier frequency components are selectively picked up by the fiber tip protruding out from the Au film[2]. Therefore, the resolution of the image become worse when aperture size is larger (Fig.3). It was found that the c-mode PSTM image strongly depended on the separation of the sample to the probe (Fig.4). This can be considered to be resulting from the localization of the high spatial frequency components of the evanescent field around the surface of the sample with small radius and volume[2]. The dependence of the image on polarization of incident light was also observed (Fig.5). This can be explained in the terms of lines of electric force in the near-field region[3]. We have also succeeded in getting the image of flagellar filaments in the water. (Fig.6)

4. REFERENCE

1.J.J.Jones and S.-I. Aizawa, *Advances Microbial Pysiol.*, 32, pp109 (1991)

2.H.Hori, "Quantum optical picture of photon STM and proposal of single atom manipulation", D.W.Pohl and D.Courjon(eds.), *Near Field Optics*, 105-114,(1993)

3.B.Labani and C. Girald, "Optical interaction between a dielectric tip and a nanometric lattice; implications for near-field microscopy" *J.Opt.Soc.Am.B*, vol.7, No.6, pp.936-943, June(1990)

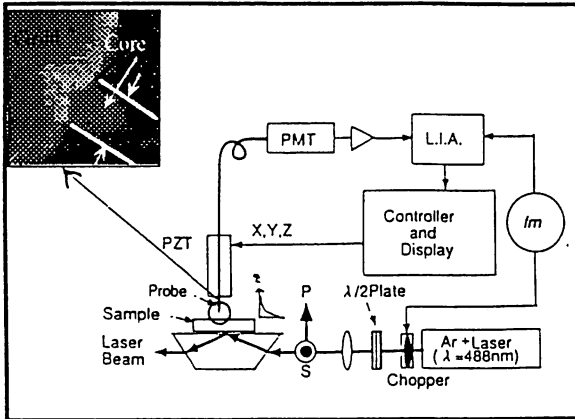


Fig.1 Experimental system of the c-mode PSTM

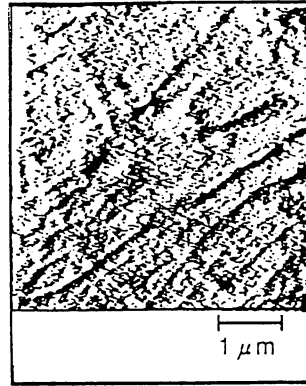


Fig.2 A PSTM image of FFS when incident light was s-polarized. The sample/probe separation was about 15 nm.

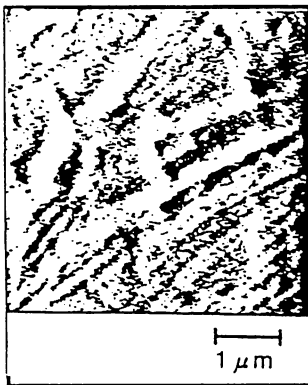


Fig.3 A PSTM image taken under the same area and the same condition as of Fig.3, except for the sample/probe separation being as large as 65 nm

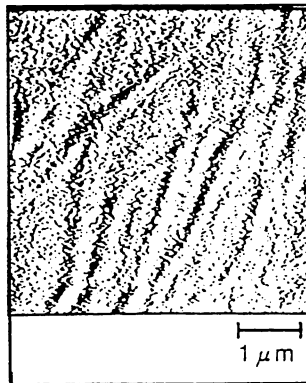


Fig.4 A PSTM image of the FFS obtained by using a tip with an aperture diameter as large as 100 nm.

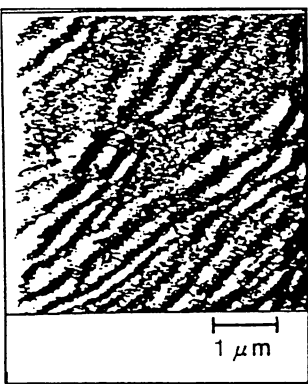


Fig.5 A PSTM image for exactly the same scan area and the same conditions except the incident light was-polarized.



Fig.6 A PSTM image of FFS in the water

FABRICATION TECHNIQUE OF PENCIL-TYPE FIBER PROBES AND NANOMETRIC APERTURES FOR PHOTON SCANNING OPTICAL MICROSCOPE

Shuji MONONOBE, Masayuki NAYA, RAJAGOPALAN Uma Maheswari, Toshiharu SAIKI,
Motoichi OHTSU

Kanagawa Academy of Science and Technology (KAST)
Ohtsu 'Photon Control' Project
KSP East, 3-2-1 Sakado, Takatsu-ku, Kawasaki, Kanagawa 213, Japan
Phone: ++(81)-44-819 2071, Fax: ++(81)-44-819 2072

KEY WORDS: photon scanning tunneling microscope, PSTM, NSOM, pencil-type fiber probe, apertured probe, nanometric aperture, selective chemical etching, optical fiber

1. INTRODUCTION

We have studied about the fabrication of a fiber probe for Photon Scanning Optical Microscopes (PSTM) or Near-field Scanning Optical Microscope (NSOM). Till now, some method based on a selective chemical etching of silica fibers with high GeO_2 doped core have been developed.¹⁻⁴ Here, we propose several new techniques to fabricate pencil-type fiber probes and nanometric apertures.

2. PENCIL-TYPE FIBER PROBE

Figure 1 and Fig. 2 show a fabrication technique of pencil-type fiber probes and finer pencil-type respectively. A pencil-type and a finer pencil-type is produced respectively with four and two step etchings consisting of NH_4F (40%)- HF (50%)- H_2O by using a GeO_2 doped fiber of a ratio about 27mol%. In the case that $X=10$ in Fig. 1, pencil-type probes have a cone angle of 20° and a tip diameter less than 10 nm shown in Fig. 3. They could be obtained with high reproducibility because the process of sharpening core at the fourth step uses efficiently a selective etching. Fig. 4 shows SEM photograph of a finer pencil-type with a cone angle of 4° which was obtained in $X=10$ in Fig. 2. For both type fiber probes, the cladding diameters can be controlled by an easy process.

3. APERTURED PROBE

To fabricate a nanometric aperture, first a pencil-type fiber probe was coated by evaporating gold on the probe with the thickness of a few hundreds nanometer. Next the coated probe was dipped in a KI-I_2 solution and a part of gold was dissolved so as to remove gold only from the top of the probe.

The resulting probe is shown in Fig. 5. The probe called apertured probe has a nanometric dielectric tip protruding out of the gold film with a base diameter of less than 30 nm and a height of 30 nm. By using these probes in a PSTM system, we have succeeded in obtaining high resolution images for biological samples such as flagellar filaments of salmonella.⁵

REFERENCES

1. T.PANGARIBUAN, M.OHTSU *et al.*: "Reproducible fabrication technique of nanometric tip diameter fiber probe for photon scanning tunneling microscope" *Jpn. J. Appl. Phys.*, **31**, L1302-L1304(1992).
2. T.PANGARIBUAN, M.OHTSU *et al.*: "Two-step etching method for fabrication of fibre probe for photon scanning tunneling microscope" *Electron. Lett.*, **29**, 1978-1979, (1993).
3. T.PANGARIBUAN, M.OHTSU *et al.*: "Highly controllable fabrication of fiber probe for photon scanning tunneling microscope" *Scanning*, **16**, 362-367 (1994).
4. R.UMA MAHESWARI, S.MONONOBE, M.OHTSU: "Control of apex shape of the fiber probe employed in photon scanning tunneling microscope by a multi-step etching method" *IEEE J.Lightwave Tech.* submitted.
5. M.NAYA, M.Ohtsu *et al.*: "Imaging experiments of bio-samples by a photon scanning tunneling microscope with an apertured fiber probe" *Proc.SPIE*, **2384**, (1995)"

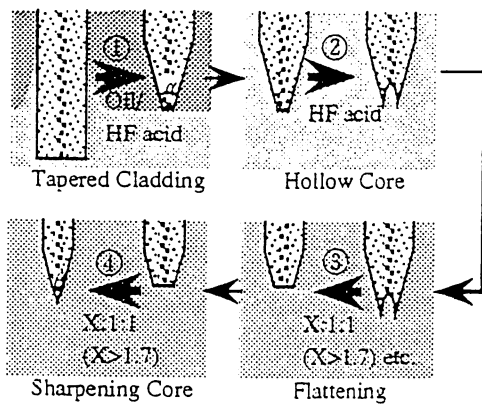


Fig.1. Fabrication technique of pencil-type fiber probe

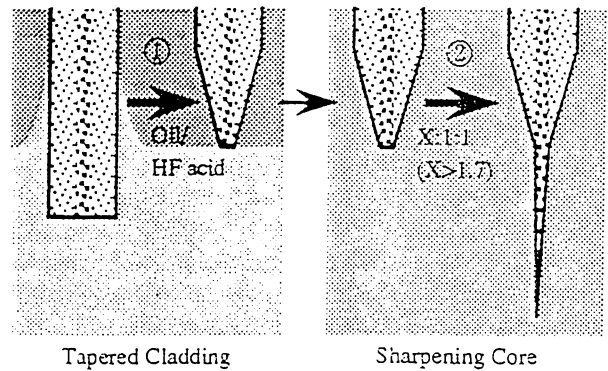
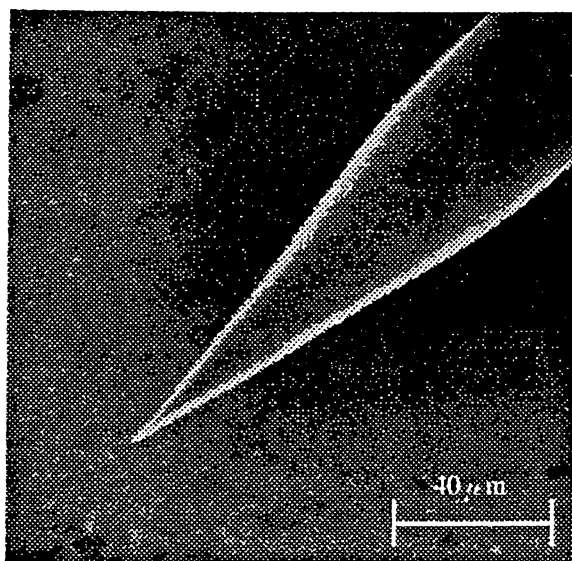
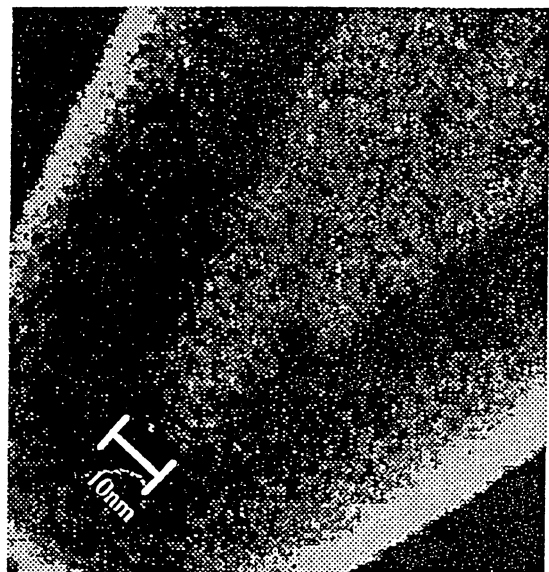


Fig.2. Fabrication technique of finer pencil-type



(a)



(b)

Fig.3.(a) SEM image of pencil type fiber probe
(b) SEM image at the top of the probe

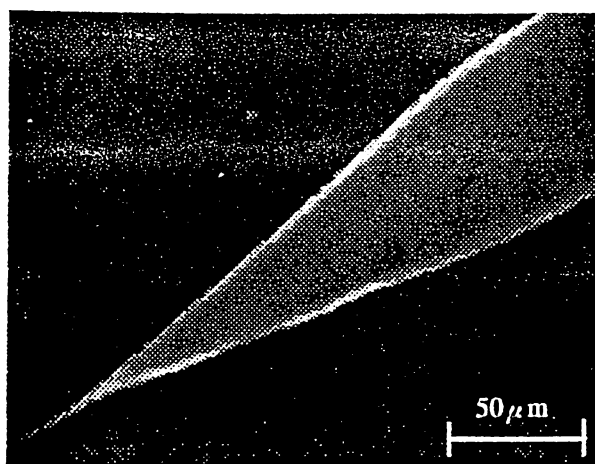


Fig.4. SEM image of finer pencil-type fiber probe

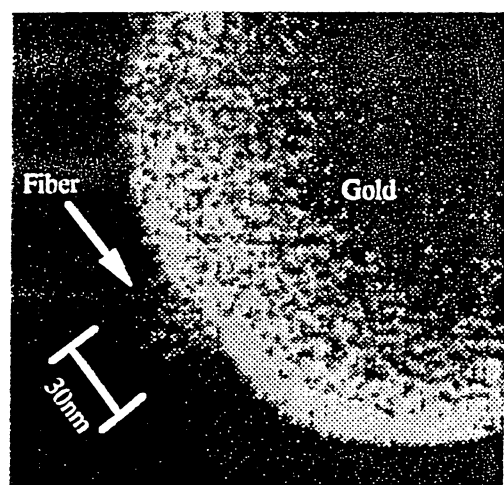


Fig.5. SEM image of apertured probe

THREE DIMENSIONAL NANO-PHOTOLITHOGRAPHY FOR FABRICATING A NANO-APERTURED PROBE AND A NANOMETRIC SUPER CUP

Takuya MATSUMOTO¹⁾ and Motoichi OHTSU^{1), 2)}

1) Ohtsu Laboratory, Interdisciplinary Graduate School of Science and Engineering, Tokyo Institute of Technology, 4259 Nagatsuta, Midori-ku, Yokohama 226, Japan
Phone: +81-45-924-5455, Fax: +81-45-921-1204
e-mail: takuya@ae.titech.ac.jp

2) Kanagawa Academy of Science and Technology, KSP East 408, 3-2-1 Sakado, Takatsu-ku, Kawasaki 213, Japan
Phone: +81-44-819-2071, Fax: +81-44-819-2072

KEY WORDS: photon scanning tunneling microscope (PSTM), nano-apertured fiber probe, three dimensional nano-photolithography, evanescent wave, super cup, supertip

1. INTRODUCTION

Photon scanning tunneling microscope is a scanning optical microscope having a very high resolution beyond the diffraction limit. The most important part in this microscope is a fiber probe having an aperture at its top. To fabricate this apertured probe with high reproducibility, we propose a new technique based on photolithography using evanescent wave. In addition, a probe having a dip at its top with a diameter of less than 100nm is proposed to fabricate a functional supertip.

2. THREE DIMENSIONAL NANO-PHOTOLITHOGRAPHY

First, a fiber is sharpened by two step chemical etching method¹ and coated with gold. Second, it is coated with photoresist and its top is selectively exposed by UV light. This makes the photoresist at the top of the fiber removed. Finally, by dipping the fiber in an etching solution, the gold at the top of the fiber is etched away and the aperture is fabricated. (Fig.1) The novelty in this method lies in the method of the exposure. In this method, to expose only the top of the fiber, UV evanescent light generated at the surface of a prism is employed. Because its intensity decreases rapidly as the distance from the prism increases, the top of the fiber is selectively exposed when the fiber is placed in the near-field region of the prism surface. (Fig.2) During the exposure, to maintain high reproducibility, shear force is used for controlling the fiber-prism separation. By this method, we can expose sub-wavelength area at the top of the fiber as shown in Fig.3 and fabricate an aperture with a diameter of 30nm as shown in Fig.4. In future, smaller aperture can be expected by decreasing the grain size of the metallic film.

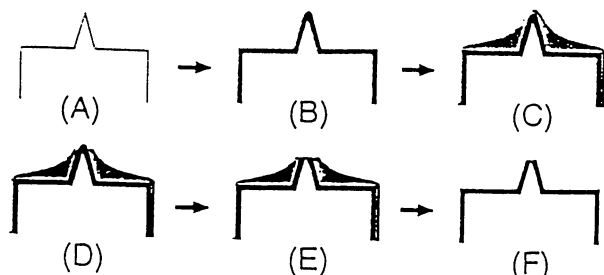


Fig. 1 Aperture fabrication steps: (A) Etching of an optical fiber (B) Coating the metallic film (C) Coating the photoresist (D) Exposure using evanescent wave and development (E) Etching of metal (F) Removal of photoresist

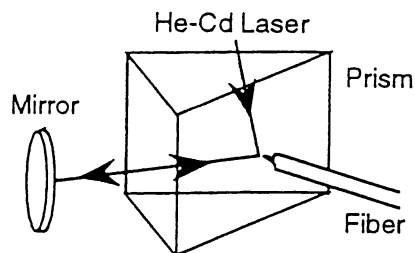


Fig.2 Illustration of the exposure method using evanescent wave

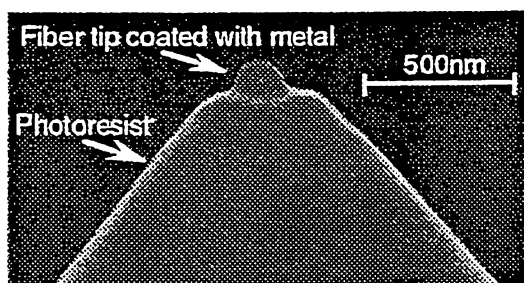


Fig.3 SEM image of a fiber after the exposure and development

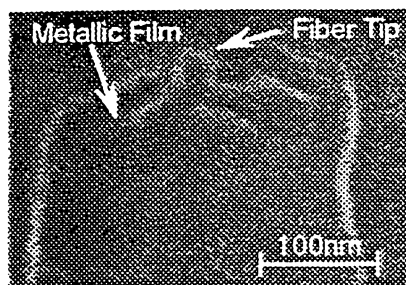


Fig.4 SEM image of the fabricated fiber probe (under the illumination of e-beam at the angle of 20°)

It should be emphasized that this method opens up the possibility of applying photolithography for the fabrication of three dimensional nanometric structures for the first time to our knowledge. This method promises to have applications not only in the fabrication of apertured probes but also in a wide variety of applications.

3. FABRICATION OF A SUPER CUP

We propose a "super cup probe" which has a dip at its top with a diameter of less than 100nm as shown in Fig.5. This is fabricated by dipping the fiber in HF solution after the etching of metal. This can be applied to a functional supertip², e.g., by injecting dye molecules into it.

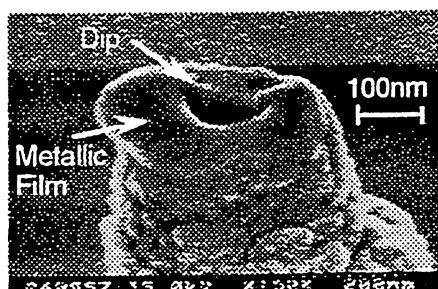


Fig.5 SEM image of a super cup

4. ACKNOWLEDGMENTS

We would like to thank Dr. T.Sakaguchi of Tokyo Institute of Technology for technical advice on photolithography and staff members of Ohtsu Photon Control Project of Kanagawa Academy of Science and Technology for helpful discussion.

5. REFERENCES

1. T.PANGARIBUAN, *et al.*: "Two-step etching method for fabrication of fiber probe for photon scanning tunneling microscope", *Electronics Lett.* **29**, 1978-1979 (1993)
2. R.KOPELMAN *et al.*: "Near field optical and exciton imaging, spectroscopy and chemical sensors" in D.W.POUL, D.COURJON (Eds): *Near field optics*, 17-24, Kluwer Acad. Publ., Dordrecht (1993)

HIGH-RESOLUTION FLUORESCENCE IMAGING WITH ENHANCED SENSITIVITY DUE TO SHORT-RANGE ELECTROMAGNETIC INTERACTION IN PHOTON STM

Toshiharu SAIKI, Shuji MONONOBE, and Motoichi OHTSU

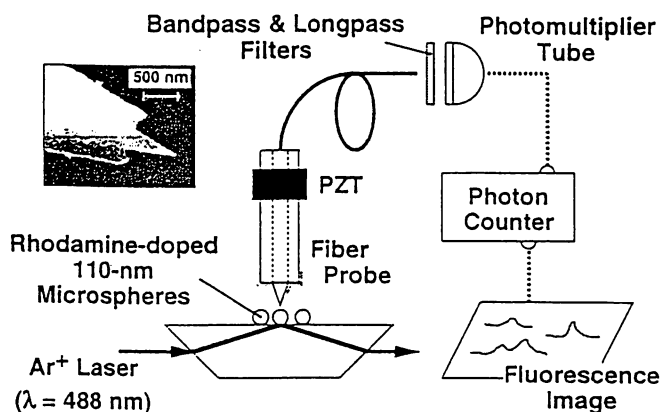
Kanagawa Academy of Science and Technology
KSP East 408, 3-2-1 Sakado, Takatsu-ku, Kawasaki, Kanagawa 213, Japan
phone : +81-44-819-2071 fax : +81-44-819-2072

KEY WORDS : Photon STM, fluorescence imaging, collection mode, pickup efficiency, short-range electromagnetic interaction

1. INTRODUCTION

High-resolution fluorescent-imaging technique [1-3] has been required especially in studying functioning biological systems. Photon STM is expected as a powerful tool to collect fluorescence with the resolution determined by the tip diameter of fiber probe. From the viewpoint of quantum optics, the high resolution of local fluorescence detection can be attributed to the short-range electromagnetic interaction between the tip and the sample. This interaction will lead to the modification of the radiation pattern of fluorescent material, which can make it possible for fiber probe to collect fluorescence effectively. Here, we demonstrate the fluorescence imaging of dye-doped microspheres with estimating the pickup efficiency and discuss its mechanism in terms of quantum electrodynamics.

2. EXPERIMENTAL



The experimental setup is shown in Fig. 1. Rhodamine-doped polystyrene microspheres of 110-nm diameter are dispersed on a silica substrate. The sharpened fiber probe with 20-nm tip diameter is fabricated by chemical etching technique [4]. A part of this tip is coated with gold to eliminate background fluorescence. With keeping the sample-probe separation of ~20nm, fluorescence from rhodamine molecules is picked up by fiber tip (collection mode) and measured with photon counting method.

Fig. 1 Experimental scheme of fluorescence detection with Photon STM

3. RESULTS

Figure 2 shows a near-field fluorescence image of microspheres. The image size of spheres are estimated as ~180 nm full width at half maximum, beyond the diffraction limit. The maximum counting rate is 2000 counts/sec. From this value, we may estimate the pick-up efficiency Γ , which is defined as the ratio of fluorescence intensity finally coupled to the waveguide mode of the fiber to the total fluorescence intensity. Applying the parameters of the dye molecules and detection systems, Γ of $2\sim 5 \times 10^3$ is obtained.

4. DISCUSSION

Here, we discuss the mechanism of fluorescence detection with high resolution. Assuming that the radiation pattern of the dye molecules is spatially homogeneous even when the probe approaches to the sphere in less than 20 nm, the pickup efficiency, Γ' , is estimated as $(0.1/4\pi)\times\gamma$ (Fig. 3(a)). In our measurement, where $\gamma \ll 1$, Γ' should be much smaller than the experimental value of Γ . From these estimations, it can be confirmed that the enhanced sensitivity of Γ is induced by the modification of radiation modes due to the strong coupling between the probe tip and the microsphere in near-field region (Fig. 3(b)). That is, the fiber probe works as something like a "nanometric integrating tip" in collection of fluorescence. This phenomenon is also expected to lead to the change of the fluorescence lifetime.

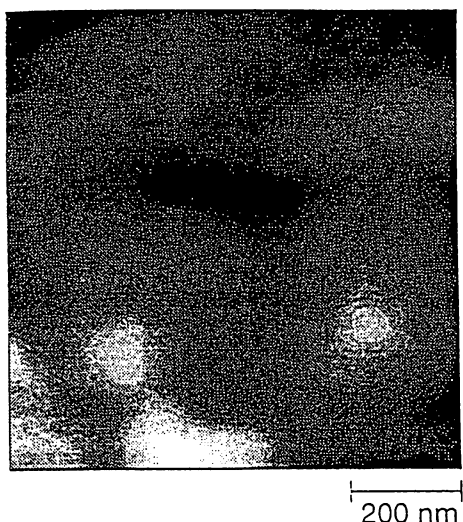


Fig. 2 Near-field fluorescence image of 110-nm microspheres

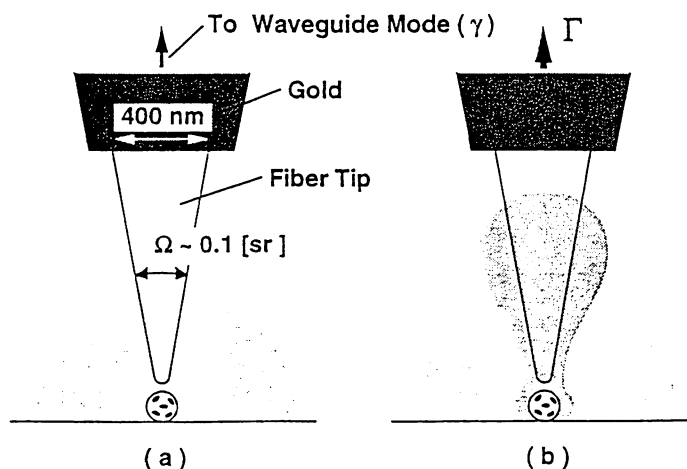


Fig. 3 (a) Pickup efficiency estimated by the solid angle at the aperture plane from the sample (Ω) and coupling coefficient to waveguide mode (γ). (b) Enhanced pickup efficiency (Γ) due to near-field coupling between the tip and the sample.

5. SUMMARY

We demonstrate that Photon STM operates as a highly sensitive fluorescence microscope in addition to high resolution. The enhancement of sensitivity can be attributed to the short-range electromagnetic interaction between the tip and the sphere. The pickup efficiency will be strongly affected by the structure of fiber probe, such as tip diameter, cone angle, aperture size, and so on. Probe-dependent pickup efficiency will be discussed in detail.

6. REFERENCES

1. E. BETZIG, R. J. CHICHESTER: "Single molecules observed by near-field scanning optical microscope" *Science*, **262**, 1422-1425 (1993)
2. W. P. AMBROSE, P. M. GOODWIN, J. C. MARTIN, R. A. KELLER: "Single molecule detection and photochemistry on a surface using near-field optical excitation" *Phys. Rev. Lett.*, **72**, 160-163 (1994)
3. X. S. XIE, R. C. DUNN: "Probing single molecule dynamics" *Science*, **265**, 361-364 (1994)
4. T. PANGARIBUAN, S. JIANG, M. OHTSU: "Highly controllable fabrication of fiber probe for photon scanning tunneling microscope" *Scanning*, **16**, 362-367 (1994)

OPTICAL GUIDANCE OF NEUTRAL ATOMS USING EVANESCENT WAVES IN A CYLINDRICAL-CORE HOLLOW FIBER

Haruhiko ITO, Keiji SAKAKI, Takeshi NAKATA, Wonho JHE, Motoichi OHTSU

Kanagawa Academy of Science and Technology
 KSP East 408, 3-2-1 Sakado, Takatsu-ku, Kawasaki 213, Japan
 Phone: +(81)-44-819-2071, Fax: +(81)-44-819-2072
 e-mail: LDJ00155@niftyserve.or.jp

KEY WORDS: atomic waveguide, evanescent wave, hollow fiber, optical potential, weakly-guiding approximation, LP mode

1. INTRODUCTION

Atom guidance by evanescent waves from optical fibers has been proposed [1]-[3]. By using a hollow fiber with a thin cylindrical-core, we plan to realize atomic waveguides [3]. Neutral atoms are guided in the hollow region while being repelled by the intense gradient force due to evanescent waves from the inner surface, as shown in Fig.1. The atomic waveguides are expected to be available for the atomic-level crystal growth. Here, we describe a specific atomic waveguide through the evaluation of optical potential under the weakly-guiding approximation. Employing the approximation, unlike the exact solutions [3], gives the clear-cut image of the potential barrier.

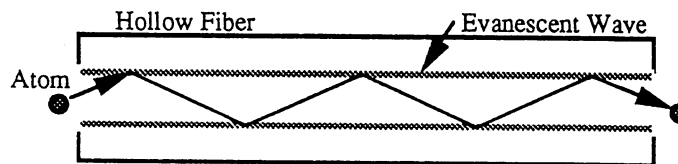


Fig. 1 Atomic waveguide using a hollow fiber

2. GUIDING MODES OF CYLINDRICAL-CORE HOLLOW FIBERS

We apply the weakly-guiding approximation to the hollow fiber, which leads to LP modes. As a result, the transverse components of electric fields of order m in the cylindrical-core hollow fiber can be expressed as follows;

$$E_t(r, \theta) \sim \begin{cases} I_m(vr) \sin(m\theta) & (r < a) \\ (C_1 J_m(ur) + C_2 N_m(ur)) \sin(m\theta) & (a \leq r \leq a + d) \\ K_m(wr) \sin(m\theta) & (r > a + d) \end{cases} \quad (1)$$

where the quantities u , v , and w are transverse propagation and attenuation constants [3]. Using the hollow fiber with the hollow diameter $2a=7 \mu\text{m}$, the core-thickness $d=3.8 \mu\text{m}$ and the relative index difference 0.18 % between core and cladding, three LP modes; LP_{01} , LP_{11} and LP_{21} ; can be excited for the wavelength 780 nm of the Rb D_2 line. Figure 2 shows (a) the mode pattern of LP_{01} excited by a diode laser and (b) the cross-sectional contour of the electric field. The LP_{01} mode has no node, but higher modes have some nodes. More than ten percent of the laser power was coupled to the LP_{01} mode.

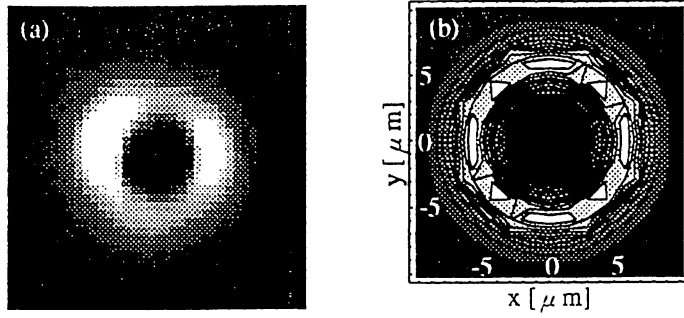


Fig. 2 LP₀₁ mode

3. POTENTIAL BARRIER FOR ATOM GUIDANCE

We evaluate the optical potential for Rb atoms in the hollow region:

$$U(r, \theta) = \frac{1}{2} \hbar \Delta \ln \left\{ 1 + \frac{s(r, \theta)}{1 + 4\Delta^2/\Gamma^2} \right\} \quad (2)$$

where Δ and Γ are the blue-detuning of laser frequency and the atomic natural linewidth, respectively. Under the weakly-guiding approximation, the saturation parameter $s(r, \theta)$ due to evanescent waves is written as

$$s(r, \theta) \sim I_m(vr)^2 \sin^2(m\theta). \quad (3)$$

Figure 3 shows (a) the cross-sectional optical potential and (b) the potential barrier in the hollow region for Rb atoms under the excitation of the LP₀₁ mode with 1 mW coupling power. As shown in Fig.3, the deep optical potential of more than 1 mK can be produced under the optimal blue-detuning.

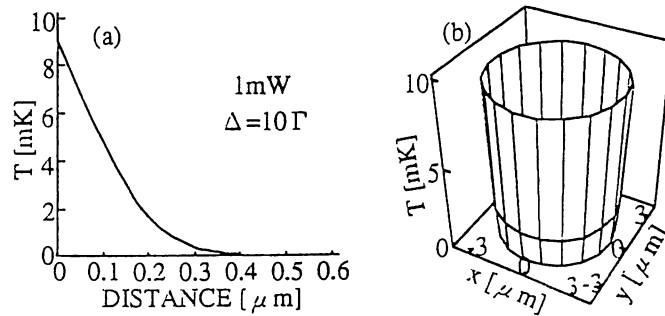


Fig. 3 Potential barrier of LP₀₁ mode

In summary, the excitation of the LP₀₁ mode is required for the stable guidance of atoms. The weakly-guiding approximation holds good for the analysis of this type of atomic waveguide.

4. REFERENCES

- [1] S.Marksteiner, C.M.Savage, P.Zoller, "Coherent atomic waveguides from hollow optical fibers: quantized atomic motion", *Phys.Rev.A* 50, 2680-2690 (1994).
- [2] W.Jhe, M.Ohtsu, H.Hori, S.R.Friberg, "Atomic waveguide using evanescent waves near optical fibers", *Jpn.J.Appl.Phys.* 33, L1680-L1682 (1994).
- [3] H.Ito, K.Sakaki, T.Nakata, W.Jhe, M.Ohtsu, "Optical potential for atom guidance in a cylindrical-core hollow fiber", *Opt.Commun.* 115, 57-64 (1995).

HIGH RESOLUTION PHOTON SCANNING TUNNELING MICROSCOPY DUE TO NANOMETRIC FIBER PROBE

M. OHTSU

Interdisciplinary Graduate School of Science and Technology,
Tokyo Institute of Technology,
4259 Nagatsuta, Midori-ku, Yokohama 226, JAPAN

Ohtsu "Photon Control" Project,
Kanagawa Academy of Science and Technology,
KSP East Rm.408, 3-2-1 Sakado, Takatsu-ku, Kawasaki, 213, JAPAN

Present status of a photon scanning tunneling microscope (PSTM) and its application are reviewed. In order to realize a nanometric apertured fiber probe, highly reproducible chemical etching process was developed to realize a sharpened fiber with the cone angle and tip diameter as small as 14 degree and 3 nm, respectively[1]. Possibility of tailoring the shapes of the sharpened fiber was presented. Chemical etching and nanometric photo-lithography were developed to fabricate a metallic aperture with the diameter of 30 nm or even smaller, on the sharpened fiber tip.

Imaging experiments with biological specimens were carried out by operating the PSTM in the collection mode and illumination mode geometries. Dependencies of these images on the polarization state of the incident light were found and a resolution of 10 nm or even smaller was achieved[2]. Nondestructive inspection of dielectric optical waveguides with sub-wavelength resolution was proposed by presenting the diagnosed results of a proton-exchanged LiTaO₃ waveguide[3]. Possibilities of diagnosing nanometric active photonic devices were also demonstrated through imaging experiments of semiconductor quantum dots. Experiments on fluorescence detection from dye-doped nanometric polystyrene spheres confirmed the enhanced efficiency of coupling of the fluorescence to the fiber tip, and this was attributed to the short-range electromagnetic interaction between the sphere and probe tip.

To demonstrate the possibilities of nanometric fabrication, high density optical storage, especially the photon-mode storage, was demonstrated to realize a stored circular pit of 100 nm diameter on an organic thin film[4]. As an ultimate goal of fabrication to explore the future technology of atomic-level material processing, an atom guide using a hollow fiber[5,6] and atom trapping by the illumination mode PSTM were proposed to control the thermal motion of freely flying atoms in vacuum[7]. The concept of virtual photon based on an intuitive modeling of the localized evanescent light was introduced to provide with a semi-classical theory of the PSTM[7]. Transfer functions of the PSTM were calculated by using this model, which agreed qualitatively with the experimental results.

References

- [1] T. Pangaribuan, et.al., Scanning, 16, 362 (1994).
- [2] M. Naya, et.al., SPIE Conf., Feb. 1995, San Jose.
- [3] Y. Toda and M. Ohtsu, IEEE Photonics Technol. Lett., 7, March 1995, in press.
- [4] S. Jiang, et.al., Opt. Commun., 106, 173 (1994).
- [5] W. Jhe, et.al., Jpn. J. Appl. Phys., 33, L1680 (1994).
- [6] H. Ito, et.al., Opt. Commun., 108, 1995, in press.
- [7] H. Hori and M. Ohtsu, Quantum Control and Measurement, North-Holland, Amsterdam, 1993, pp.197-202.

A high resolution Photon Scanning Tunneling Microscope for observation of sub cellular structures of neurons

R. Uma Maheswari*, Masayuki Naya*,** , Motoichi Ohtsu*,*** , Hitoshi Tatsumi**** , Yoshifumi Katayama****

* Kanagawa Academy of Science and Technology, ** Fuji Photo Film Co., Ltd., *** Tokyo Institute of Technology, **** Tokyo Medical and Dental University

Photon Scanning Tunneling Microscope (PSTM) or near-field scanning microscope has been getting popularity over conventional optical microscope in the field of biological sciences for the possibility of attaining high resolution beyond diffraction limit introduced by the wave length of light. In this work, we present some results of high contrast imaging of subcellular structures of neurons by an illumination mode PSTM.

In our PSTM system, the nano-aperture has been fabricated by metal coating of sharpened fiber probe with flattened tip made by chemical etching technique [1] and has got a diameter of less than 30nm. The neuron samples fixed on a glass substrate were taken from the hippocampus region of brain of a wistar rat and were labelled with tracing, blue and gold colloid of 23nm. The sample mounted on a xyz piezo stage was illuminated by argon ion laser light (wave length is 488nm) through the nano aperture and the scattered light was collected by an objective lens of high numerical aperture (0.8). While scanning the sample, the probe-sample separation was controlled to be around 10nm by monitoring the shear force originating between them [2]. Bundles of microtubulins present inside the axon lying under protein sheaths can be imaged very well with high contrast by PSTM while in the corresponding topographic image, only a constant field could be observed. Moreover, from a line scan of intensity variation, the full width at half maximum was estimated to be 26nm and this value agrees very well with diameter of 24nm of tubulin measured by other means (TEM or SEM) after removing overlaying sheaths. Thus, the resolution of our system could be estimated to be around several nanometers and to our knowledge, this is one of the highest resolutions to be reported concerning imaging of biological samples. The capability of our system in resolving details smaller than the diameter of the aperture is believed to be arising out of the aperture edges existing at the boundary between the sharpened silica fiber and the metal coating covering this fiber [3]. In future, we plan to improve our system to be able to operate under liquid atmosphere that will make it possible to conduct dynamic observations.

1. R.Uma Maheswari et.al., OSA Annual meeting digest, p.179 (1994).
2. E.Betzig et.al., Science, 257 (1992) 189.
3. M. Specht et.al., Phys.Rev.Lett., 68 (1992) 476.

PROGRESS OF NANOMETRIC RESOLUTION PHOTON SCANNING TUNNELING MICROSCOPY

M. OHTSU^{1, 2)}

(1) Tokyo Institute of Technology, Graduate School
4259 Nagatsuta, Midori-ku, Yokohama 226

(2) Kanagawa Academy of Science and Technology,
KSP East Rm 408, 3-2-1 Sakado, Takatsu-ku, Kawasaki 213

1. INTRODUCTION

A photon scanning tunneling microscope (PSTM) realizes nanometric resolution by picking up an evanescent light localized on a sample surface using a nanometric probe tip. It promises to be a leading edge of optical microscopy and can be used for biomedical studies because it can work in air or solution, optical resonance phenomena can be observed, and optical manipulation is possible.

2. PROBE FABRICATION

Selective etching of optical fiber with high doping of GeO₂ in core have realized sharpened fiber with the tip diameter of smaller than 10 nm and a cone angle of 14 degree with high reproducibility. Advantage of this etching is the capability of tailoring the shape of the sharpened probes. After the sharpened fiber is coated by an Au film, it was also etched to fabricate a sub-wavelength aperture of diameter smaller than 30 nm. Three-dimensional nanometric photo-lithography has been developed for this purpose. A super-tip was also fabricated by fixing a Rhodamine 6G droplet on the top of the sharpened fiber.

3. IMAGING EXPERIMENTS

The flagella filaments of salmonella (nominal diameter: 25 nm) were observed by the collection-mode PSTM. Dependence of image profiles on the polarization of incident light was explained by the spatial distribution of induced polarization on the surface. An illumination-mode PSTM succeeded in measuring microtubules in a branching axon of neurons from the hippocampus region of rat, for which resonance light absorption by tracing blue has increased the contrast of the image. From these experiments, spatial resolution within 10 nm was confirmed. Operating the PSTM in water is now under preparation.

4. OTHER RELATED EXPERIMENTS

Fluorescence from dye doped latex spheres (110 nm diameter) was detected by collection-mode PSTM, for which photon counting method was employed. It was found that the collection efficiency was enhanced by the short-range electromagnetic interaction between the probe tip and dye molecules to modify the spatial mode of emitted fluorescence. This phenomenon of quantum electrodynamics can help increasing sensitivity of fluorescence detection.

Photon-mode high density optical storage was carried out with amphiphilic azobenzene derivative ultrathin film using illumination-mode PSTM employing localized evanescent UV light. The diameter of stored memory was about 50 - 100 nm, which can be further decreased by reducing thermal fluctuations of the probe.

5. SUMMARY

Nanometric resolution of PSTM was realized and application to nanometric fabrication was demonstrated. It is expected that the PSTM and its wide range of applications can open a new field of interdisciplinary optical sciences and technology.

Imaging experiments of bio-samples by a Photon Scanning Tunneling Microscope with an apertured probe

Masayuki Naya^{1),2)}, Shuji Mononobe¹⁾, R.Uma Maheswari¹⁾, Tosiharu Saiki¹⁾
Motoichi Ohtsu^{1),3)}

- 1) *Kanagawa Academy of Science and Technology,
KSP east Rm408,3-2-1, Sakato,Takatsu-ku,Kawasaki-shi,Kanagawa-ken,213 Japan*
- 2) *Fuji Photo Film Co.,Ltd. Miyanodai Technology Development Center
798, Miyanodai, Kaisei-machi, Ashigarakami-gun, Kanagawa, 258, Japan*
- 3) *Graduate School, Tokyo Institute of Technology
4259 Nagatsuta, Midori-ku, Yokohama 226, Japan*

Abstract

In this presentation, we describe about the high resolution imaging of flagellar filaments of a salmonella with a diameter of 25 nm by a photon scanning tunneling microscope (PSTM). In our PSTM system, we have used a metal coated fiber probe with a nanometric dielectric protrusion fabricated by indigenous technique developed by us. By using this probe, flagellar filaments could be imaged as having a full width at half maximum of 50 nm. Obtained images strongly depended on the the separation of the sample and to the probe, and the diameter of the aperture polarization of the irradiated light.

1.Introduction

Photon Scanning Tunneling Microscopy (PSTM), sometimes called Scanning Nearfield Optical Microscope (SNOM), based on the short-range electromagnetic interaction between a small dielectric tip and a sample in an evanescent field induced by light irradiation¹⁻³, has been recently developed. Because of the possibility of realizing nanometric resolution without any special sample processing, many applications have been proposed¹.

The PSTM technique is commonly implemented in two modes. One is illumination mode (i-mode), using a nanometric aperture as an evanescent light source, and scattered light is detected in the far field¹. By this technique, super resolution is realized due to the sub-wavelength diameter of the aperture used⁴⁻⁸. The other scheme is the collection-mode (c-mode) using a nanometric dielectric tip as a scatterer¹⁻³. When the tip is introduced in the evanescent-field generated on the sample surface by the incident light under the condition of total reflection, the non-radiative evanescent light is converted to the scattering light which propagates to the collection optics. Here, the intensity of the evanescent field decays in an exponential fashion with increasing sample-probe separation and this signal itself can be advantageously used as a control signal while performing 2-D scanning of the sample at constant inten-

sity mode. Furthermore parallel or perpendicular polarization states of the incident light with respect to the sample plane can be selected. However, because of lack of realization of a nanometric dielectric tip, satisfactory results of high resolution as in i-mode PSTM have not been obtained till now.

In this paper, we demonstrate high resolution imaging by c-mode PSTM with a nano-apertured probe we have developed recently. To evaluate the resolution and properties, we used straight-type flagellar filaments of salmonella (FFS) with diameter of 25nm, as a standard sample. Furthermore, dependency of resolution on such parameters as sample/probe separation, tip size, and polarization of the incident light have been investigated.

In section 2 we describe about the experimental system, the probe and the sample. Section 3 gives a discussion of the experimental results and section 4 finally gives a summary.

2. Experiments

(1) Scanning system : Figure 1 shows our experimental system of the PSTM. An Ar+ laser with a wavelength of 488nm was used as a light source and a $\lambda/2$ plate was installed to rotate the polarization of the incident light. A thin cover glass was used as a substrate for the sample which was fixed on a glass prism with index matching oil to which the laser beam was incident under total reflection condition. The evanescent field generated at the sample surface was scattered and picked up by an optical fiber probe. The probe is set on a PZT tube to scan in the XYZ direction. A photomultiplier tube and a lock in amplifier were used for the phase sensitive detection of the picked up power. A commercial AFM controller (Seiko Instruments Inc.; SPA3700) was used for scanning and image processing. By utilizing the rapid decrease of the evanescent light power from the sample surface, the sample/probe separation was controlled so as to maintain the detected evanescent light power constant. The response time of the controller was slower than 0.1 sec, and scanning speed was 2Hz. Scanning area was $5 \mu\text{m}$. Therefore, only in regions with spatial variation greater than 500 nm, the controller scanned with feed back on and for spatial variations less than 500 nm the scanning was done in free running mode. As in this technique, no auxiliary system such as shear force which generates mechanical force between the sample and the probe was used, this system is potentially strong for observing soft samples, like biological specimens without causing damage.

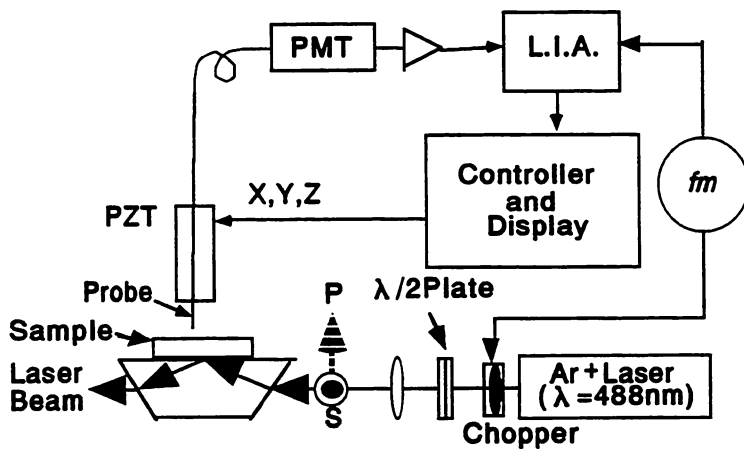


Fig.1 Experimental system of the PSTM. Polarization of incident light is controlled to s \bullet or p \blacktriangle by rotating $\lambda/2$ plate.

(2) Probe : The most important element of the PSTM is the probe. For detecting only the high spatial-Fourier frequency components of the evanescent field, and for achieving high resolution , a probe with a small dielectric tip is indispensable^{1,3}. To realize such a tip, we have developed a technique for fabrication of a probe with nanometer sized fiber tip protruding out of Au film as shown in Fig2-(a). An optical fiber was sharpened to have a tip with about 10 nm radius by using the selective chemical etching technique in a reproducible manner^{10,11}. Next, the sharpened fiber was coated with an Au film for an average of about 150 nm. Because the optical skin depth of Au is about 30 nm, the coated film of 150 nm thickness was sufficient to block the light. Then it was dipped into a KI/I₂ solution to remove the gold film only from the top of the tip to form a sub-wavelength aperture. Figure2-(b) shows a SEM (scanning electron microscope) image of the apertured probe. Although the diameter at the foot of the protruded fiber is found to be 30 nm from this figure, its real value should be even smaller because the protruded fiber can be buried in the contamination at the stage of SEM observation. So, the effective aperture diameter governing the resolution can be even smaller because the high spatial-Fourier frequency components of the evanescent light is preferably scattered at the protruded fiber tip.

(3) Sample : The samples used were straight-type flagellar filaments of salmonella(FFS). Figure3 shows a transmission electron microscope (TEM) image of FFS. The shape of FFS was cylindrical with a diameter of 25 nm, and this size was nearly same as the dimensions of the tip of the probe. They were fixed on a hidrophilized glass plate without coating. The FFS is interesting not onlfor its use as a standard sample to evaluate the performances of the PSTM because of its well-calibrated size but also for its importance as a molecular motor¹².

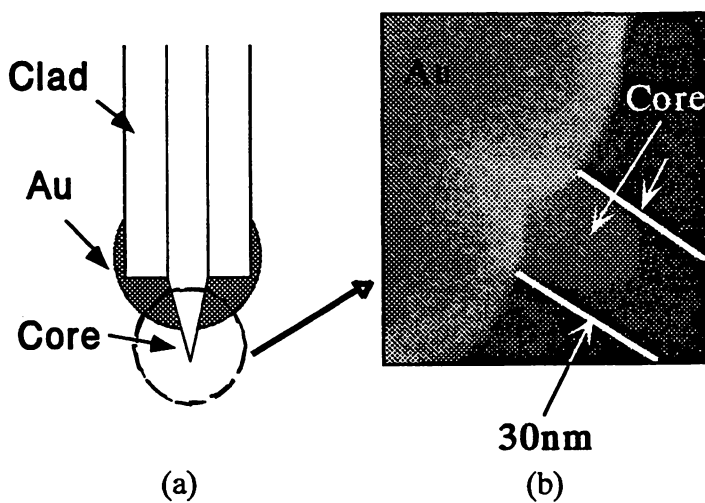


Fig.2 (a)Schematic of apertured fiber probe (b)SEM image of probe tip. The diameter at the foot of protruded fiber is found to be 30nm.

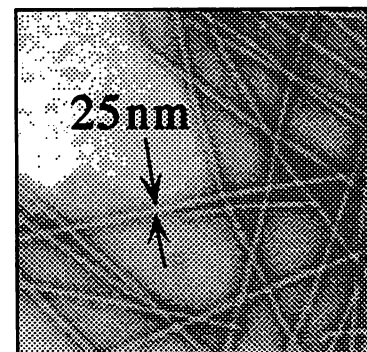


Fig.3 TEM image of the straight-type flageller filaments of salmonela. The diameter of each filament was found to be 25nm. These samples and the TEM image were provided by Prof. Shinich Aizawa.

3. Results and discussion

(1)High resolution detection : Figure 4-(a) is a PSTM image of the FFS when the incident light was s-polarized. Scanning area is $5 \mu\text{m} \times 5 \mu\text{m}$ with corresponding number of pixels being 256×256 . Therefore size of one pixel is about 20 nm. For this scan, the separation of the sample to the probe was about 15 nm. FFS lying perpendicular to the direction of the incident beam were well imaged with high contrast. The bright line corresponds to filament of FFS while the dark region on either sides of the line correspond to shadow formed by the filament. This can be clearly seen from a cross-section profile of the detected signal intensity (Figure 4-(b)). Here full width at half maximum (FWHM) of the bright region correspond to the FFS is 50 nm. Considering the pixel size and comparing the FWHM of the obtained PSTM image with the nominal width of the filament measured using TEM images of FFS, the resolution can be estimated to be smaller than the aperture diameter estimated diameter using SEM. Such a high resolution was caused by the fact that, the high-spatial Fourier frequency components are selectively picked up by the fiber tip protruding out of the Au film¹⁻³. The principal advantage of the present PSTM system lies on the possibility of obtaining high resolution images solely from optical feed back without any auxiliary control system such as STM (Scanning Tunneling microscope) or SFM (Scanning Force Microscope).

(2)Dependence of resolution on Sample/Probe separation : Figure 5 shows an image taken under the same condition as Fig. 4-(a), except for the sample/probe separation being as large as 65 nm. Almost the same image was obtained, except that the FWHM of the cross-sectional profile of the detected signal intensity of image was increased to about 150 nm. This dependency of resolution on sample/probe separation can be considered to be resulting from the localization of the high spatial frequency components of the evanescent light which acts as an intermediary of the electromagnetic interaction between dipoles caused by light irradiation around the surface of sample with small radius, and volume. Therefore, for efficient pick up, the probe must be brought closer to the sample.

(3)Dependence of resolution on tip size : Figure 6 shows the PSTM image of the same sample obtained by using the probe tip with the aperture diameter as large as 100nm. Comparison with Fig.4-(a) confirms that the resolution is lower for a large aperture. This can be considered due to the fact that the evanescent light with high-spatial Fourier frequency around the small sample is picked up most efficiently by a probe with same size as the sample¹⁻³. Therefore, a probe with larger aperture picks up rather lower-spatial Fourier frequency components, and hence the resolution become lower.

(4)Dependence of image on the polarization of incident light : Figure 7 shows the PSTM image for exactly the same scanned area as that of Fig.4-(a) taken when the incident light was P-polarized. This image was apparently different from the image of Fig4-(a). Only the FFS lying perpendicular to the incident beam could be observed with a resolution relatively lower than that obtained in Fig.4-(a). The reason for this dependence on polarization of the incident can be explained by considering the evanescent light as the field mediating the short-range electromagnetic interaction between the polarizations induced on the surface by the incident light².

In order to explain the difference in contrast of the images obtained in p- and s-polarizations, we consider the schematic shown in Figs.8-(a),(b) which depict the electric field around the filament of FFS fixed on the glass substrate perpendicular to the direction of propagation of the beam. In the case of

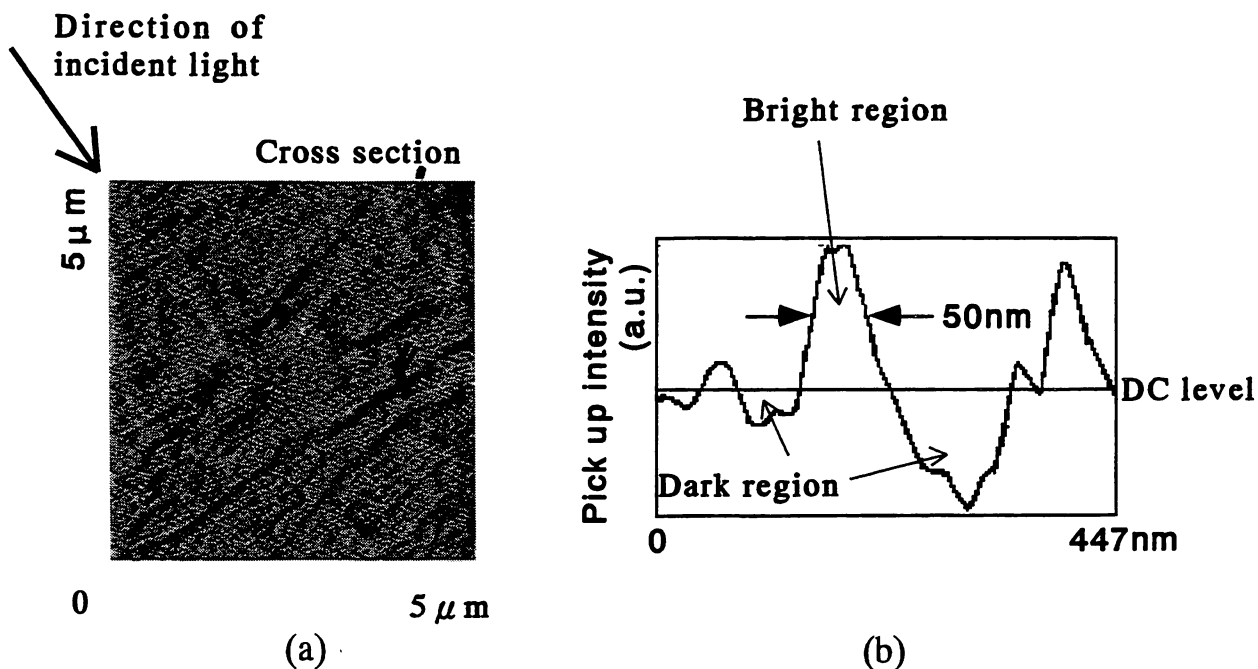


Fig.4 (a) A PSTM image of the flagellar filaments of salmonela (FFS) when incident light was s-polarized. The sample/probe separation was about 15nm. Arrow is the direction of the incident light. (b) A cross section profile of the detected signal intensity corresponding along the line marked in the Fig.4-(a). The bright region corresponds to the FFS, and full width at half maximum is 50nm.



Fig.5 A PSTM image taken under the same area and under the same conditions as of Fig.4-(a), except for the sample/probe separation being as large as 65nm.

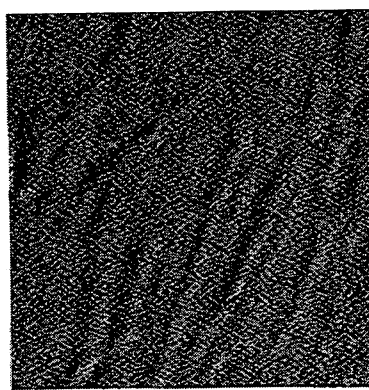


Fig.6 A PSTM image of the FFS obtained by using a tip with an aperture diameter as large as 100nm.

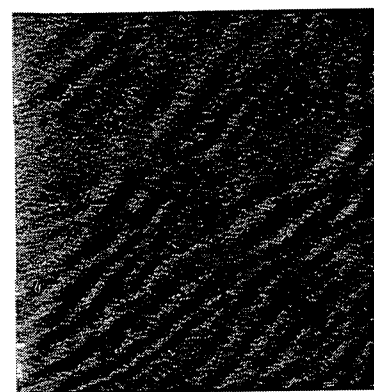


Fig.7 A PSTM image for exactly the same scan area and the same conditions, when the incident light was p-polarized.

s-polarization, as shown in Fig.8-(a), the directions of the electric lines of force in the near-field region are parallel to that of the filament because the direction of the induced polarization lies parallel to that of the filament. Thus, when the probe tip is brought above the sample, the electric lines of force bridges to the probe tip mainly from the sample, and when it is above the substrate, the electric lines of force couple to the probe tip mainly from the substrate. On the other hand, as shown in Fig.8-(b) the electric field of the p-polarized incident light can induce only the dipoles which are not parallel to the filament axis. As a result, the lines of electric force can be coupled with the probe tip not only from the filament but also from its vicinity. Due to this difference in the spatial distribution of reoriented the electriclines of force in the near-field region, s-polarization could realize higher resolution and better image of the FFS sample than under p-polarization.

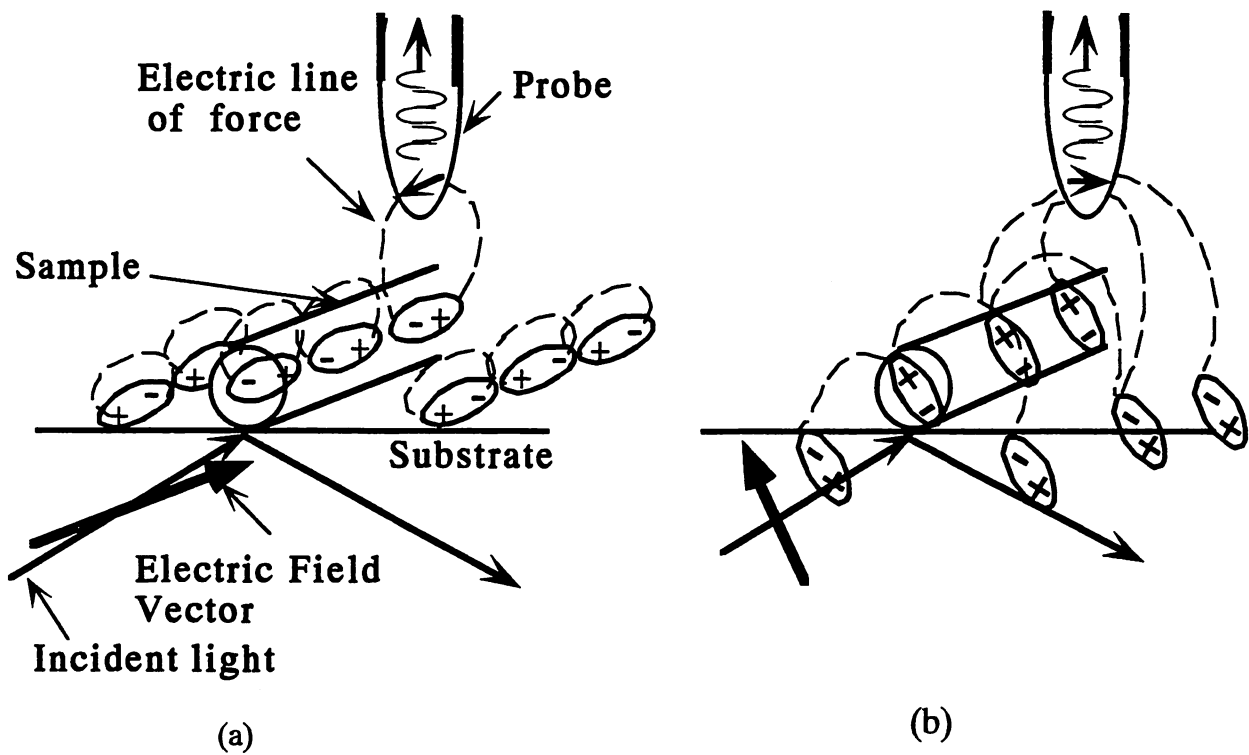


Fig.8 .Schematic explanation of electrical interaction between probe and sample induced by the incident light. The distribution of the electric line of force, represented by broken curves, is different between for (a) s-polarization and (b) p-polarization.

5. Summary

This paper demonstrates the capability of high resolution imaging of a c-mode PSTM with a indignously developed nano-apertured probe. The features of the present study are:

- (1) The system could be operated under all optical mode without any auxiliary control by taking advantage of the exponential dependence of the evanescent intensity.
- (2) High contrast and high resolution imaging of FFS of nominal diameter diameter of 25 nm and the observed image has a FWHM 50 nm.
- (3) A rough estimate of the resolution was found to be less than the diameter of aperture which was approximately < 30 nm.
- (4) The dependence of resolution on the sample/probe separation, and diameter of the aperture was studied.
- (5) The dependence of the image on the polarization of incident light was observed and this result was explained in terms of the lines of electric force in the near-field region.

Finally, we believe these results lay a foundation to understand the physics of the Near Field Optics.

Acknowledgement

The authors wish to thank Prof. Shinichi Aizawa at Teikyo Univ. for providing the flagellar filaments of salmonella.

References

1. H. Heizelmann and D. W. Pohl, " Scanning near field optical microscopy ", *Appl. Phys. A*, 59 , 89-101 (1994)
2. B. Labani and C. Giraldo, " Optical interaction between a dielectric tip and a nanometric lattice: implications for near-field microscopy ", *J. Opt Soc. Am. B*, vol. 7, No. 6, pp. 936-943, June (1990)
3. H. Hori, " Quantum optical picture of photon STM and proposal of single atom manipulation ", *D. W. Pohl and D. Courjon (eds.), Near Field Optics*, 105-114, (1993)
4. E. Bezig and J. K. Trautman, " Near-Field Optics : Microscopy, Spectroscopy, and Surface Modification Beyond the Diffraction Limit ", *Science* vol. 257 , 10, July, 189-195 (1992)
5. E. Bezig, J. K. Trautman, J.S. Weiner, T.D. Harris and R. Wolfe, " Polarization contrast in near-field scanning optical microscopy ", *Appl. Opt.* vol. 31, No. 22, 1 August, 4563-4568 (1992)
6. J. K. Trautman, E. Bezig, J. S. Weiner, D.J. DiGiovanni, T. D. Harris, F. Hellman and E. M. Gyorgy , " Image contrast in near-field optics ", *J. Appl. Phys.* , 71 (10), 15 May (1992)
7. S. Jiang, J. Ichihashi, H. Monobe, M. Fujita and M. Ohtsu , " Highly localized photochemical processes in LB films of photo chromic material by using a photon scanning tunneling microscope ", *Opt. Com.*, 106, 173-177 , (1994)
8. M. Ohtsu, S. Jiang, T. Pangaribuan and M. Kohzuma, " Nanometer resolution photon STM and single atom manipulation ", *D. W. Pohl and D Courjon (eds), Near Field Optics*, 131-139, (1993)

9.S. Jiang, H.Ohsawa, K.Yamada, T.Pangari-Buan, M. Ohtsu and K.Imai, " Nanometric Scale Biosample Observation Using a Photon Scanning Tunneling Microscope", *Jpn. J. Appl. Phys.* , vol. 31, part 1, No. 7, pp. 241-246, july (1992)

10. T. Pangaribuan, K. Yamada, S. Jiang, H. Ohsawa and M. Ohtsu, " Reproducible Fabrication Technique of Nanometric Tip Diameter Fiber Probe for Photon Scanning Tunneling Microscope", *Jpn. J. Appl. Phys.* , vol. 31, Part 2, No. 9A, pp L1302-L1304, September (1992)

11. T. Pangaribuan, S. Jiang and M. Ohtsu, " Two-step etching method for fabrication of fibre probe for photon scanning tunneling microscope", *Elect. Lett.*, vol. 29, No. 22, pp. 1978-1979, 28 October (1993)

12. J.J.Jones and S.-I. Aizawa , *Advances Microbial Pysiol.* , 32, pp109 (1991)

PROGRESS OF HIGH RESOLUTION PHOTON SCANNING TUNNELING MICROSCOPE WITH A NANOMETRIC FIBER PROBE

Motoichi OHTSU

Interdisciplinary Graduate School of Science and Engineering,
Tokyo Institute of Technology
4259 Nagatsuta, Midori-ku, Yokohama 227, Japan

Ohtsu "Photon Control" Project,
Kanagawa Academy of Science and Technology
3-2-1 Sakado, Takatsu-ku, Kawasaki 213, Japan

1. INTRODUCTION

Advanced technology in the fabrication of submicrometer sized device leads to the realization of near field optical microscopes with super-resolution beyond the diffraction limit[1-4]. A photon scanning tunneling microscope (PSTM) is a type of the near field optical microscope picking-up the evanescent light around the sample surface which is generated under total internal reflection and modulated by the sample[5,6]. Thus, it can be interpreted as an optical analog of the scanning tunneling microscope (STM). Since PSTM and its modified versions can be used not only as a microscope but also as a nanometric fabrication tool and a manipulator of nanometric particles, a variety of applications have been proposed and significant progress has been made recently in the field of near field optics[7].

This paper reviews the recent progress of our study on PSTM. As our PSTM employs a sharpened optical fiber as a probe tip, it can be considered as a version of optical fiber sensor. However, because of the subwavelength size of the optical fiber-probe tip (OFPT), unique and novel properties can be found which can open up a new field of optical fiber sensor.

2. PRINCIPLE OF OPERATION

Figure 1 shows the principle of operation of our PSTM, employing a sharpened optical fiber as an OFPT. A nanometric sample is fixed on a clean prism irradiated by laser light at an incident angle of total internal reflection. The sharpened OFPT picks up or scatters the evanescent light in the vicinity of a nanometric sample into the propagating light. This OFPT is scanned by using a piezoelectric transducer and the powers of the scattered light power are measured by a photo-detector on the other end of the OFPT. When the OFPT with its curvature radius of extremity as small as the nanometric sample is employed, the efficiency of the scattering process depends strongly on the position of the OFPT due to the localized nature of the evanescent field. Mapping the scattered light with respect to the relative position of the OFPT, one can obtain a topographical image of the nanometric sample as a PSTM picture.

The resolution, being far beyond the diffraction-limit is determined by the radius of curvature of the sharpened OFPT. The advantages of using the OFPT are the high efficiency of collecting scattered light and the availability of reproducible production process.

3. HIGHLY CONTROLLABLE FABRICATION OF OPTICAL FIBER PROBE-TIP

Although methods such as pulling of heated glass capillaries past the breaking point[4] and sharpening quartz rods or optical fibers by chemical etching[1,3] have been applied for probe tip fabrication, we have proposed a highly controllable and reproducible fabrication technique for the OFPT with nanometric tip diameter by selectively etching a single mode optical fiber

in buffered HF solution[8]. Since the OFPT is an essential device in the PSTM system, detailed description on its fabrication is given in this section.

Selective chemical etching, using a buffered HF acid has been widely used in the processing of dielectric materials. An etching solution composed of NH_4F , HF and H_2O was used to sharpen a fiber with pure silica cladding and GeO_2 -doped silica core for fabrication of OFPT. Comparing the preliminary experimental results of the dissolution rate of GeO_2 -doped silica core and pure silica cladding, it was found that the dissolution rate of the core was faster than that of the cladding and a dip is formed at the end of the fiber core. To obtain a lower dissolution rate of the GeO_2 -doped core, NH_4F is added to HF as a buffered solution. In this case, the difference in the solubility of the generated $(\text{NF}_4)_2\text{SiF}_6$ and $(\text{NH}_4)_2\text{GeF}_6$ in the etching solution leads to the difference in the etching rate between core and cladding. Therefore, by adjusting the composition of the etching solution, i.e., the volume ratio of NH_4F , and the doping ratio of GeO_2 , fiber probes with various cone angle and tip diameters can be fabricated.

The sharpness of the OFPT which is denoted by the cone angle θ_1 , was investigated by etching five kinds of fibers. The first four fibers have pure silica cladding and GeO_2 -doped cores with doping ratios of 3.6, 8.5, 14, and 23mol%. The fifth fiber has a silica cladding doped with 2.1mol% F and a silica core doped with 22mol% GeO_2 . The etching solution was composed of 40% (weight %) NH_4F , 50% HF and H_2O . The buffering condition was controlled by varying the volume ratio of NH_4F , denoted as X, while the volume ratios of HF and H_2O were maintained at 1:1. All the experiments were carried out at the temperature of $22 \pm 1^\circ\text{C}$.

The dependence of cone angle θ_1 on X is shown in Fig.2. Curves A - E are the results for the five fibers, respectively. It is seen that the θ_1 becomes smaller with increasing the value of X and the doping ratios. The sharpest OFPT with θ_1 of 14° was obtained by etching the fifth fiber with X=5 for 40 minutes. Using the etching solution with X=1, instead of sharpening, the fiber even gives a "negative cone angle", which is expressed by the cone angles larger than 180° in curves A, C, and D. In these cases, the etching rate of the core became larger than that of the cladding. Although it was reported that the difference in etching rate and θ_1 is dependent only on doping ratio of GeO_2 [9], we found that θ_1 is dependent also on X, especially in the case of the fiber with high Ge_2O doping ratio[8]. Moreover, in the case of the fifth fiber, the presence of F in the cladding leads to the increase of etching rate and the decrease of cone angle.

Figure 3(a) shows the SEM image of the OFPT with cone angle of 20° (coated with 7nm-thick Pt-Pd). Figure 3(b) shows the magnified image. The image of the original coated OFPT is the inside part and the observed outside part with thickness C_t is supposed to be the image of contamination from the SEM chamber. From this image, the tip diameter is estimated to be about 3nm, considering the coating thickness was 7nm. As for the OFPT, this is, to the authors' knowledges, the smallest tip diameter which has ever been reported. For confirming the reproducibility of our method, a series of experiments with identical etching procedure was carried out and the results have shown that the standard deviation of the cone angle was smaller than 0.5° .

We also investigated the minimum etching time for required sharpening in order to avoid the degradation on the tip sharpness due to over etching. An optical fiber with pure silica cladding and GeO_2 -doping core ratio of 23 mol% was used. The relation between θ_1 , the necessary minimum etching time T_m , and the corresponding value X is shown in Fig.4.

Although we have succeeded in fabricating a very sharp OFPT, Fig.3(a) shows that the cladding diameter is more than 16 times the length of the conical tip. This large ratio means that the tip-sample separation (several tens of nanometers) which is

applied during scanning may not be maintained without contact between the edge of the cladding and the sample surface. To avoid this contact, we propose a two-step etching method as a controllable technique for reducing the cladding diameter while retaining the sharpness[10].

The first-step etching is used to reduce the cladding diameter d_0 to d_1 . It was found that the cladding diameter decreased linearly with increasing etching time, and for the same d_1 , a longer etching time is necessary with increasing X . We also find that the etching solution with value of $X < 3$ produced an almost flat fiber end and the etching process mainly acted for reducing the cladding diameter. Furthermore, since the fiber end was in a concave-type when etching with $X < 1.7$, the etching solution with value of $X = 1.7$ was used in the first-step etching, and for such solution, the reducing rate of cladding diameter was found to be $-0.95 \mu\text{m}/\text{min}$. Although the cladding diameter can be reduced to nearly zero by increasing the etching time, the minimum cladding diameter should be two times of core diameter d_c in order to maintain the negligible optical transmission losses[11]. Therefore, in the first-step etching, the value of d_1 is adjusted to $d_1 > 2d_c + d_x$, where d_x is the cladding diameter reduced with the minimum^x etching time for each value of X . The value of d_x was about $20 \mu\text{m}$, which does not change as long as the temperature of etching solution is constant.

The second-step etching is used to sharpen the fiber whose cladding diameter is reduced by the first-step etching. The desired cone angle of the OFPT is obtained by using the etching solution with value of $X=3$ or larger and by following the sharpening technique of Fig. 2. Combining the reducing rate of cladding diameter when $X = 1.7$ with obtained d_1 , the cladding diameter d_2 limited by $d_1 - d_x > d_2 > 2d_c$ obtained after two-step etching can be empirically expressed as $d_2 = d_0 - 0.95t_1 - d_x$, where t_1 is the first-step etching time. Therefore by adjusting t_1 and following the above-mentioned second-step etching, OFPT with the desired cone angle and cladding diameter can be obtained. Figure 5 is the SEM image of the OFPT which was fabricated by using the etching solutions with the value of $X = 1.7$ and 10 in the first- and second-step etchings, respectively. Here, the first-step etching time was 102 minutes. The θ_2 and d_2 are 20° and $8 \mu\text{m}$, respectively. It is clear that the cladding diameter has been reduced of more than one order. Furthermore, the relation of $d_2 > d_c$ is well maintained and the value of θ_2 produced by the two-step etching is guaranteed equal to the value of θ_1 produced by the one-step etching. From a series of experimental results for the fiber with 23 mol% GeO_2 core-doping ratio, it was found that the relative difference of the cone angles defined by $(\theta_1 - \theta_2)/\theta_1$ was less than 2%.

In order to realize a more advanced OFPT, we have further modified etching process in two ways. One is to realize a pencil-shaped OFPT by a four-step etching method[12]. The first-step make a tapered cladding by using a HF-oil interface. The second-step is to form a dip at the core by HF solution. The third-step is to flatten the top of the core by using the solution with the volume ratio of $X=1.5$. The fourth-step is to sharpen the top of the core by employing the selective etching method by the etching solution with the volume ratio of $X:1:1$. Figure 6 shows the SEM image of the pencil-shape OFPT fabricated by the solution with $X=5$. The tip diameter is reduced to smaller than 10nm . One of the advantages of such a pencil-shape OFPT is high reproducibility of coating a metallic film to prevent picking up stray light, which is due to the lack of the cladding edge.

The other is to realize an OFPT with a flattened top of the core[13]. In this method, a two-step etched fiber is further etched for a short time in a ten times diluted solution with $X=10$ to get a flattered tip as shown by Fig.7. During the flattening process, we have got some evidence showing morpho-

logical changes of mesoscopic nature of the OFPT. This phenomenon has been found to have a limit cycle characteristics with the tip taking a rounded or a flattened shape depending on the time of etching. The advantages of this flattened OFPT are the possibilities of coating a metallic film only on its sides in order to form a nanometric aperture at the flattened top and of fixing a nanometric fluorescent material on the flattened top to realize a fluorescent super-tip.

A technique of three-dimensional and nanometric photolithography has been also developed to fabricate a nanometric aperture at the top of the OFPT by removing a portion of the coated metal film.

4. IMAGING EXPERIMENTS

We have obtained the images of latex spheres with 80nm diameter, bacteriophage T4 with the body of 9nm diameter, and so on, with the resolution higher than 20 nm[5,6]. Furthermore, we have recently obtained near field images of the guided mode of a dielectric optical waveguide (see Fig.8) and identified the positions and sizes of the scattering sources which would induce a transmission loss of the waveguide[14]. Such a high resolution diagnostic technique could provide with a novel information to the waveguide design and fabrication engineering.

For obtaining higher resolution and sensitivity, it would be essential to improve the control accuracy of the probe tip position. For this purpose, a slender OFPT fabricated by the two-step etching was installed to the PSTM system with the tilted angle of five degree and the atomic force induced bending of such a OFPT was detected. This detection of atomic force is more effective for position control because of the critical dependence of the atomic force on the tip-sample separation. Such a PSTM system works simultaneously as an atomic force microscope (AFM), hence the PSTM image can be compared with and calibrated by the AFM image.

5. APPLICATIONS TO NANOMETRIC FABRICATION TOOLS AND MANIPULATORS

One of the possible applications of the OFPT to the nanometric fabrication could be the high density optical storage which utilizes the high density evanescent light power leaked from an aperture on the top of the OFPT. Although thermal-mode storage with a density of 45GB/inch² has been demonstrated by using magneto-optic materials[15], the photon-mode optical storage which we have carried out offers the possibility of erasable optical memory[16]. In our experiment, the memory material was the amphiphilic azobenzene derivative in a Langmuir-Blodgett (LB) film. For storage, the LB film was irradiated with the evanescent light of 350nm wavelength on the top of the OFPT to induce the local photochemical transition from trans- to cis-isomer, by which the optical transmission of the LB film was increased. By detecting this local increase of optical transmission using the PSTM system, stored memories can be read.

Figure 9 shows the result of reading the bits of stored memories. The diameter of each bit was about 130nm which was blurred by thermal drift of the position of the OFPT. Smaller diameter could be expected by improving the sensitivity of writing and reading. It should be noted that this photon-mode storage is also one of the applications to localized spectroscopy.

As an example of the ultimate fabrication and manipulation by using an OFPT, we have proposed a method of trapping a freely flying atom in vacuum by utilizing momentum exchange between the atom and the evanescent photon around the OFPT[17]. This proposal aims at realizing single atom optical memory and the single atom crystal growth. As a preliminary experiment, momentum exchange between the atom and the two-dimensional evanescent photon was observed by using the technique of Dop-

pler-free pump-probe laser spectroscopy[18]. The cavity quantum electrodynamics effect to the atom should be analyzed for more quantitative estimation of experimental parameters.

6. INTERACTION PICTURE OF THE PSTM

The fundamental process of the PSTM is described in terms of quasi-static short-range electromagnetic interaction between microscopic dielectric particles induced by laser irradiation. We present a simple quantum optical picture of the interaction by introducing virtual photons with nanometric Compton wavelength which corresponds to the size of the microscopic particles[17]. Although conventional treatments based on the boundary problem[19] or many-body electromagnetic interaction between small dielectric spheres[20] might be still valid in the nanometric region, the intuitive virtual photon model helps the understanding of the PSTM process in a generalized framework of the tunneling microscopes including STM, AFM, and so on. It is emphasized that the tunneling process is, in general, associated with a mechanical action between microscopic sample and probe tip. Although it has not been observed yet in the case of PSTM, the tunneling of evanescent photons should exhibit mechanical force, due to the extraordinary large field momentum resulting from locality.

It is confirmed from the PSTM experiment that the interaction between the microscopic sample and probe tip via evanescent electromagnetic field is localized in the narrow region determined by the scale of the probe tip. This meets the Heisenberg's uncertainty principle that, since the resolution of the microscope is determined by the shortest wavelength available in the measurement, the electromagnetic field with extraordinary large wave-vector, or momentum, is concerned with the PSTM measurement due to locality of the interaction. It is natural to describe the fundamental process of PSTM by a short-range quasi-static interaction via evanescent photons scattered from/to propagating photons in the material medium. Here the microscopic particles are the sample object and the probe tip, and the term "quasi-static" is used in the sense that the propagation or retardation effects can be neglected because of the short distance between the microscopic particles. A simple and intuitive picture of PSTM seems to be required for understanding the nature of the fundamental process in terms of the generalized framework of tunneling microscopes.

The minimal feature describing PSTM, the short-range quasi-static interaction, can be modeled simply by employing the idea of virtual photons with nanometric Compton wavelength and describing the field in terms of the Yukawa potential. The virtual photon, therefore, has an effective mass due to the coupling of electromagnetic field to the fundamental excitations in the material medium. The model makes it possible to interpret the optical near field problem as a particle tunneling through the effective potential barrier between the gap of microscopic dielectric particles. Compared with the surface plasmon near field microscope[21], the virtual photon employed here may be described in terms of polaritons representing the electromagnetic field coupled to the mechanical vibration in the dielectric medium via induced polarization.

In order to demonstrate validity of virtual photon picture, the Yukawa potential model is applied for calculation of evanescent field near a small circular aperture irradiated by propagating light with wavelength, much smaller than the aperture radius. Assuming the Compton wavelength of the virtual photons equal to the aperture radius, the intensity distribution in the near field region was estimated simply by taking the gradient of the potential given by integrating the contribution from small surface elements over the aperture using Yukawa potential. Figures 10(a) and (b) shows the numerical results; (a) the intensity distribution on the aperture axis

and (b) in three dimensions, respectively. In Fig.9(a), the result from the Yukawa potential model shows a good agreement with the numerical results given by Leviatan[19] based on the boundary problem.

More basic theoretical analysis describing the non-equilibrium interaction between matter and field is required in order to establish a new theoretical model of virtual photon model.

6. SUMMARY

We have reviewed our recent progress on the PSTM with main focus on describing the fabrication of nanometric optical fiber-probe tip. It was pointed out that the PSTM can be used not only as a super-resolution optical microscope but also as a nanometric fabrication tool for high density optical storage and single atom trapping. Novel theoretical model as also proposed in order to understand the fundamental process of PSTM in terms of the generalized framework of tunneling microscopes.

As a future outlook, it should be noted that fabrication of a functional probe tip and a probe tip array, system operation in liquid, and more reliable preparation of samples, etc. are required for the PSTM system as being used as a powerful tool in the field of biotechnology and chemistry. Careful investigations on unique features of PSTM, which are related to cavity quantum electrodynamics, quantum optics, etc., could open a new field of study on light and matter.

REFERENCES

- [1] D.W. Pohl, et.al., Appl. Phys. Lett., Vol.44 (1984) 651
- [2] R.C. Redick, et.al., Phys. Rev. B, Vol.39 (1989) 767
- [3] H. Pagnia, et.al., Optik, Vol.86 (1990) 87
- [4] K. Liberman, et.al., Science, Vol.247 (1990) 59
- [5] S. Jiang, et.al., Jpn. J. Appl. Phys., Vol.30 (1991) 2107
- [6] S. Jiang, et.al., Jpn. J. Appl. Phys., Vol.31 (1992) 2282
- [7] See for example, "Near Field Optics", Ed. by D.W. Pohl and D. Courjon, NATO ASI Series E: Applied Sciences Vol.242 (1993)
- [8] T. Pangaribuan, et.al., Jpn. J. Appl. Phys., Vol.31 (1992) L1302
- [9] M. Kawachi and T. Edahiro, Electron. Lett., Vol.21 (1982) 71
- [10] T. Pangaribuan, et.al., Electron. Lett., Vol.29 (1993) 1978
- [11] B.J. Ainslie, et.al., IEEE Trans. Microwave Theory Tech., Vol. MTT-30 (1982) 360
- [12] S. Mononobe, et.al., submitted to Jpn. J. Appl. Phys.
- [13] R. U. Maheswari, et.al., submitted to Electron. Lett.
- [14] Y. Toda and M. Ohtsu, submitted to Electron. Lett.
- [15] E. Betzig, et.al., Appl. Phys. Lett., Vol.61 (1992) 142
- [16] S. Jiang, et.al., Opt. Commun., Vol.106 (1994) 173
- [17] H. Hori, et.al., Tech. Digest of the 18th Int. Quantum Electron. Conf. (June, 1992, Vienna) MoM7
- [18] Kozuma, et.al., Tech. Digest of the 19th Int. Quantum Electron. Conf. (May, 1994, Anaheim) QFA7
- [19] Y. Liviatan, J. Appl. Phys. Vol.60 (1986) 1577
- [20] C. Girard and D. Courjon, Phys. Rev., Vol. B40 (1990) 9340
- [21] M. Specht, et.al., Phys. Rev. Lett., Vol.68 (1992) 476

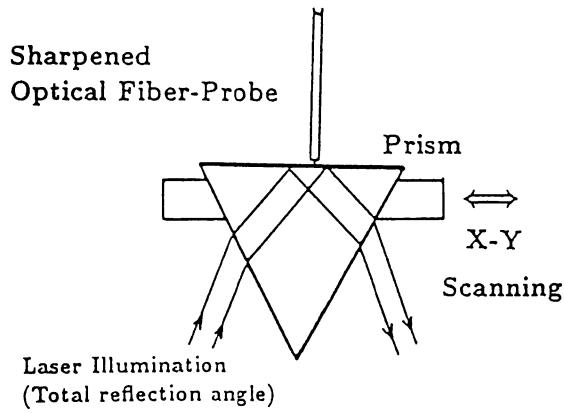


Fig.1 Schematic explanation of a PSTM system.

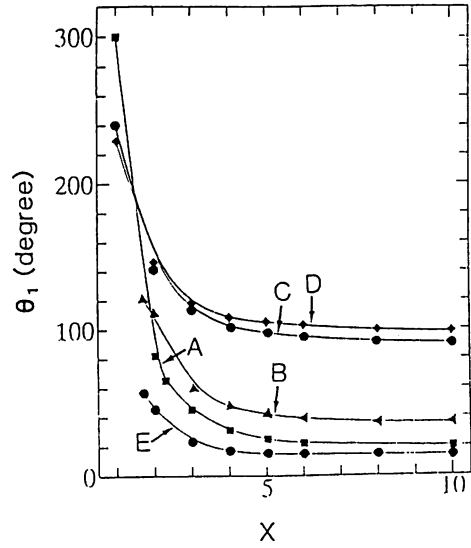
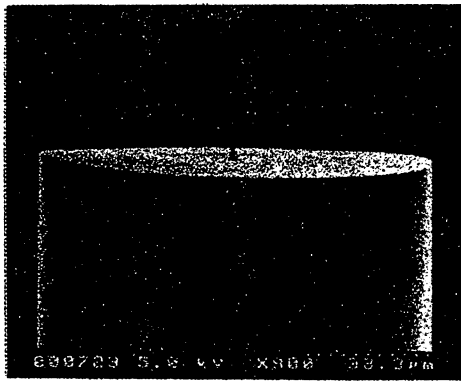


Fig.2 Dependence of the cone angle θ_1 on X.



(a)



(b) C_t

Fig.3 (a) The SEM image of the OFPT with cone angle of 20° . (b) Magnified image.

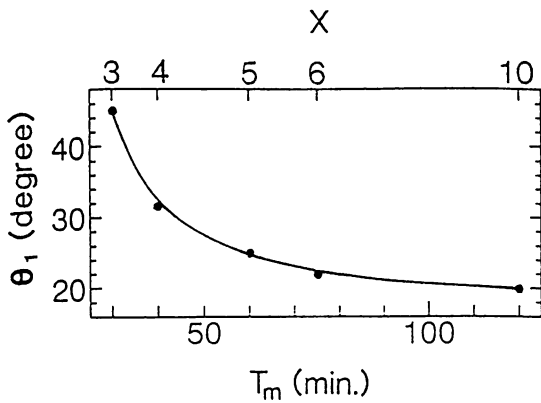


Fig.4 Relation between the cone angle θ_1 , the necessary minimum etching time T_m , and X.



Fig.5 The SEM image of the OFPT fabricated by the two-step etching.

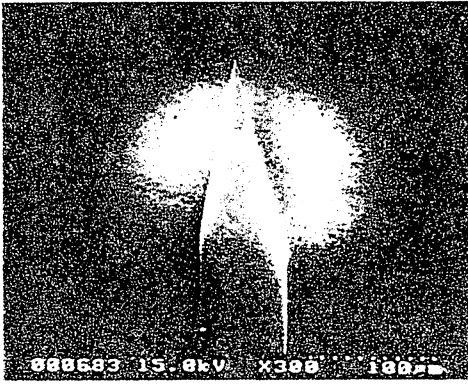


Fig.6 The SEM image of a pencil-shape OFPT.

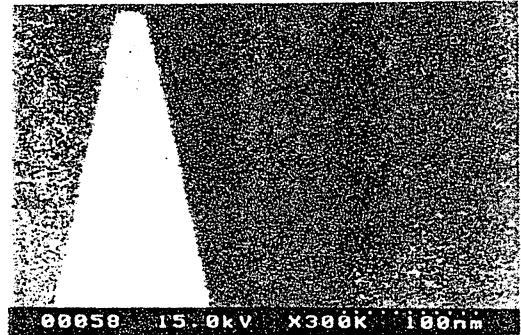


Fig.7 The SEM image of a flattened OFPT.

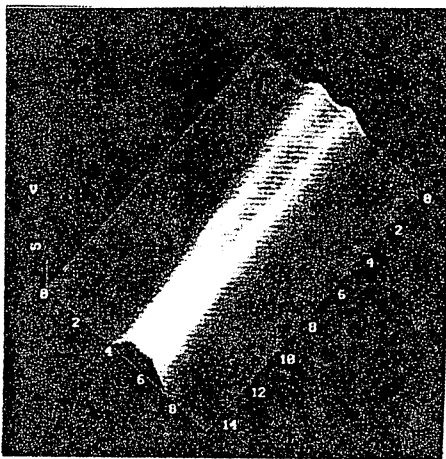


Fig.8 The PSTM image of a guided mode in a Y-branched proton-exchanged LiTaO_3 optical waveguide.

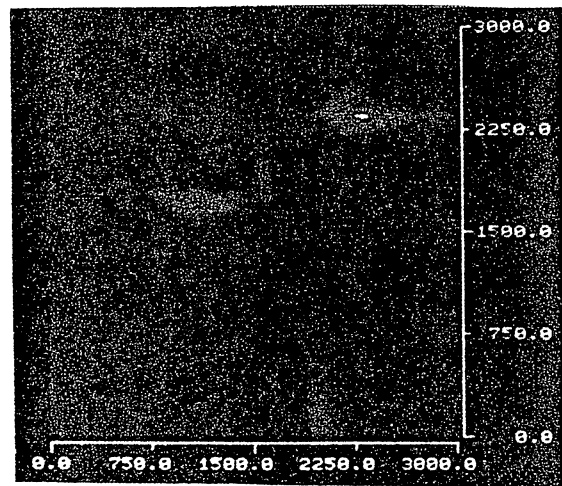
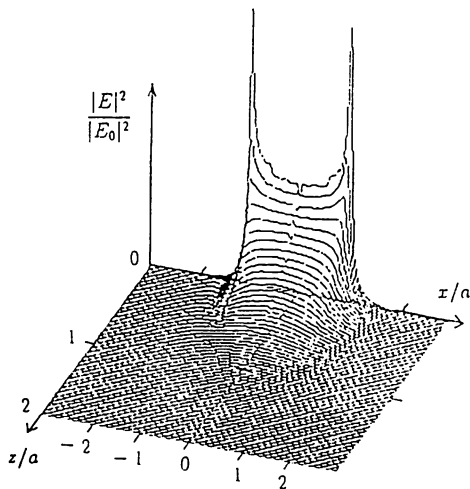
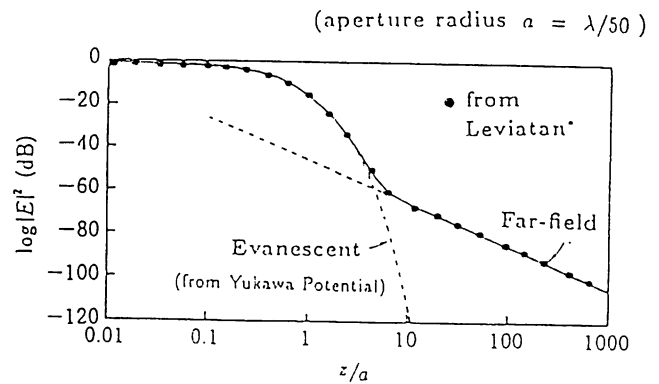


Fig.9 The PSTM image of the photon-mode recorded region of the LB film.



(a)



(b)

Fig.10 The application of the Yukawa potential model for the intensity distribution of the near field of a small circular aperture of diameter a irradiated by propagating light with wavelength of $50a$. (a) Intensity distribution on the symmetry axis, compared with the numerical results of Leviatan[18]. (b) Three dimensional intensity distribution.

TuS5

11:30 am

Photon-scanning tunneling microscopy for diagnosing propagating characteristics of optical waveguides, Yasunori Toda, Motoichi Ohtsu,* *Interdisciplinary Graduate School of Science and Engineering, Tokyo Institute of Technology, 4259 Nagatsuta, Midoriku, Yokohama, Kanagawa 227, Japan.* A high-resolution diagnostics technique for optical waveguides using a photon-scanning tunneling microscope is proposed. The performance of this technique was evaluated by measuring the propagating mode profile of a Y-branch LiTaO₃ waveguide. The propagating attenuation coefficient along the center of two branches is 2.3×10^{-2} dB/ μ m.

*Also with Kanagawa Academy of Science and Technology.

ThEEE2**3:45 pm**

Fabrication of a fiber probe with nano-aperture for photon scanning tunneling microscope (PSTM), R. Uma Maheswari, S. Mononabe, M. Naya, T. Saiki, M. Ohtsu,* *Kanagawa Academy of Science and Technology, Sakado 3-2-1, Takatsu Ku, Kawasaki 213, Japan.* We propose a method based on chemical etching for fabricating fiber probes with flattened tips suitable for fabrication of a nano-aperture through vacuum deposition. By this method, tips with diameter of approximately 15 nm can be produced. We also report some cyclic morphological changes of the tip observed during etching.

* Also with the Tokyo Institute of Technology.

[2]

PHOTON CONTROL IN THE FREQUENCY DOMAIN



Generation of Frequency-Tunable Light and Frequency Reference Grids Using Diode Lasers for One-Petahertz Optical Frequency Sweep Generator

Weizhi Wang and Motoichi Ohtsu, *Senior Member, IEEE*

Abstract—Generation of frequency-tunable light and frequency reference grids in a wide frequency span for a diode laser based optical frequency sweep generator has been performed. Frequency tuning and noise characteristics in nonlinear frequency conversions have been discussed. By using AlGaAs, InGaAsP lasers and their frequency conversions in the type II angle phase-matching KTP crystal, highly coherent frequency-tunable outputs have been obtained from 600 THz (0.5 μm) to 170 THz (1.7 μm). Use of the DFB lasers ensures the continuous tuning with a frequency range as wide as 1 THz. Atomic potassium and molecular iodine absorption resonances have been employed as frequency references for stabilizing the frequencies of lasers and the generated light with the frequency stability of 10^{-9} – 10^{-10} . Optical frequency comb generation has been realized at the 0.8 μm wavelength with a two-sided sidebands span of 4 THz. We have also proposed and demonstrated specific frequency-tunable systems based on sum and difference-generations of diode lasers.

I. INTRODUCTION

WIDE-BAND highly coherent frequency-tunable light sources have become more important in different fundamental research fields, such as ultra-high resolution spectroscopy, quantum optics, chemistry, medicine, as well as some applications such as multichannel coherent optical communications. For providing continuous-wave (cw) laser systems which could offer highly coherent light (spectrally and spatially) with tunability capable of covering the desired regions, immense efforts have been made in searching for laser media which have broad emission band and in designing of a tunable laser system. Indeed, cw tunable solid-state and chemical dye lasers have been developed to satisfy the practical requirements to some extent. The drawbacks of these systems are the inherent large noise due to fluctuations of pump power or dye jet, and the requirement of a complicated pump system, which leads to a large system volume and susceptibility to environmental influences. Efforts have been made to improve the coherence especially in reduction of FM noise of these lasers by using active feedback control with various schemes

[1], [2]. However, these large and costly systems make them not to be always available. Nonlinear optic effects have been employed for building tunable light sources such as optical parametric oscillators (OPO) [3], [4]. However, there are technical and principle difficulties in realizing continuous-wave OPO with a wide frequency-tunable range.

On the other hand, semiconductor lasers are tunable, compact and efficient, and cw high-power and single-mode laser devices have been also developed. Frequency tuning and frequency/intensity modulation which can be easily carried out by changing and modulating the temperatures and injection currents or external gratings of the diode lasers, and extremely low amplitude noise compared to most other laser sources are inherent advantages for the above-mentioned purposes [5], [6]. Furthermore, in recent years the remarkable results have been achieved: 1) Hypercoherent diode lasers with a linewidth of hertz-order have been realized by use of optical and electrical feedback control [7], and diode lasers based optical phase locking with high frequency tracking accuracy has been achieved [8], [9]. 2) High-quality diode laser devices have become commercially available, frequency sweeping range can be wider than terahertz by use of distributed-feedback (DFB) lasers or grating-extended cavity diode lasers [10]–[12]. 3) Optical frequency comb (OFC) generation with a sideband span as wide as several terahertz has been realized by use of a microwave resonant electro-optic modulator [13], [14]. These development and achievements in diode lasers and the related techniques make it possible to build a diode-laser-based wide-band coherent optical frequency sweep generator (OFSG) with a frequency coverage of ~ 1 PHz from ultraviolet to near infrared.

We describe our proposed scheme of the OFSG and present the experimental results of generation of frequency reference grids towards realization of such a system. The paper is arranged as follows: In Section II, the principle of the OFSG are shown and theoretical analyses of frequency noise and frequency tuning characteristics related to nonlinear frequency conversions of diode lasers are given. In Section III, experimental results of both frequency up and down conversions are presented. In Section IV, absolute frequency stabilization and frequency linking between diode lasers and the converted light are performed for the purpose of establishing frequency reference grids in the OFSG. In Section V, demonstration of frequency-tunable systems and discussion are presented, and Section VI gives a summary.

Manuscript received March 3, 1994; revised October 5, 1994. This work was supported by a Grant-in-Aid for Scientific Research (Grants 04228102 and 05452110).

W. Wang is with Interdisciplinary Graduate School of Science and Engineering, Tokyo Institute of Technology, 4259, Nagatsuta-cho, Midori-ku, Yokohama 227, Japan.

M. Ohtsu is with Interdisciplinary Graduate School of Science and Engineering, Tokyo Institute of Technology, 4259, Nagatsuta-cho, Midori-ku, Yokohama 227, Japan and Kanagawa Academy of Science and Technology, KSP East, Rm. 408, 3-2-1 Sakado, Takatsu-ku, Kawasaki 213, Japan.

IEEE Log Number 9408601.

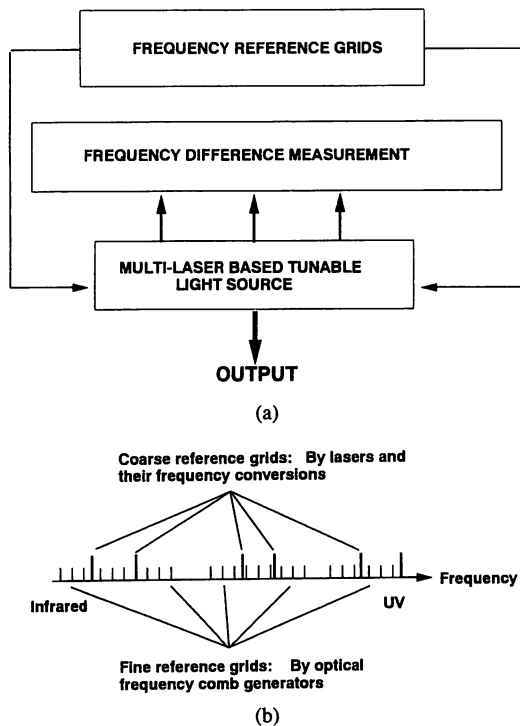


Fig. 1. (a) Schematic construction of the OFSG. The frequency reference grids consist of coarse and fine frequency reference grids generated by diode lasers and their frequency conversions and by frequency combs, respectively. The multilaser based tunable light source contains various diode lasers and their frequency converters. The frequency difference measurement consists of optical heterodyne schemes. (b) Explanation of the coarse and fine frequency reference grids.

II. PRINCIPLE OF A WIDEBAND OPTICAL FREQUENCY SWEEP GENERATOR

A. Construction of an Optical Frequency Sweep Generator

Fig. 1 is a block diagram to show the systematic configuration of the OFSG which is capable of carrying out simultaneously absolute frequency stabilization, continuous frequency tuning and precision measurement of frequency difference. The system consists basically of three parts as follows.

1) *Frequency Reference Grids for Absolute Frequency Stabilization*: Choosing of frequency references which concerns to the accuracy of the frequency determination depends on the available laser power, available spectroscopic results and stabilization schemes. In principle, one quantum transition, for example the molecular iodine transition at 633 nm or the atomic calcium transition at 657 nm, is a promising candidate with high frequency stability for the frequency reference grids in OFSG by use of the cascade frequency combs, in which different frequency comb generators driven at the primary reference frequencies and their converted frequencies are cascaded by phase-locking. However, the presently available diode lasers do not satisfy such a continuous lasing spectrum. Therefore a multi-reference scheme is necessary for the OFSG. It means that the coarse frequency reference grids are obtained alternatively by use of commercially available diode lasers and their frequency conversions and multiple atomic or molecular transitions, while fine frequency reference grids are realized by frequency comb. For this purpose, indeed, the cascade combs scheme in different frequency region is still necessary.

2) *Multilaser-Based Frequency-Tunable Light Source*: This part of the system is constructed similarly to part 1, which employs multiple diode lasers and their frequency converters. In contrast to the tuning mechanisms of the conventional tunable lasers in which wavelength selective elements or wavelength filters are employed over a wide gain range, this system contains multiple highly coherent diode lasers with their own tunability, that makes it possible to use fully the advantages of diode lasers and the related control techniques.

3) *Frequency Difference Measurement System*: For the purpose of measuring precisely the frequency difference between the tunable output and the frequency reference, the tunable output is heterodyne phase-locked to one of the frequency reference grids in the corresponding region. The frequency sweeping accuracy can be sufficiently high with the help of the optical phase locking. It should be noted that the frequency measurement using optical heterodyne signal is basically limited by the response bandwidth of the photodetector. Therefore, the fine frequency reference grids by use of OFC generators in the system make it possible to measure the frequency difference larger than 1 THz.

B. Frequency Tuning Characteristics in Frequency Conversions

The parametric interactions in the frequency domain are divided into frequency up and down conversions, corresponding to the sum- and difference-frequency generations. For effective energy transfer from fundamental waves at frequencies ν_1 and ν_2 to the generated frequency ν_3 , both energy and momentum conservation (phase matching) must be satisfied. In the case of using collinear phase matching, they can be expressed as

$$\nu_3 = \nu_2 \pm \nu_1 \quad (1)$$

and

$$\frac{n_3}{\lambda_3} = \frac{n_2}{\lambda_2} \pm \frac{n_1}{\lambda_1} \quad (2)$$

where λ_i ($i = 1, 2, 3$) represents the fundamental wavelengths and the generated wavelength in vacuum, respectively, n_i represents the refractive index of the crystal corresponding, respectively, to each wavelength. The signs \pm denote sum- and difference-frequency generation respectively. The birefringence phase matching can be satisfied by controlling temperature, wavelengths and polarizations of the fundamental waves, and crystal orientation.

Frequency tuning is characterized by two kinds of parameters: frequency tuning range and tolerances of tuning parameters. The frequency tuning range is defined as the frequency span in which the phase matching condition can be satisfied while maintaining a reasonable effective nonlinear coefficient. In this paper, we discuss only potassium titanyl phosphate (KTiOPO₄; KTP) in frequency conversion without losing generality of the method to other nonlinear crystals. We carried out theoretical calculation of the frequency tuning range. The results show that the upper limit of the generated light frequency is ~ 680 THz (0.45 μm) in the case of sum-frequency generation. This is in contrast to the case of using second-harmonic generation in which the generated

wavelength is limited to be longer than $\sim 0.5 \mu\text{m}$ [15]. The difference-frequency generation in the present case can provide infrared light from 300 THz ($1 \mu\text{m}$) to the frequency as low as ~ 100 THz ($3 \mu\text{m}$). Furthermore, generation of the light in the above-mentioned entire frequency span can be possible by using only type II angle tuning at room temperature.

To evaluate the tolerance of a certain tuning parameter of KTP, we express the phase mismatch, according to (2), as

$$\Delta kL = 2\pi L \left[\frac{n_3}{\lambda_3} - \left(\frac{n_2}{\lambda_2} \pm \frac{n_1}{\lambda_1} \right) \right]. \quad (3)$$

The tolerance is defined as the changeable bandwidth of this parameter (while the other tuning parameters are fixed) when the output frequency-converted power drops to its half maximum.

As the KTP crystal is insensitive to the temperature variation [16]–[19], which is a particularity in use of KTP, the temperature tolerance of the KTP crystal is sufficiently large ($>10^\circ$) to endure usual temperature fluctuations of the experimental condition. Hence we do not deal with this respect and consider only angle and wavelength/frequency tolerances.

1) *Tolerance of angle θ* : In the case of type II, θ phase matching, only one wave, namely λ_1 , is the so-called extraordinary wave. The refractive index of this wave n_1 can be obtained from the Fresnel equation describing propagation of light in crystal as

$$n_1^{-2} = n_{1x}^{-2} \cos^2 \theta + n_{1z}^{-2} \sin^2 \theta. \quad (4)$$

Then we have

$$\delta(\Delta kL) = \frac{\pi L}{\lambda_1} \sin 2\theta \frac{n_{1z}^{-2} - n_{1x}^{-2}}{(n_{1x}^{-2} \cos^2 \theta + n_{1z}^{-2} \sin^2 \theta)^{3/2}} \delta\theta. \quad (5)$$

2) *Tolerances of Fundamental Wavelengths*: In the case that the wavelength of the extraordinary wave, λ_1 , is fixed, the tolerance of wavelength λ_2 is obtained as

$$\delta(\Delta kL) = 2\pi L \cdot \left(\frac{1}{\lambda_3} \frac{\lambda_1^2}{(\lambda_1 \pm \lambda_2)^2} \frac{\partial n_3}{\partial \lambda_3} - \frac{1}{\lambda_2} \frac{\partial n_2}{\partial \lambda_2} + \frac{(n_2 - n_3)}{\lambda_2^2} \right) \delta\lambda_2. \quad (6)$$

In the case that the wavelength of the ordinary wave, λ_2 , is fixed, the tolerance of wavelength λ_1 is obtained as

$$\delta(\Delta kL) = 2\pi L \cdot \left(\pm \frac{1}{\lambda_3} \frac{\lambda_2^2}{(\lambda_1 \pm \lambda_2)^2} \frac{\partial n_3}{\partial \lambda_3} \mp \frac{1}{\lambda_1} \frac{\partial n_1}{\partial \lambda_1} \pm \frac{(n_1 - n_3)}{\lambda_1^2} \right) \delta\lambda_1. \quad (7)$$

The upper and lower signs in (6) and (7) correspond to the sum and difference frequency generations. It should be noted that because n_1 corresponds to the extraordinary wave, (4) must be used for (7). By using (6) and (7), wavelength tuning bandwidths can be estimated as the crystal is fixed in orientation and the frequency tuning bandwidth can be converted by using $\delta\nu = -c\delta\lambda/\lambda^2$. The specific results of these tolerances will be shown later in the experiments.

C. Frequency Noise Characteristics in Nonlinear Frequency Conversion

In cw operation, the frequency noise of the generated light is an important characteristics in our frequency conversion

based system. Because the typical frequency noise spectra of diode lasers have been shown to have an almost flat profile from megahertz to gigahertz, e.g., 3-electrode DFB lasers at $1.5 \mu\text{m}$ [10], the white noise model is considered as a good approximation. We discuss here the FM noise in terms of the field spectral linewidth which can be conveniently related to the FM power spectral density. The power spectral density of electric field amplitude is employed as a conventional measure for describing randomly fluctuating time-dependent quantity of light. The laser spectral linewidth is defined as the full width at half maximum of the line shape which is calculated by the Fourier transform auto-correlation function of the electric field.

Assuming that the electric field of light take the form of

$$E = E_0 \exp \{j(2\pi\nu t + \phi(t))\}, \quad (8)$$

Then the auto-correlation function of the field can be approximated as [20]

$$R_E(\tau) = \exp \left\{ j2\pi\nu\tau - \frac{1}{2} \langle \delta\phi^2 \rangle \right\}. \quad (9)$$

Where the amplitude is simplified as unity, and

$$\delta\phi = \phi(t) - \phi(t + \tau). \quad (10)$$

The relation between the linewidths of the participating light fields and that of the generated light field is derived directly from the definitions with approximation in the following way. The electric field of the generated light E_3 , assuming the depletion of the fundamental waves be negligible, is given by

$$E_3 = A d_{eff} E_1 E_2 \int_0^L \exp \{j\Delta k z\} dz, \quad (11)$$

$$= A d_{eff} E_1 E_2 L \frac{\exp \{j\Delta k L\} - 1}{\Delta k L}, \quad (12)$$

where

$$E_i = E_{i0} \exp \{j(2\pi\nu_i t + \phi_i(t))\}, \quad (i = 1, 2), \quad (13)$$

corresponds to each of the two fundamental electric fields. A is a coefficient, d_{eff} is the effective nonlinear coefficient, L represents the crystal length. E_2 should be replaced by E_2^* if the difference-frequency generation is considered. Under the phase-matching condition, ΔkL should be a very small quantity, then, we can expand the phase term due to phase mismatch in (12) as

$$\frac{\exp \{j\Delta k L\} - 1}{\Delta k L} \approx j - \frac{1}{2} \Delta k L. \quad (14)$$

From this expression we can conclude that the fluctuations of phase mismatch, which can be caused by temperature fluctuations and vibrations besides the frequency fluctuations of the fundamental lasers, have no contribution to the phase fluctuations of the generated wave in the first order approximation. As the frequency of the generated wave, ν_3 , satisfies the energy conservation by (1), and then the auto-correlation function of the generated light field E_3 is expressed as:

$$R_{E_3}(\tau) = \exp \left\{ j2\pi\nu_3\tau - \frac{1}{2} \langle \delta\phi_3^2 \rangle \right\}, \quad (15)$$

where $\delta\phi_3$ is determined by initial phases of the fundamental

waves, and can be expressed as:

$$\delta\phi_3 = \delta\phi_1 \pm \delta\phi_2. \quad (16)$$

Provided that the two fundamental waves are from two independent lasers, implying that the initial phases are not correlated, we have

$$\langle \delta\phi_3^2 \rangle = \langle \delta\phi_1^2 \rangle + \langle \delta\phi_2^2 \rangle. \quad (17)$$

The relation between S_E and $R_E(\tau)$ can be also expressed by [5]

$$R_E(\tau) = \exp \left[j2\pi\nu\tau - 2\pi\tau \int_0^\infty S_E(f) \text{sinc}^2(\pi f\tau) d(\pi f\tau) \right]. \quad (18)$$

The field spectral profile is given by the absolute value of the Fourier transform of R_{E_3} , i.e.,

$$I(\nu - \nu_3) = \int_0^\infty R_{E_3}(\tau) \exp \{-j2\pi\nu\tau d\tau\} + \text{c.c.} \quad (19)$$

Under the white-noise assumption, i.e.,

$$S_{E_i}(f) = a_i(\text{const.}), \quad (20)$$

and

$$\langle \delta\phi_i^2 \rangle = a_i\tau, \quad (21)$$

where $i = 1, 2$ denotes either of the fundamental waves. Hence, the field spectral profile exhibits a Lorentzian and linewidths of the fundamental waves, respectively, take values of

$$\Delta\nu_i = \pi a_i, \quad (i = 1, 2). \quad (22)$$

Based on (17), (21), and (22), the linewidth of the generated wave is the summation of these of fundamental waves, i.e.,

$$\Delta\nu_3 = \Delta\nu_1 + \Delta\nu_2. \quad (23)$$

It is found that in the case of second-harmonic generation using one laser, i.e., the two fundamental waves comes from the same laser, the linewidth of second-harmonic wave takes the value of

$$\Delta\nu_{SHG} = 4\Delta\nu_{Laser}. \quad (24)$$

When the $1/f$ noise is added to the above discussion for describing diode lasers, i.e.,

$$\langle \delta\phi_i^2 \rangle = a_i\tau + a'_i\tau^2, \quad (25)$$

the line profile and linewidth are modified, but can be still evaluated easily with the help of the "Plasma Dispersion Function" [20], [21].

The above discussion shows that the linewidth of the generated field in nonlinear frequency conversion is determined by that of the fundamental lasers.

III. GENERATION OF FREQUENCY-TUNABLE LIGHT IN A WIDE FREQUENCY SPAN

Because the available wavelengths of the present diode lasers exist discontinuously in the region from 0.6 to 1.5 μm with some gaps, we should use frequency conversions

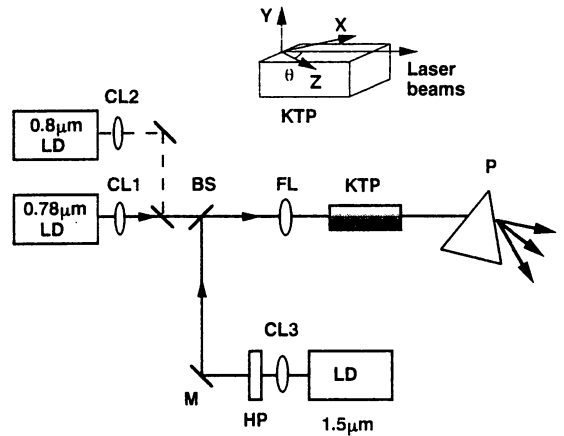


Fig. 2. Experimental setup for both sum- and difference-frequency generations. CL1, CL2, collimating lenses; M, reflecting mirror; BS, beam splitter; FL, focusing lens; P, prism. The half wavelength plate, HP, was used to adjust the polarization from the 1.5 μm laser for satisfying the type II phase matching condition.

to extend coverage of frequency to the region where direct diode laser spectra are not available. For this purpose, parametric processes involving the second-order nonlinearity, i.e., second-harmonic generation [22], sum-frequency generation and difference-frequency generation or parametric amplification [23], [24], have been experimentally performed by using AlGaAs (0.78/0.8 μm) and InGaAsP (1.5 μm) DFB lasers. Since the continuous tuning range of a DFB laser can overlap with that of a conventional Fabry–Perot (FP) type diode laser even though the FP type laser experiences mode hops, use of the DFB laser in frequency conversions offers a continuous frequency tuning range wider than 1 THz and ensures the continuous frequency coverage of the entire frequency-tunable span determined by the two lasers.

Fig. 2 shows the system configuration for both sum- and difference-frequency generations. Multi-electrodes corrugation-pitch-modulated MQW-DFB lasers [10] at 1.5 μm with a maximum output power of 50 mW and a MHz-linewidth, 100 mW single-mode AlGaAs lasers (SDL-5311) at 0.8 μm and 50 mW 0.78 μm single-mode AlGaAs lasers (HL7852) were used as the fundamental laser sources. The linewidths of AlGaAs lasers in experiment were narrowed to less than 100 kHz by using optical feedback from an external confocal FP cavity [25]. A 10 mm long KTP (cut with $\theta = 54^\circ$, $\phi = 0$, and two facets were coated with antireflection films at both 0.78 and 1.5 μm) was put in the θ plane, i.e., $\phi = 0^\circ$, with the y axis in the vertical direction.

For sum-frequency generation, the polarization of the 1.5 μm laser was perpendicular to the θ plane and the polarization of the 0.78/0.8 μm laser was in the θ plane for satisfying the type-II phase matching. The two laser beams were focused into the crystal and the angular phase matching was obtained around $\theta = 60^\circ$ which is in accordance with the calculated result using the Sellmeier equation given by Bierlein [16]. The sum-frequency output has the polarization along the y axis with the wavelength determined by

$$\lambda_3^{-1} = \lambda_1^{-1} + \lambda_2^{-1}. \quad (26)$$

where the subscript numbers 1, 2, and 3 denote the two input

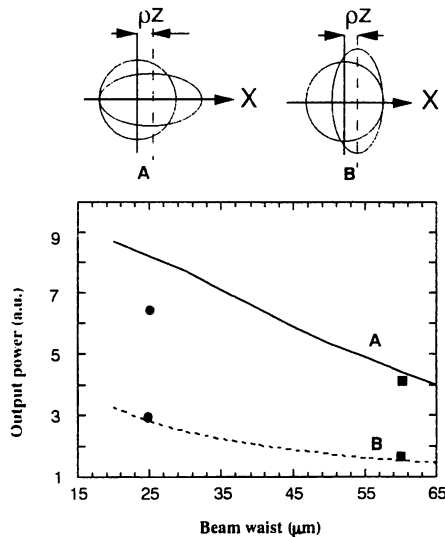


Fig. 3. Sum-frequency output powers vs. beam waists. ρz represents deviation of the beam overlap in the propagation length z due to walk-off; ρ is the walk-off angle. Curves A and B correspond to the cases that the walk-off occurs along the long- and the short-axis of the elliptical Gaussian beam, respectively. One of the participating beams is circular and its diameter is equal to the short-axis diameter of the elliptical beam. Two sets of measured values (filled circles and rectangles) correspond to the different beam waists.

fundamental waves and one output wave, respectively. The output power of the generated sum-frequency can be expressed as

$$P_{out} = 1.1 \times 10^{-4} P_1 P_2, \quad (27)$$

in the unit of watt, where P_1 and P_2 represent the input powers of the two lasers in units of watt. The reduction factor in Boyd and Kleinman's theory due to the walk-off effect [26], which was included in the coefficient of (29), was estimated as 0.07 when the beam walk-off angle was 1.5° and the beams waists were 20 and 40 μm for 0.7/0.8 μm and 1.5 μm diode lasers, respectively.

It should be noted that in use of diode lasers, the elliptical Gaussian beams will lead to some deviation of the obtained results from the calculation for circular beams [27]. Especially in presence of walk-off like the case of KTP angle phase matching, arrangement of the orientation of the elliptical beam shape can result in 2~3-fold power difference in output [23]. Both experiment and calculation have shown, as in Fig. 3, that it is preferable to make the walk-off direction occur along the long-axis of the elliptical cross-section.

The acceptance angle defined by the FWHM of the curve of the output power versus phase mismatch was measured to be $\sim 0.5^\circ$, while the calculated value is $\sim 0.36^\circ$ using (5), noting the converted output power can be approximated by $\text{sinc}^2(\Delta k L/2)$ [28]. The larger obtained value is attributed to the strong focusing of laser beams in experiment, which causes relief of angle mismatch. The frequency-tunable characteristics in the sum-frequency generation was also investigated by fixing the crystal orientation and injection currents of fundamental lasers, and changing operation temperature of the 1.5 μm DFB laser. The measured frequency tuning bandwidths defined in Section II-B were ~ 100 GHz in both cases when another fundamental laser was at 0.78 and 0.8 μm . The

calculated values using (6) are 85 and 90 GHz for a 1-cm KTP, respectively. The calculation also gives a frequency tuning bandwidth of 350 GHz, using (7), for a 1-cm KTP when the 0.78/0.8 μm laser is tuned. However, the experimental confirmation was difficult for the mode hopping. Accompanying with the large acceptance angle for phase matching, a tuning range of the sum-frequency output about 15 nm (16 THz) can be expected with a phase-matching angle change of 1° . By using combination of these diode lasers, highly coherent frequency-tunable green light has been obtained from 0.51 to 0.56 μm (50 THz) with a continuous tuning range of ~ 1 THz by the DFB laser.

For generating the difference-frequency of two diode lasers [23], we used the same lasers as previously. Because of the limited detectable band of an optical spectrum analyzer (Anritsu MS9702B), only difference-frequency between the 0.78 μm and the 1.5 μm lasers was measured, which satisfies

$$\lambda_3^{-1} = \lambda_1^{-1} - \lambda_2^{-1}, \quad (28)$$

and was around 1.6 μm in the present case. The polarization of the 0.78 μm laser was perpendicular to the θ plane and the polarization of the 1.5 μm laser was in the θ plane. The phase matching angle was 52° which was in agreement with the calculated value. A 0.3 μW output was obtained, by which the generation of the near infrared light using difference-frequency generation was demonstrated. The tunable range was larger than 5 THz (1.58–1.62 μm) which corresponded to the wavelength range of the AlGaAs laser from 0.78 to 0.79 μm by controlling the operation temperatures and currents of the lasers. This range can be further enlarged by using a grating extended cavity diode laser or by installing the laser inside a vacuum chamber to increase the adjustable temperature range.

To confirm the feasibility of difference-frequency generation in a wide frequency span using diode lasers, we performed difference-frequency generation with the help of a Ti:sapphire laser which replaced the AlGaAs laser in the above experiment. The tuning characteristics was investigated by tuning the input lasers and the angle of the crystal simultaneously. Both experiment and calculation show that the frequency tuning bandwidth was 200 GHz for a 1-cm KTP by temperature tuning the 1.5 μm DFB laser. Fig. 4(a) and (b) show the measured output power and the phase-matched angle θ as functions of the pump wavelength. The obtained tunable range was from 1.38 to 1.67 μm (38 THz) which corresponded to the pump wavelength from 0.73 to 0.80 μm . The output power in Fig. 4(a) was calibrated as the pump power was 100 mW since the power from the Ti:sapphire laser could not keep constant during the tuning. The obtained phase-matched angle agreed with the calculation except for the wavelength near 0.8 μm . The reason for this discrepancy is unclear and under investigation. The maximum available tuning range can be as wide as 600 nm (65 THz) around 1.54 μm which is limited only by the present crystal size when the Ti:sapphire laser was used.

This experiment can also be considered as optical parametric amplification of a diode laser in the KTP pumped by the Ti:sapphire laser. Thus it provided useful information for designing a cw optical parametric oscillator in this frequency

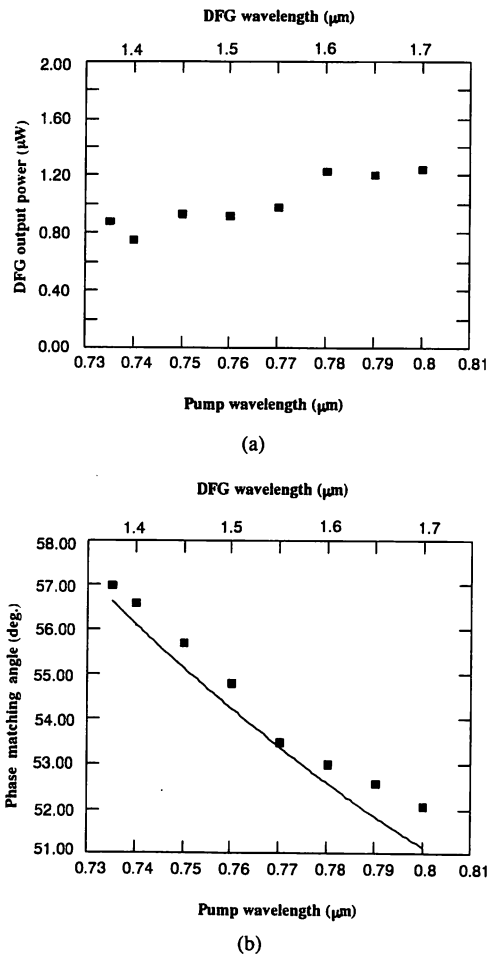


Fig. 4. Relation between output power and the wavelength (a), and measured dependence of the phase-matched crystal angle on the wave-length (b). The pump and diode laser powers were 100 and 5 mW respectively.

region which is especially important for optical communications. The degenerate optical parametric gain was estimated to be 5×10^{-4} when the pump power was 200 mW and the beam waist was $15 \mu\text{m}$ by using the small gain formula [29]

$$g = 8\pi^2 d_{eff}^2 l^2 P_1 h / \epsilon_0 c \lambda_2 \lambda_3 n_1 n_2 n_3 A, \quad (29)$$

as $d_{eff} = d_{24} \sin \theta \simeq 6 \text{ pm/V}$ and $l = 10 \text{ mm}$, where l is the crystal length, n is the refractive index, P is the power, A is the pump beam cross section. The reduction factor h in the present case of the KTP was estimated to be $\sim 1/15$ which was subject to the deviation from the ideal collimation of the diode laser beam. The output power

$$P_3 = gP_2, \quad (30)$$

was calculated to be $2.5 \mu\text{W}$ for the degenerate case, while the measured value was $1.9 \mu\text{W}$. The reason was deduced to be imperfect mode matching of the experimental condition and also the unsure practical nonlinear coefficient of the KTP. From the above experimental result, we conclude that difference-frequency generation by diode lasers can provide us the highly coherent cw tunable light over the wide near infrared region limited by the transparent band of the KTP crystal. When the Ti:sapphire laser is replaced by a high power and highly coherent AlGaAs laser diode which has

been realized by using a coherent addition technique [25], the fundamental lights with linewidths in the order of 10 kHz and powers in the order of 100 mW ensure that μW order highly coherent output power is still available if optimization of elliptical beam profile is performed as described previously.

IV. ATOMIC/MOLECULAR RESONANCE STABILIZED FREQUENCY REFERENCE GRIDS

To perform absolute frequency stabilization, use of an atomic/molecular absorption resonance is the most popular scheme. In addition, the atomic/molecular transition is possible in principle to be measured accurately by means of a frequency chain [30], [31] so as to offer a tunable output with a known frequency value.

Various atoms and molecules can be chosen as possible frequency reference grids in a wide frequency span. To reduce the number of independent atomic/molecular transitions in one system, that is also important for making it easy to measure absolutely frequencies of these transitions, frequency linking between multiple lasers becomes necessary, by which more than two frequencies are stabilized using one reference. For this purpose, two methods can be considered. 1) To use the pump-probe or saturation spectroscopy scheme to one atomic transition or two transitions (known as the two-step excitation), for which pump and probe beams can be from different type lasers with the help of nonlinear frequency conversion. 2) To use optical phase locking technique with the help of a frequency comb which is composed of sidebands generated from an optical phase modulator, by which the frequency difference between the two lasers can be as large as the usable span of sidebands of the frequency comb. It is clear that method 1) provides only a link with a fixed frequency interval determined by the atomic energy level structure, while method 2) offers more options in the frequency interval of a link but has a limited frequency span. Combination of 1) and 2) extends the capability of the frequency linking.

We present here two schemes for generating the coarse frequency grids and the OFC generation for the fine frequency grids.

A) Frequency Reference and Linking Using Optical Double Resonance in Potassium

Potassium (^{41}K) was chosen for our experiment since a high-power and highly coherent distributed feedback (DFB) laser is available at $1.54 \mu\text{m}$ [10], and the second harmonic of which just coincides with the $^{41}\text{K} - D_1$ line (770.109 nm in vacuum). By using this scheme, the coarse frequency reference grids can be obtained at $0.77, 1.54 \mu\text{m}$ and their sum-frequency at $0.51 \mu\text{m}$ simultaneously [32].

To prepare two lasers for the pump-probe spectroscopy which is shown by Fig. 5, the second-harmonic wave of a $1.54 \mu\text{m}$ DFB laser, which was used as a probe, was generated in a 10 mm long KTP crystal. Type-II, angle-tuning phase matching at room temperature was employed as the crystal was installed along the θ plane ($\phi = 0, \theta = 54^\circ$). The fundamental power was 40 mW and the detected power after the spectroscopic system was measured to be 20 nW. The pump laser was a grating-feedback AlGaAs laser, and the laser

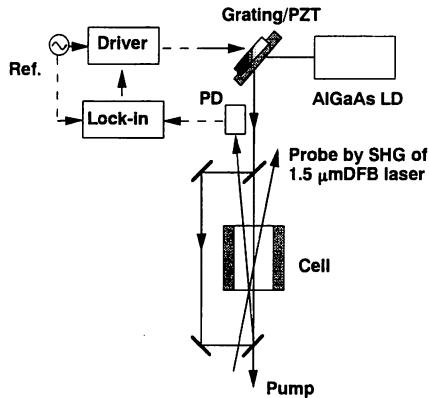
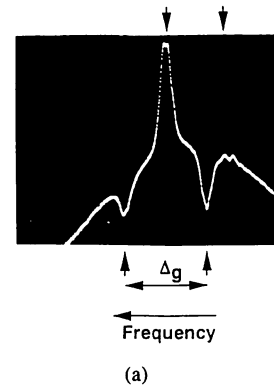


Fig. 5. Experimental setup for the pump-probe spectroscopy for both co- and counter-propagating schemes. The pump laser frequency was stabilized using the saturation-spectroscopy scheme. All parts were fixed on an invar plate to improve the thermal stability. The probe was the second harmonic wave of the $1.54 \mu\text{m}$ DFB laser.

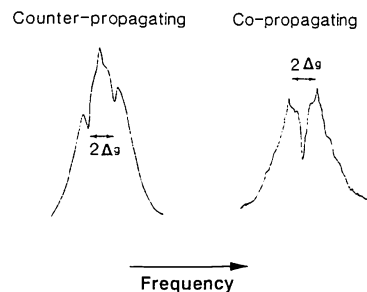
facet was coated with an anti-reflection (AR) film to extend the tunability which is accomplished using an external grating (1200 lines/mm). The operating injection current was 100 mA while the threshold was ~ 85 mA due to the AR coating, and the output power used was 1.4 mW.

A conventional saturation-spectroscopy scheme was arranged for locking the laser frequency to the saturated absorption resonance, referring to Fig. 5. The laser beam was divided into two parts, one for the pump and the other one for the probe in counter-propagating directions. The atomic cell containing ^{41}K (2 cm long) was installed inside an oven to maintain the temperature close to 60°C . At this temperature, total absorption was measured to be 40~50%, and the Doppler width was ~ 800 MHz. The Doppler-free absorption resonances were observed to verify that the pump laser was on the potassium D_1 resonance line and in a real single-mode regime. Fig. 6(a) shows the Doppler-free absorption profile when the laser frequency was tuned to the top of the Doppler profile. The laser beam intensity used was $\sim 4 \text{ mW/cm}^2$. We also measured the hyperfine splitting of the $4P_{1/2}$ state of ^{41}K as ~ 29 MHz from our observed absorption resonance profile based on the ground state ($4S_{1/2}$) hyperfine splitting of 254 MHz [33], which was not documented in literature yet to the authors' knowledge. It is clear from the obtained profile that the spectroscopic resolution was up to the nature linewidth limit (~ 10 MHz) [32].

Frequency stabilization of the pump laser was carried out by locking the laser frequency to the cross-over absorption peak of the $^{41}\text{K} - D_1$ line by using the phase-sensitive technique through a lock-in amplifier. The modulation frequency applied to the PZT of grating was 3 kHz and the time constant was 30 ms. The residual frequency fluctuations were estimated to be less than 50 kHz from the error signal, implying a frequency stability as high as 10^{-10} . This result demonstrated that the Doppler-free absorption line of potassium also provides an absolute frequency reference for AIGaAs lasers. It should be noted that estimation of the frequency stability in this paper was based on the error signal of the feedback loop although Allan variance of two independent systems is necessary to evaluate the real frequency stability.



(a)



(b)

Fig. 6. (a) The Doppler-free resonances obtained for stabilizing the pump laser frequency. The upper arrows indicate the cross-over resonance (high peaks) and the isotope ^{39}K (small peaks). The lower arrows indicate the two dips corresponding to the two hyperfine sublevels in the ground state ($4S_{1/2}$). (b) Saturated absorption profiles in counter- and co-propagating schemes probed by the second-harmonic generation. The frequency intervals between two dips in the counter-propagating case, and between two peaks in the co-propagating case, are two times that of the hyperfine splitting of the ground state ($\Delta_g = 254$ MHz).

For the pump-probe spectroscopy, the second-harmonic wave of the $1.54 \mu\text{m}$ DFB laser was arranged as a probe co- and counter-propagating to the pump beam as shown in Fig. 5. For improving the signal-to-noise ratio, the probe beam was intensity-modulated by a chopper with a frequency of 1 kHz and the output absorption profile was obtained from a lock-in amplifier while the probe frequency was swept. In the counter-propagating scheme, the pump-probe beam angle was about 5 mrad, while in the co-propagating scheme, two crossed polarizers were used to block the direct incidence of the pump beam to the detector so as to maintain the angle between pump and probe beams to be less than 1 mrad.

Fig. 6(b) shows the absorption profiles in both co- and counter-propagating schemes. It was found that a high contrast ($>60\%$) of the nonlinear absorption was obtained in the co-propagating scheme, which was preferable for frequency stabilization.

B. Frequency References Using Molecular Iodine Absorption Resonances

Because the pair of the fundamental lasers must be linked with each other through the second-harmonic generation in the previous experiment, the frequency range is limited. In order to extend further the tunable frequency span, different kinds of AIGaAs laser, e.g., in the $0.8 \mu\text{m}$ region, are mixed with the InGaAsP laser. A second scheme for providing

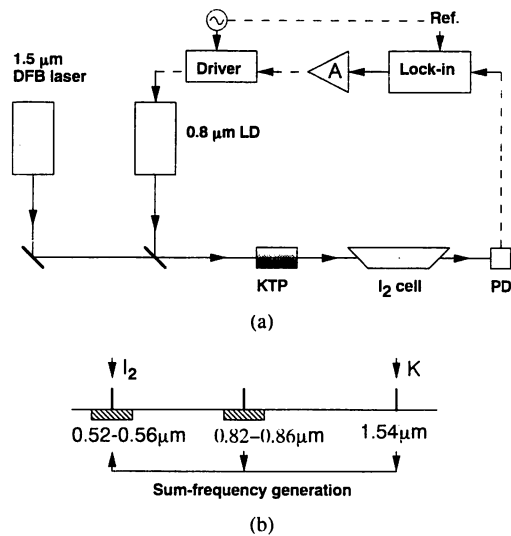


Fig. 7. (a) Experimental scheme for stabilizing sum-frequency by controlling only one fundamental laser. PD, photodetector. The feedback is applied to the 0.8 μm LD using the error signal from the lock-in amplifier. (b) Explanation of frequency grids generation in the corresponding regions.

frequency references is considered, which does not limit the another laser frequency but needs a frequency reference in the generated frequency region. For the 1.5 μm based frequency conversion, this scheme offers more options to provide frequency references in other wavelength region. Molecular iodine (I_2) was chosen for a frequency reference for our experiment because of its plenty of absorption lines covering a very large frequency range in the green region [34]. Also, both linear and saturated absorption resonances of I_2 offer the possibility of obtaining high frequency stability [35], [36]. A linear absorption resonance is very convenient to be used as a frequency reference since only a power as low as the detectable limit of a photodetector is needed.

Fig. 7 shows the experimental configuration and explanation of the frequency grids generation in the corresponding regions. This scheme based on the fact that in the sum/difference-frequency generation, frequency stabilization of the output radiation can be carried out by controlling only one participating laser [37], i.e., the conventional error signal with respect to a frequency reference obtained by using the generated light and is fed back to one of the two fundamental lasers. This scheme can work well as long as two conditions are satisfied. One is the locking range should be sufficiently large for compensating the frequency drift of the free-running laser. The other one is the power fluctuation, which results from the phase mismatch in the nonlinear conversion when the frequency of the fundamental laser varies, should be sufficiently low. In our case, a typical value of the frequency drift of a temperature-stabilized diode laser was observed to be less than 10 MHz/min, which implies that only several μA of the injection current is needed to compensate the frequency drift. Such a value corresponds to a power variation ratio smaller than 10^{-4} . Estimation of the influence of the phase mismatch (3) shows the power ratio due to fluctuation is less than 10^{-5} .

For frequency stabilization, the generated green light passed through a 15 cm-long I_2 cell which contains natural iodine. A

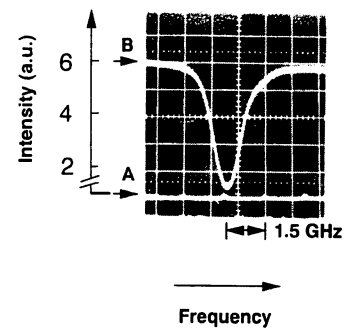


Fig. 8. Molecular iodine absorption resonance at 536.32 nm as the injection current of the 0.82 μm fundamental laser was swept (trace B). Trace A is the transmission resonances of a confocal optical resonator with a FSR of 1.5 GHz for calibrating the width of the absorption resonance.

Si-photodetector was used to detect the transmitted power of the green beam. The maximum power of the sum-frequency generation was 0.6 μW.

Among the obtained linear absorption resonances of I_2 spreading over a ~100 GHz span which were observed when the 0.82 μm fundamental laser was swept by changing the injection current, the largest absorption was measured to be 65%. Fig. 8 shows one resonance used as the reference at 536.32 nm (560 THz) with an absorption of 55%, and the used intensity of the green light was 15 μW/cm². This absorption resonance had a width of 1.2 GHz when the cell was cooled to 6°C, for which a water-circulator was used. The observed width was much wider than the temperature-determined Doppler width (~400 MHz) because of the hyperfine splitting inside the observed resonance.

The phase-sensitive technique was employed to stabilize the 0.82 μm laser while the 1.54 μm laser was in free-running. The temperature of the cell was maintained at 6°C. The modulation with a frequency of 5 kHz was applied to the injection current of the 0.82 μm laser, and the error signal from a lock-in amplifier was fed back to the current source. The frequency drifts were attributed mainly to the thermal and current fluctuations of the two diode lasers. The residual frequency fluctuations were estimated to be within ±0.5 MHz from the error signal, implying a normalized frequency stability better than 10^{-9} at the optical frequency of 560 THz. This result shows that the use of a broad resonance maintains a wide locking range for frequency stabilization and is preferable in frequency stabilization by controlling one fundamental laser in the three-wave frequency mixing.

C. Optical Frequency Comb Generation at 0.8 μm wavelength

As described above, the fine frequency grids are indispensable for providing frequency references by which frequency-tunable output can be obtained through optical phase locking in a wide frequency span. Highly efficient optical frequency comb generators using both optical and microwave resonant cavities at 1.5 and 1.06 μm have been developed [13], [38]. Here, we present the result of an OFC generator at 0.8 μm for the first time.

The principle of the OFC generation in this paper is based on the enhanced generation of modulation sidebands of an EO modulator. The microwave driven EO modulator is installed

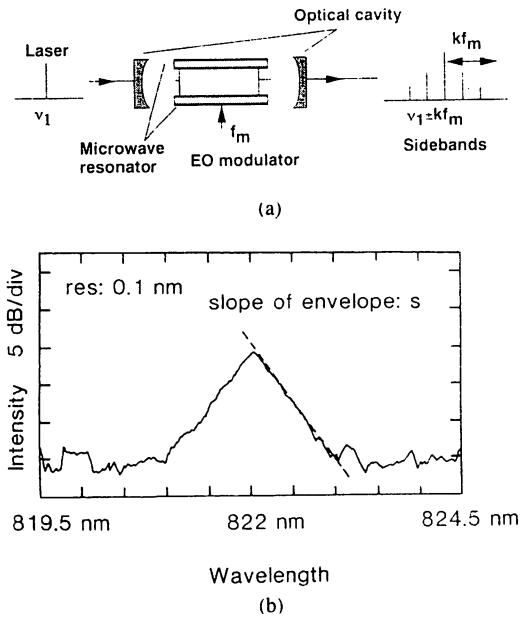


Fig. 9. (a) Optical frequency comb generator. (b) Envelope of sidebands generated from the optical frequency comb generator at $0.82 \mu\text{m}$, which was observed by an optical spectrum analyzer. The slope, s , of the envelope in the log-scale was 32 dB/THz .

into an optical FP type resonator. When the modulation frequency is equal to the free spectral range of the optical cavity or its integer times, the generated sidebands which space with a frequency interval of the modulation frequency are largely enhanced. The EO crystal is inserted into a microwave waveguide to make the modulation efficiency as high as possible, referring to Fig. 9(a). For matching the phase velocities of both microwave and optical wave inside the EO crystal, the size of the waveguide must be carefully chosen. Fig. 9(b) shows the observed modulation-induced extended field profile using an optical analyzer. Because the modulation frequency was less than the resolution of the optical analyzer, the observed profile gives the envelope of all generated sidebands. As the power of each sideband can be expressed as [13]

$$P_k = P_0 \exp(-\pi(\nu - \nu_0)/mFf_m), \quad (31)$$

where P_0 is the power coefficient determined by modulation and cavity efficiency, k is the order of sideband, m is the modulation index, F is the finesse of the FP cavity, f_m is the modulation frequency, ν_0 is the central frequency (carrier) and ν is the frequency of the k th sideband. Therefore the slope of the envelope in a log-scale is

$$s = \pm\pi/mFf_m. \quad (32)$$

It should be noted that the modulation index m is proportional to the optical carrier frequency when the other conditions are fixed, thus one can expect a higher modulation efficiency at shorter wavelength region. In our experiment, a $1 \text{ mm} \times 1.25 \text{ mm} \times 20 \text{ mm}$ lithium niobate with antireflection coating ($\sim 0.1\%$ around $0.8 \mu\text{m}$) was installed inside a $1 \text{ mm} \times 15 \text{ mm} \times 25 \text{ mm}$ microwave guide, and the c -axis (z axis) of the crystal was perpendicular to the light propagation direction (y axis). The driven microwave power was $\sim 8 \text{ W}$. Then they were put in an symmetrical optical cavity

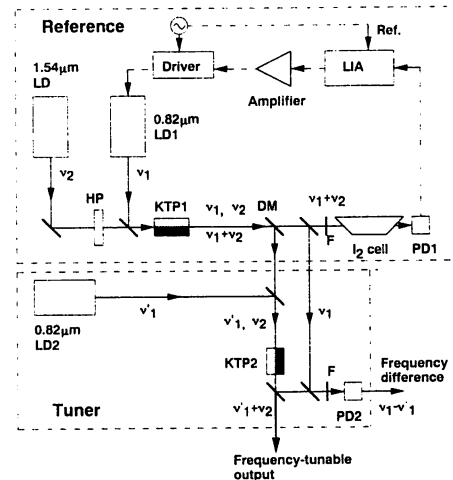


Fig. 10. System configuration of the precision frequency-tunable light source using sum-frequency generation. LD1, 2, two $0.82 \mu\text{m}$ single-mode diode lasers; KTP1, 2, potassium titanyl phosphate crystals with lengths of 10 mm and 5 mm, respectively; LIA, lock-in amplifier; F, filter with high transmission only for green light; PD1, Si-photodiode; PD2, avalanche photodiode; HP, half-wave plate at $1.5 \mu\text{m}$.

(reflectivity of mirrors is $\sim 99.3\%$ from 760 to 860 nm). The measured transmission efficiency and finesse of cavity were 2% and 175, respectively. The observed slope of the envelope of the modulation generated sidebands, as shown in Fig. 9(b), was 32 dB/THz at the modulation frequency of 5.9 GHz when the input laser power was 2 mW. Although the center frequencies of sidebands are determined by microwave synthesizer, because of the high microwave power, cooling and temperature stabilizing are necessary to maintain the stable output powers of sidebands and linewidths of the sidebands. It is reasonable to estimate, based on the used incident laser power and the obtained slope of the envelope, that this frequency comb has a usable two-sided span wider than 4 THz since a single-mode laser with a power of 100 mW at this wavelength region is available.

V. SYSTEM DEMONSTRATION AND DISCUSSION

A. Frequency-Tunable System Using Sum-Frequency Generation

Fig. 10 shows a compact frequency-tunable system in the green region, which is composed of two parts: the reference part and the tuner part.

In the reference part, the sum-frequency was generated in a first KTP (KTP1) and stabilized by using the absorption line of I_2 as described previously. Two fundamental lasers were at $0.82 \mu\text{m}$ (LD1) and $1.54 \mu\text{m}$ (LD). The obtained frequency stability of 10^{-9} was limited mainly by the present low output power from the frequency conversion. However, the resettability of this system is better than the conventional tunable systems in which frequency stabilization is performed using external optical resonators as the frequency reference.

The tuner part of the system was arranged by using another $0.82 \mu\text{m}$ diode laser (SDL5311) (LD2) and a second 5 mm long KTP crystal (KTP2). A dichroic mirror with high transmission at $0.82 \mu\text{m}$ and high reflectivity at $1.54 \mu\text{m}$ was used

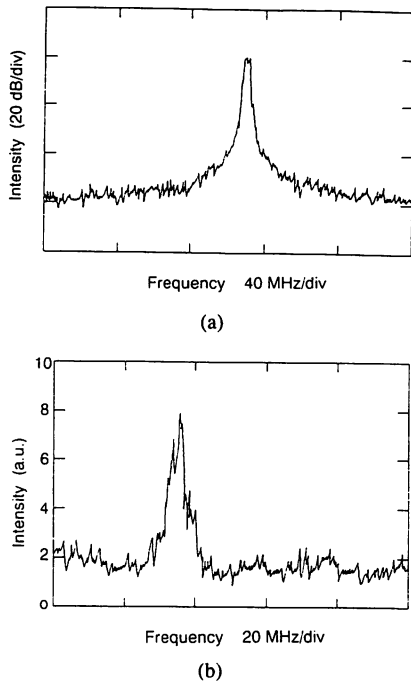


Fig. 11. (a) Heterodyne beat signal between two $0.82 \mu\text{m}$ fundamental lasers. The 3-dB width of this beat signal shows the linewidth of each diode laser was less than 2 MHz. (b) Heterodyne beat signal between two green lights to show the feasible detection in the case of weak power. Each power of both green lights was less than 70 nW. The broadening width of this beat signal compared with (a) was attributed to the linewidth of the $1.5 \mu\text{m}$ DFB laser which was estimated to be less than 4 MHz.

to separate the $1.54 \mu\text{m}$ laser component for the second sum-frequency generation with LD2 in KTP2. When the tuner was in operation, the frequency-tunable green light was obtained by changing the temperature and injection current of LD2. To monitor the frequency difference between the reference and the frequency-tunable output, the heterodyne signal between the two $0.82 \mu\text{m}$ diode lasers was detected using an avalanche photodiode. Fig. 11(a) and (b) show the measured heterodyne beat signals between two $0.82 \mu\text{m}$ lasers, and between two green lights, respectively. The scanning time constant was 50 ms.

The tunable frequency range of ~ 5 THz was obtained by changing the temperatures of LD2. It is equivalent to employ the $1.5 \mu\text{m}$ DFB laser in the tuner, that ensures a continuous frequency tuning with a range of ~ 1 THz. This value prevails over the conventional tunable systems whose continuous frequency tuning ranges are less than 50 GHz, and shows the potential of the utilization of DFB lasers. Further extension of the continuous tuning range can be expected by using grating extended cavity lasers.

The frequency difference measurement was limited by the responsible bandwidth of the conventional photodetector which is at most several tens gigahertz. The precision frequency tuning range up to 1 THz can be expected by using the OFC in Section IV-C. In this case, the heterodyne beat signal is obtained between LD2 and a sideband of LD1. The experimental result in Fig. 11(b) shows the feasibility of the optical heterodyne phase locking in the case that a signal power is very low since each power of both beams for the

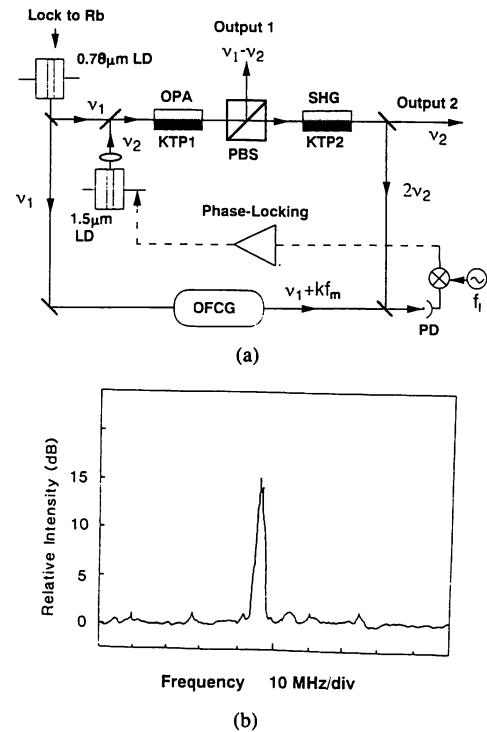


Fig. 12. (a) Proposed scheme of OPA-based precision frequency-tunable source in the $1.5 \mu\text{m}$ region using an optical frequency comb and the phase locking technique. OPA, optical parametric amplifier; SHG, second-harmonic generation; OFCG, optical frequency comb generator; PBS, polarized beam splitter; f_m , modulation frequency of OFCG; k , order of the sideband; f_i , frequency of the tunable microwave local oscillator; PD, photodetector. (b) Heterodyne beat signal between the second-harmonic generation and a Ti:sapphire laser.

obtained beat signal was less than 70 nW. The observed linewidth of the beat-note also confirmed our theoretical analysis (23) in Section II-C.

B. Frequency-Tunable Scheme Using Difference-Frequency Generation

This scheme is proposed for providing highly coherent light in near-infrared region especially the 1.5 – $2.0 \mu\text{m}$ which is of great interest for near-future optical coherent communications [24]. It is constructed basically by the OPA arrangement described in Section III, as shown in Fig. 12(a). A high-power $0.78 \mu\text{m}$ laser (ν_1) is used for pump a first KTP crystal (KTP1). Potassium or rubidium can be chosen as the precision frequency reference. In the case of using potassium, the frequency stability of 10^{-10} was shown in this work. The output of the $1.5 \mu\text{m}$ diode laser (ν_2) is incident to a second KTP crystal (KTP2) to generate the second-harmonic wave [32]. A portion of the $0.78 \mu\text{m}$ laser power passes through an OFC generator to generate sidebands with frequencies $\nu_1 \pm kf_m$, where k is the sideband order and f_m is the modulation frequency of the OFC generator. The beat signal between the doubled-frequency $2\nu_2$ of the $1.5 \mu\text{m}$ laser and one of the sidebands $\nu_1 \pm kf_m$ from the OFC generator is used for heterodyne phase-locking of the $1.5 \mu\text{m}$ laser. Thus, the OPA output (output 1) at the difference frequency $\nu_1 - \nu_2$ between the two lasers, and the output 2 in Fig. 12(a) from the $1.5 \mu\text{m}$ laser itself ν_2 construct two frequency-tunable outputs.

For the purpose of the frequency linking between two kinds of lasers, one preliminary result to show the feasibility of the proposed system, as shown in Fig. 12(b), is a heterodyne beat signal obtained by heterodyning the second-harmonic wave of the 1.54 μm laser and a Ti:sapphire laser. A 15 dB signal-to-noise ratio was obtained when the second-harmonic generation power was lower than 10 nW generated by a 10 mW DFB laser and another laser power was ~ 1 mW. Because the measurement of the frequency difference in this system is carried out by heterodyning the second-harmonic wave of the 1.5 μm laser and the sideband of the 0.78 μm laser, we also performed the second-harmonic generation with an external buildup cavity for enhancing the fundamental power [22]. The result shows that the enhancement factor for the fundamental power was 12 and the second-harmonic output power was 1.0 μW when the fundamental power was only 8 mW, by which the signal-to-noise ratio of the heterodyne beat is expected to be improved [39].

Comparing with the system which uses an OPO to construct an optical synthesizer [40], the advantage of the present scheme is that the continuous tuning range can be realized by employing a diode laser through OPA rather than the doubly resonant OPO (DRO) to circumvent the discrete oscillation which is due to the cluster effect in DRO, and the inherent low system stability.

C. Discussion

Based on the consideration shown in Fig. 1, a wide-band frequency-tunable system should be constructed by combining the similar systems demonstrated above in different frequency regions. We have carried out nonlinear frequency conversions using diode lasers and generation of frequency reference grids in a frequency span from 170 THz (1.7 μm) to 600 THz (0.5 μm). For realizing the intended 1-Petahertz system, this span should be extended to 900 THz (0.3 μm) by adding InGaAlP visible diode lasers [41] and InGaAsP lasers at 1.3 μm region to the present system. There is no principle limitation on the frequency region for continuous tuning in our system, however, several technical challenges remain for realization of the optical frequency sweep generator (OFSG). For example, extension of continuous frequency tuning range of diode lasers to 10 THz by using grating-extended cavity scheme; and computer-controlled synchronization of frequency tuning and heterodyne phase locking. In addition, OFC generators in different frequency regions should be also realized. In fact, the thin films coated on the facets of the EO modulator and the crystal itself bring dispersion and losses which limits the effective span of sidebands.

Enhancement of the output power of the OFSG is another key task, because the frequency stability of the frequency reference grids depends on the signal-to-noise ratio of the used atomic or molecular absorption spectrum. The present results show that the single-pass nonlinear frequency conversion in a bulk crystal only offers an output power of μW by using single-mode diode lasers. Since nonlinear crystals with high coefficients are limited, enhancement of fundamental power or intensity is considered as the main approach. Buildup

cavities for the fundamental waves have been shown as effective ways in spite of a relatively complicated configuration. Furthermore, more efficient devices such as waveguide quasi-phase-matching devices are promising options [4]. We have also employed interferometric coherent addition method to add coherently the powers of multiple diode lasers [25], such an approach for enhancing the fundamental power is effective when a critical power is needed and the power from the single item is not sufficient, e.g., to provide a pump source for an OPO.

VI. SUMMARY

Generation of frequency-tunable light and frequency reference grids in a wide frequency span has been performed for the proposed OFSG. Frequency tuning and noise characteristics in nonlinear frequency conversions have been discussed. By using AlGaAs, InGaAsP lasers and their frequency conversions in type II angle phase-matching KTP, highly coherent frequency-tunable outputs have been obtained from 600 THz (0.5 μm) to 170 THz (1.7 μm). Use of the DFB lasers ensures the continuous tuning with a frequency range as wide as 1 THz. ^{41}K and I_2 absorption resonances have been employed as frequency references for stabilizing the frequencies of lasers and the generated light with the frequency stability of 10^{-9} – 10^{-10} . Optical frequency comb generation has been realized at the 0.8 μm wavelength with a two-sided sidebands span of 4 THz. These results show that both coarse and fine frequency reference grids have been generated in a wide frequency span. We have also demonstrated and proposed specific sum/difference-generation based frequency-tunable systems. By making use of diode lasers and the developed techniques, the optical frequency sweep generator will replace, in the near future, the present bulky tunable laser systems to satisfy the requirement of the highly coherent and widely tunable characteristics in precision measurements, high resolution spectroscopy, quantum optics and other investigations of the fundamental physics.

ACKNOWLEDGMENT

The authors would like to thank Dr. M. Okai of Hitachi Corp. for helpful discussions on DFB lasers, and Dr. A. M. Akulshin of Lebedev Physical Institute, Russia, for his comments and cooperation.

REFERENCES

- [1] J. Hall, "Frequency stabilized lasers: A parochial review," *SPIE Proc.*, vol. 1837, pp. 2–15, 1992.
- [2] M. Zhu and J. Hall, "Stabilization of optical phase/frequency of a laser system: application to a commercial dye laser with an external stabilizer," *J. Opt. Soc. Am. B*, vol. 10, pp. 802–816, 1993.
- [3] D. Lee and N. C. Wong, "Stabilization and tuning of a doubly resonant optical parametric oscillator," *J. Opt. Soc. Am. B*, vol. 10, pp. 1659–1667, 1993.
- [4] M. L. Bortz, M. A. Arbore, and M. M. Fejer, "Quasi-phasematched optical parametric oscillation between 1.4–1.7 μm in LiNbO_3 waveguide." *CLEO'94*, postdeadline paper vol. CPD13-1, pp. 29–30, 1994.
- [5] M. Ohtsu, *Highly Coherent Semiconductor Lasers*. Boston: Artech House, Inc., ch. 2–5, 1992.
- [6] C. E. Wieman and Leo Hollberg, "Using diode lasers for atomic physics," *Rev. Sci. Instrum.*, vol. 62, pp. 1–20, 1991.

- [7] C. H. Shin and M. Ohtsu, "Stable semiconductor laser with a 7 Hz linewidth by an optical-electrical double-feedback technique," *Opt. Lett.*, vol. 15, pp. 1455-1457, 1990.
- [8] ———, "Heterodyne optical phase-locked loop by confocal Fabry-Perot cavity coupled AlGaAs lasers," *IEEE Photon. Technol. Lett.*, vol. 2, pp. 297-299, 1990.
- [9] U. Gliese, T. N. Nielsen, M. Bruun, E. L. Christensen, K. E. Stubkjar, S. Lindgren, and B. Broberg, "A wideband heterodyne optical phase locked loop for generation of 3-18 GHz microwave carriers," *IEEE Photon. Technol. Lett.*, vol. 4, pp. 936-938, 1992.
- [10] M. Okai, T. Tsuchiya, K. Uomi, N. Chinone, and T. Harada, "Corrugation-pitch-modulated MQW-DFB laser with narrow spectral linewidth (170 kHz)," *IEEE Photon. Technol. Lett.*, vol. 2, pp. 529-530, 1990.
- [11] A. T. Schremer and C. L. Tang, "External-cavity semiconductor laser with 1000 GHz continuous piezoelectric tuning range," *IEEE Photon. Technol. Lett.*, vol. 2, pp. 3-5, 1990.
- [12] F. Favre and D. Le Guen, "82 nm of continuous tunability for an external cavity semiconductor laser," *Electron. Lett.*, vol. 27, pp. 183-184, 1991.
- [13] M. Kurogi, K. Nakagawa, and M. Ohtsu, "Wide-span optical frequency comb generator for accurate optical frequency difference measurement," *IEEE J. Quantum Electron.*, vol. 29, pp. 2693-2701, 1993.
- [14] N. C. Wong, "Optical frequency counting from UV to the near IR," *Opt. Lett.*, vol. 17, pp. 1155-1157, 1992.
- [15] K. Asaumi and T. Orito, "Phase Matching of the second harmonic generation in KTiOPO₄," *Optronics* (in Japanese), vol. 5, pp. 193-198, 1992.
- [16] J. D. Bierlein and H. Vanherzeele, "Potassium titanyl phosphate: properties and new applications," *J. Opt. Soc. Am. B*, vol. 6, pp. 622-633, 1989.
- [17] J.-C. Baumert, F. M. Schellenberg, W. Lenth, W. P. Risk, and G. C. Bjorklund, "Generation of blue cw coherent radiation by sum frequency mixing in KTiOPO₄," *Appl. Phys. Lett.*, vol. 51, pp. 2192-2194, 1987.
- [18] K. Kato, "Temperature insensitive SHG at 0.5321 μm in KTP," *IEEE J. Quantum Electron.*, vol. 28, pp. 1974-1976, 1992.
- [19] W. Wiechmann, S. Kubota, T. Fukui, and H. Masuda, "Refractive-index temperature derivatives of potassium titanyl phosphate," *Opt. Lett.*, vol. 18, pp. 1208-1210, 1993.
- [20] M. Ohtsu, H. Fukada, T. Tako, and H. Tsuchida, "Estimation of the ultimate frequency stability of semiconductor lasers," *Jpn. J. Appl. Phys.*, vol. 22, pp. 1157-1166, 1983.
- [21] M. Ohtsu and S. Kotajima, "Derivation of the spectral width of a 0.8 μm AlGaAs laser considering $1/f$ noise," *Jpn. J. Appl. Phys.*, vol. 23, pp. 760-764, 1984.
- [22] W. Wang, K. Nakagawa, Y. Toda, and M. Ohtsu, "1.5 μm diode laser-based nonlinear frequency conversions by using potassium titanyl phosphate," *Appl. Phys. Lett.*, vol. 61, pp. 1886-1888, 1992.
- [23] W. Wang and M. Ohtsu, "Frequency-tunable sum- and difference-frequency generation by using two diode lasers in a KTP crystal," *Opt. Commun.*, vol. 102, pp. 304-308, 1993.
- [24] ———, "Continuous-wave optical parametric amplifier that uses a diode laser for a wideband coherent frequency sweep generator," *Opt. Lett.*, vol. 18, pp. 876-878, 1993.
- [25] W. Wang, K. Nakagawa, S. Sayama, and M. Ohtsu, "Coherent addition of injection-locked high-power AlGaAs diode lasers," *Opt. Lett.*, vol. 17, pp. 1593-1595, 1992.
- [26] G. D. Boyd and D. A. Kleinman, "Parametric interaction of focused Gaussian light beams," *J. Appl. Phys.*, vol. 39, pp. 3597-3639, 1968.
- [27] D. J. Kuizenga, "Optimum focusing conditions for parametric gain in crystals with double refraction," *Appl. Phys. Lett.*, vol. 21, pp. 570-572, 1972.
- [28] F. Zernike and J. E. Midwinter, *Applied Nonlinear Optics*. New York: Wiley, ch. 2-3, 5-7, 1973.
- [29] S. E. Harris, "Tunable optical parametric oscillators," *Proc. IEEE*, vol. 57, pp. 2096-2113, 1969.
- [30] W. Demtröder, "Laser Spectroscopy. Springer Series in Chemical Physics, Springer-Verlag, Berlin, 1988, ch. 6, pp. 313-316.
- [31] O. Acef, J. J. Zondy, M. Abed, D. G. Rovera, A. Clairon, Ph. Laurent, Y. Millieroux, and P. Juncar, "A CO₂ to visible optical frequency synthesis chain: accurate measurement of the 473 THz HeNe/₁₂ laser," *Opt. Commun.*, vol. 97, pp. 29-34, 1993.
- [32] W. Wang, A. M. Akulshin, and M. Ohtsu, "Pump-probe spectroscopy in potassium using an AlGaAs laser and the second-harmonic generation of an InGaAsP laser for frequency stabilization and linking," *IEEE Photon. Technol. Lett.*, vol. 6, pp. 95-97, 1994.
- [33] E. Arimondo, M. Inguscio, and P. Violino, "Experimental determinations of the hyperfine structure in the alkali atoms," *Rev. Mod. Phys.*, vol. 49, pp. 31-75, 1977.
- [34] W. Wang and M. Ohtsu, "Iodine absorption line-stabilized frequency-tunable green light using sum-frequency generation of diode lasers," *Jpn. J. Appl. Phys.*, vol. 33, pt. 1, pp. 1648-1651, 1994.
- [35] A. Arie, S. Schiller, E. K. Gustafson, and R. L. Byer, "Absolute frequency stabilization of diode-laser-pumped Nd:YAG lasers to hyperfine transitions in molecular iodine," *Opt. Lett.*, vol. 17, pp. 1204-1206, 1992.
- [36] Arie and R. L. Byer, "Frequency stabilization of the 1064 nm Nd:YAG laser to Doppler-broadened lines of iodine," *Appl. Opt.*, vol. 32, pp. 7382-7386, 1993.
- [37] Kasuhiko Sugiyama and Jun Yoda, "Stabilization of sum or difference frequency by controlling one of the fundamental lasers of frequency mixing," *Opt. Commun.*, vol. 95, pp. 77-80, 1993.
- [38] N. C. Wong, D. Lee, and L. R. Brothers, "Optical frequency counting based on parametric downconversion," *Tech. Dig., In. Symp. Atomic Frequency Standards and Coherent Quantum Electron.*, Nara, Japan, Aug. 18-20, 1993, pp. 14-17.
- [39] H. R. Telle, D. Meschede, and T. W. Hänsch, "Realization of a new concept for visible frequency division: Phase locking of harmonic and sum frequencies," *Opt. Lett.*, vol. 15, pp. 532-534, 1990.
- [40] N. C. Wong, "Optical frequency division using an optical parametric oscillator," *Opt. Lett.*, vol. 15, pp. 1129-1131, 1990.
- [41] M. J. Brinkman, A. Romanovsky, and D. A. G. Deacon, "Efficient ultraviolet generation from red laser diodes," *CLEO'94*, postdeadline paper CPD18-1, pp. 40-42, 1994.



Weizhi Wang was born in Kashi, China, on September 19, 1963. He received the B.E. and M.E. degrees in optical engineering from Zhejiang University, China, in 1984 and 1987, respectively, and received the Ph.D. degree in quantum optoelectronics in 1994 from the Tokyo Institute of Technology.

From 1987 to 1990, he worked on single crystal fiber laser at Zhejiang University. From 1990 to 1991, he joined Tokyo Institute of Technology as a visiting scholar and worked on solid-state waveguide laser and cavity quantum electrodynamics effect in microcavity. Since 1994, he joined Edward L. Ginzton Laboratory of Stanford University, Stanford, CA, as a post doctoral fellow. His main interests are highly coherent diode laser based tunable light sources and frequency control, and their applications in nonlinear frequency conversions and laser spectroscopy, and nonlinear waveguide devices.

Dr. Wang is a member of Optical Society of China and Applied Physics Society of Japan.



Motoichi Ohtsu (M'88-SM'90) was born in Kanagawa, Japan, on Oct. 5, 1950. He received the B.E., M.E., and Dr.E. degrees in electronics engineering from Tokyo Institute of Technology, Tokyo, Japan, in 1973, 1975, and 1978, respectively.

In 1978, he was appointed as a Research Associate, and in 1982 he became Associate Professor at Tokyo Institute of Technology. From 1986 to 1987, while on leave from Tokyo Institute of Technology, he joined the Crawford Hill Laboratory, AT&T Bell Laboratories, Holmdel, NJ. In 1991, he became a

Professor at Tokyo Institute of Technology. Since April 1993 onwards, he has been concurrently the leader of "PHOTON CONTROL" project of Kanagawa Academy of Science and Technology, Kanagawa, Japan. His main fields of interest are photon scanning tunneling microscopy, its application to nano-scale photonics and quantum optics, and laser frequency control.

Dr. Ohtsu has written over 130 papers, received a number of patents. He is the author and coauthor of thirteen books including two in English, entitled *Highly Coherent Semiconductor Lasers* (Boston, MA: Artech House, 1992) and *Coherent Quantum Optics And Technology* (Dordrecht: Kluwer Academic, 1993). He has been a tutorial lecturer of the SPIE and OSA. He has been awarded eight prizes from academic institutions including Issac Koga Gold Medal of URSI in 1984, Japan IBM Science Award in 1988, and two awards of the Japan Society of Applied Physics in 1982 and 1990. He is a member of the Institute of Electronics, Information and Communication Engineering of Japan, the Institute of Electrical Engineering of Japan, the Japan Society of Applied Physics, and the Optical Society of America.

High-frequency-stability laser at 1.5 μm using Doppler-free molecular lines

M. de Labachellerie,* K. Nakagawa, Y. Awaji, and M. Ohtsu

Graduate School at Nagatsuta, Tokyo Institute of Technology, 4259 Nagatsuta-cho, Midori-ku, Yokohama 227, Japan

Received September 19, 1994

An extended-cavity 1.5- μm semiconductor laser was frequency stabilized to saturated-absorption lines of acetylene. Its long-term frequency stability is of the order of 10^{-12} , with a reproducibility of ± 10 kHz. Using the lines of C_2H_2 or HCN, we could obtain such a high stability with the same laser at many wavelengths covering the 1.51–1.56- μm band.

Laser frequency metrology generally requires absolute optical frequency standards at the wavelength of interest. Such standards already are established with a high accuracy in the visible or the mid-infrared region.^{1,2} However, despite their usefulness for applications such as frequency-division-multiplexed optical communication,³ high-quality frequency references in the 1–2- μm wavelength band are missing. Although several studies have been devoted to the frequency stabilization of 1.5- μm laser diodes to molecular lines^{4–6} or to absorption lines from atomic excited states,^{7–9} the measured stabilities were of the order of 10^{-10} , which is difficult to improve with wide Doppler-broadened lines. Moreover, even in the case of sub-Doppler atomic lines, no literature describing significant improvement has been published to our knowledge. On the other hand, the recent detection of sub-Doppler molecular lines is likely to give much better stabilities as well as access to many reference lines covering the 1.51–1.56- μm region.¹⁰ To demonstrate this possibility, we have constructed extended-cavity semiconductor lasers (ECSL's) that can be locked to tens of acetylene lines, and in this Letter we report their locked-frequency stability, which is, to our knowledge, the best recorded at this wavelength.

A careful ECSL design is essential to yield a tunable though stable source whose free-running mode stability does not limit the performances of the stabilized source. The laser structure (see Fig. 1) uses a 1.55- μm laser diode, antireflection coated on the output facet and coupled through an aspheric lens to a 1200-line/mm Littrow-mounted grating. This grating is rotated with a screw and a piezoelectric translator (PZT#1), and its rotation axis is set to a position at which mode hops can be suppressed during wavelength tuning.¹¹ To obtain high mechanical stability, we glued the intracavity lens to a mechanical support. The slight movement of the lens during hardening of the glue was corrected with an antireflection-coated wedged plate inserted between the lens and the grating. The whole ECSL (4-cm laser cavity length) is mounted upon a temperature-stabilized brass plate; its output beam was extracted from the rear facet of the diode and

collimated by another aspheric lens. The initial 120-nm tuning range was then limited by the mechanical supports to 1.51–1.58 μm after they were glued. For a 100-mA diode current, a single-mode output of more than 5 mW power could be obtained through this entire range. The fine frequency tuning was provided by a PZT#1-driven grating rotation over 2.3 GHz and by laser diode current adjustments with a 20-MHz/mA sensitivity.

The mode-hop suppression proved effective; we never observed any mode hop when the ECSL was electrically tuned with the PZT#1. Under free-running conditions without acoustic isolation, the laser linewidth was ~ 1 MHz for a few seconds of observation time. The Fabry–Perot (FP) cavity containing the gas was a hemispherical-type 20-cm-long cavity mounted on a silica tube. The input mirror was plane, and the output mirror, which was mounted upon another piezoelectric translator (PZT#2), had a 1-m radius of curvature. Both had a reflectivity of 99%, which provides a 2.2-MHz mea-

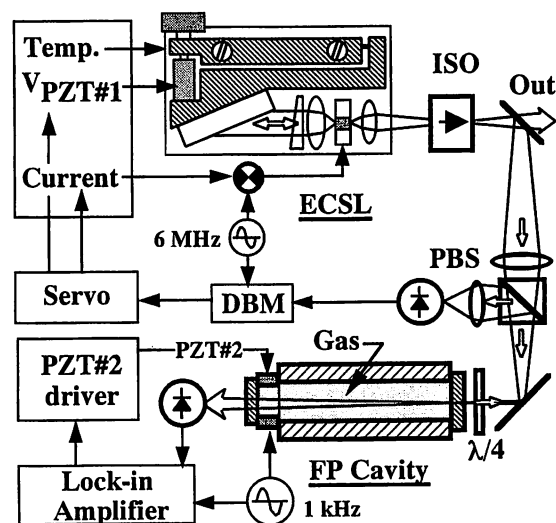


Fig. 1. Experimental setup showing the ECSL structure, the FP cavity, and the arrangement for long-term stabilization. ISO, 60-dB isolator; PBS, polarizing beam splitter; $\lambda/4$, quarter-wave plate; DBM, double-balanced mixer.

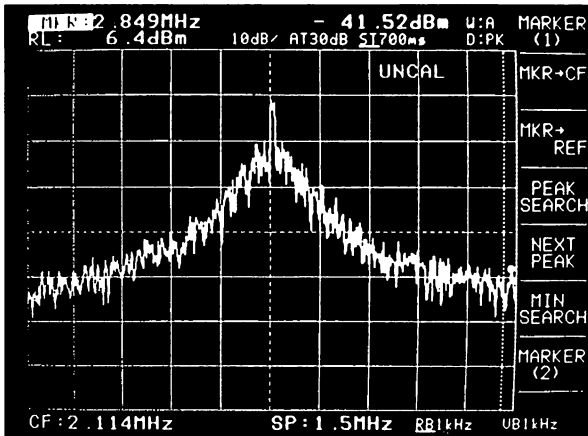


Fig. 2. Beat spectrum between two ECSLs locked independently on two FP cavities.

sured FP-cavity linewidth. The laser frequency was locked to the FP resonance by the Pound–Drever¹² method: 6-MHz FM sidebands were added to the laser frequency through a modulation of the laser current, and the beam reflected from the cavity was used to detect the error signal. With a single integrator, the correction signal was fed back to the laser diode current driver for fast frequency corrections and simultaneously fed back to PZT#1 for large frequency corrections, through another integration stage. The current-loop bandwidth was ~ 30 kHz, while the PZT#1 loop bandwidth did not exceed 50 Hz. Because of the high mechanical stability and mode-hop suppression of the free-running laser, the frequency locking to the FP resonance could be continuously maintained for more than 8 h.

We made two identical sets and analyzed their frequency beat to measure frequency fluctuations. A beat spectrum between two lasers locked to independent FP cavities is shown in Fig. 2. The optical energy is concentrated in a narrow peak at the top, which results from the frequency correction by the feedback loop, and a pedestal that corresponds with uncorrected frequency fluctuations is also visible. Therefore the 30-dB linewidth of the free-running laser is ~ 30 kHz, but when the laser is locked a rather large fraction of the optical power is concentrated in a narrow peak whose linewidth could not be measured because of the rather large FP resonance frequency drift. While the laser frequency stayed locked to the FP resonance, it could be swept on ~ 1 GHz with the PZT#2, which allowed it to reach the gas saturated-absorption line. The FP cavity was filled with acetylene at a pressure of 10–20 mTorr, and we recorded the saturated absorption of the gas by detecting the FP transmitted beam power. With this setup, many narrow sub-Doppler lines were recorded with both ^{12}C and ^{13}C isotopes of acetylene or with HCN. Even weak lines at the edge of the absorption band gave a saturated signal with a high signal-to-noise ratio. For instance, the line $P(27)$ of $^{13}\text{C}_2\text{H}_2$ at 1550.18 nm [Fig. 3(b)] and the line $P(27)$ of HCN at 1556.37 nm were successfully saturated. Therefore, with the same ECSL, high frequency stability can be obtained easily, for each gas, on more than 40 narrow absolute-

frequency references that cover a 30–40-nm band. The saturation-dip linewidth was of the order of 1 MHz, which is roughly half of that obtained in our previous experiments.¹⁰ Because the FP spatial mode diameter was doubled, we concluded that the saturated linewidth probably is limited mainly by the transit-time broadening. Moreover, the linewidth broadening that is due to saturation becomes comparatively larger, and for a very low power (400- μW laser power at FP input), we observed a 700-kHz saturated-absorption linewidth.

To lock the laser frequency to the saturated-absorption absolute reference, we dithered the FP frequency at 1 kHz by modulating the voltage of PZT#2, and a lock-in amplifier provided the error signal, which was fed back directly to PZT#2. The effective bandwidth of the feedback loop was ~ 10 Hz. For frequency-stability measurements we have chosen the $P(13)$ line of $^{12}\text{C}_2\text{H}_2$, whose error signal is shown in Fig. 3(a). One laser was frequency shifted by 80 MHz by means of an acousto-optic modulator to yield a nonzero beat frequency that was recorded with a frequency counter and a microcomputer (Fig. 4). The origin of the frequency scale corresponds to the frequency of the acousto-optic modulator, and the maximum frequency fluctuations were of the order of 2 kHz. The corresponding Allan variance measurements for each laser are shown in Fig. 5. The short-term stability of the laser locked to the FP cavity only is better than the long-term stability because, in the latter case, frequency noise and frequency modulation are added to PZT#2 through the voltage supply. This noise, however, is corrected by the second loop for longer times, and the relative frequency stability reaches a 10^{-12} floor for an integration time of ~ 1 s. Nevertheless, some drifts are observed for longer times, and they prevent further improvements of stability. These drifts are seen clearly in Fig. 4, in which the periodic feature corresponds to the tem-

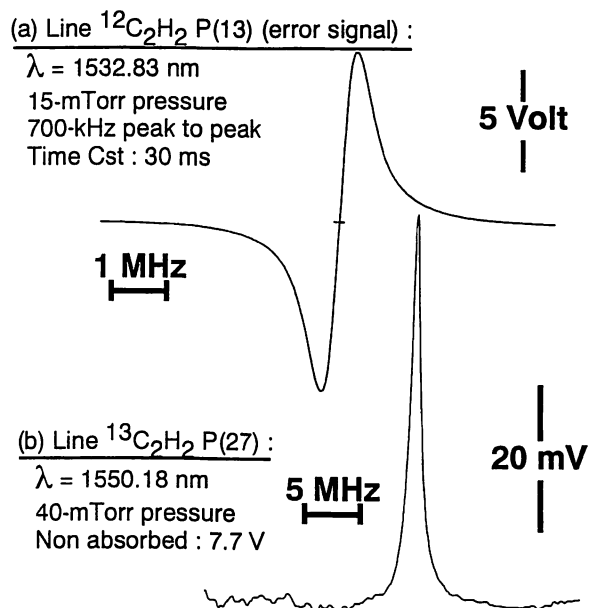


Fig. 3. (a) Derivative of the line that was used for frequency stability measurements. (b) Longest wavelength sub-Doppler line recorded with $^{13}\text{C}_2\text{H}_2$.

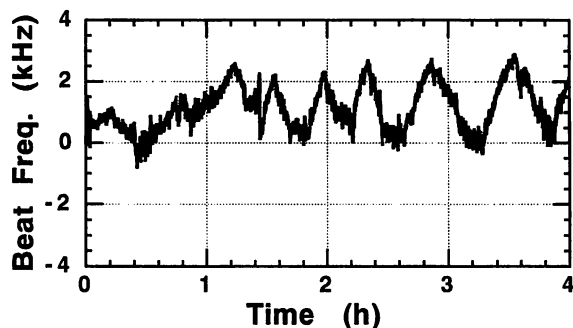


Fig. 4. Beat frequency measurement of two lasers independently stabilized to the $^{12}\text{C}_2\text{H}_2$ $P(13)$ saturation dip.

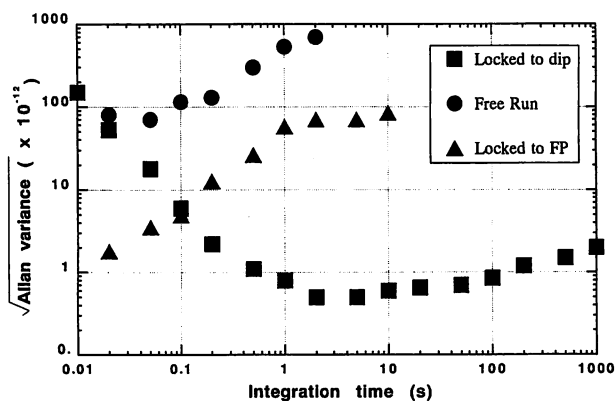


Fig. 5. Laser relative frequency stability versus measurement time.

perature cycles of the room air conditioning. They were found to be directly related to slight offsets in the first feedback loop (laser locking to FP), which depend on beam alignment and may fluctuate with temperature.

The frequency reproducibility is closely related to the following effects: it is ± 2 kHz when one laser is switched off but all adjustments are kept constant, and it increases to ± 10 kHz when all the adjustments are changed. Also, residual cavity effects in the optical path can convert the 6-MHz frequency modulation into a spurious amplitude modulation and lead to temperature-dependent offsets in the first loop. In both cases, the results could be improved further by careful design; a more sophisticated detection method (laser frequency modulation that uses an external electro-optic modulator, for instance) will probably be required if higher stabilities are needed.

In conclusion, we have demonstrated experimentally that, with the use of $1.5\text{-}\mu\text{m}$ molecular lines, it is possible to construct an ECSL system that can be stabilized with a $\approx 10\text{-kHz}$ accuracy and a $\sim 10^{-12}$ frequency stability on tens of regularly spaced absolute frequency references between 1.51 and $1.56\ \mu\text{m}$. Compared with other devices that use atomic lines,⁷⁻⁹ this one is more flexible and still fairly simple. We therefore believe that it is currently the most efficient way to provide frequency references for coherent or multiwavelength optical communications or for high-resolution spectroscopy near $1.5\ \mu\text{m}$.

The authors acknowledge help from H. Sasada for all experiments involving HCN.

*Permanent address, Laboratoire de l'Horloge Atomique, Centre National de la Recherche Scientifique, Bât. 221, Université Paris-Sud, 91405 Orsay, France.

References

1. V. A. Alekseev, M. A. Gubin, and E. D. Protsenko, *Laser Phys.* **1**, 221 (1991).
2. O. Acef, J. J. Zondy, M. Abed, D. G. Rovera, A. H. Gerard, A. Clairon, P. Laurent, Y. Millerieux, and P. Juncar, *Opt. Commun.* **97**, 29 (1993).
3. D. J. E. Knight, P. S. Hansell, H. C. Leeson, G. Duxbury, J. Meldau, and M. Lawrence, *Proc. Soc. Photo-Opt. Instrum. Eng.* **1837**, 106 (1992).
4. M. Labachellerie, C. Latrasse, K. Diomandé, P. Kemssu, and P. Cerez, *IEEE Trans. Instrum. Meas.* **40**, 185 (1991).
5. Y. Sakai, S. Sudo, and T. Ikegami, *IEEE J. Quantum Electron.* **28**, 75 (1992).
6. P. Bertinetto, *Proc. Soc. Photo-Opt. Instrum. Eng.* **1837**, 154 (1992).
7. A. J. Lucero, Y. C. Chung, S. Reilly, and R. W. Tkach, *Opt. Lett.* **16**, 849 (1991).
8. M. Breton, P. Tremblay, N. Cyr, C. Julien, and M. Têtu, *Proc. Soc. Photo-Opt. Instrum. Eng.* **1837**, 134 (1992).
9. S. L. Gilbert, *Proc. Soc. Photo-Opt. Instrum. Eng.* **1837**, 146 (1992).
10. M. de Labachellerie, K. Nakagawa, and M. Ohtsu, *Opt. Lett.* **19**, 840 (1994).
11. P. McNicholl and H. Metcalf, *Appl. Opt.* **24**, 2757 (1985).
12. K. Nakagawa, M. Kourogi, and M. Ohtsu, *Opt. Lett.* **17**, 934 (1992).

A Waveguide-Type Optical-Frequency Comb Generator

T. Saitoh, *Member, IEEE*, M. Kourogi, and M. Ohtsu, *Senior Member, IEEE*

Abstract—A waveguide type optical frequency comb (WG-OFC) generator was developed at 1.56 μm wavelength region by utilizing a waveguide type phase modulator. It was confirmed that the envelope of sideband spectra had a width of 2.7 THz and the slope of the envelope profile was 28 dB/THz. The maximum measurable frequency difference, limited by the shot noise, was estimated to be 3.2 THz.

HIGHLY ACCURATE laser frequency measurement is an indispensable technique for the development of coherent optical communication systems and precise measurements of physical constants. Measurement of absolute frequency for establishing frequency standards requires a measurement of the frequency difference among lasers that are spaced in a span as wide as several terahertz. However, it is not straightforward to measure such a high frequency difference because the response bandwidth of conventional photo-detector (PD) is at the most several ten GHz. Although the response bandwidth of a metal-insulator-metal diode is as wide as 2.5 THz [1], it is not practical because of its short lifetime.

In order to overcome these difficulties, an optical frequency difference measurement system using an optical frequency comb (OFC) generator has been proposed [2]–[7], which is composed of a phase modulator and an optical resonator. Recently, it has been reported that a monolithic OFC generator has generated the modulation sidebands in a span as wide as 6.1 THz with the modulation frequency of 5.9 GHz at 1.5 μm wavelength region [8]. This result implies that about 1 000 modulation sidebands have been generated.

In this letter, we report on a compact waveguide type optical frequency comb (WG-OFC) generator that was fabricated by coating high reflection films on the facets of a Ti:LiNbO₃ waveguide. As compared to the bulky OFC generator, modulation index and modulation frequency were increased so that a span of the generated modulation sidebands could be extended.

Fig. 1 shows a structure of the WG-OFC generator that is composed of two elements, i.e., a phase modulator and an optical resonator, to increase the modulation efficiency. An optical waveguide (Anritsu SC3B01A) working at 1.5 μm wavelength was used as a phase modulator and an optical resonator was formed by coating high reflection films on the

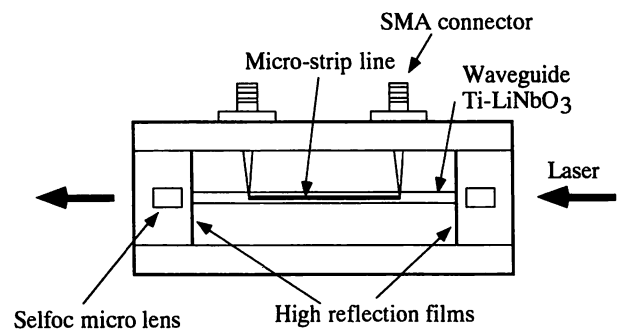


Fig. 1. Schematic explanation of a WG-OFC generator.

two end facets of the waveguide. Their reflectivities were estimated to be higher than 95%. The waveguide was made by diffusing Ti into 40 mm long LiNbO₃. The free spectral range (FSR) and the finesse of the optical resonator were measured to be 1.70 GHz and 12, respectively. A micro-strip line was formed on the upper surface of the waveguide. By feeding the microwave to the microstrip line, the phase of the light is modulated. By controlling a thickness of the micro-strip line, a microwave velocity is matched to velocity of a propagation laser light. This phase modulator is a traveling wave type because only the light co-propagating along the microwave is modulated. Microwave voltage V_π for π radian phase modulation is 7 V.

We have evaluated performances of the WG-OFC generator. A laser light output from a distributed feedback laser diode with the linewidth narrower than 10 MHz was focused onto the waveguide by using two selfoc micro lenses. The output light from the WG-OFC generator was connected to an optical spectrum analyzer for observing the spectral profile of the envelope of the generated modulation sidebands. A microwave signal from a synthesizer was amplified by a traveling wave tube amplifier (TWTA) and was fed to the WG-OFC generator.

Fig. 2 shows the envelope of the modulation sidebands measured by the optical spectrum analyzer with the resolution band width of 0.2 nm (=25 GHz). The modulation frequency was 11.91 GHz, which was 7 times FSR of the optical resonator. The span of the envelope increases with increasing modulation frequency, which is due to the increase of the spacing between the modulation sidebands. However, under the condition of constant microwave power, further increases in modulation frequency increase the transmission loss and velocity mismatching, by which the modulation index and span are decreased. Thus, this WG-OFC generator has its optimum modulation frequency, which was found to be 11.91 GHz, as

Manuscript received August 31, 1994; revised October 14, 1994.

T. Saitoh is with the Kanagawa Academy of Science and Technology, Takatsu-ku, Kawasaki, Kanagawa 213, Japan, and the Anritsu Corporation, Atsugi, Kanagawa 243, Japan.

M. Kourogi and M. Ohtsu are with the Kanagawa Academy of Science and Technology, Takatsu-ku, Kawasaki, Kanagawa 213, Japan, and also with the Interdisciplinary Graduate School of Science and Engineering of the Tokyo Institute of Technology, Midori-ku, Yokohama, Kanagawa 227 Japan.

IEEE Log Number 9407950.

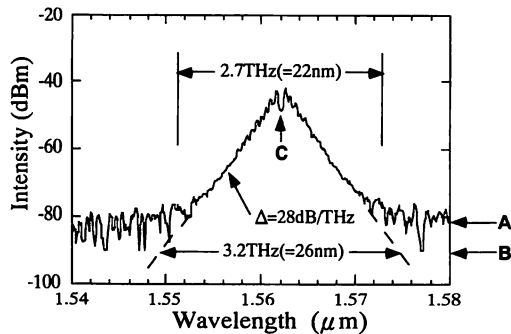


Fig. 2. Envelope of the modulation sidebands measured by an optical spectrum analyzer with the resolution band width of 0.2 nm (=25 GHz). The laser frequency ν_{LD} was tuned to the resonance frequency $\nu_{r,0}$ of the optical resonator. A: Noise level of the optical spectrum analyzer. B: Estimated shot noise level of the heterodyne detection.

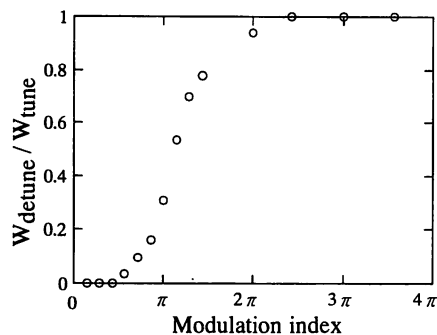


Fig. 3. Calculated result of ratio of W_{detune} , and W_{tune} , where W_{tune} and W_{detune} are the span of envelope of the modulation sidebands when $\nu_{r,0}$ is tuned to ν_{LD} and $\nu_{r,0}$ is detuned to $\nu_{LD} + FSR/2$, respectively.

was described above. By this optimum frequency, the highest microwave power applicable to the device was 3.0 W, by which a modulation index of 3.0π was realized. From Fig. 2, the slope of the envelope was found to be 28 dB/THz. Measured frequency span of the envelope, limited by the noise level of the optical spectrum analyzer (the level A in Fig. 3), was 2.7 THz.

If lasers having linewidths of 100 kHz and 1 mW power are used along with the present WG-OFC generator for optical frequency difference measurement by heterodyne detection, the shot noise limited power of modulation sideband is estimated to be -90 dBm from (6) in [4]. This value is shown as level B in Fig. 2, and from the level B, the maximum measurable frequency difference was estimated to be 3.2 THz.

It has been confirmed by [5] that the highest modulation efficiency is realized when the resonance frequency $\nu_{r,0}$ of the optical resonator is tuned to the laser frequency ν_{LD} . Thus, one may consider that the precise length and the temperature control of the device is required to maintain this frequency tuning. Fig. 3 shows a calculated result of ratio of W_{detune} and W_{tune} , where W_{tune} and W_{detune} are the span of envelope of the modulation sidebands when $\nu_{r,0}$ is tuned to ν_{LD} and $\nu_{r,0}$ is detuned to $\nu_{LD} + FSR/2$, respectively. It is seen from this figure that the span of envelope of the sidebands is not influenced very much by the tuning condition at the

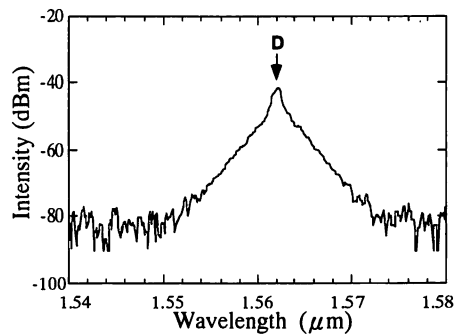
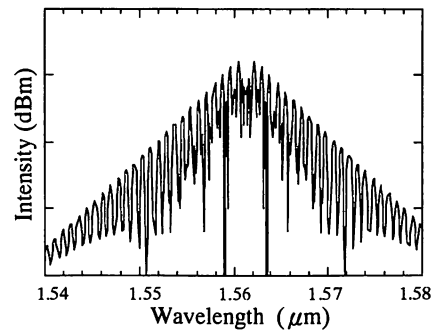
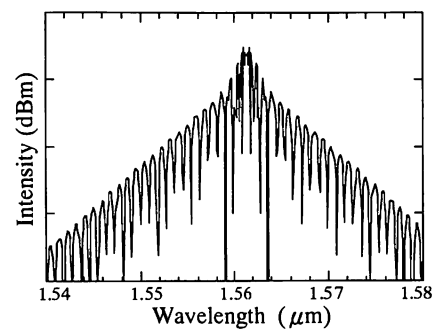


Fig. 4. Envelope of the modulation sidebands, where $\nu_{r,0} = \nu_{LD} + FSR/2$.



(a)



(b)

Fig. 5. Calculated results of the modulation sidebands. (a) $\nu_{r,0} = \nu_{LD}$. (b) $\nu_{r,0} = \nu_{LD} + FSR/2$.

modulation index above 2π , because W_{detune} is nearly equal to W_{tune} . The WG-OFC generator can generate the modulation sidebands efficiently even without the precise length and temperature control because the modulation index is as large as 3π . Fig. 4 shows the envelope of the modulation sidebands for condition of $\nu_{r,0} = \nu_{LD} + FSR/2$. Comparing Fig. 2 and this figure, it is confirmed that the spans of the envelopes in both figures are equal with each other even though the curve in Fig. 2 has a dip [C] in the center while that of Fig. 4 has a bump [D]. This fact is confirmed based on the Fourier transformation of the time varying output intensity of the WG-OFC generator to a frequency domain. The results of this Fourier transform are shown in Fig. 5, where (a) $\nu_{r,0} = \nu_{LD}$ (b) $\nu_{r,0} = \nu_{LD} + FSR/2$. Good agreements are seen between the envelopes of the curves of Fig. 5 (a) and (b) with those of Figs. 2 and 4, including the dip and bump at the tops.

In summary, a WG-OFC generator was developed by using a waveguide type Ti:LiNbO₃ optical phase modulator. It was confirmed that the envelope of the modulation sidebands extended to a span as wide as 2.7 THz around the wavelength of 1.56 μm and the slope of envelope profile of the modulation sidebands envelope slope was 28 dB/THz. The maximum measurable frequency difference, limited by shot noise, was estimated to be 3.2 THz. One of the advantageous properties of this method was that the resonator length did not have to be controlled precisely because the modulation index was larger than 2π . Due to this large tolerance in a resonator length control, the WG-OFC generator was operated without an active temperature control.

REFERENCES

- [1] R. E. Drullinger, K. M. Evenson, D. A. Jennings, F. R. Petersen, J. C. Bergquist, and L. Burkins, "2.5-THz frequency difference measurement in the visible using metal insulator-metal diodes," *Appl. Phys. Lett.*, vol. 42, pp. 137–138, 1983.
- [2] M. Kourogi, N. Nakagawa, C. H. Shin, M. Teshima, and M. Ohtsu, "Accurate frequency measurement system for 1.5 μm wavelength laser diodes," in *Proc. Conf. Lasers and Electro-Opt.*, Baltimore, May 1991, paper number CThR57.
- [3] M. Kourogi and M. Ohtsu, "A highly accurate frequency counting system for 1.5 μm wavelength semiconductor lasers," in *Proc. SPIE Frequency-Stabilized Lasers and Their Application*, Boston, Nov. 1992, vol. 1837, pp. 205–215.
- [4] M. Kourogi, K. Nakagawa, and M. Ohtsu, "A wide-span optical frequency comb generator for a highly accurate laser frequency measurement," in *Proc. Int. Quantum Electron. Conf.*, Vienna, June 1992, paper number TuM5.
- [5] M. Kourogi, K. Nakagawa, and M. Ohtsu, "Wide-span optical frequency comb generator for accurate optical frequency difference measurement," *IEEE J. Quantum Electron.*, vol. 29, no. 10, pp. 2693–2701, 1993.
- [6] N. C. Wong, D. Lee, and L. R. Brothers, "Optical frequency counting based on parametric oscillation," in *Tech. Dig. Int. Symp. on Atomic Frequency Standards and Coherent Quantum Electronics*, Aug. 1993, pp. 14–17.
- [7] L. R. Brothers, D. Lee, and N. C. Wong, "Terahertz optical frequency comb generation and phase locking an optical parametric oscillator at 665 GHz," in *Optics Lett.*, vol. 19, no. 4, pp. 245–247, 1994.
- [8] M. Kourogi, T. Enami, and M. Ohtsu, "A monolithic optical frequency comb generator," *IEEE Photon. Technol. Lett.*, vol. 6, no. 2, pp. 214–217, 1994.

Highly precise 1-THz optical frequency-difference measurement of 1.5- μm molecular absorption lines

K. Nakagawa, M. de Labachellerie,* Y. Awaji, M. Kourogi, T. Enami, and M. Ohtsu

Interdisciplinary Graduate School of Science and Engineering, Tokyo Institute of Technology,
4259, Nagatsuta-cho, Midori-ku, Yokohama 227, Japan

Received July 22, 1994

We demonstrate precise optical frequency-difference measurement of acetylene (C_2H_2) absorption lines at 1.5 μm . With an optical comb generator, the frequency difference between two lasers locked to saturated absorption dips of C_2H_2 rovibrational lines can be measured up to ~ 1 THz with a precision of better than 100 kHz. A precise frequency table of C_2H_2 1.5- μm lines will be useful for frequency-division-multiplexed optical communication systems and high-resolution molecular spectroscopy.

Accurate optical frequency standards are required in atomic and molecular spectroscopy, optical communications, and metrology. Several optical frequency standards have been established with an accuracy of 10^{-11} – 10^{-13} in the infrared and visible regions.^{1,2} However, because the laser frequency of interest is often far from such accurate standards, we need many frequency standards distributed over wide frequency regions. In the mid-infrared region, many CO_2 laser frequencies have been used as precise secondary references,³ whereas the iodine atlas has been generally used as a rather coarse reference in the visible and near-infrared regions.⁴ In the 1.5- μm region we recently demonstrated the feasibility of a reference frequency atlas with a 10^{-9} accuracy,⁵ using saturated absorption lines of many molecular transitions such as C_2H_2 (Ref. 6) and HCN.⁷ Such frequency references would be especially useful for frequency-division-multiplexed optical communication systems,⁸ provided that their relative frequencies are measured with a high accuracy. In this Letter we demonstrate a highly precise relative frequency measurement of C_2H_2 absorption lines at 1.5 μm by using our recently developed optical frequency comb generator.⁹ This device efficiently generates high-order modulation sidebands; thus we can measure optical frequency differences up to more than 1 THz with the precision of the microwave modulation frequency. We also discuss the possibility of absolute frequency measurement of these lines.

The experimental setup is shown in Fig. 1. We use two antireflection-coated 1.5- μm diode lasers in a grating feedback extended cavity configuration.¹⁰ Their tuning range is roughly from 1.50 to 1.58 μm , and their output power is typically 5 mW in that tuning range. The laser output is divided by a beam splitter: one part is introduced into the external Fabry–Perot buildup cavity absorption cell filled with C_2H_2 gas, and the other is used for the heterodyne frequency measurement. With an external buildup cavity with a finesse of ~ 300 , the saturation spectroscopy of the weak $\nu_1 + \nu_3$ overtone band of C_2H_2 can be obtained with only 1 mW of diode laser power.⁵ Using current modulation, we lock the laser frequency to the buildup cavity resonance frequency,⁵ which is stabilized to the saturation dip of C_2H_2 ab-

sorption by modulation of the Fabry–Perot cavity length. The typical linewidth of the saturation dip is 1–2 MHz under a C_2H_2 pressure of ~ 15 mTorr. We prepared two identical stabilized laser systems. The output from one laser is introduced into an optical frequency comb generator.⁹ This device is made of a LiNbO_3 electro-optic phase modulator, which is also used as a monolithic optical cavity with a finesse of 250.¹¹ This LiNbO_3 crystal is installed inside a microwave waveguide cavity driven by a 5.87-GHz modulation frequency, which is twice the free spectral range of the optical cavity. When more than 5 W of microwave power is applied to the modulator, modulation sidebands spread over several terahertz around the input carrier frequency.¹¹

The transmitted beam from the LiNbO_3 modulator is mixed with the beam of laser 2 and detected by a fast InGaAs P-I-N photodiode. As the modulation frequency is ~ 5.87 GHz, the bandwidth required for beat detection is ~ 3 GHz. Typical beat signals between laser 2 and high-order sidebands of laser 1 are shown in Fig. 2. We measured frequency differences between various combinations of two rovibration lines of the $^{12}\text{C}_2\text{H}_2$ $\nu_1 + \nu_3$ band. As an example of adjacent rotational lines, the beat note for the case of $P(7)$ and $P(8)$ is shown in Fig. 2(a). The frequency dif-

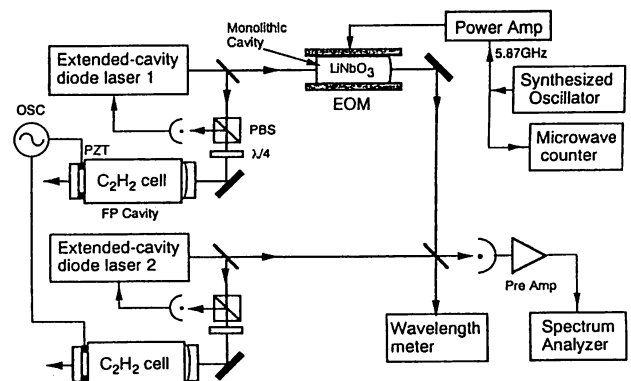


Fig. 1. Schematic diagram of the optical frequency-difference measurement. EOM, electro-optic modulator; PBS, polarization beam splitter; $\lambda/4$, quarter-wave plate; PZT, piezoelectric transducer; OSC, oscillator; FP, Fabry–Perot.

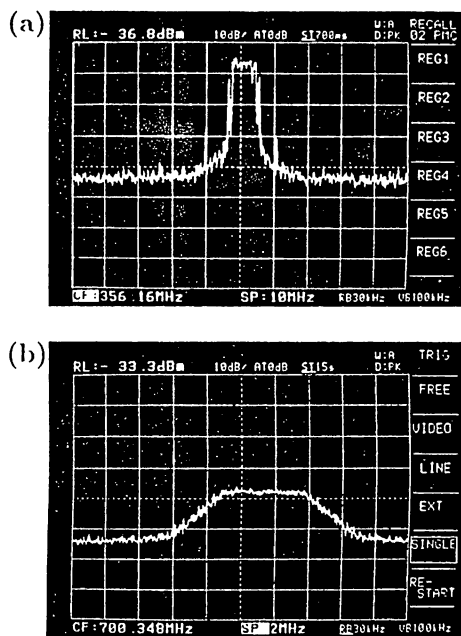


Fig. 2. Heterodyne beat spectra between the m th-order sideband of laser 1 and laser 2. (a) Two lasers locked to $P(7)$ and $P(8)$ transitions ($m = 13$, $\Delta \approx 76$ GHz). The horizontal frequency scale is 1 MHz/division. (b) Two lasers locked to $P(9)$ and $P(21)$ ($m = 167$, $\Delta \approx 979$ GHz). The frequency scale is 0.2 MHz/division. In both cases, the vertical scale is 10 dB/division and the resolution bandwidth is 30 kHz.

ference between these lines is ~ 76 GHz. The beat signal was 40 dB higher than the noise level. This noise level was determined mainly by the laser intensity noise, which was slightly higher than the shot noise at high frequencies. As an example of the maximum frequency difference that we have measured, the beat note for the case of $P(9)$ and $P(21)$ is shown in Fig. 2(b). It corresponds to a frequency difference of 979 GHz, nearly 1 THz. It is, to our knowledge, the highest frequency difference measured between two lasers in the 1.5- μm wavelength region. In the visible region, a 2.5-THz frequency difference was compared with a 119- μm far-infrared laser frequency by metal-insulator-metal diodes.¹² In our case the frequency difference can be directly compared with a microwave frequency. The signal-to-noise ratio was still higher than 10 dB for a frequency difference of ~ 1 THz. Further optimization of the beat detection will allow for the measurement of frequency differences higher than 1 THz.

To stabilize the laser frequency to the saturation dip, it was necessary to dither slightly the Fabry-Perot cavity length using its piezoelectric transducer, which caused a broadening of the beat linewidth of ~ 1 MHz [Fig. 2(a)]. When both lasers were synchronously modulated with carefully adjusted amplitude and phase, this beat linewidth was reduced to approximately 300–500 kHz [Fig. 2(b)]. Residual linewidth is probably due to the frequency jitter of lasers during the beat measurement time of 15 s. From this beat signal we can determine the center frequency of the beat with a precision of 30–50 kHz.

The frequency difference between the lasers is given by

$$\Delta = \nu_2 - \nu_1 = m \times \nu_m \pm \nu_B \quad (\text{for } \nu_2 > \nu_1), \quad (1)$$

where ν_1 and ν_2 are the frequencies of lasers 1 and 2, respectively, m is the order of the sideband, ν_m is the modulation frequency, and ν_B is the beat frequency. The sideband order m was easily determined from the wavelength measurement of these laser by use of a Michelson-type wavelength meter, which had an accuracy of a few parts in 10^6 . We determine the sign in the above equation by slightly changing the modulation frequency ν_m . If the beat frequency increases as the modulation frequency increases, the sign in Eq. (1) is minus, and vice versa.

In the beat frequency measurement, the frequency scale of the spectrum analyzer was carefully calibrated by a microwave counter. The error in the frequency scale of the spectrum analyzer was negligibly small compared with the measurement resolution of several tens of kilohertz. More crucial is the accuracy of the modulation frequency because this error should be multiplied by the sideband order m . Thus, the modulation frequency, which was provided by the synthesized oscillator, was also calibrated by a microwave counter. The typical frequency error of the synthesized oscillator was measured to be 1.6×10^{-7} , corresponding to an error of 160 kHz for a 1-THz optical frequency difference. The reproducibility of lasers locked on the saturation dip of C_2H_2 is ~ 10 kHz, and it can be reduced to less than a few kilohertz if the feedback control is optimized. Therefore, in future experiments, we will have to use a microwave frequency reference with an accuracy of 10^{-8} to permit 10-kHz accuracy for a 1-THz optical frequency difference. The remaining problem is a pressure shift of absorption lines. It has not been well examined yet for this C_2H_2 1.5- μm band, and it was only coarsely estimated to be less than 200 kHz/Torr from the Doppler-broadened spectrum.¹³ Although this shift can be neglected for the present precision, it should be carefully evaluated for higher precision in future measurements.

The relative frequency atlas of the rovibrational lines from $P(3)$ to $P(21)$ of the C_2H_2 $\nu_1 + \nu_3$ band was derived from all the frequency-difference measurements, and the frequency differences between adjacent lines are listed in Table 1. It should be noted that these frequencies were determined from both the direct measurements of difference between adjacent lines and the measurements of difference between widely separated lines up to ~ 1 THz. Thus, the frequency differences between any two lines in the above range can be derived from Table 1 within a precision of ~ 100 kHz. We fitted these relative frequencies of rovibrational lines by using the following expression for the $P(J)$ transition:

$$\nu = \nu_0 - (B' + B'')J + (B' - B'' + D'' - D')J^2 + 2(D'' + D')J^3 + (D'' - D')J^4, \quad (2)$$

where ν_0 is the band origin, J is the rotational quantum number, B'' and D'' are the molecular constants in the lower state, and B' and D' are those in the upper state. The molecular constants determined by a polynomial fit are given in Table 2. The residuals between the observed and calculated difference

Table 1. Frequency Differences between Rovibrational Lines of the $\nu_1 + \nu_3$ Band of C_2H_2

	Frequency (MHz)	$o-c$ (MHz) ^a
$P(3)-P(4)$	72 857.60	0.13
$P(4)-P(5)$	73 624.26	-0.17
$P(5)-P(6)$	74 389.78	-0.08
$P(6)-P(7)$	75 154.07	-0.13
$P(7)-P(8)$	75 917.43	0.14
$P(8)-P(9)$	76 679.09	-0.02
$P(9)-P(10)$	77 439.65	0.00
$P(10)-P(11)$	78 198.99	0.11
$P(11)-P(12)$	78 956.77	-0.04
$P(12)-P(13)$	79 713.23	-0.17
$P(13)-P(14)$	80 468.73	0.09
$P(14)-P(15)$	81 222.46	-0.07
$P(15)-P(16)$	81 975.06	0.02
$P(16)-P(17)$	82 726.11	-0.05
$P(17)-P(18)$	83 475.88	0.01
$P(18)-P(19)$	84 224.09	-0.07
$P(19)-P(20)$	84 970.98	-0.04
$P(20)-P(21)$	85 716.42	0.00

^aThe residuals between the observed and calculated frequencies.

Table 2. Molecular Constants of the $\nu_1 + \nu_3$ Band of C_2H_2 in Inverse Centimeters^a

Constants	Present Work	Previous Work	Ref.
B'	1.163781(4)	1.163755(4)	6
$D' \times 10^6$	1.594(15)	1.5924(34)	6
B''	1.176649(4)	1.17664632(18)	14
$D'' \times 10^6$	1.615(15)	1.62710(27)	14

^aNumbers in parentheses are one standard error in units of the last digit in the parameters.

frequencies ($o-c$) are given in Table 1. These residuals are all within ± 0.2 MHz or the same order of measurement precision. For a comparison, previously reported values of these constants are also given in Table 2. The upper-state and lower-state constants were determined from the measurements of the $\nu_1 + \nu_3$ band⁶ and the far-infrared vibrational bands,¹⁴ respectively. When we calculate the residuals by using the previous constants, they become much larger than a megahertz. As a result of the lack of a number of data, especially R -branch data, the individual constants were not so precisely determined from the present fit. The B' and B'' constants reasonably agree with the previous values; however, the discrepancy is rather large for the D'' constant. Because the measurement precision is high enough, we will be able to determine these constants with higher accuracy if we increase the number of data. Extensive experiments and detailed analysis are now in progress.

The absolute frequencies of these C_2H_2 lines have not to our knowledge been measured until now. With a Michelson-type wavemeter, the wavelength and frequency of the C_2H_2 $P(9)$ line were reported to be $1.530371 \mu\text{m}$ and $195\,895\,330(50)$ MHz, respectively.⁸ However, the frequency uncertainty of 50 MHz is rather large compared with our 100-kHz precision for relative frequencies. One candidate for a more-precise frequency reference is the two-photon absorption of Rb at $0.778 \mu\text{m}$, whose absolute fre-

quency was recently determined with an accuracy of approximately 10^{-11} .¹⁵ Half of this Rb frequency is within 2 GHz of the $P(27)$ transition of the HCN $1.5\text{-}\mu\text{m}$ band⁷; therefore we should be able to determine the absolute frequency of this HCN line at $1.556 \mu\text{m}$ with nearly the same accuracy as for the Rb line. Using this HCN line as an absolute reference, we will be able to determine the absolute frequencies of all other HCN and C_2H_2 lines in the $1.5\text{-}\mu\text{m}$ region.

In conclusion, we have demonstrated relative frequency measurements of $1.5\text{-}\mu\text{m}$ narrow absorption lines of C_2H_2 up to 1 THz with a 100-kHz precision by using an optical frequency comb generator. Such a technique should be a powerful tool for a high-resolution molecular spectroscopy to obtain precise molecular constants or structures and will provide a table of more than 100 optical frequency references with a 10^{-9} accuracy between 1.51 and $1.56 \mu\text{m}$, using C_2H_2 and HCN saturated-absorption lines.

The authors thank H. Sasada of Keio University for useful discussion.

M. Kourogi and M. Ohtsu are also with the Kanagawa Academy of Science and Technology, Kanagawa, Japan.

*Permanent address, Laboratoire de l'Horloge Atomique, Centre National de la Recherche Scientifique, Bât. 221, Université de Paris-Sud, 91405 Orsay, France.

References

- V. A. Alekseev, M. A. Gubin, and E. D. Protsenko, *Laser Phys.* **1**, 221 (1991).
- O. Acef, J. J. Zondy, M. Abed, D. G. Rovera, A. H. Gerard, A. Clairon, Ph. Laurent, Y. Millierieux, and P. Juncar, *Opt. Commun.* **97**, 29 (1993).
- F. R. Petersen, D. G. McDonald, J. D. Cupp, and B. L. Danielson, *Phys. Rev. Lett.* **31**, 573 (1973).
- S. Gerstenkorn and P. Luc, *Atlas du Spectre d'Absorption de la Molecule d'Iode* (Editions du CNRS, Paris, 1978).
- M. de Labachellerie, K. Nakagawa, and M. Ohtsu, *Opt. Lett.* **19**, 840 (1994).
- S. Kinugawa and H. Sasada, *Jpn. J. Appl. Phys.* **29**, 611 (1990).
- H. Sasada and K. Yamada, *Appl. Opt.* **29**, 3535 (1990).
- D. J. E. Knight, P. S. Hansell, H. C. Leeson, G. Duxbury, J. Meldau, and M. Lawrence, *Proc. Soc. Photo-Opt. Instrum. Eng.* **1837**, 106 (1992).
- M. Kourogi, K. Nakagawa, and M. Ohtsu, *IEEE J. Quantum Electron.* **29**, 2693 (1993).
- M. de Labachellerie, C. Latrasse, K. Diomandé, P. Kemssu, and P. Cerez, *IEEE Trans. Instrum. Meas.* **40**, 185 (1991).
- M. Kourogi, T. Enami, and M. Ohtsu, *IEEE Photon. Technol. Lett.* **6**, 214 (1994).
- R. E. Drullinger, K. M. Evenson, D. A. Jennings, F. R. Petersen, J. C. Bergquist, and L. Burkins, *Appl. Phys. Lett.* **42**, 137 (1983).
- Y. Sakai, S. Sudo, and T. Ikegami, *IEEE J. Quantum Electron.* **28**, 75 (1992).
- Y. Kabbadj, M. Herman, G. Di Lonardo, and L. Fusina, *J. Mol. Spectrosc.* **150**, 535 (1991).
- F. Nez, F. Biraben, R. Felder, and Y. Millierieux, *Opt. Commun.* **102**, 432 (1993).

Frequency Chain Towards the Ca Intercombination Line Based on Laser Diodes: First Step

A. M. Akulshin^{*}, K. Nakagawa, M. Ohtsu

Interdisciplinary Graduate School of Science and Technology, Tokyo Institute of Technology, 4259, Nagatsuta-cho, Midori-ku, Yokohama 227, Japan (Fax: +81-45/921-1204)

Received 19 November 1993/Accepted 9 December 1993

Abstract. Stable, narrow linewidth operation of red and 1.3 μm free-running laser diodes with external gratings in non-Littrow geometry is demonstrated. The resonance of the saturated fluorescence of an atomic beam with a contrast of 25% and a linewidth of 400 ± 50 kHz of the Ca intercombination line $4^1S_0-4^3P_1$ ($\lambda=657$ nm) is shown. A high-power (110 mW) single-mode external cavity laser diode at 1.3 μm is used for second-harmonic generation in a KTP crystal. The beat signal (signal to noise ratio about 25 dB) of 10 nW second-harmonic radiation at 1.3 μm and the radiation of a laser diode in the visible spectrum, as a step to realize a frequency chain, is observed.

PACS: 42.60, 32.30, 43.65

The intercombination line of laser cooled Ca vapor sample is one of the promising candidates for a frequency standard in the optical region [1]. However, even though the recoil splitting of the ^{40}Ca intercombination line was resolved many years ago and several experiments of dye-laser frequency stabilization to the ^{40}Ca line were reported [2, 3], as far as we know, accurate measurements of frequency stability using two independent laser systems have not been carried out to date. In order to estimate the stability, accuracy and reproducibility of an optical standard, the comparison with an independent laser and direct measurements of the optical frequency are required. The frequency chain from the ^{40}Ca reference at 657 nm to a Cs atomic clock is being developed in several laboratories [4] and a new scheme of the frequency chain from the Ca line to the microwave region based on Laser Diodes (LDs) only has been proposed recently [5].

A number of experiments on nonlinear spectroscopy of the intercombination transitions of Ca, Ba and Sr [6–10] have been carried out by using highly coherent LDs. It is clear now that LDs can be used to develop a portable frequency/wavelength standard in optics.

^{*} Permanent address: P. N. Lebedev Physics Institute, Leninsky pr. 53, 1179224 Moscow, Russia (Fax: +7-095/135-7880; +7-095/334-0610)

The elaboration of highly coherent LDs in the visible and at 1.3 μm suitable for a frequency chain is the main purpose of this work. We present here also the results of preliminary experiments on nonlinear spectroscopy of the Ca line at 657 nm using a LD in the visible and the observation of the beat signal between this laser and the second harmonic of a 1314 nm LD as a step to realize a frequency chain towards the Ca intercombination line.

1 Laser Diode with External Cavity

High spectral resolution demands narrow laser linewidth, precise frequency tunability and good long-term stability. There are a lot of techniques to improve the spectral characteristics of LDs. Their advantages and peculiarities have been discussed elsewhere [6]. A method of the weak optical feedback from an external high- Q Fabry-Perot cavity is not very effective for LDs in the visible because frequency-noise reduction is limited by strong enhancement of relaxation oscillations [10]. Therefore, the extended-cavity technique using an AntiReflection (AR) coated LD and a dispersive element in the extended cavity was applied.

For LD linewidth narrowing by this technique both high efficiency and high resolution of the dispersive element are desirable. A holographic grating of total internal reflection with high diffraction efficiency ($\approx 70\%$) and selectivity (3200 lines/mm) is convenient for the External Cavity Laser Diode (ECLD), especially in the case of two-facet-emitting LDs [7]. However, with a commercial LD emitting light in one direction we have to utilize the zeroth order of the grating as the output beam which is rather weak due to the high efficiency of the holographic grating. Beside of that, the direction of the output zeroth-order reflection from a grating in Littrow configuration depends on the laser wavelength, which complicates the alignment of the experimental setup. That is why we prefer another optical scheme of an external cavity with a conventional grating [11].

The scheme of the ECLD is shown in Fig. 1. The external dispersive cavity consisted of the LD, a coupling objective lens ($\text{NA}=0.65$), a PZT-driven 100% dielectric mirror, an

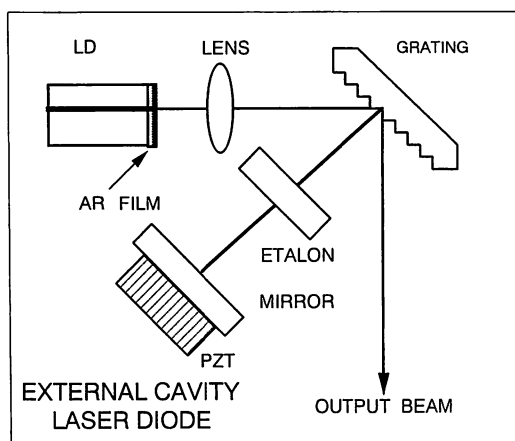


Fig. 1. Optical scheme of the external cavity laser diode. The zeroth-order reflection from the grating is used as output

etalon (10 mm thick, 30% reflectivity) and a grating (1300 lines/mm, blazed for 700 nm). All the elements of the laser cavity were mounted on an invar base plate isolated from the optical table with a damping spacer. The $p-n$ junction of the LD was parallel to the grooves of the grating. The angle of incidence on the grating was 55° . Under these conditions the efficiency of the first order of the grating was measured to be 30%. A servo system was used to stabilize the temperature of the LD close to 14°C .

The external cavity was constructed with a commercial InGaAlP laser diode (TOLD 9220). It is well-known that an AR coating of the LD facet is necessary for efficient linewidth narrowing of LDs in the visible. It is difficult to provide strong coupling with an external cavity without AR coating and, therefore, the typical laser linewidth is a few MHz in this case [8, 10]. It is insufficient for high-resolution spectroscopy. So, the LD output facet was coated with a HfO_2 AR film. The laser threshold currents before and after AR coating were 48 mA and 58 mA, respectively. The AR-coated LD operated in the multi-longitudinal mode regime (Fig. 2, curve a). Under selective optical feedback the threshold current was reduced to 45 mA. The ECLD spectrum was single mode from the threshold up to 62 mA. The maximum power of the zeroth-order output beam was 2.5 mW. The suppression of the nondominant modes was greater than 30 dB (Fig. 2, curve b). As compared with a

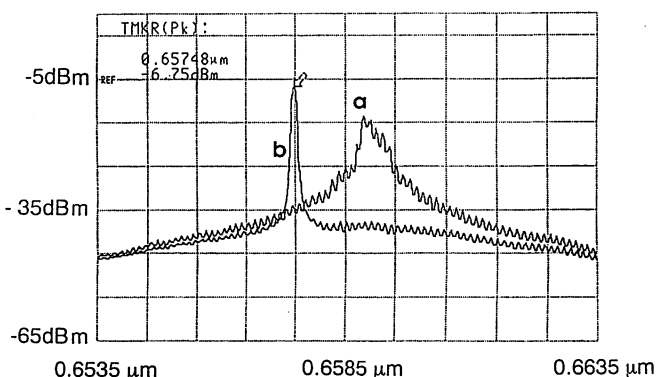


Fig. 2. Longitudinal mode spectra of the antireflection-coated LD. (a) with no optical feedback; (b) with selective optical feedback

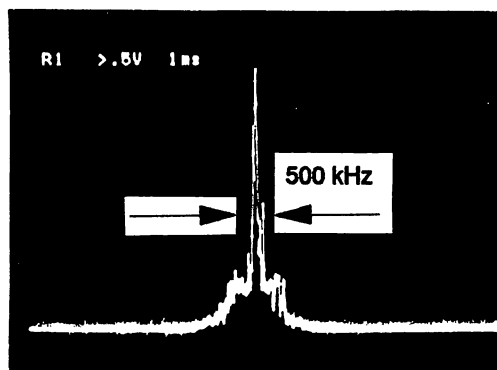


Fig. 3. Transmission resonance of the high- Q Fabry-Perot cavity. The side bands are due to the frequency modulation of the ECLD at 250 kHz

Littrow configuration, the folded scheme of the external cavity has the following advantages.

- The direction of the output beam is kept stable while the frequency tuning is accomplished by rotation of the output mirror.
- It is possible to find a proper relationship between the diffraction efficiency of the grating and its selectivity by variation of the angle of incidence.
- The spectral selectivity is higher due to double reflection from the grating.

Frequency fine tuning in the range of approximately 1 GHz was provided by changing the voltage applied to the PZT on which the output mirror was mounted. Stable single-mode operation was easily obtained for cavity lengths within 5 cm to 20 cm. A Fabry-Perot supercavity was used to monitor the spectrum. It was a PZT-tunable planospherical (1 m curvature radius) cavity with high reflection ($R \approx 0.9999$) mirrors and an invar spacer ($L = 10$ cm). The cavity linewidth was estimated to be 100 kHz. The Fabry-Perot cavity was placed inside a chamber to reduce the disturbances produced by vibration and acoustic noise.

To reduce the influence of acoustic noise the ECLD was placed inside an acoustically insulated box. The random frequency drift was reduced from 15 MHz/min to 1–2 MHz/min in this way. The linewidth of the free-running ECLD was estimated to be less than 100 kHz by using the supercavity (Fig. 3). The frequency-noise measurement made with a low finesse cavity as a discriminator showed approximately the same value of the laser linewidth (35 kHz). Further linewidth reduction can be obtained by frequency stabilization to a resonance of a stable optical cavity using an electrical feedback method [12].

2 Nonlinear Spectroscopy of the Ca Intercombination Line

The experiment on nonlinear spectroscopy of the intercombination line $4^1S_0-4^3P_1$ of ^{40}Ca ($\lambda = 657$ nm) using an ECLD was carried out with an atomic beam. The characteristics of the Ca atomic beam apparatus have been described else-

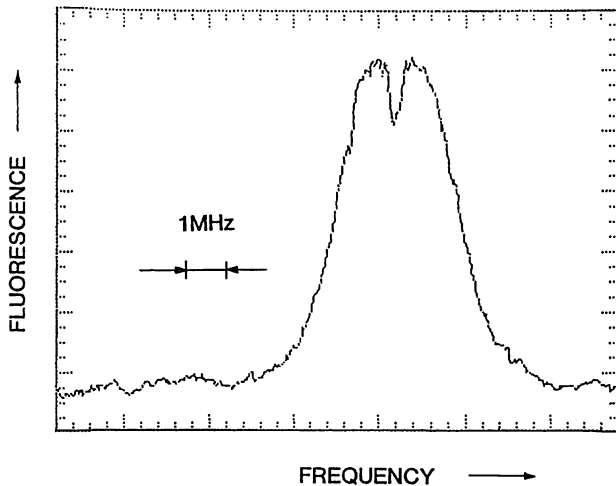


Fig. 4. Nonlinear fluorescence signal of the atomic beam on the intercombination line $4^1S_0-4^3P_1$ of ^{40}Ca ($\lambda=657$ nm) as a function of laser frequency

where [3]. Collimation of the atomic beam provided the residual Doppler broadening of about 4 MHz. The laser beam (1.5 mW) crossed the Ca atomic beam perpendicularly and was reflected with a cat's eye reflector. The cat's eye reflector was composed of a 250 mm focus lens and a flat mirror in the focal plane. The 1 cm spatial separation of the two counterpropagating beams excluded multiphoton processes [13] and parasitic optical feedback to the LD. The fluorescence from the excited Ca atoms was detected with a photomultiplier placed about 30 cm downstream from the excitation zone. To provide a frequency scale, the ECLD was FM modulated at 7 MHz, which gives two additional peaks of fluorescence corresponding to side bands. A transverse magnetic field was applied to the interaction region so that only the π -transition ($\Delta m=0$) was excited by the linearly polarized laser light.

A saturation dip on the Doppler-broadened spectral profile of fluorescence is shown in Fig. 4. The dip contrast defined with respect to the Doppler-broadened line is about 25%. The laser beam cross section was $2\text{ mm} \times 3\text{ mm}$, so the maximum intensity of the exciting light was about 25 mW/cm^2 . The nonlinear dip was observed even at a laser intensity of 5 mW/cm^2 . The minimum width of the nonlinear dip (FWHM) is $400 \pm 50\text{ kHz}$. The spectral resolution was mainly limited by the frequency jitter of the free-running ECLD.

3 1.3 μm Laser Diode and Second-Harmonic Generation

According to the scheme of the proposed frequency chain from the microwave range to the Ca line [5] it is necessary to have a Second Harmonic (SH) of 1314 nm and sum-frequencies corresponding to 1314 nm and 657 nm simultaneously. It is difficult to accomplish this with a low-power LD and two independent build-up cavities for SH generation and sum-frequency mixing. Consequently, we have used for the nonlinear frequency conversions two single-pass schemes and a high-power LD.

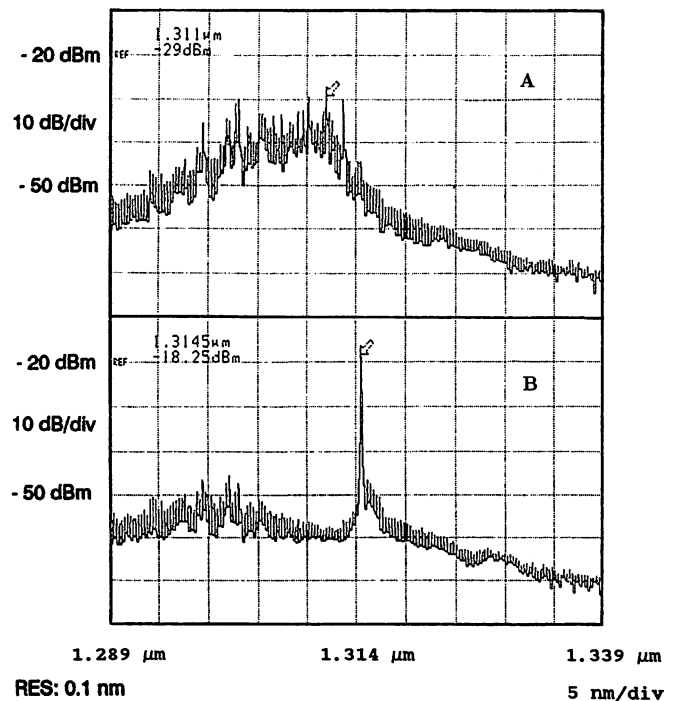


Fig. 5A, B. Longitudinal mode spectra of a high-power LD at $I=450$ mA ($I_{th}=50$ mA). A With no optical feedback; B with selective optical feedback (output power 110 mW)

A high-power multimode LD emitting up to 200 mW at $1.3\text{ }\mu\text{m}$ was used as an active element of an ECLD. The same folded scheme (see Fig. 1) of an external cavity was applied for longitudinal mode selection and linewidth narrowing. In order to rise the power of the output beam the angle of incidence on the grating (1200 lines/mm) was increased up to 85° . The LD junction plane was oriented to be parallel to the lines of the grating. The laser spectrum was analyzed with a confocal cavity having a free spectral range of 300 MHz and a finesse of 200. Under optical feedback a spectrum of the ECLD was completely single mode even if the threshold current was exceeded by a factor of up to 9 (Fig. 5). The maximum single-mode power of the output beam was 110 mW at $\lambda=1314$ nm.

An effect of polarization switching by optical feedback [14] during alignment of the external cavity when the orientation of the LD junction was not exactly parallel to the grooves of the grating was observed. It happened because the dispersion efficiencies of the grating for two orthogonal polarization components of incident radiation are essentially different. The switching of the LD radiation from TE mode to TM mode led to stronger optical feedback and, consequently, to better side-mode suppression (more than 40 dB). However, also to an unwanted decreasing of the zeroth-order beam power by 3–4 times. The effect of polarization switching by external optical feedback in this scheme requires further investigation, because it may be useful for some applications.

A 5 mm long nonlinear KTP crystal with critical phase matching was used for SH generation. The angles of incidence of the laser beam were varied to optimize phase matching. About 100 mW of fundamental light yielded up to 11 nW of SH in a single-pass scheme.

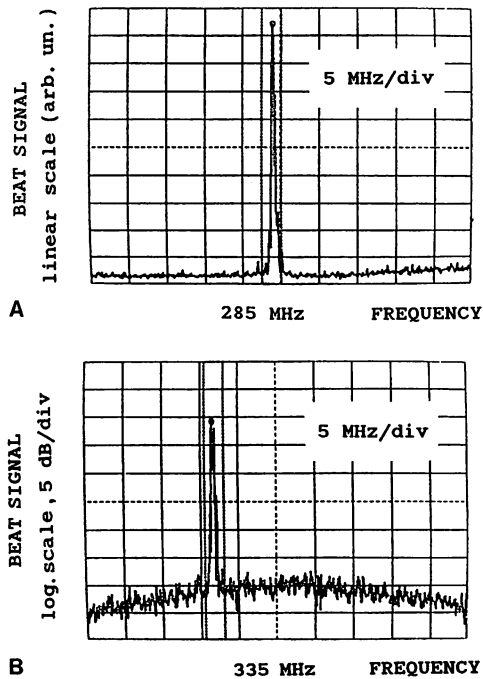


Fig. 6. Beat-note spectrum of an ECLD in the visible and SH radiation of the 1314 nm ECLD. Resolution bandwidth: 30 kHz; video bandwidth: 10 kHz; sweeping time: 500 ms

After separation of the fundamental light, the SH beam was mixed with radiation of the red ECLD (657 nm) on a Si avalanche photodetector. The beat note recorded on an rf spectrum analyzer is shown in Fig. 6a, b. The heterodyne spectrum shows that the linewidth of both LDs was less than 500 kHz for a sampling time of 500 ms. The signal to noise ratio is about 25 dB in a 30 kHz bandwidth. This ratio can be further improved by increasing the efficiency of SH generation.

4 Summary

The narrow-linewidth (less than 100 kHz) external-cavity laser diode operating at 657 nm with good long-term free-running stability was demonstrated. To obtain a sub-kHz linewidth level of the LD one has to use a fast electronic servo system to control the laser frequency to a stable high- Q reference cavity [12]. The laser was used for nonlinear spectroscopy of the Ca intercombination line. The resonance of saturated fluorescence with a contrast of 25% and a linewidth of 400 ± 50 kHz was shown.

Note added in proof. When the manuscript was ready for publication we have learned that the recoil splitting of Ca was resolved by using an extended-cavity diode laser at the Physikalisch-Technische Bundesanstalt (PTB), Braunschweig, Germany [15].

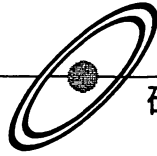
The 110 mW single-mode external-cavity laser diode at 1.3 μm was used for second-harmonic generation in a KTP crystal. An effect of polarization switching by optical feedback during alignment of the external cavity was observed.

The 600 kHz beat signal (sampling time of 500 ms) between the 10 nW second-harmonic radiation of 1.3 μm and the fundamental radiation of the ECLD was observed. The signal to noise ratio was more than 25 dB which is high enough to use phase-locking.

Acknowledgements. We are very grateful to N. Ito for the permission to work with the Ca-beam machine at the National Research Laboratory of Metrology, Tsukuba, Japan, and for his kind support. We thank the OKI company for supplying the high power 1.3 μm laser diode. We also acknowledge useful discussions with M. de Labachellerie and V. Velichansky.

References

- J.L. Hall, M. Zhu, P. Buch: *J. Opt. Soc. Am. B* **6**, 2196 (1989)
- J.C. Bergquist, R.L. Barger, D.J. Glaze: In *Laser Spectroscopy IV*, ed. by H. Walther, K.W. Rothe, Springer Ser. Opt. Sci., Vol. 21 (Springer, Berlin, Heidelberg 1979) pp. 120, and references therein
- A. Morinaga, F. Riehle, J. Ishikawa, J. Helmcke: *Appl. Phys. B* **48**, 165 (1989)
- A. Morinaga, N. Itoh, J. Ishikawa, K. Sugiyama, T. Kurosu: *IEEE Trans. IM-42* (1993)
- H. Schnatz, S. Ohshima, H.R. Telle, F. Fiehle: *IEEE Trans. IM-42*, 273 (1993)
- K. Nakagawa, M. Kourogi, M. Ohtsu: *Appl. Phys. B* **57**, 425 (1993)
- L. Hollberg, R. Fox, N. Mackie, A.S. Zibrov, V.L. Velichansky, R. Ellingsen, H.G. Robinson: In *Laser Spectroscopy X*, ed. by M. Ducloy, E. Giacobino, G. Camy (World Scientific, Scingapore 1992) p. 347
- R.W. Fox, H.G. Robinson, A.S. Zibrov, N. Mackie, J. Marquardt, J. Magyar, L.W. Hollberg: In *Frequency-Stabilized Lasers and their Applications*, ed. by Y.C. Chung, SPIE Proc. **1837**, 360 (1992)
- A. Akulshin, A. Celikov, V. Velichansky: *Opt. Commun.* **93**, 54 (1992)
- G.M. Tino, M. Barsanti, M. de Angelis, L. Giafranty, M. Inguscio: *Appl. Phys. B* **55**, 397 (1992)
- A. Akulshin, A. Celikov, M. Ohtsu, K. Nakagawa, V. Velichansky: *Jpn. J. Appl. Phys.* **32**, L1356 (1993)
- H.R. Simonsen: *IEEE J. QE-29*, 877 (1993)
- K.C. Harvey, C.J. Myatt: *Opt. Lett.* **16**, 910 (1991)
- M. Ohtsu, M. Murata, M. Kourogi: *IEEE J. QE-26*, 231 (1990)
- J. Ishikawa, F. Riehle, J. Helmcke, Ch.J. Bordé: In *Laser Spectroscopy X*, ed. by M. Ducloy, E. Giacobino, G. Camy (World Scientific, Singapore 1992) p. 418
- T. Fujita, A. Schreemer, C. Tang: *Electron. Lett.* **23**, 803 (1987)
- A. Celikov, F. Riehle, V. Velichansky, J. Helmcke: *Opt. Commun.* (submitted)



光領域の周波数コム発生器

興 梶 元 伸^{*,**} ・ 大 津 元 一^{*,**}

レーザーとレーザーとの間の差周波数を広範囲に測定するために、光領域の周波数コム発生器を開発した。モノリシック共振器型の光周波数コム発生器を用い、7 THz の範囲に広がる光周波数コムが発生したことを示した。さらに、発生させた光周波数コムに含まれる側波帯の一つに他方のレーザー光を位相同期させ、0.5 THz の周波数間隔をもつ 2 台のレーザー間の差周波数と位相を安定化させることに成功した。光周波数コム発生器は光通信や、高精度物理計測への広い分野へ応用が可能である。

Keywords : optical frequency comb, optical phase locking, laser frequency measurement, laser frequency stabilization

1. ま え が き

光通信、計測などへの応用や、光領域にある分子、原子などの吸収線の周波数の精密測定のために、レーザーの絶対周波数の高精度測定は重要である。しかし、100 THz 以上もあるレーザー周波数を測定するためには、レーザー周波数をマイクロ波周波数まで変換する必要がある。実際、高出力のマイクロ波、ミリ波、レーザーなどの発振器といくつかの非線形応答する素子によりレーザー周波数をマイクロ波周波数に変換して、光領域のいくつかの分子、原子などの吸収線の絶対周波数が測定されている¹⁻³⁾。

しかしながら、この方法では発振器の周波数がほぼ固定されているために、限られた周波数範囲でしか測定できない。そのため、一つの吸収線の絶対周波数を決定しても、その周波数から離れた吸収線の絶対周波数を決定することは難しい。これを行うには、複数のレーザー間の差周波数を広範囲に測定する技術が必要となる。

2 台のレーザーの差周波数を測定することは、両レーザーの波面を重ねたときに生じるうなり（ビート信号）の周波数を測定することである。こうして検出できる差周波数の最大値は光検出器の帯域で制限され、市販の半導体光検出素子を用いた場合には 10 GHz 程度である。

そこで、測定できる差周波数を拡大する方法がいくつか提案されている。例えば金属-絶縁体-金属 (MIM) 構造のダイオード⁴⁾ や高温超伝導薄膜を用いた超高速光検出器⁵⁾ を用いる方法である。また、レーザーとレーザーとの間の差周波数を 1/2, 1/4 と徐々に小さくして測定する方法も提案されている^{6,7)}。それは、非線形光学結晶を用いた周波数変換と光位相同期技術を用いて、2 台のレーザーの中

心の周波数に別のレーザーの周波数を正確に制御する方法である。この方法を繰り返して、2 台のレーザーの差周波数の間隔を 1/2, 1/4 と徐々に小さくし、2 台のレーザー間の差周波数を十分低くしてからビート信号を測定する。

さらに別の方法は、光領域の周波数コム発生器を用いる方法である⁸⁻¹⁰⁾。コムとは電磁波の線スペクトルが周波数間隔一定に複数並んだ櫛 (comb) 状のスペクトル形状を表し、マイクロ波周波数領域でよく用いられる用語である。光領域でのこのようなスペクトル形状を、光周波数コム (以下 OFC と書く) と呼んでいる。レーザー光を外部変調器で変調すると、当初のレーザー周波数を中心に変調周波数に等しい間隔で変調側波帯が周波数軸上に並び OFC となる。こういった OFC 発生器を局部発振器として用いると、複数のレーザーの大きな差周波数を測定することができる。

広範囲に OFC の発生を行う高効率の外部変調には二つの方法がある。一つは、電気光学位相変調器 (以後 EO 変調器と書く) をファブリー・ペロー共振器 (以後 FP 共振器と書く) に挿入した FP 共振器型 EO 変調器を用いる方法である¹¹⁾。もう一つの方法は、音響光学変調器をレーザー共振器内に挿入する方法である^{12,13)}。後者は光領域の利得媒質を用いているので、発生する OFC のパワーが大きい利点がある。それに対して前者の方法は、構造が簡単で、任意の波長帯で製作できる利点がある。そこで、われわれは前者の方法を用いて OFC 発生器を開発した。ここでは、OFC 発生器を用いた差周波数測定の方法と、われわれが開発したモノリシック共振器型 OFC 発生器について述べ、OFC 発生器を用いたヘテロダイン型光位相同期に応用した実験を紹介する。

* 東京工業大学総合理工学研究科 〒227 横浜市緑区長津田町 4259.

** 神奈川科学技術アカデミー・フォトン制御プロジェクト 〒213 川崎市高津区坂戸 3-2-1, KSP 東棟 408 号.

A frequency-comb generator in optical region. Motonobu KUROGI^{***} and Motoichi OHTSU^{***}.

* Interdisciplinary Graduate School of Science and Engineering, Tokyo Institute of Technology. 4259 Nagatsuta, Midori-ku, Yokohama 227.

** Kanagawa Academy of Science & Technology. KSP East Building, Room 408, 2-1, Sakado 3 chome, Takatsu-ku, Kawasaki 213.

2. 光周波数コム発生器の原理

基本的な OFC 発生器による、周波数 ν_1 , ν_2 の 2 台のレーザーの差周波数測定構成を図 1(a) に示す。鏡を互いに向かい合わせに設置した FP 共振器のなかに EO 変調器を挿入している。この EO 変調器に、レーザー光が FP 共振器内を往復する周期に同期する周波数 f_m の正弦波状の変調電圧を加えると、入射レーザー光が FP 共振器内を多重往復する間に高効率変調が行われ、出力光は OFC となる。この OFC に対して周波数 ν_2 のレーザー光を重ね合わせる。このとき図 1(b) に示されるように、 ν_2 に一番近い周波数をもつ第 N 次の側波帯とのビート信号を観測し、このビート周波数 $\Delta\nu$ を測定すれば、2 台のレーザー間の差周波数、すなわち $\Delta\nu + f_m \times N$ の値が明らかになる。 N の値と $\Delta\nu$ の符号は、 f_m の値を微小変化させたときの $\Delta\nu$ の変化量から決定できる。

この OFC の特性を明らかにするために、まず OFC の時間軸上での特性を説明する。時間軸上での特性が明らかになれば、周波数軸上の特性は理解しやすい。FP 共振器内の EO 変調器は、共振器の長さを変調しているので、高速

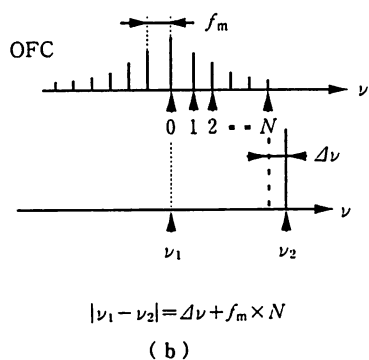
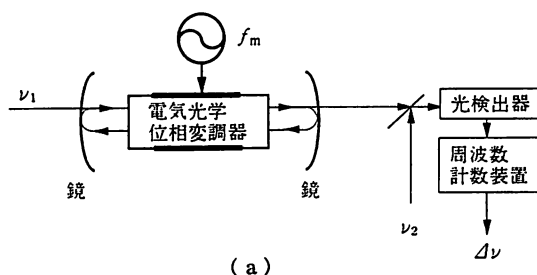


図 1 (a) OFC 発生器の構成と、それを用いた差周波数測定装置。ファブリー・ペロー共振器中の電気光学位相 (EO) 変調器を周波数 f_m のマイクロ波で駆動すると、入射した周波数 ν_1 のレーザー光が変調され光周波数コムが発生する。発生した光周波数コムの第 N 次の側波帯と周波数 ν_2 のレーザー光とのビート周波数 $\Delta\nu$ を観測すると、レーザー間の差周波数 $|\nu_1 - \nu_2|$ が決定される。(b) ν_1 , ν_2 と光周波数コムの周波数の関係。

に FP 共振器の共振周波数を変調しているとみなすことができる。そのため、EO 変調器の駆動電圧が正弦的に一周期変化する間に、レーザー周波数と FP 共振器の共振周波数が 2 度一致し、その瞬間レーザー光が FP 共振器を通過することになる。したがって、出力光は $2f_m$ の周期のパルス列となる。

パルスの形状は FP 共振器の共振曲線の形状を反映し、ローレンツ関数により表される。変調指数を β , FP 共振器のフィネスを F とすると、パルス幅は $\tau = 1/2F\beta f_m$ となる。例えば $F=100$, $\beta=1$, $f_m=10$ GHz と、典型的な値を用いて計算すると τ は 0.5 ps となる。そのため、こういった OFC 発生器はサブピコ秒光パルス発生器としても用いられている¹¹⁾。

周波数軸上の第 N 次の側波帯のパワー P_N は、パルス列のフーリエ変換を行えば計算でき、 $P_N = (\pi f_m \tau)^2 P_i \exp(-2\pi f_m |N|)$ となる。ここで、 P_i は入射レーザーのパワーである。 $\tau=0.5$ ps, $f_m=10$ GHz の値を用い、 P_i を 1 mW とし第 100 次、すなわちキャリア周波数から 1 THz 離れた側波帯パワーを計算すると 10 nW になる。もう 1 台のレーザー光との間のビート信号を検出する際の信号対雑音比 SNR は、もう 1 台のレーザー強度が大きい場合、量子限界 $P_N a / e B$ となる。ここで、 a は光検出器の受光感度、 e は電荷素量、 B はビート信号のスペクトル線幅である。例えば a を 1 A/W, B を 10 kHz とし、第 100 次の側波帯とのビート信号の SNR は約 60 dB と大きな値となる。

光強度が小さくても線幅の小さいレーザーを用いれば、ビート信号が高い SNR で観測できることが、OFC 発生器を用いた差周波数測定の大きな利点である。SNR が 0 dB の状態を観測限界と考えれば、上記の条件の場合、6 THz の差周波数を測定できることになる。

3. モノリシック共振器型光周波数コム発生器

さて、実際には図 1 のような EO 変調器と FP 共振器を組み合わせた OFC 発生器は大型であり、機械的安定性に問題がある。また EO 変調器用結晶の端面がむき出しであるので、光損失の原因となり、FP 共振器のフィネスを大きくすることを妨げる。これらの問題を解決するため、EO 変調器と FP 共振器を一体化したモノリシック共振器型 OFC 発生器が有利と考えられる⁹⁾。モノリシック共振器型 OFC 発生器とは、EO 変調器用結晶の入出力端面を高反射率の鏡面とすることによって、EO 変調器用結晶自体をモノリシック化された FP 共振器とする構造の OFC 発生器である。

製作した波長 0.8 μm 帯で動作するモノリシック共振器型 OFC 発生器を図 2 に示す。EO 変調器用結晶には LiNbO₃ 結晶を $1.2 \times 1 \times 21$ mm³ の大きさに切り出して用

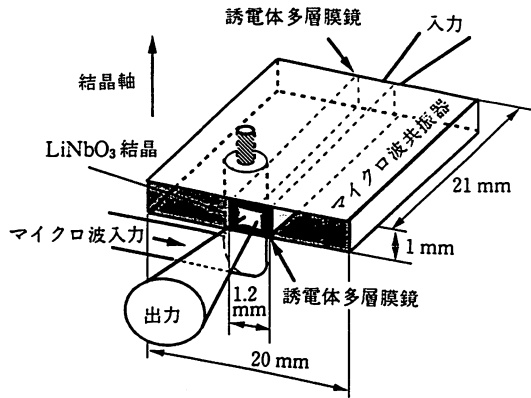


図2 モノリシック共振器型光周波数コム発生器の構成。EO変調器用結晶の入出力端面を高反射率の鏡面として、フアブリー・ペロー共振器を構成している。

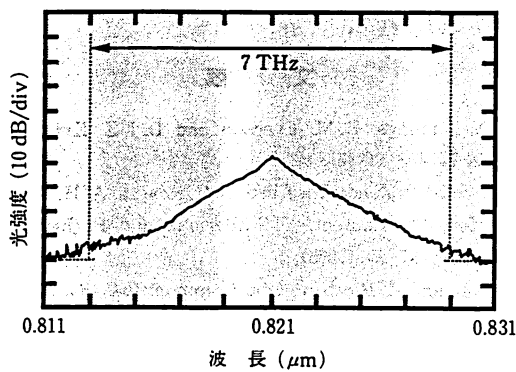


図3 モノリシック共振器型光周波数コム発生器により得られた、光周波数コムの包絡線のスペクトル形状。波長0.821 μmの半導体レーザーを用いた。測定分解能0.5 nm。測定分解能が変調周波数より大きいため、光周波数コムの包絡線が示されている。光周波数コムが7 THzの範囲にわたって広がっていることがわかる。

い、両方の結晶端面をそれぞれ凸面と平面に研磨し、さらにその面に反射率99.5%の誘電体多層膜を蒸着してFP共振器とした。この結果、FP共振器としてのフィネスの測定値は350に達した。EO変調器として高効率に動作させるために、図2のように結晶をマイクロ波共振器に挿入した。ここで使用したマイクロ波共振器は、結晶の厚みに等しい高さのマイクロ波導波路を結晶と同じ長さにして用いる。このEO変調器を共振状態で駆動すると、結晶上のマイクロ波電界強度が大きくなり、さらにマイクロ波導波路の幅が結晶内部のマイクロ波とレーザー光の速度が一致するように設計されているので高効率の位相変調が行える。この結果 $f_m=6.3$ GHz、マイクロ波パワーが10 Wのとき $\beta=1$ が得られた。これらの数値から推定される τ の値は0.2 psである。

図3に変調されたレーザー光のスペクトル形状を示す。測定分解能が変調周波数 f_m より大きいため、OFCの包絡線が示されている。OFCの発生は約7 THzの範囲で確認できる。もう1台のレーザーとの間のビート信号を高感度で測定すれば、より広範囲のOFCが確認できると思われる。モノリシック共振器型OFC発生器の場合にはFP共振器のフィネスを十分に大きくできるために、OFC発生

範囲の限界はEO変調器用結晶の波長分散によって決まると推定される⁹⁾。上記のモノリシック共振器型OFC発生器の場合、OFC発生範囲の限界値は約9 THzと見積もられた。

結晶の分散による限界は、より効率の高いEO変調を行うことで大きくできる⁹⁾。その一つの方法は、光導波路型EO変調器を用いることである。この型のEO変調器は狭い領域にマイクロ波と光を集中させるため、高効率のEO変調が可能である。

実際に変調周波数 $f_m=12$ GHz、変調指数 $\beta=10$ のLiNbO₃光導波路型EO変調器を用いて、波長1.5 μm帯で動作するOFC発生器を製作した¹⁴⁾。いまのところ、光損失が結晶長1 cm当たり5%程度あり、そのためフィネス F の値はたかだか12であった(ただし、この値は他の光導波路による場合¹⁵⁾よりは高い)。現在2.7 THzの範囲のOFCの発生を確認しているが、分散によるOFC発生範囲の限界値が約14 THzと見積もられているので、光導波路の損失が減少すれば10 THzを超える範囲のOFCの発生が可能となるであろう。また、小林¹⁶⁾らの提案している疑似速度整合による高効率EO変調器を用いても、10 THz以上のOFCの発生を行える可能性があることを付記しておく。

4. 光周波数コム発生器を用いたヘテロダイン型光位相同期の実験

次に、OFC発生器を用いて、レーザー光のヘテロダイン型光位相同期を行った実験を紹介する⁹⁾。図4にその実験系を示す。ここでは光通信応用に重要な波長1.5 μm帯の半導体レーザーおよび、この波長帯で動作するOFC発生器を製作して用いた。EO変調器用結晶はLiNbO₃である。レーザー1の出力光を変調周波数 $f_m=5.8$ GHz、 $\tau=1$ psのOFC発生器に入射し、発生した側波帯とレーザー2の出力間のビート信号を検出する。これと局部発振器の出力信号との位相差を、レーザーの電流に負帰還を行い制御した。これによりレーザー1の側波帯の一つとレーザー2の間のビート信号の位相および周波数は、マイクロ波の位相および周波数におおの同期、追従することになる。

図5は、第84次の側波帯に位相同期したときのビート信号スペクトルである。この図にみられる線スペクトルの左右にみられるコブは、制御できなかった位相誤差によるものである。これの大きさから位相誤差分散は0.01 rad²と推定された。変調周波数 f_m が5.8 GHzであるので、非変調時のレーザー1とレーザー2の差周波数が約0.5 THz(=5.8 GHz×84)の状態、これらのレーザーの間の位相揺らぎが0.1 rad(= $\sqrt{0.01 \text{ rad}^2}$)まで制御されたこ

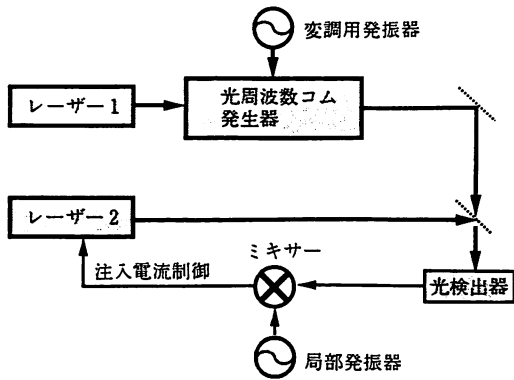


図4 光周波数コム発生器を用いたヘテロダイン型光位相同期の実験系。レーザーには $1.5 \mu\text{m}$ 帯半導体レーザーを用いた。また光周波数コム発生器には、 5.8 GHz で動作するEO変調器を $1.5 \mu\text{m}$ 帯のフアブリー・ペロ共振器に挿入して製作した。レーザー1の光周波数コムの側波帯の一つとレーザー2のビート信号を、局部発振器の出力信号と位相比较し、レーザー2の注入電流に負帰還する。

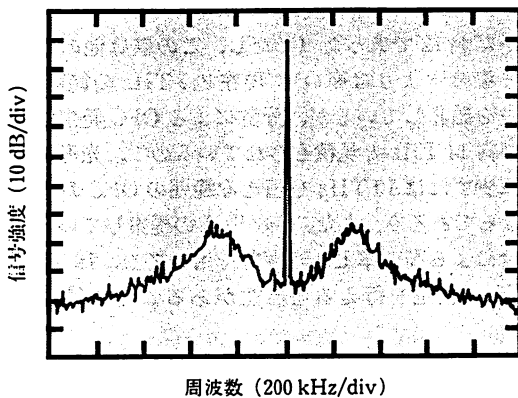


図5 光周波数コムの第84次の側波帯に、レーザー2を、ヘテロダイン型光位相同期したときのビート信号スペクトル。測定分解能 1 kHz 。変調周波数が 5.8 GHz であるので、約 0.5 THz のヘテロダイン型光位相同期を行ったことになる。位相誤差分散は 0.01 rad^2 以下と推定されている。

とになる。

このようなOFC発生器による光位相同期を用いれば、レーザーの絶対周波数測定も簡便になり¹⁷⁾、高精度の光領域の周波数シンセサイザーも可能になるであろう。また、複数のレーザーを、複数のOFC発生器を用いて位相同期を行えば、さらにOFCの発生範囲を広げることも可能である。このような技術は通信、計測への広い分野へ応用が可能である。

5. お す び

レーザー間の差周波数を広範囲に測定するために、光領域の周波数コム発生器を開発する研究を紹介した。モノリシック共振器型光周波数コム発生器では、 7 THz にわたる範囲のOFCの発生を確認した。さらに、 10 THz 以上のOFCの発生可能性を示した。また、OFC発生器によって

生成された変調側波帯に、他のレーザー光の位相を追従させることによって 0.5 THz のヘテロダイン型光位相同期を実現させた。

謝 辞

貴重なご助言とご討論をたまわった小林哲郎教授(大阪大学)、森本朗裕博士(大阪大学)に感謝いたします。なお、この研究は科学技術庁科学技術振興調整費、文部省科学研究費補助金一般研究(B)(課題番号05452110)および同重点領域研究(課題番号04228102)からの研究費補助を受けて行われた。

文 献

- 1) D. A. Jennings, K. M. Evenson and D. J. E. Knight: Proc. IEEE 74, 168 (1986).
- 2) O. Acef, J. J. Zondy, M. Abed, D. G. Rovera, A. H. Gérard, A. Clarion, Ph. Laurent, Y. Millerioux and P. Juncar: Opt. Commun. 97, 29 (1993).
- 3) F. Nez and F. Biraben: Opt. Commun. 104, 432 (1993).
- 4) R. E. Drullinger, K. M. Evenson, D. A. Jennings, F. R. Petersen, J. C. Bergquist and L. Burkings: Appl. Phys. Lett. 42, 137 (1983).
- 5) M. Lindgren, V. Trifonov, M. Zorin, M. Danerud, D. Winkler, B. S. Karasik, G. N. Gol'tsman and E. M. Gershenzon: Appl. Phys. Lett. 64, 3036 (1994).
- 6) H. R. Telle, D. Meschede and T. W. Hänsch: Opt. Lett. 15, 532 (1990).
- 7) N. C. Wong: Opt. Lett. 15, 1129 (1990).
- 8) M. Kourogi, K. Nakagawa and M. Ohtsu: IEEE J. Quantum Electron. 29, 2693 (1993).
- 9) M. Kourogi, T. Enami and M. Ohtsu: IEEE Photon. Technol. Lett. 6, 214 (1994).
- 10) L. R. Brothers, D. Lee and N. C. Wong: Opt. Lett. 19, 245 (1994).
- 11) T. Kobayashi, T. Sueta, Y. Cho and Y. Matsuo: Appl. Phys. Lett. 21, 341 (1972).
- 12) P. Coppin and T. G. Hodgkinson: Electron. Lett. 26, 28 (1990).
- 13) P. Jessen and M. Kristensen: Appl. Opt. 31, 4911 (1992).
- 14) M. Kourogi, T. Saito, T. Enami and M. Ohtsu: Proc. Int. Conf. Lasers and Electro-Optics, Anaheim, 1994, p. 272.
- 15) T. Suzuki, J. M. Marx, V. P. Swenson and O. Eknayan: Appl. Opt. 33, 1044 (1994).
- 16) A. Morimoto, E. Saruwatari and T. Kobayashi: Proc. Int. Conf. Lasers and Electro-Optics, Anaheim, 1994, p. 21.
- 17) K. Nakagawa, M. Kourogi and M. Ohtsu: Appl. Phys. B 57, 425 (1993).

(1994年6月13日 受理)

Absolute frequency stability of a diode-laser-pumped Nd:YAG laser stabilized to a high-finesse optical cavity

K. Nakagawa, A. S. Shelkownikov, T. Katsuda, and M. Ohtsu

We report the frequency stabilization of a diode-laser-pumped monolithic ring Nd:YAG laser locked to a high-finesse optical cavity. With an independent cavity as a frequency discriminator, the absolute frequency noise was measured to be as low as 2×10^{-2} Hz/Hz^{1/2} at the Fourier frequency of approximately 3 kHz. We also measured the heterodyne beat note between two lasers locked to the independent cavities. The beat linewidth is narrower than 30 Hz and the minimum root Allan variance is approximately 6×10^{-14} .

1. Introduction

Frequency-stabilized lasers are required in many fields such as high-resolution spectroscopy, metrology, and interferometric gravitational-wave detection.^{1,2} In the case of the gravitational-wave detector, both ultra-low-frequency noise of the order of 10^{-6} Hz/Hz^{1/2} and a high output power of more than 10 W are required for the laser source. The recently developed diode-laser-pumped Nd:YAG laser is a promising candidate for the realization of the above requirements because of its low intrinsic amplitude and frequency noises and its scalable high output power. Frequency stabilizations of the diode-laser-pumped Nd:YAG lasers have been demonstrated and their excellent performance has been reported.³⁻⁶ In these examinations, the frequency stability relative to the reference cavity has been well examined.³⁻⁵ However, the absolute frequency stability of laser is mainly determined by the mechanical and thermal stability of the reference cavity.⁶⁻⁹ Through the use of a suspended cavity inside a vacuum chamber, the reference cavity can be well isolated from external

disturbance,⁷ and until now absolute laser linewidths of the order of 10 Hz have been recorded.^{8,9} Spectral analysis of the frequency noise is needed to examine the mechanical stability of the reference cavity, and it is also useful for various applications of stabilized lasers.⁷ For ultrahigh-resolution spectroscopy,⁸ which requires a herz-order laser linewidth, the frequency noise at low frequencies is important because it mainly determines the laser linewidth, whereas the frequency noise near 1 kHz is important for gravitational-wave detectors.

Here we report the performance of frequency-stabilized diode-laser-pumped Nd:YAG lasers. The spectrum of absolute frequency noise was measured with the independent cavity as a frequency discriminator. We also measured the heterodyne beat note between two stabilized lasers and compared it with the results of the frequency-noise measurement.

2. Frequency Stabilization and Frequency-Noise Measurement Techniques

The experimental setup for the frequency stabilization and frequency-noise measurement is shown in Fig. 1. We use a diode-laser-pumped monolithic ring Nd:YAG laser (Lightwave Electronics Model 122-300) with an output power of 300 mW. The laser frequency can be tuned by a piezoelectric transducer (PZT) bonded to the Nd:YAG crystal. Using the Pound-Drever technique,¹⁰ we frequency-stabilize the laser to a high-finesse reference optical cavity (cavity 1). This reference cavity is made of a Zerodur spacer ($L = 0.46$ m), a flat mirror, and a concave ($R = 1$ m) mirror. These mirrors are superpolished fused-silica substrates with a high reflective ($R \sim 0.9999$)

The authors are with the Interdisciplinary Graduate School of Science and Engineering, Tokyo Institute of Technology, 4259, Nagatsuta-cho, Midori-ku, Yokohama 227, Japan. K. Nakagawa and M. Ohtsu are also with the Kanagawa Academy of Science and Technology, Kanagawa, Japan. The permanent address for A. S. Shelkownikov is the P. N. Lebedev Physics Institute, Moscow, Russia.

Received 10 February 1994; revised manuscript received 30 March 1994.

0003-6935/94/276383-04\$06.00/0.

© 1994 Optical Society of America.

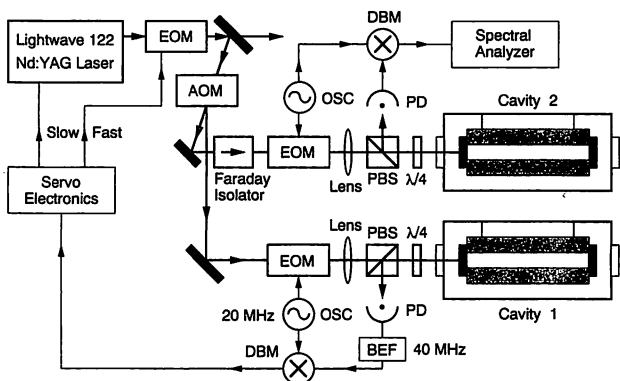


Fig. 1. Experimental setup for the frequency stabilization and frequency-noise measurement. EOM's, electro-optic modulators; AOM, acousto-optic modulator; OSC's, oscillators; PD's, photo-diodes; DBM's, double-balanced mixers; PBS's, polarizing beam splitters; BEF, band-elimination filter.

coating, and they are glued onto the spacer with epoxy. This cavity is suspended by five wires⁷ and mounted in a vacuum chamber. The cavity linewidth and finesse are measured to be 18 ± 2 kHz and approximately 18,000, respectively. The reflection-fringe contrast on resonance is higher than 75%. In our previous experiment only the PZT was used for frequency feedback.¹¹ The feedback bandwidth was limited by the mechanical resonance of the PZT and was approximately 30 kHz. To get a wide (> 100 kHz) frequency-feedback bandwidth, we use an external electro-optic modulator for fast phase correction.^{12,13} The detail design and performance of this fast frequency feedback are described elsewhere.¹⁴

A part of the laser output is introduced into the second optical cavity (cavity 2). The second cavity is nearly the same as the first except that the spacer is made of ultralow-expansion glass, Corning 7971 ($L = 0.3$ m), and its linewidth is approximately 28 kHz. This cavity is also suspended by five wires and mounted in a vacuum chamber. We used the same Pound-Drever method for the frequency-noise measurement. Because both cavities are nontunable, one of the sidebands generated by an electro-optic modulator is tuned to the resonance of the second cavity. The slope of the dispersive signal of the upper or lower sideband component is used as a frequency discriminator. The rf sideband frequency is typically between 10–80 MHz and the typical modulation index is approximately 0.1. The rf frequency is manually tuned to the cavity resonance with a synthesized rf oscillator. During the measurement time (~ 10 s), the sideband is kept on the resonance of the cavity without the use of active feedback to a rf frequency.

3. Spectral Analysis of Frequency Noise

Figure 2 shows the linear spectral density of the frequency noise of the stabilized laser. The upper curve is the absolute frequency noise measured with the second cavity, whereas the lower curve is the frequency noise obtained from the error signal of the

frequency-feedback system. The frequency noise from the error signal (lower curve) is reduced to less than 3×10^{-4} Hz/Hz^{1/2} at frequencies lower than 10 kHz. The shot-noise level for the frequency-stabilization system is approximately 4×10^{-4} Hz/Hz^{1/2} with an input power of nearly 2 mW. Throughout the frequency region, the real frequency noise (upper curve) is higher than that from the error signal. The absolute frequency noise reaches nearly 2×10^{-2} Hz/Hz^{1/2} in the frequency region between 3–30 kHz. The shot-noise level for the upper curve is nearly 10^{-2} Hz/Hz^{1/2}, which is verified by shifting the rf frequency off-resonance from the second cavity. This shot-noise level is rather high compared with that of the frequency stabilization from a lower modulation index of ~ 0.1 . Considering the cut-off frequency of the cavities, both frequency-noise spectra in Fig. 2 are compensated at frequencies higher than the half-linewidth of the individual cavities. The increase of the absolute frequency noise (upper curve) to higher than 20 kHz is due to this compensation. This noise level is determined by the shot noise, and the real frequency noise is probably lower than this shot-noise level. The mechanical resonance frequencies of the stretching vibration of the cavities is estimated to range from 5–10 kHz. A weak noise peak at 12 kHz is probably one of the resonances; however, its identification is not clear in the present measurement. In the lower-frequency region, the frequency noise becomes higher and there are two strong peaks at several hertz, probably caused by the resonance frequencies of the pendulum motion of suspended cavities. The isolation of the cavities from external vibration and acoustic noise is not enough for frequencies less than 1 kHz. At 1 kHz, the absolute frequency noise is nearly 50 dB higher than the shot-noise level of the frequency stabilization.

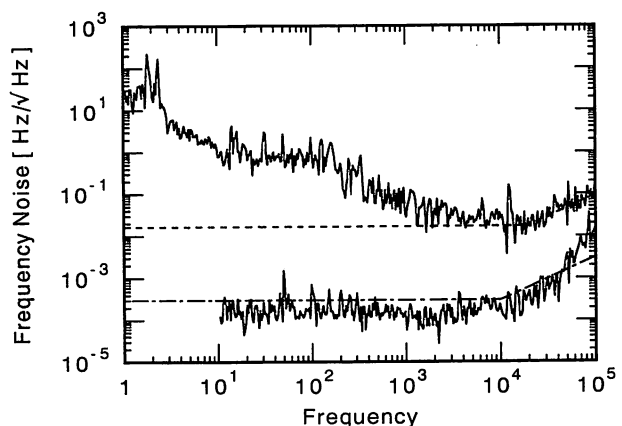


Fig. 2. Linear spectral density of the frequency noise. Upper curve: the frequency noise measured with the second cavity. Lower curve: the frequency noise obtained from the frequency-feedback error signal. Upper dashed line: shot-noise level of the frequency-noise measurement. Lower dotted-dashed line: shot-noise level of the frequency-feedback loop.

4. Heterodyne Measurements

To measure the spectral linewidth and the frequency stability, we prepared identical two-laser systems and measured the beat note between them.⁶ The first system is exactly the same as that described in Section 2. The second system is nearly the same except that the laser is a Lightwave Model 122-500, the reference cavity is made of ultralow-expansion glass ($L = 0.3$ m, $\Delta\nu_c = 28$ kHz), and only the PZT frequency feedback is used. The heterodyne beat note is detected by a fast p-i-n photodiode. The beat photocurrent is amplified and introduced into a rf spectrum analyzer. Figure 3 shows a typical beat-note spectrum. The beat linewidth is 30 Hz and is limited by the resolution width of the spectrum analyzer. The drift rate of the beat frequency is approximately 50 Hz/s, caused mainly by the pressure fluctuation in the vacuum chamber. Prior to the above experiment, both chambers were evacuated with turbomolecular pumps, and the pressure was reduced to lower than 10^{-6} Torr. These pumps are disconnected from the chambers during the experiment. The pressure inside the sealed chambers is of the order of 10^{-3} torr because of outgassing. The spectral linewidth is mainly determined by the frequency noise at lower than 20 Hz.

Using a time-interval counter (Stanford Research Model SR620), we measured the variance of the beat frequency. Figure 4 shows the root Allan variance $\sigma_y(\tau)$ of stabilized lasers. The minimum root variance is approximately 6×10^{-14} at the sampling time $\tau = 0.01$ s. At $\tau > 0.01$ s, the variance becomes large mainly because of the frequency drift induced by the thermal and pressure fluctuations of the cavity. At $\tau < 10^{-4}$ s, the measured variance is mainly determined by the instrumental resolution of the time-interval counter.

The relation between the Allen variance and the frequency noise is given by⁷

$$\sigma_y^2(\tau) = 2 \int_0^\infty \frac{S(f)}{\nu_0^2} \left(\frac{\sin^2 \pi f \tau}{\pi f \tau} \right)^2 df,$$

where τ is the sampling time, $S(f)$ is the power

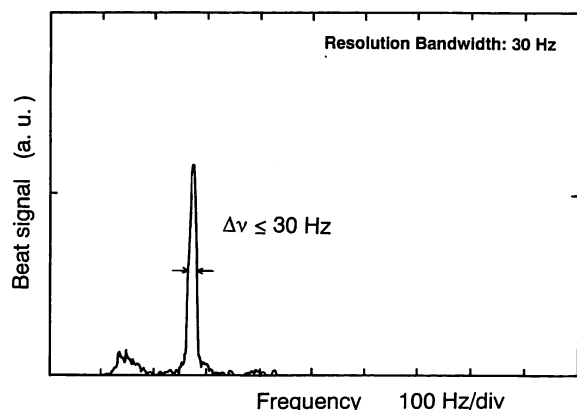


Fig. 3. Beat-note spectrum between two stabilized lasers. The center frequency is approximately 60 MHz.

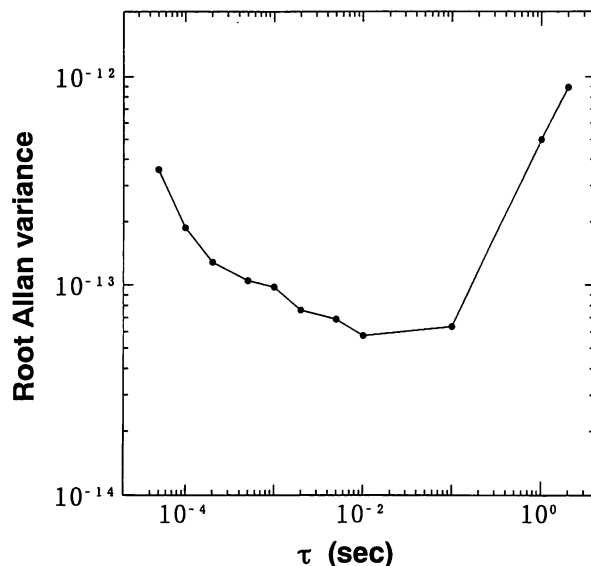


Fig. 4. Root Allan variance of the beat note between two stabilized lasers: τ , sampling time.

spectral density of frequency noise in hertz squared per hertz, and ν_0 is the laser frequency. $S(f)$ is the square of the linear spectrum density shown in Fig. 2. The root Allan variances calculated from the frequency noise are 1.7×10^{-14} ($\tau = 0.001$ s), 3×10^{-14} ($\tau = 0.01$ s), 3.5×10^{-14} ($\tau = 0.1$ s), 7×10^{-14} ($\tau = 1$ s). The increasing of variance against the sampling time τ is due to the large frequency noise at low Fourier frequencies. At $\tau = 0.1$ s, the variance calculated from the frequency noise is roughly consistent with that from the beat-note measurement.

5. Discussion

To realize a detection sensitivity of 10^{-21} in interferometric gravitational-wave detectors,² the frequency-noise level of 10^{-6} Hz/Hz^{1/2} is required at ~ 1 kHz. This noise level is nearly 10^{-7} smaller than that of the monolithic diode-laser-pumped Nd:YAG laser in free-running operation.⁴ Because the feedback bandwidth and gain are limited, it is not easy to realize the above noise level directly through the use of one feedback stage. Our first goal is to realize a noise level of 10^{-4} Hz/Hz^{1/2} at the first stage. Using a reference cavity linewidth of 20 kHz and an incident laser power of 300 mW, we calculated the shot-noise-limited noise level to be 3×10^{-5} Hz/Hz^{1/2}. In this work, the noise level of the feedback error signal was limited by the shot noise at frequencies less than 10 kHz, with the incident power of 2 mW (Fig. 2). As the feedback gain is still high at 1 kHz, the above noise level (10^{-6} Hz/Hz^{1/2}) can be obtained, in principle, by an increase in the incident laser power. The frequency-noise measurement through the independent cavity showed that the absolute frequency noise that we achieved is the lowest level reported to date; however, it was still much higher than that of the feedback error signal. A further improvement is needed for vibrational isolation of the reference cavity. Next we are going to use a two-stage suspension for

the reference cavity.² The shot-noise-limited detection sensitivity in the frequency noise measurement also needs to be reduced by an increase in the laser power or rf power for sideband generation.

For gravitational-wave detectors, the long-term stability of the laser frequency is not so important, but it is important for other applications, such as high-resolution spectroscopy. In the present experiment, the laser linewidth is mainly determined by the low-frequency components of the frequency noise. In our next study we are preparing new cavities with optical contact mirrors and ion-sputtering pumps for continuous pumping of the vacuum chambers to improve the long-term stability. We also plan to stabilize the temperature of the reference cavity to reduce the frequency drift in future experiments.

6. Conclusions

We have measured the absolute frequency stability of diode-laser-pumped Nd:YAG lasers locked to high-finesse cavities. The absolute frequency noise was reduced to 2×10^{-2} Hz/Hz^{1/2} at 3 kHz. The beat-note linewidth between two stabilized lasers was narrower than 30 Hz. The absolute frequency stability is determined mainly by the mechanical and thermal stability of the reference cavity and not by the frequency-feedback system. This frequency-noise measurement provides useful information for further improvement of the frequency-stabilized laser for gravitational-wave detectors.

We thank K. Ueda of the Electro Communication University and M. Kouroggi of the Tokyo Institute of Technology for their helpful discussions. This work was supported by Grant-in-Aid for Scientific Research 04234204 from the Ministry of Education, Science, and Culture of Japan.

References

1. K. S. Thorne, "Gravitational radiation," in *300 Years of Gravitation*, S. W. Hawking and W. Israel, eds. (Cambridge U. Press, Cambridge, 1987), Chap. 9 pp. 330–458.
2. D. Shoemaker, R. Schilling, L. Schnupp, W. Winkler, K. Maischberger, and A. Rüdiger, "Noise behavior of the garching

- 30-meter prototype gravitational wave detector," *Phys. Rev. D* **38**, 423–432 (1988).
3. D. Shoemaker, A. Brillet, C. N. Man, O. Cregut, and G. Kerr, "Frequency-stabilized laser-diode-pumped Nd:YAG laser," *Opt. Lett.* **14**, 609–611 (1989).
4. T. Day, E. K. Gustafson, and R. L. Byer, "Sub-hertz relative frequency stabilization of two-diode laser-pumped Nd:YAG lasers locked to a Fabry–Perot interferometer," *IEEE J. Quantum Electron.* **28**, 1106–1116 (1992).
5. N. Uehara and K. Ueda, "193-mHz beat linewidth of frequency-stabilized laser-diode-pumped Nd:YAG ring lasers," *Opt. Lett.* **18**, 505–507 (1993).
6. N. M. Sampas, E. K. Gustafson, and R. L. Byer, "Long-term stability of two-diode-laser-pumped nonplanar ring lasers independently stabilized to two Fabry–Perot interferometers," *Opt. Lett.* **18**, 947–949 (1993).
7. J. Hough, D. Hills, M. D. Rayman, Ma L.-S., L. Hollberg, and J. L. Hall, "Dye-laser frequency stabilization using optical resonators," *Appl. Phys. B* **33**, 179–185 (1984).
8. J. C. Bergquist, W. M. Itano, F. Elsner, M. G. Raizen, and D. J. Wineland, "Single ion optical spectroscopy," in *Light-Induced Kinetic Effects on Atoms, Ions and Molecules*, L. Moi, S. Gozzini, C. Gabbanini, E. Arimondo, and F. Strumia, eds. (ETS Editrice, Pisa, Italy, 1991) p. 291–299.
9. J. L. Hall, "Frequency stabilized lasers—a parochial review," in *Frequency Stabilized Lasers and Their Applications*, Y. C. Chung, ed., *Proc. Soc. Photo-Opt. Instrum. Eng.* **1837**, 2–15 (1992).
10. R. W. P. Drever, J. L. Hall, F. V. Kowalski, J. Hough, G. M. Ford, A. J. Munley, and H. Ward, "Laser phase and frequency stabilization using an optical resonator," *Appl. Phys. B* **31**, 97–105, (1983).
11. K. Nakagawa, Y. Shimizu, T. Katsuda, and M. Ohtsu, "Highly stable and high power Nd:YAG lasers," in *Frequency Stabilized Lasers and Their Applications*, Y. C. Chung, ed., *Proc. Soc. Photo-Opt. Instrum. Eng.* **1837**, 40–48 (1992).
12. J. L. Hall and T. W. Hänsch, "External dye-laser frequency stabilizer," *Opt. Lett.* **9**, 502–504 (1984).
13. G. A. Kerr, N. A. Robertson, J. Hough, and C. N. Man, "The fast frequency stabilization of an argon laser to an optical resonator using an extra-cavity electro-optic modulator," *Appl. Phys. B* **37**, 11–16 (1985).
14. K. Nakagawa, A. S. Shelkovich, T. Katsuda, and M. Ohtsu, "Fast frequency stabilization of a diode-laser-pumped monolithic Nd:YAG laser with an extra-cavity electro-optic modulator," *Opt. Commun.* (to be published).

レーザー解説

半導体レーザーの周波数制御 — 高効率位相変調と非線形周波数変換 —

大津元 —*,**

(1994年6月30日 受理)

Frequency Control of Semiconductor Lasers — Highly Efficient Phase Modulation and Nonlinear Frequency Conversion —

Motoichi OHTSU*.**

(Received June 30, 1994)

Performances of an optical frequency comb generator and nonlinear optical frequency conversion of semiconductor lasers were reviewed. They are studied for realizing frequency reference grids for an accurate and wideband optical frequency sweep. Semiconductor lasers were used as light sources by improving their frequency stability to 2.1×10^{-12} and by reducing their field spectral linewidth to 7 Hz. A precise and continuous frequency sweep for 64 GHz was realized by heterodyne-type optical phase locking. Frequency reference grids with a span of 0.1 THz was realized by the optical frequency comb generator. Second harmonics, sum-frequency and difference frequency signals were generated by using nonlinear optical crystals for the 180-577 THz range, i. e., the wavelength range of 0.52-1.67 μm .

Key Words: Semiconductor, Frequency, Comb, Nonlinear

1. まえがき

光源としてのレーザー装置の理想的な形態の一つとして、

- ① 高コヒーレントな光、
- ② 広帯域にわたり精密に周波数掃引可能な光、

を発生することが考えられる。すなわちマイクロ波周波数領域の電磁波のように滑らかな波としての光を発生させる装置ということができる。このような高性能の光源が実現すれば、計測、加工、通信などの工学的システムに適用可能であるばかりでなく、量子光学、原子物理学などの理学的研究を推進する道具として使え、

* 東京工業大学大学院総合理工学研究科(〒227横浜市緑区長津田4259)

** 神奈川科学技術アカデミー大津「フォトン制御」プロジェクト(〒213 川崎市高津区坂戸3-2-1)

* Interdisciplinary Graduate School of Science and Engineering, Tokyo Institute of Technology, (4259 Nagatsuta, Midori-ku, Yokohama 227)

** Ohtsu "Photon Control" Project, Kanagawa Academy of Science and Technology, (3-2-1 Sakado, Takatsu-ku, Kawasaki 213)

これにより新しい現象が発見されれば、さらに性能の高いレーザー装置を開発する基礎知識が得られる。

以上の考え方にに基づき我々は従来より半導体レーザーを対象として研究を行ってきた。これまでに上記の①に関する研究内容は多数の研究機関で活発な研究が行われている^{1,2)}。それに対し②は近年国内外で研究が活発になりつつある。高コヒーレントな電磁波源であるマイクロ波発振器では周波数を広帯域掃引することは難しいが、半導体レーザーであればそれが可能になると思われる。そこで本稿では半導体レーザーを基本光源として用い、特に②を実現するための研究をご紹介したい。

2. レーザーシステムの構成

波長250 nm付近の紫外域には半導体工学の基本元素であるシリコン原子の共鳴波長が存在する³⁾、また波長1.4~2 μm 以上の赤外域の光は可視光に比べ人体の眼に対してずっと安全である。従って、0.2~2.0 μm の波長域で周波数掃引ができると多数の応用が可能となる。ここではこの波長域、すなわち周波数150 THz~1.5 PHzの範囲での掃引が可能な光源を実現することを目標とする。すなわち周波数掃引可能範囲は約1 PHzである。

現在までのところこのような広帯域周波数掃引を単独のレーザーで実現することは困難と考えられるので、我々は複数のレーザー、特に半導体レーザーを組み合わせたシステムを考えている。最近では各種の半導体レーザーが入手可能であり、その主な発振波長帯は1.5 μm 、1.3 μm (光通信用)、1.48 μm (光ファイバ増幅器励起用)、0.8 μm (光ディスク読み出し用)、0.6 μm (光計測用など)、にわたっている。さらに最近では波長0.49 μm の青色光の半導体レーザーの進歩がめざましい^{4,5)}。このような技術的進歩の現状を考えると複数の半導体レーザーを用いることが有利であることがわかるが、この他にも他種のレーザーを複数用いる場合にくらべシステム全体の寸法が小さく保てること、

消費電力が低いこと、など実用上の利点がある。以下に半導体レーザーを用いたシステムにおいて1.節の①を実現するための方法を示す。

2.1 高コヒーレント化

1.節の①を実現するために本システムで使用する半導体レーザーの高コヒーレント化を行う。すなわち光の位相または周波数揺らぎを抑圧する。揺らぎの大きさはパワースペクトル密度により表されるが、そのうちのフーリエ周波数がほぼ1 Hz以下の低周波揺らぎを抑圧するために気体原子、分子の共鳴スペクトルを周波数基準として用い、これにレーザー周波数が安定化されるように制御を行う。たとえばルビジウム原子の共鳴スペクトルを周波数基準として用い、波長0.8 μm の半導体レーザーの注入電流を制御して周波数安定化し、周波数安定度 2.1×10^{-12} (フーリエ周波数0.5 mHzにおいて)が得られている⁶⁾。この周波数安定化システム全体が計算機により制御され最適動作している。また、波長1.5 μm 帯ではアンモニア、水、アセチレン、シアンなどの気体分子スペクトルが周波数基準として用いられるが、最近ではアセチレンやシアンの飽和吸収スペクトルが周波数基準に用いられるようになった⁷⁾。そのスペクトルの幅の測定値は従来用いられていた線形吸収スペクトルに比べると1/100程度狭く、数 MHzであるので高い制御利得を得るのに有利である。

より高いフーリエ周波数(およそ数 MHzまで)領域での揺らぎの大きさはレーザー発振スペクトル線幅により表現されることが多い。最近では半導体レーザー素子製作の段階で歪み超格子・多重量子井戸構造などを導入し、非常に狭いスペクトル線幅のレーザー素子が実現している⁸⁾。例えば波長1.5 μm 帯でスペクトル線幅3.6 k Hzが得られている⁹⁾。ただし、このような素子に対してもさらに揺らぎを抑圧するためには上記の周波数安定化の場合と同様の制御が必要である。この際、周波数安定化の場合にくらべて広いフーリエ周波数範囲での制御、すなわち数 MHz~数100 MHzの制御帯域が必要であ

る。自動制御としては半導体レーザーの注入電流を制御する方法が標準的であり、再現性が高い¹⁰⁾。一方、レーザーの出射光をレーザー自身に再入射したときに自己注入同期が発生することを利用した光帰還の方法も広く用いられている¹¹⁾。両者を同時に用いることにより発振スペクトル線幅が7 Hzまで狭くされている¹²⁾。数 MHz以上の高いフーリエ周波数領域の揺らぎはパワースペクトル密度の値により評価すればよいが、その抑圧のための自動制御装置の設計には通常の電子回路における雑音抑圧のための自動制御系設計と同様の方法を用いればよい¹⁰⁾。

2.2 高精度周波数掃引の方法

周波数を掃引するには掃引可能な半導体レーザー素子が必要である。最近では回折格子をレーザーとともに集積化することにより波長 $1.55\ \mu\text{m}$ の半導体レーザーの発振波長範囲が50 nm(周波数に換算すると6.2 THz)に達する素子も開発されている¹³⁾。将来はこのような広帯域周波数掃引可能な半導体レーザーが多くの波長帯で実現することを期待して、ここではこのような半導体レーザー素子を複数用いることを考える。ただし、このような半導体レーザー素子の温度や注入電流を掃引したのみでは周波数掃引精度は必ずしも高くない。計算機を用いて温度や注入電流を掃引するシステムも考案されているが¹⁴⁾、ここでは2.1節で実現した高コヒーレントな特性を維持したまま掃引することを考える。

このための第一段階としてFig. 1に示すように原子、分子の共鳴スペクトルを周波数基準に用いて周波数安定化された半導体レーザーを基準とし、もう一台の半導体レーザーの注入電流を制御してヘテロダイン形の位相同期を施す。このレーザーの位相および周波数の揺らぎは基準レーザーの揺らぎまで抑圧可能である。また、このレーザーの周波数は基準周波数と局部発振器用マイクロ波発振器の周波数との和になるので、位相同期を施したままマイクロ波周波数を

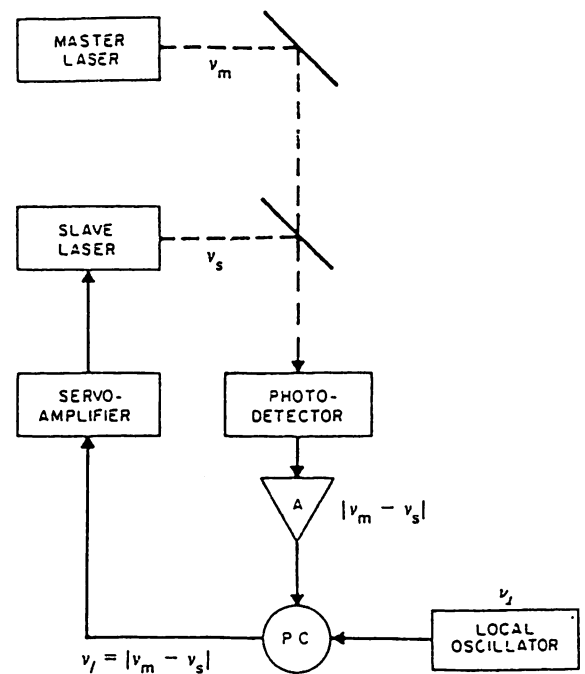


Fig. 1 Experimental setup for heterodyne-type optical phase locking. P. C.: Phase comparator. ν_m , ν_s , ν_l : Frequencies of a master laser, a slave laser and a microwave local oscillator, respectively, where the master laser frequency ν_m is locked to an atomic or a molecular resonance spectral frequency.

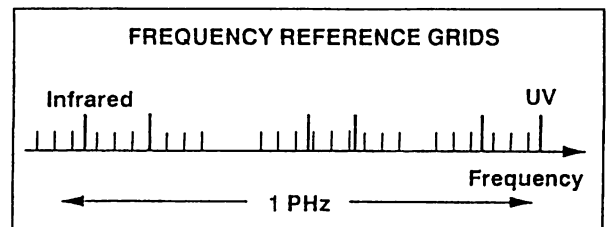


Fig. 2 Schematic explanation of frequency reference grids. Two kinds of grids are shown. They are; ① the grid with several THz span and several GHz separation between each frequency component (, represented by shorter lines in this figure). ② the grid with about 1 PHz span and several THz separation between each frequency component (, represented by longer lines in this figure.)

掃引すれば、レーザー周波数は安定に、かつマイクロ波周波数の掃引精度と同等の精密さを

保ったまま掃引される。この方法により少なくとも64 GHzの範囲にわたり周波数掃引できる¹⁵⁾。

これ以上の周波数範囲にわたり精密に掃引するには、さらにいくつかの技術を開発することが必要であるが、その一つの試みとして、我々はFig. 2に示すように周波数軸上において適当な周波数間隔で、広い周波数範囲にわたって周波数基準の格子を形成することを行っている。これは次の二つからなる：

- ① 数 GHzの間隔で、数THzの範囲にわたる周波数基準の格子；この格子の一つを基準としてヘテロダイン形の位相同期技術により周波数掃引可能レーザーを制御し、周波数を数 GHzの範囲にわたって精密掃引し、その後はとなりの格子を基準にして同様の精密掃引を行う。以下、これを繰り返せば数 THzの範囲にわたり精密周波数掃引する方法になる可能性がある。
- ② 数 THzの間隔で、約1 PHzの範囲にわたる周波数基準の格子；この数値は2.節冒頭で示した周波数掃引範囲を実現するためのものである。

以上の二つの周波数基準の格子のうち前者を実現するために我々は高効率位相変調器である光周波数コム発生器を開発している。後者のためには非線形光学結晶を用いた周波数変換技術を開発している。そこで、以下の節ではこれらの二つの話題についてご紹介したい。

3. 光周波数コム発生器

数 GHzの間隔で数THzの範囲にわたり周波数基準の格子を作る方法の一つはレーザー光を数 GHzの変調周波数で高効率に位相変調することである。そのための装置の一つがFig. 3に示す光周波数コム発生器である¹⁶⁾。発生した変調側波帯が周波数基準の格子となるが、この側波帯のスペクトルの分布がFig. 3に示すように櫛(Comb)のように見えることからこの名前がつけられた。マイクロ波周波数帯ではコム発生器はすでに実用的に用いられている装置であ

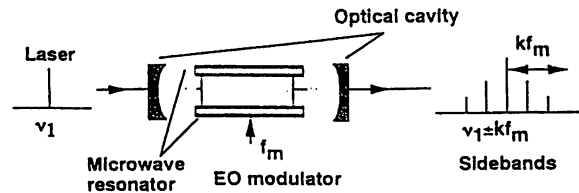


Fig. 3 Schematic configuration of an optical frequency comb generator.

るが、ここでは光周波数領域でこれを実現する。

我々は電気光学効果を利用した位相変調器を用いた。この電気光学結晶をファブリ・ペロー共振器の中に設置し、変調用のマイクロ波周波数 f_m をファブリ・ペロー共振器の自由スペクトル域FSRの整数倍にする。これによりファブリ・ペロー共振器内を往復する光が同じ位相で変調され、高効率の位相変調が実現する。電気光学結晶をマイクロ波共振器内に設置し、結晶上でのマイクロ波電界強度を大きくする。ここで結晶中でのマイクロ波と光の速度が一致するようにマイクロ波共振器が設計されている。

この光周波数コム発生器は損失がマイクロ波で変調されているファブリ・ペロー共振器と見なすことができる。従って、ファブリ・ペロー共振器損失が小さくなった瞬間に入射光は装置を透過するので、透過光は時間軸上ではファブリ・ペロー共振器の共振曲線を反映してローレンツ形のパルス列となる。その繰り返し周期は $2f_m$ である。変調指数を β 、ファブリ・ペロー共振器のフィネスを F とするとパルス幅は

$$\tau = 1/2F\beta f_m \tag{1}$$

となる。この装置は元来、このように超短光パルス発生のために考案された¹⁷⁾。関連する内容については本特集号の森本、小林両氏による解説記事をご一読頂きたい。

ここでは周波数軸上で議論する。発生した変調側波帯の間隔は f_m であるが、第 N 次の側波帯のパワー P_N は上記のローレンツ形曲線のフーリエ変換により求められ

$$P_N = \gamma_{FP} P_i (\pi/2F\beta)^2 \exp(-\pi |N|/F\beta) \tag{2}$$

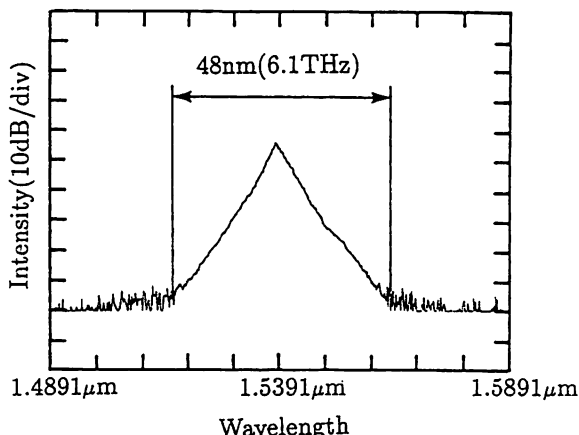


Fig. 4 Spectrum of the envelope of optical frequency combs observed by an optical spectrum analyzer, with the resolution of 0.2 nm.

により与えられる。ここで η_{FP} はファブリ・ペロー共振器の効率、 P_i は入射光パワーである¹⁸⁾。

我々は電気光学結晶として長さ23mmのLiNbO₃結晶を用い、波長1.5 μ mの光に対して動作する光周波数コム発生器を製作した。結晶の両端面に反射率99%の誘電体多層膜を蒸着しファブリ・ペロー共振器とした。そのフィネス F と効率 η_{FP} の測定値はそれぞれ250, 60%であった。結晶はTE₁₀モードのマイクロ波導波路を利用して作ったマイクロ波共振器に設置した。変調周波数 $f_m = 5.87$ GHz, パワー10 Wのマイクロ波を加えたところ、変調指数 $\beta = 0.22\pi$ が得られた。これらの数値を(1)式に代入すると、推定されるパルス幅 τ の値は0.5 psとなる。

Fig. 4に光周波数コム発生器の出力光のスペクトル形状測定結果を示す¹⁸⁾。この測定には光スペクトラムアナライザを用いたが、その分解能は変調周波数 f_m の値より大きいため、この図に描かれているものは多数の側波帯の包絡線の形状であり、それは(2)式で表される指数関数の形をしている。このスペクトル形状の幅は測定系の雑音により制限されているが、図によると6.1 THz(波長に換算すると48 nm)である。すなわち1040本の側波帯が得られている。高次の側波帯のパワーは小さいが、他のレーザー光を用いてヘテロダイン検出を行えば光スペクト

ラムアナライザによる測定の場合よりずっと高い感度を得られるので、さらに多数の側波帯が測定されると期待される。側波帯の包絡線の幅の最大値は電気光学結晶の屈折率の波長分散によって制限されると推定されているが¹⁶⁾, Fig. 4の光周波数コム発生器の場合、その幅の値は約7 THzと見積られている。

この他に光導波路形電気光学位相変調器を用いて光周波数コム発生器を構成し、マイクロ波と光のパワーを狭い導波路に集中させ、高効率の位相変調を実現する試みもある¹⁹⁾。この様にして数GHzの間隔で、数THzの範囲にわたり周波数基準の格子が実現している。さらに、光周波数コム発生器の出力の側波帯の一つと、もう一台の非変調レーザーとの間でヘテロダイン形位相同期が実現している¹⁶⁾。この場合光周波数コム発生器への入力光ともう一台の非変調レーザー光の周波数差が0.5 THzに相当するが、このように大きな周波数差での位相同期は、本研究が目指す精密な周波数掃引のための基礎技術として有用と考えられる。

4. 非線形光学結晶を用いた周波数変換

数THzの間隔で約1 PHzの範囲にわたる周波数基準の格子を作る方法の一つは非線形光学結

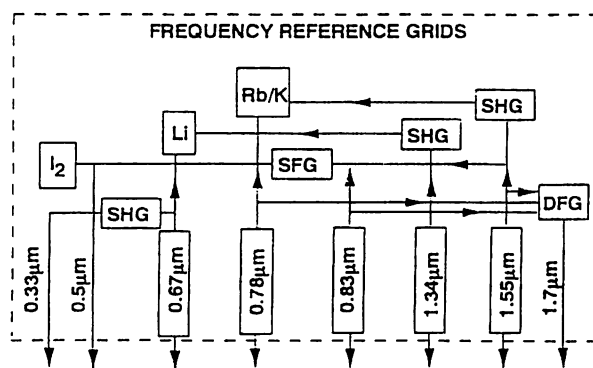


Fig. 5 Schematic explanation of generating frequency reference grids by the techniques of second harmonics generation (SHG), sum-frequency generation (SFG), and difference-frequency generation (DFG) using nonlinear optical crystals. This figure also shows that some of these generated lights are frequency-locked to atomic or molecular resonance spectral frequencies.

晶を用いた周波数変換である。たとえばFig. 5には市販の波長0.67, 0.78, 0.83, 1.34, 1.55 μm 半導体レーザーの第二高調波発生(SHG), 和周波数発生(SFG), 差周波数発生(DFG)により波長0.33~1.7 μm の範囲(周波数に換算すると176 THz~910 THz)をカバーする光を得る概念を示している。これらの発生光の周波数はRb, K, Li, I_2 などの原子, 分子の共鳴スペクトル周波数に合致するので, これらに固定されるよう周波数安定化できることを示している。これにより0.7 PHzの範囲にわたる周波数基準の格子を作ることができる。

なお, この図中の各光周波数の間隔は数THzに比べればまだ大きい。しかし, 半導体レーザーは結晶成長の段階で活性層の化合物半導体の組成のモル比を微調することにより発振波長を微調できることに注目すると, 上記の五種の半導体レーザーの波長のまわりに細かく波長を調節することができる。これにより近い将来, 不等間隔ながら平均数 THzの間隔で多数の周波数基準の格子を作ることが可能であると考えられる。

以上の構想に基づき, 非線形光学結晶を用いたSHG, SFG, DFGの実験を行ったので, 以下ではそれらの概略を記す。

(1) 非線形光学結晶としてKTPを用いて波長1.5 μm (電極を分割した多重量子井戸DFB型InGaAsPレーザー(出力パワー50 mW)を使用)の光のSHGを発生させた²⁰⁾。KTPは大きな非線形光学係数を持ち, 位相整合の際の結晶方位角, 温度の範囲許容幅が大きいので従来よりよく使われている。ここではタイプIIの位相整合を用いた。SHG効率を上げるために長さ1 cmのKTPをファブリ・ペロー共振器中に設置し, 波長1.5 μm 光パワーを蓄積した。パワー1.0 μW のSHGが発生した。

(2) 上記(1)の波長1.5 μm の光と波長0.78 μm の光(ファブリ・ペロー共振器型AlGaAsレーザー(出力パワー50 mW)を使用)との間のSFG, DFGを行った²¹⁾。これらの波長に対してSFG, DFGを行うとき, 上記SHGの場合と同じくKTPが使用できることが特長である。ここではSHGの場合のようなファブリ・ペロー共振器を使っていないので, SFG, DFGの出力パ

ワーはそれぞれ0.7 μW , 0.3 μW と小さい。SFGの結果生じた緑色光(波長0.52 μm)の周波数は波長1.5 μm レーザーの温度, 注入電流を変化させて周波数を掃引することにより100 GHz掃引することができた。また計算によると波長0.78 μm レーザー周波数を掃引すれば350 GHz掃引可能であることが見積られた。これらより, 両レーザー光の周波数掃引を適切に組み合わせればSFGの緑色光の周波数の連続掃引範囲1 THz, 全掃引範囲50 THz(波長に換算すると0.51~0.56 μm の範囲)が得られることが見積られた²¹⁾。

一方, DFGの結果生じた赤外光の周波数はレーザーの温度, 注入電流を変化させることにより38 Hz(波長に換算すると1.38~1.67 μm)の範囲で掃引可能であった²²⁾。

以上の周波数変換で得られた光のパワーは小さいが, 将来は結晶の性能やパワー蓄積用のファブリ・ペロー共振器の性能の向上, さらに光増幅器の使用, などにより高パワー化が期待される。ここではこれらの周辺技術の向上に先行して, 現在可能な技術により周波数基準の格子を作ることを試みている。

なお, このような低パワーの光でもその周波数を原子, 分子の共鳴スペクトルに固定するための制御に使うことができる。そのような例として, 上記(2)のSFGの結果得られた緑色光の周波数を I_2 分子の共鳴スペクトル周波数に固定するための制御が行われ, 周波数揺らぎが0.5 MHz以下に抑圧されている²³⁾。さらにK原子の共鳴スペクトル周波数を仲介とするポンプ・プローブ分光法により波長0.77 μm AlGaAsレーザー光の周波数と波長1.54 μm InGaAsPレーザーのSHG光の周波数を固定する実験も行われている²⁴⁾。これらの実験は得られた周波数基準の格子の周波数安定度を向上させるために試みられた。

我々の他にも非線形光学結晶を用いた周波数変換の実験が国内外で活発に進められている。たとえばごく最近RDA結晶を用いて波長0.69 μm の赤色半導体レーザー光のSHGを実現し, 紫外光を得た報告がある²⁵⁾。結晶をパワー蓄積用ファブリ・ペロー共振器の中に設置して

SHG効率を上げ、紫外光パワー258 μW を得ている。この他、非線形光学結晶を用いた周波数基準の格子として二台のレーザーの周波数の平均値の周波数を次々発生させる試み²⁶⁾、また、半導体レーザーでは実現していないが、光パラメトリック発振器とコム発生器を組み合わせるものが報告されている²⁷⁾。

5. まとめ

高コヒーレント、かつ広帯域にわたり精密に周波数掃引可能な光源の実現をめざした研究について御紹介した。このような装置はレーザーを開発したり使ったりする立場から見ると「夢の光源」の一形態といえよう。これに対し、ここで示した研究例はその実現へ向けて踏み出した第一歩にすぎないが、半導体レーザーを基本光源として用いたシステムにおいて周波数安定度 2.1×10^{-12} 、発振スペクトル線幅7 Hz、ヘテロダイン形位同期期により精密かつ連続周波数掃引範囲64 GHz、光周波数コム発生器により間隔5.87 GHz、範囲6.1 THzにわたる周波数基準の格子が実現している。さらに非線形光学結晶を用いた周波数変換により、波長0.52~1.67 μm (周波数で表すと180~577 THz)の範囲で数本の周波数掃引可能な周波数基準の格子を実現させた。

今後は材料、デバイス、制御システムなどの知見と技術を融合し、駆使して目標実現へ向けてさらに研究が進展すると期待される。

謝辞

光周波数コム発生器に関し御教示頂いた大阪大学基礎工学部の小林哲郎、森本朗裕両先生、半導体レーザーに関し御討論頂いた日立製作所中央研究所の岡井誠博士、さらに原稿内容に関し御検討頂いた東京工業大学総合理工学研究科の興梠元伸博士に感謝致します。なお、本研究の一部は文部省科学研究補助金(重点領域研究・課題番号04228103、一般研究(B)・課題番号05452110)、テレコム先端技術研究センター「電気通信フロンティア研究開発」助成金、科学技術庁科学振興調整費の補助を受けて行われた。

参 考 文 献

- 1) M. Ohtsu: *Highly Coherent Semiconductor Lasers*, Artech House, Inc., Boston (1992).
- 2) M. Ohtsu, K. Nakagawa, M. Kourogi and W. Wang: *J. Appl. Phys.* 73 (1993) R1.
- 3) 清水富士夫: 応用物理 60 (1991) 864.
- 4) 藤田茂夫: 電子情報通信学会誌 76 (1993) 833.
- 5) 石橋晃: 応用物理 63 (1994) 596.
- 6) J. Kawakami, M. Kourogi, and M. Ohtsu: *Jpn. J. Appl. Phys.* 33 (1994) 1623.
- 7) M. de Labachellerie, C. Latrasse, K. Nakagawa, and M. Ohtsu: *Tech. Digest of the Int. Sympo. on Atomic Freq. Standards and Coherent Quantum Electron.*, *Jpn. Soc. Appl. Phys.* (1993) 5.
- 8) 岡井誠: 応用物理 63 (1994) 2.
- 9) M. Okai, M. Suzuki, T. Taniwatari, and N. Chinone: *Jpn. J. Appl. Phys.* 33 (1994) 2563.
- 10) M. Ohtsu: *J. Lightwave Technol.* 6 (1988) 245.
- 11) N. A. Olsson and J.P. Van der Ziel: *J. Lightwave Technol.* 5 (1987) 510.
- 12) C.-H. Shin and M. Ohtsu: *Opt. Lett.* 15 (1990) 1455.
- 13) Y. Tohmori, F. Kano, H. Ishii, Y. Yoshikuni, and Y. Kondo: *Electron. Lett.* 29 (1993) 1350.
- 14) B. Glance, O. Scaramucci, T.L. Koch, and J. Stone: *Electron. Lett.* 25 (1989) 1193.
- 15) K. Kuboki and M. Ohtsu: *IEEE J. Quantum Electron.* 25 (1989) 2084.
- 16) M. Kourogi, K. Nakagawa, and M. Ohtsu: *IEEE J. Quantum Electron.* 29 (1993) 2693.
- 17) T. Kobayashi, T. Sueta, Y. Cho, and Y. Matsuo: *Appl. Phys. Lett.* 21 (1972) 341.
- 18) M. Kourogi, T. Enami, and M. Ohtsu: *IEEE Photonics Technol. Lett.* 6 (1994) 214.
- 19) M. Kourogi, T. Enami, M. Ohtsu, and T. Saito: *Conference on Lasers and Electro-Optics Vol. 8 (1994) OSA Technical Digest Series (Optical Society of America, Washington, D.C., 1994) 272.*
- 20) W. Wang, K. Nakagawa, Y. Toda, and M. Ohtsu: *Appl. Phys. Lett.* 61 (1992) 1886.
- 21) W. Wang and M. Ohtsu: *Opt. Commun.* 102 (1993) 304.
- 22) W. Wang and M. Ohtsu: *Opt. Lett.* 18 (1993) 876.
- 23) W. Wang and M. Ohtsu: *Jpn. J. Appl. Phys.* 33 (1994) 1648.
- 24) W. Wang, A.M. Akulshin, and M. Ohtsu: *IEEE Photonics Technol. Lett.* 6 (1994) 95.
- 25) M.J. Brinkman, A. Romanovsky, and D. A. G. Deacon: *Conference on Lasers and Electro-Optics Vol. 8 (1994) OSA Technical Digest Series (Optical Society of America, Washington, D.C., 1994) CPD18.*
- 26) H. R. Telle, D. Meschede, and T. W. Hänsch: *Opt. Lett.* 15 (1990) 532.
- 27) N. C. Wong: *Opt. Lett.* 17 (1992) 1155.

Pulling of the emission frequency of an injection laser by Doppler-free absorption resonances in an intracavity cell

A M Akul'shin, M Ohtsu

Abstract. Optical frequency locking of two injection lasers was achieved with the aid of a Doppler-free absorption resonance, as the result of simultaneous interaction of radiations from two lasers with rubidium vapour inside an intracavity cell. Narrowing of the emission line width by a factor of 8 and a reduction in the frequency noise by 15 dB were achieved in a band up to 350 kHz. A nonlinear frequency pulling by a resonance of coherent population trapping in an intracavity cell was demonstrated for the first time.

Injection lasers are used widely in spectroscopy, metrology, and fibre-optic communications because of their outstanding spectral characteristics, and also because of their relative simplicity and low cost. Frequency chains for linking the optical and microwave ranges, based on injection lasers, have been proposed and are being actively developed [1, 2]. Generation of the second harmonics of injection lasers and generation of the sum-frequency radiation of two lasers makes it possible to access the green and blue parts of the visible range [2]. Optical heterodyning can be used to generate a beat signal at the difference frequency, which can be tuned rapidly from the rf to the microwave ranges. This can be done by employing injection lasers emitting at any wavelength. However, the use of atomic absorption lines as the frequency standards can increase the reproducibility and long-term stability of the emission frequency. Moreover, Doppler-free spectroscopy based on the D lines of Li, K, Rb, and Cs in a system of unidirectional beams from two independent lasers provides a series of contrast resonances with the following important property: their spectral positions depend on the difference frequency of the two lasers [4]. These resonances are due to compensation of rate-selective optical pumping or coherent population trapping (Λ resonances). The use of these resonances has made it possible to lock the frequencies of two injection lasers by a single electronic servo system and to obtain a stable beat signal at the frequencies of the hyperfine splitting of rubidium [3, 4].

An optical method for locking two injection lasers has also been proposed: the locking is due to pulling of the

emission frequency by a narrow Λ resonance resulting from the interaction of radiations from two lasers in an intracavity nonlinearly absorbing cell [3]. In the present paper we report the first experimental realisation of optical locking of the frequencies of two lasers. Fig. 1 shows the optical part of the apparatus. A distributed-feedback injection laser was tuned to the D_2 absorption line of rubidium ($\lambda = 780$ nm) at 37 °C. In the absence of external optical feedback the width of the emission line was 30 MHz and the output power was 10 mW. An injection laser of this type made it possible to achieve stable single-frequency emission with an external nonselective resonator cavity containing a cell. The cavity length was 7 cm. The sealed glass cell was 3 cm long and had no antireflection coatings on its windows. The cell contained saturated vapour of ^{87}Rb without a buffer gas and was placed on a support whose temperature was controlled. After passage through a beam-splitting mirror the radiation intensity at the entry to the cell was 17 mW cm^{-2} . Continuous frequency tuning was performed by altering the length of the external cavity

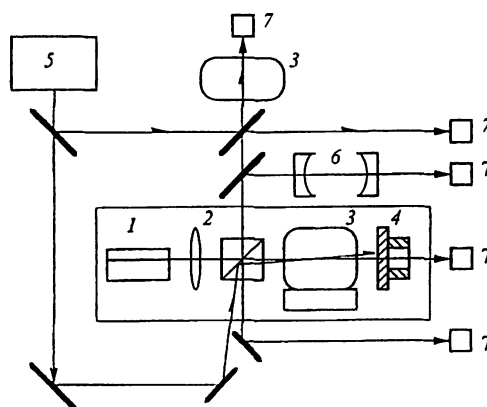


Figure 1. Optical part of the apparatus: (1) distributed-feedback injection laser; (2) collimating micro-objective (numerical aperture 0.5); (3) cell with rubidium vapour; (4) 100%-reflecting dielectric mirror with a piezoelectric ceramic support; (5) injection laser with an external dispersive cavity; (6) confocal interferometer; (7) photodiode.

or the pump current.

The spectral characteristics were determined with a confocal Fabry–Perot interferometer (free spectral range 1.5 GHz, instrumental width 50 MHz) by a heterodyne method in which an independent injection laser with an external dispersive cavity was used. The width of the emission line of this laser did not exceed 100 kHz in the

A M Akul'shin P N Lebedev Physics Institute, Russian Academy of Sciences, Moscow

M Ohtsu Tokyo Institute of Technology, Yokohama, Japan

Received 27 April 1994 675–614
Kvantovaya Elektronika 21 (7) 000–000 (1994)
Translated by A Tybulewicz

free-running regime [4].

Since the intensity of a standing wave in the intracavity cell considerably exceeded the intensity needed for saturation of the optical transitions corresponding to the D_2 absorption line of rubidium (for the cyclic $F = 2 - F' = 3$ transition this intensity was $I_{\text{sat}} = 0.14 \text{ mW cm}^{-2}$, whereas for 'open' transitions the value of I_{sat} was a further 2–3 orders of magnitude less), the profile of the absorption spectrum was strongly saturated. The emission frequency of the injection laser experienced nonlinear pulling by Doppler-free absorption resonances. This effect appeared most strongly for the $F = 2 - F' = 3$ transition and at adjacent cross resonances. For example, when the rubidium vapour temperature was $32 \text{ }^\circ\text{C}$, the self-stabilisation factor S for the $F = 2 - F' = 3$ transition, measured with the interferometer, was 6.2. The frequency noise of the radiation in a band from 100 Hz to 300 kHz then decreased by 10 dB, in agreement with theoretical estimates [5], and the width of the emission line decreased by a factor of 8 (from 4 MHz to 500 kHz) when the averaging time was 1.5 s.

The radiation from a highly coherent laser was injected into the cavity via a beam-splitting mirror in order to saturate further the absorption in the intracavity cell and to induce a Λ resonance. The intensity of the radiation from the injection laser with an external dispersive cavity was about 8 mW cm^{-2} at the entry to the cell. The angle between the two laser beams did not exceed 5 mrad.

The radiation of the injection laser with an external dispersive cavity, tuned to the $F = 2 - F' = 2$ transition, enabled us to realise stronger pulling of the emission frequency by a contrast resonance due to the interaction of the two laser beams with rubidium vapour at frequencies of the $F = 2 - F' = 2$ and $F = 2 - F' = 3$ transitions. This resulted in mutual frequency locking of the two lasers with an offset equal to the splitting of the $F' = 2$ and $F' = 3$ sublevels of the excited state. It manifested itself by stabilisation of the frequency of the beats of the radiation of the two lasers. Bleaching of the resonant medium because of coherent population trapping occurred when the two lasers were tuned to different hyperfine sublevels, $F = 2$ and $F = 1$, and the mutual frequency offset was precisely equal to the hyperfine splitting of the ground state of ^{87}Rb .

By way of illustration, Fig. 2 shows a fragment of the absorption profile in the vicinity of the $F = 1 - F' = 2$ transition, recorded in the external cell when unidirectional beams from two lasers were used and the highly coherent laser was tuned to the $F = 2 - F' = 2$ transition. The radiation from this laser was blocked at the entry to the

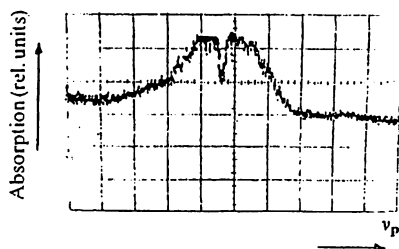


Figure 2. Doppler-free absorption peak in an external cell, induced by compensation of the optical pumping with a Λ resonance of width $\sim 6 \text{ MHz}$, resulting from the coherent population trapping at the peak when the radiation from the injection laser with an external dispersive cavity was blocked at the entry to the intracavity cell.

intracavity cell. A Λ resonance was observed against the background of a Doppler-free absorption peak due to the compensation of the optical pumping. The width of this resonance ($\sim 6 \text{ MHz}$) was governed by the relaxation time of the ground state, by the field broadening, and by the width of the emission lines of the two independent lasers.

When the Λ resonance occurred in the intracavity cell, frequency pushing in the case of the nonlinear absorption peak and pulling of the emission frequency to the centre of the Λ resonance were observed (Fig. 3). The upper part of Fig. 3 shows the transmission resonance of the interferometer. When the cavity length was varied, discontinuities were found in the variation of the emission frequency. The degree of pulling was deduced from the ratio of the slopes of the interferometer transmission profile inside and outside the locking region. In view of the small width of the Λ resonance the frequency pulling was twice as strong (with the self-stabilisation factor of 15) than in the case

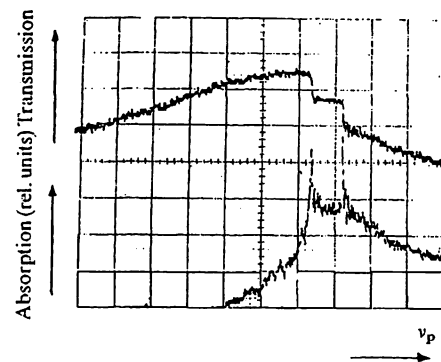


Figure 3. Transmission resonance of the confocal interferometer (upper trace) and the absorption profile in the intracavity cell (lower trace) in the case of nonlinear pulling of the emission frequency by a Λ resonance.

when the two lasers were tuned to the same sublevel.

Such optical locking of the radiation frequency not only makes it possible to obtain a frequency-stable beat signal, and this is true also of the microwave range, but also opens up unique opportunities for further narrowing of the emission line of a laser with a nonlinearly absorbing cell, so that the strong optical feedback can be made highly selective.

References

1. Telle H R, Meschede D, Hansch T W *Opt. Lett.* 15 532 (1990)
2. Ohtsu M, Makagava K, Kouroggi M, Wang W J. *Appl. Phys.* 73 (12) R1 (1993)
3. Akulshin A M, Celikov A A, Velichansky V L *Opt. Commun.* 84 139 (1991)
4. Akulshin A M, Celikov A A, Ohtsu M, Nakagava K, Velichansky V L, Vasiljev V V *Technical Digest of Papers presented at International Conference on Quantum Electronics, Vienna, 1992* Vol. 9, p. 24
5. Belenov É M, Velichanskiĭ V L, Zibrov A S, Pak G T, Petrakova T V, Senkov N V, et al. *Kvantovaya Elektron. (Moscow)* 15 1730 (1988) [*Sov. J. Quantum Electron.* 18 1076 (1988)]

FO5

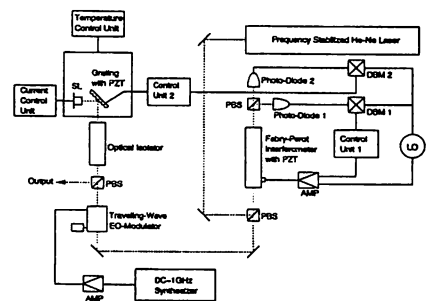
1445

Sideband-locked stabilized semiconductor laser for accurate frequency tunability

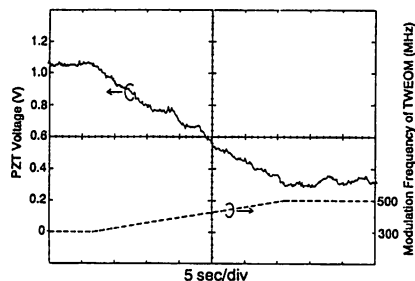
Takashi Fujii, Takuya Nayuki,
Koshichi Nemoto, Motonobu Kourogi,*
Motoichi Ohtsu,* *Electrophysics Department,
Komae Research Laboratory, Central Research
Institute of Electric Power Industry 11-1
Iwado Kita 2-chome, Komae-shi, Tokyo 201,
Japan*

In laser isotope separation, spectroscopy and lidar, a frequency-tunable laser and a technique to stabilize the frequency at a required value are important. There have been several reports on stabilizing the semiconductor laser (SL) frequency. However, frequency stabilization has been achieved only at particular values, for example, the resonance frequency of an atom such as rubidium,¹ or discrete values defined by the free spectral range (FSR) of the Fabry-Perot interferometer (FPI).² In this paper, we propose a new method to stabilize the laser frequency at the required value by locking the sideband generated by passage through the traveling-wave EO-modulator (TWEOM) to an actively stabilized FPI. Moreover, we report the result of frequency stabilization and tunability of a SL using this method.

Figure 1 shows the experimental apparatus of the sideband-locked stabilized SL. The FPI has FSR of 2 GHz, and its length was piezoelectrically modulated at a frequency of 20 kHz. The output beam of a frequency stabilized He-Ne laser is injected into the FPI. By controlling the length of the FPI to pass the maximum



FO5 Fig. 1. Experimental apparatus of sideband-locked stabilized semiconductor laser. PBS: polarizing beam splitter; DBM: double balanced mixer; LO: local oscillator.



FO5 Fig. 2. Variation of modulation frequency of TWEOM and PZT voltage used for controlling diffraction grating angle of SL external cavity.

value of the He-Ne laser beam, the FSR of the FPI can be stabilized.^{2,3} The linewidth of Littrow-type external cavity SL (780 nm, Hitachi Corp. HL7952G) is suppressed by optical feedback to lower than 60 MHz measured by the scanning FPI. After the SL output beam passes through a TWEOM, the spectrum of the SL generates sidebands. The frequency difference between the carrier and the sidebands can be precisely controlled by the modulation frequency of the TWEOM. Therefore, by locking one of the sidebands to the resonant frequency of the stabilized FPI and controlling the frequency difference between the carrier and the sideband, the SL frequency can be stabilized at the required value. The SL frequency is stabilized by controlling the diffraction grating angle with electrical feedback from the signal detected by a photo-diode. In this experiment, the modulation frequency of the TWEOM can be varied from DC to 1 GHz. By using this TWEOM, the gap between resonant frequencies of 2 GHz can be covered in the range in which the sidebands do not overlap each other or the carrier.

Figure 2 shows the variation of the piezoelectric transducer (PZT) voltage used for controlling the diffraction grating angle of the SL external cavity, when one of the sidebands was locked to the stabilized FPI and the modulation frequency of the TWEOM was varied from 300 MHz to 500 MHz. It is shown that the PZT voltage varies following the modulation frequency of the TWEOM. By this operation, the frequency of the carrier stabilized at 300 MHz from the FPI resonant frequency was varied smoothly by 200 MHz because the sideband was locked, and was stabilized at 500 MHz from the FPI resonant frequency. This result shows that the SL frequency can be stabilized at a required value in the frequency range which can be oscillated by the SL without mode hopping.

**Interdisciplinary Graduate School of Science and Engineering, Tokyo Institute of Technology, 4259 Nagatsuta, Midori-ku, Yokohama, Kanagawa 226, Japan*

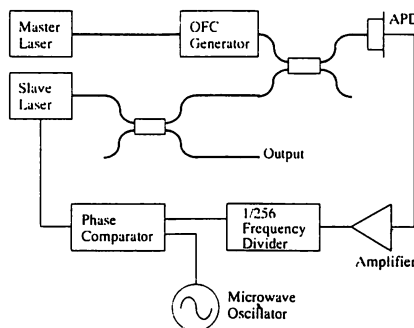
1. M. Kozuma, M. Kourogi, M. Ohtsu, H. Hori, *Appl. Phys. Lett.* **61**, 1895 (1992).
2. H. Tsuchida, M. Ohtsu, T. Tako, *Jap. J. Appl. Phys.* **20**, L403 (1981).
3. R. L. Barger, J. B. West, T. C. English, *Appl. Phys. Lett.* **27**, 31 (1975).

P17

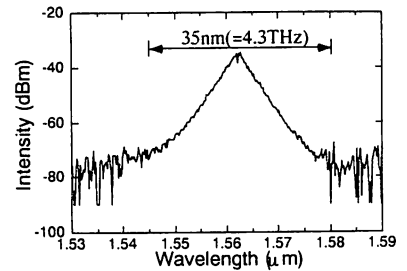
A frequency resettable semiconductor laser system for 1.2 THz frequency span at 1.5 micron wavelength

Takanori Saitoh,* Eric Durand, Motonobu Kourogi,** Motoichi Ohtsu,** Kanagawa Academy of Science and Technology, KSP East Building, Room 408, 3-2-1 Sakado, Takatsuku, Kawasaki, Kanagawa 213 Japan

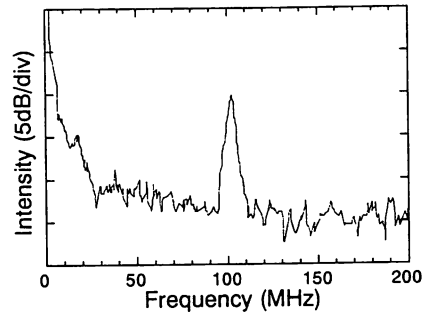
A semiconductor laser source, whose frequency is stabilized and resettable to a definite value, is necessary to realize an optical heterodyne communication. We have developed such a laser system using an optical frequency comb (OFC) generator and two semiconductor lasers at 1.5 μm wavelength. Figure 1 shows a schematic explanation of this laser source. The OFC generator is a Ti-LiNbO₃ waveguide type of OFC generator.¹ An optical waveguide (Anritsu SC3B01A) working at 1.5 μm was used as a phase modulator and an optical resonator was formed by coating high reflection films (refractivities = 97%) on the two facets of the waveguide. The linewidths of the master and slave lasers were reduced to 1 MHz by employing an external cavity structure using a grating. Figure 2 shows a spectral envelope of the comb, i.e., modulation sidebands, which was generated by the waveguide type OFC generator. This OFC generator could generate modulation sidebands whose power was higher than -80dBm in the frequency span as wide as 4.3 THz (\approx 35 nm). The modulation frequency and the modulation index were 13 GHz and 2π , respectively. Figure 3 shows a heterodyne signal between a 47th modulation sideband and a slave laser. A frequency difference between a master laser and the slave laser was 0.6 THz. A frequency offset locking between the 47th modulation sideband and the slave laser was carried out by controlling the injection current of the slave laser so as to nullify the phase difference between the heterodyne signal and a microwave local oscillator signal. A capture range of the frequency offset locked loop was \pm 200 MHz for each



P17 Fig. 1. Schematic explanation of a frequency resettable semiconductor laser system.



P17 Fig. 2. Spectral envelope of an optical frequency comb.



P17 Fig. 3. A heterodyne signal between a sideband and a slave laser under the condition of frequency offset locking.

modulation sidebands. The range of modulation sidebands to which the slave laser can be frequency-offset-locked, was \pm 0.6 THz around their carrier frequency, i.e., the master laser frequency. It was estimated that this range could expand to be up to 2 THz by reducing the noise of the feedback system. The slave laser frequency can be improved by locking the master laser frequency to an absorption line of molecular reference such as acetylene.² Using a multiplex OFC generation system,³ it is expected that one can develop a frequency resettable laser source which can cover almost whole optical window region of a low-loss optical fiber, i.e., as wide as 10 THz.

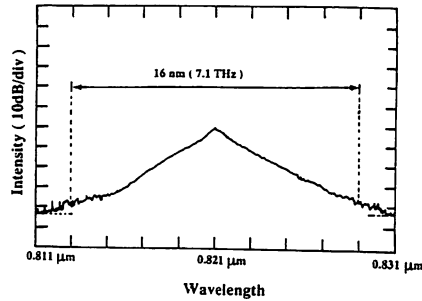
In summary, a frequency resettable laser source at 1.5 μm wavelength was developed by using a waveguide type OFC generator and two semiconductor lasers. A frequency resettable range was \pm 200 MHz for about 100 modulation sidebands which were generated in the range of 1.2 THz around the carrier frequency.

*ANRITSU CORPORATION, 1800 Onna,

Atsugi, Kanagawa 243 Japan

**Interdisciplinary Graduate School of Science and Engineering, Tokyo Institute of Technology, 4259 Nagatuta, Midori-ku, Yokohama, Kanagawa 226 Japan

1. T. Saitoh, *et al.*, IEEE Photon. Tech. Lett. in press, Feb. (1995).
2. S. Kinugawa, *et al.*, Jpn. J. Appl. Phys. 29, 611-612 (1990).
3. T. Saitoh, *et al.*, SPIE's Int. Sym. Opt. Microphotonic, & Laser Tech., San Jose, 2378-26 (1995).



CFG5 Fig. 2. Envelope of the generated sidebands at 0.8- μ m wavelength observed by using an optical spectrum analyzer. Its resolution was 0.5-nm. Modulation frequency: 6.3-GHz.

CFG5 (Invited)

11:30 am

Nonlinear frequency conversion and comb generation for stable reference grids in the visible and near-infrared region

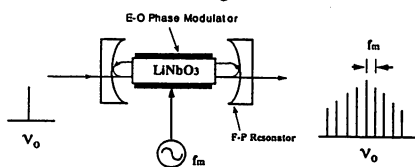
M. Ohtsu,¹ M. Kourogi,² T. Saito,³ Ohtsu
 "Photon Control" Project, Kanagawa Academy
 of Science and Technology, KSP East Room 408,
 3-2-1 Sakado, Takatsu-ku, Kawasaki 213, Japan

Wide-span optical frequency reference grids (OFRG) are required as markers for accurate control and sweep of lightwave frequency. The OFRG covering 0.3–1.7 μ m wavelength region has been realized by employing the technique of nonlinear optical frequency conversion, e.g., SHG, SFG, and DFG, of highly coherent semiconductor lasers by using inorganic crystals.¹

However, as the separation between any two adjacent elements of this OFRG is about 10 THz or even larger, a secondary OFRG is required to fill this gap. To meet this requirement, we have developed an optical frequency comb generator (OFCG). The OFCG is an optical phase modulator employing an electro-optical crystal.² In order to realize a high modulation efficiency, the crystal is installed in an optical cavity (see Fig. 1) and is driven by a microwave whose frequency is integral multiples of the free spectral range of the cavity. Modulation sidebands are efficiently generated and their spectra look like a "comb." Thus, the OFCG can be used as a THz signal generator, and furthermore, as a sub-pico second optical pulse train generator.

A LiNbO₃ was used as the electro-optical crystal and its facets were coated by high-reflection films to form an optical cavity. Figure 2 shows the envelope of the generated sidebands by injecting narrow-linewidth diode laser beam of 0.8- μ m wavelength. Measured frequency span was 7.1 THz, containing more than one thousand sidebands.

We have also fabricated a waveguide-type OFCG by using a Ti-diffused LiNbO₃ waveguide at 1.5- μ m wavelength. Although the finesse of the optical cavity was low, a modulation index as high as 3π was obtained

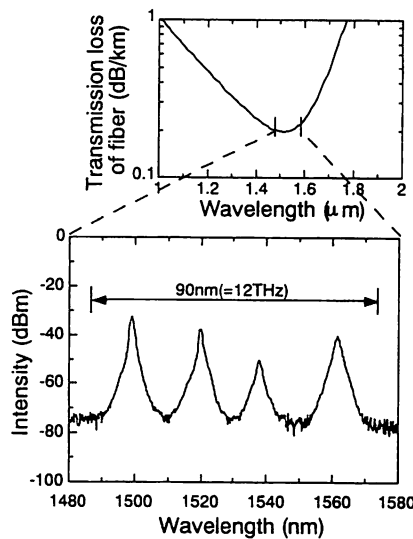


CFG5 Fig. 1. The structure of an optical frequency comb generator.

power will be also demonstrated at the session.

¹Also with Interdisciplinary Graduate School, Tokyo Institute of Technology, 4259 Nagatsuta, Midori-ku, Yokohama 226, Japan; ²Also with ANRITSU Corporation, 1800 Onna, Atsugi, Kanagawa 243, Japan

1. W. Wang, M. Ohtsu, IEEE J. Quantum Electron., in press.
2. M. Kourogi, T. Enami, M. Ohtsu, IEEE Photonics Technol. Lett. 6, 214 (1994).



CFG5 Fig. 3. Envelopes of the sidebands at 1.5- μ m wavelength generated when four diode laser beams were simultaneously injected into the waveguide-type optical frequency comb generator. Modulation frequency: 13-GHz.

due to high optical power density in the guiding layer. Figure 3 shows the spectral profiles of the envelopes measured when four diode lasers with different wavelengths were simultaneously injected into the waveguide via a fiber coupler. Total frequency span of the four envelopes was as wide as 12 THz, which could cover the optical window region of the optical fiber. Optical phase locking between the adjacent family of sidebands can realize an ultra-wide span OFCG. For this phase locking, the beat signal was detected even when the difference in laser carrier frequencies was as large as 1 THz.

A third mirror was installed in front of the OFCG to form a recycling cavity so as to increase the coupling efficiency of the incident light into the OFCG. An increase of 15-dB in the transmitted optical power was obtained. Furthermore, a fourth mirror was installed behind the OFCG to form a cavity for sideband selection, and each sideband was selectively transmitted by tuning this cavity.

Several results of investigating nonlinear optical phenomena observed for high laser

Waveguide type optical frequency comb generator

T.SAITOH(1)(2),E.DURAND(1),M.KOUROGI(1)(3),M.OHTSU(1)(3)

(1)Kanagawa Academy of Science and Technology,
KSP East Building,Room 408,3-2-1 Sakado,
Takatsu-ku,Kawasaki,Kanagawa 213 Japan.

(2)ANRITSU CORPORATION,
1800 Onna,Atsugi,Kanagawa 243 Japan.

(3)Interdisciplinary Graduate School of Science and Engineering of Tokyo Institute of Technology,
4259 Nagatuta,Midori-ku,Yokohama,Kanagawa 226 Japan.

ABSTRACT

A waveguide type optical frequency comb (WG-OFC) generator was developed at $1.5\ \mu\text{m}$ wavelength region by utilizing a waveguide type phase modulator. It was confirmed that the envelope of sidebands spectrum had a width of 4.3THz. A multiplex optical frequency comb generation system was assembled, and modulation sidebands were generated on a space as wide as 10THz. A heterodyne signal between two OFCs whose central frequencies are separated as large as 0.4THz was detected. By utilizing the signal, a frequency offset locked loop system was realized between the two OFCs.

1.INTRODUCTION

Highly accurate laser frequency measurement is an indispensable technique for the development of coherent optical communication systems and precise measurements of physical constants. Measurement of absolute frequency for establishing frequency standards requires a measurement of the frequency difference among lasers which are spaced in a span as wide as several THz. However, it is not straightforward to measure such a large frequency difference because the response bandwidth of conventional photo-detector (PD) is at the most several ten GHz. Although the response bandwidth of a metal-insulator-metal diode is as wide as 2.5THz[1], it is not practical because of its short lifetime. In order to overcome these difficulties, an optical frequency difference measurement system using an optical frequency comb (OFC) generator has been proposed[2]-[7], which is composed of a phase modulator and an optical resonator. It has been reported that a monolithic OFC generator has generated the modulation sidebands in a span as wide

as 6.1THz with the modulation frequency of 5.9GHz at 1.5 μm wavelength region[8]. Recently, we have reported a compact waveguide type optical frequency comb (WG-OFC) generator which was fabricated by coating high reflection films on the facets of a Ti:LiNbO₃ waveguide[9]. As compared with the bulky OFC generator, modulation index and modulation frequency were increased so that a span of the generated modulation sidebands could be extended. In this paper, we presents our recent progress of the experiments on expanding the span and on realizing the frequency link between two OFCs.

2. WAVEGUIDE TYPE OPTICAL FREQUENCY COMB GENERATOR

Figure 1 shows a structure of the WG-OFC generator which is composed of two elements, i. e., a phase modulator and an optical resonator to increase the modulation efficiency. An optical waveguide (Anritsu SC3B01A) working at 1.5 μm wavelength was used as a phase modulator and an optical resonator was formed by coating high reflection films on the two end facets of the waveguide. Their reflectivities were estimated to be higher than 97%. The waveguide was made by diffusing Ti into 38mm long LiNbO₃. The free spectral range (FSR) and the finesse of the optical resonator were measured to be 1.86GHz and 30, respectively. A micro-strip line was formed on the upper surface of the waveguide. By feeding the microwave to the micro-strip line, the phase of the light is modulated. By controlling a thickness of the micro-strip line, a microwave velocity is matched to velocity of a guided laser light. This phase modulator is a traveling wave type because only the light co-propagating along the microwave is modulated. Microwave voltage V_{π} for π radian phase modulation is 7V.

We have evaluated performances of the WG-OFC generator. A laser light output from a distributed feedback laser diode with the linewidth narrower than 10MHz was incident to the waveguide. The output light from the WG-OFC generator was connected to an optical spectrum analyzer for observing the spectral profile of the envelope of the generated modulation sidebands. A microwave signal from a synthesizer was amplified by a traveling wave tube amplifier (TWTA) and was fed to the WG-OFC generator.

Figure 2 shows the envelope of the modulation sidebands measured by the optical spectrum analyzer with the resolution band width of 0.2nm (=25GHz). The modulation frequency was 13.089GHz, which was be 7 times FSR of the optical resonator. The highest microwave power applicable to the device was 1.0W, by which a modulation index of 2.0π was realized. From this figure, the slope of the envelope was found to be 23 dB/THz. Measured frequency span of the envelope, limited by the noise level of the optical spectrum analyzer (the level A in figure 2) was 4.3THz.

3. MULTIPLEX OFC GENERATION

A multiplex OFC generation system was assembled which consisted of only one WG-OFC generator and four lasers. Figure 3 shows an experimental setup of this system. Since these laser frequencies are almost equally spaced on a frequency axis, total span of the four families of OFCs can be much wider than that from the solitary laser. Figure 4 shows a result of the multiplex OFCs. Each OFC has a span of about 20nm, and a total span of the four families of OFCs was 80nm(=10THz). By comparing with the broken curve of this figure, it is found that these OFCs covers almost whole optical window region of a low-loss optical fiber.

The optimum modulation frequency which maximizes the span of OFC, may depend on an incident laser wavelength because of the refractive index dispersion of the waveguide. Figure 5 shows the measured result of this dependency, from which it was found that the optimum modulation frequency falls within the range of 13.085 ± 0.005 GHz for the wavelength range of between 1500-1560nm. Figure 6 shows the measured dependency of the frequency span of the OFC on the microwave detuning from its optimum frequency, from which it was confirmed that the span of the OFC did not change within the detuned frequency smaller than 0.01FSR(=19MHz). Thus, from figures 5 and 6, it is concluded that there is no significant effect of the refractive index dispersion on generating the modulation sidebands as long as the span was narrower than 10THz. Furthermore, since figure 5 shows that the change of the optimum modulation frequency at 1500-1560nm wavelength range(=frequency range of 7.7THz) falls within the tolerable range(= ± 19 MHz) given by figure 6, one can expect further increase of the span of the multiplex OFC up to 29THz by neglecting a dependence of reflectivities of the two end facets on laser wavelength.

4. LINK OF OPTICAL FREQUENCY COMBS

Since the four lasers oscillated independently, their frequency links are required to realize a frequency/phase correlated OFC. To meet this requirement, a frequency offset locking between the adjacent two OFCs was carried out. Figure 7 shows an experimental setup of the frequency offset locked loop system. In this figure, a heterodyne signal of 40MHz frequency is phase-compared with a reference oscillator of 160kHz frequency to provide an error signal used to control the current of LD1, after the signed frequency is divided by 256 by a frequency divider. Figure 8 shows a schematic explanation of a heterodyne detection between the two OFCs. In this heterodyne detection, although the heterodyne signal is superposition of many heterodyne signals between the

pairs of the nearest modulation sidebands, only modulation sideband pairs (in the ranges of A,B and C in this figure) for which the power of modulation sidebands are higher than a spontaneous emission noise level, can contribute to the detectable heterodyne signal. However, the pairs of modulation sidebands in the range of B do not contribute to the heterodyne detection because of the π -radian phase difference between the heterodyne signals generated from adjacent pairs of sidebands. Therefore, the heterodyne signals of from the ranges A and C were detected. Figure 9 shows the envelope of the two OFCs whose central frequencies are separated as large as 0.4THz. To close the frequency offset locked loop, figure 10 shows the spectrum of the stabilized heterodyne signal observed under the condition of frequency offset locking.

5.SUMMARY

A waveguide type optical frequency comb (WG-OFC) generator was developed at $1.5\ \mu\text{m}$ wavelength region by utilizing a waveguide type phase modulator. It was confirmed that the envelope of sidebands spectrum had a width of 4.3THz. For further expansion of this span of the OFC, a multiplex optical frequency comb generation system was assembled, , and modulation sidebands were generated for a span as wide as 10THz. By the heterodyne detection between two OFCs whose central frequencies are separated as large as 0.4THz, a frequency offset locking between the two OFCs was realized.

6.REFERENCES

- [1] R.E.Drullinger, K.M.Evenson, D.A.Jennings, F.R.Petersen, J.C.Bergquist, and L.Burkins, "2.5-THz frequency difference measurement in the visible using metal insulator-metal diodes," *Appl. Phys. Lett.*, vol. 42, pp. 137-138, 1983.
- [2] M.Kouroggi, N.Nakagawa, C.H.Shin,M.Teshima, and M.Ohtsu, "Accurate frequency measurement system for $1.5\text{-}\mu\text{m}$ wavelength laser diodes," in *Proc. Conf. on Lasers and Electro-Opt.*, Baltimore, paper number CThR57, May 1991.
- [3]M.Kouroggi, M.Ohtsu, "A highly accurate frequency counting system for $1.5\ \mu\text{m}$ wavelength semiconductor lasers," in *Proc, SPIE Frequency-Stabilized Lasers and Their Applications*, Boston, vol.1837, pp.205-215, November 1992.
- [4] M.Kouroggi, K.Nakagawa, and M.Ohtsu, "A wide-span optical frequency comb generator for a

highly accurate laser frequency measurement," in Proc. International Quantum Electronics Conf., Vienna, paper number TuM5, June 1992.

[5] M.Kouroggi, K.Nakagawa, and M.Ohtsu, "Wide-span optical frequency comb generator for accurate optical frequency difference measurement," IEEE J.Quantum Electron., vol.29, No.10, pp.2693-2701, October 1993.

[6] N.C.Wong, D.Lee and L.R.Brothers, "Optical frequency counting based on parametric oscillation," in Technical Digest of the International Symposium on Atomic Frequency Standards and Coherent Quantum Electronics, Nara, pp.14-17, August 1993.

[7] L.R.Brothers, D.Lee, and N.C.Wong, "Terahertz optical frequency comb generation and phase locking an optical parametric oscillator at 665 GHz," in Optics Letters, vol.19, No.4, pp.245-247, February 1994

[8] M.Kouroggi, T.Enami and M.Ohtsu, "A monolithic optical frequency comb generator," IEEE Photon. Technol. Lett., vol.6, No.2, pp214-217, February 1994.

[9] T.Saitoh, M.Kouroggi and M.Ohtsu, "A waveguide type optical frequency comb generator," IEEE Photon. Technol. Lett., in press

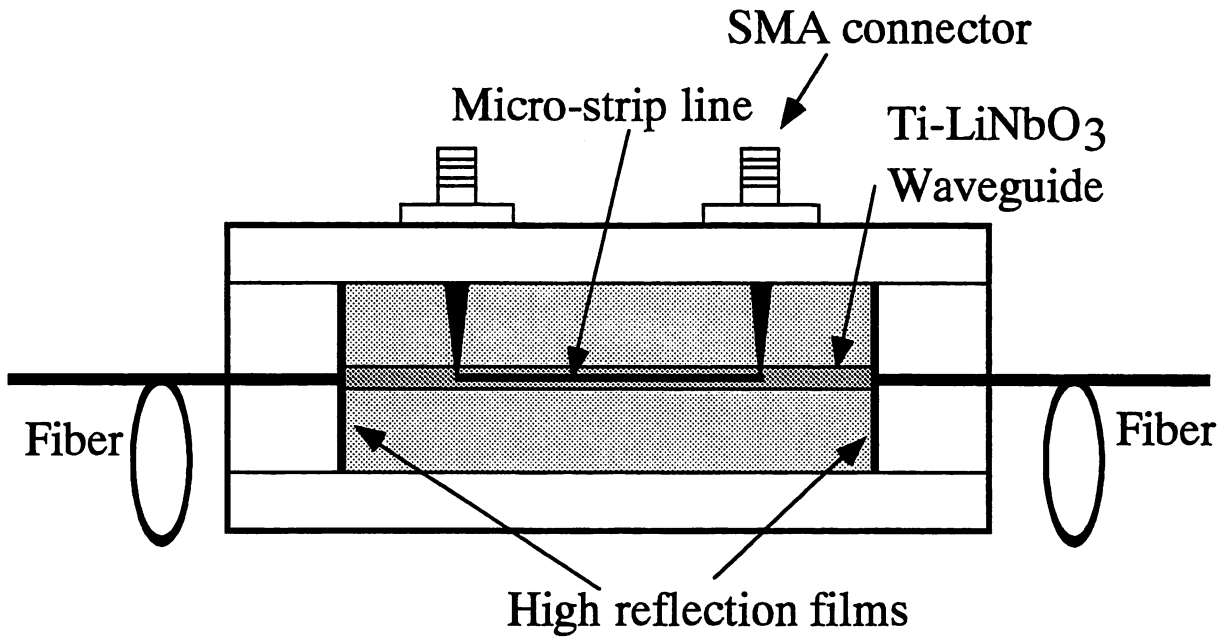


Figure 1 Schematic explanation of a WG-OCF generator

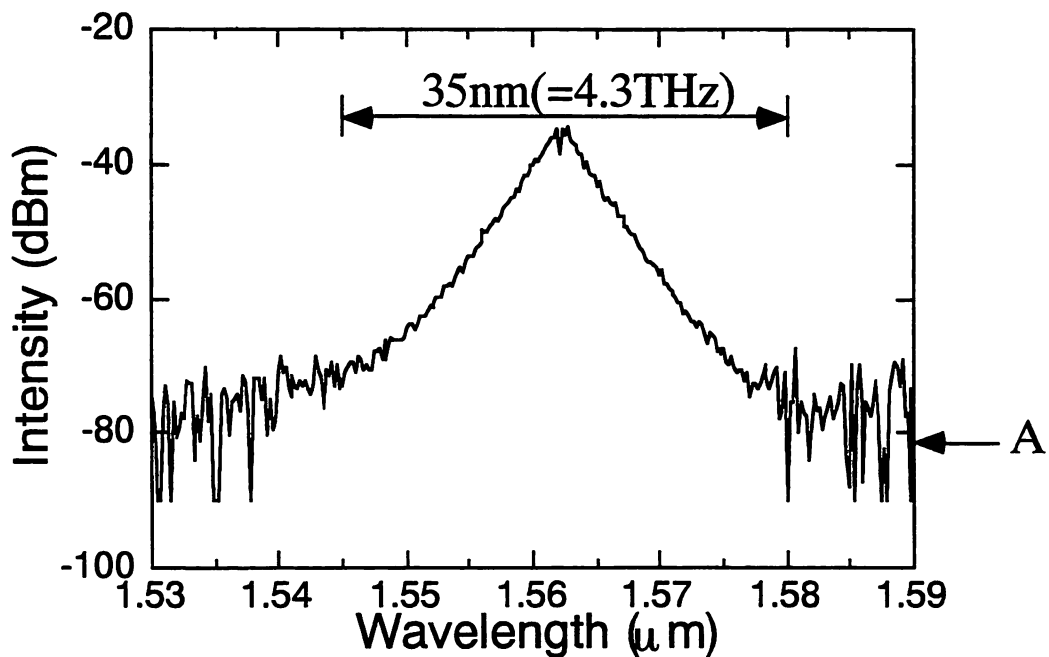


Figure 2 Envelope of the modulation sidebands measured by an optical spectrum analyzer

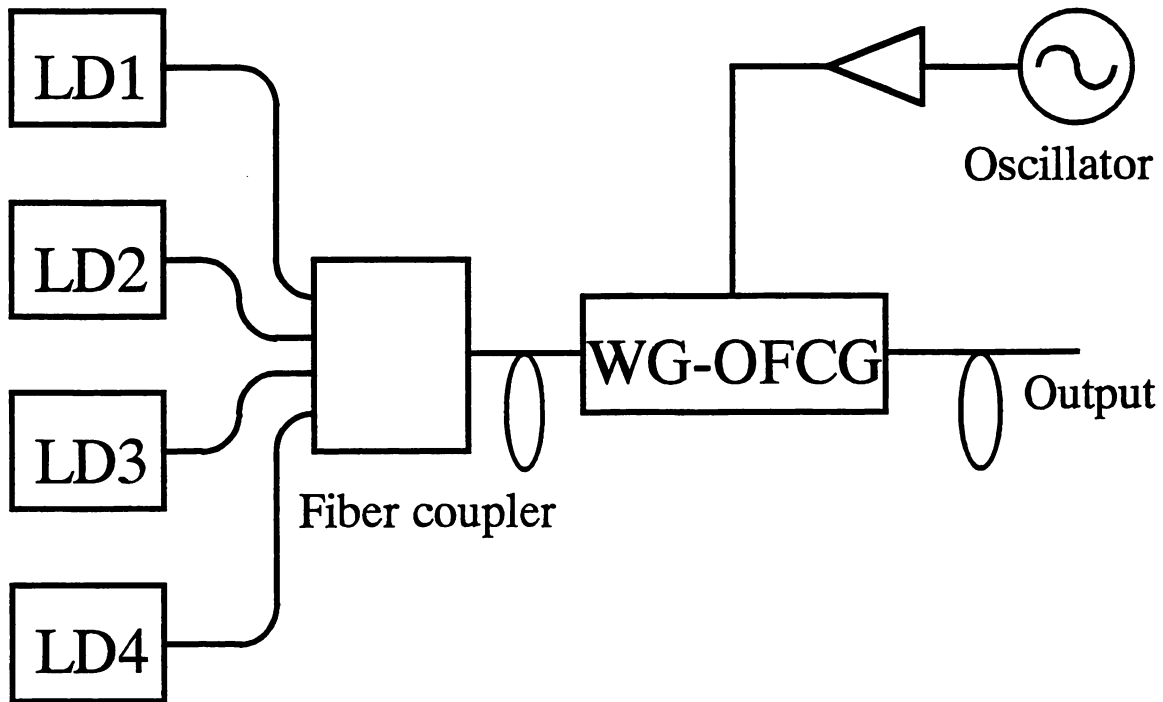


Figure3 Multiplex optical frequency comb generation system

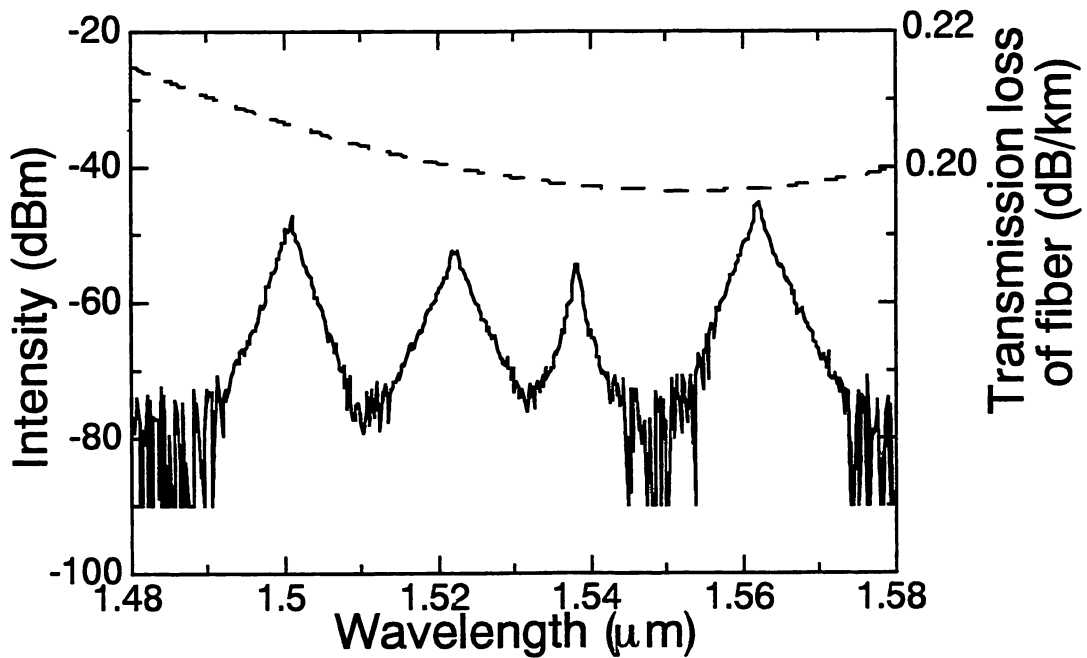


Figure 4 Envelopes of Multiplex optical frequency combs

Wavelengths of four lasers are 1.50, 1.52, 1.54 and 1.56 μm .
A broken curve represents the transmission loss of an optical fiber.

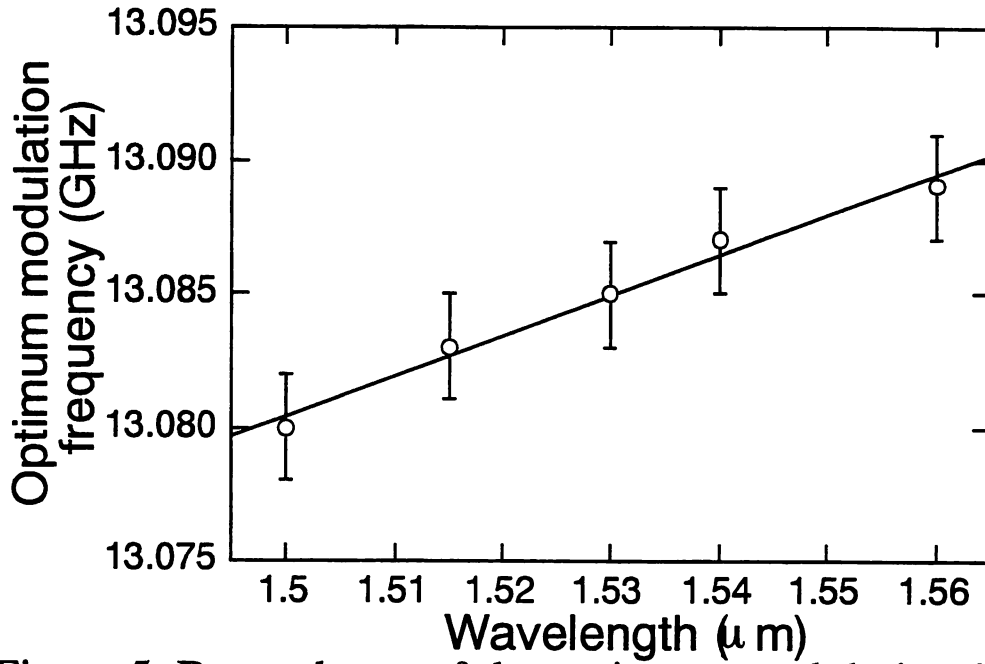


Figure 5 Dependence of the optimum modulation frequency on the optical wavelength

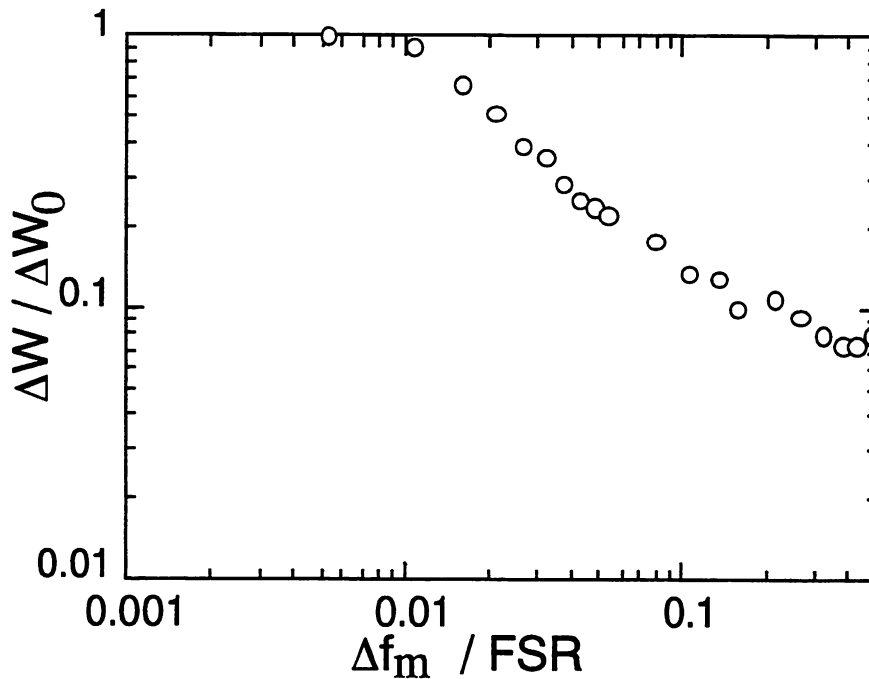


Figure 6 Dependence of the span ΔW of the OFC on a microwave detuning Δf_m from the optimum frequency

ΔW_0 : The value of ΔW at $\Delta f_m=0$.

FSR : The free spectral range of the optical resonator.

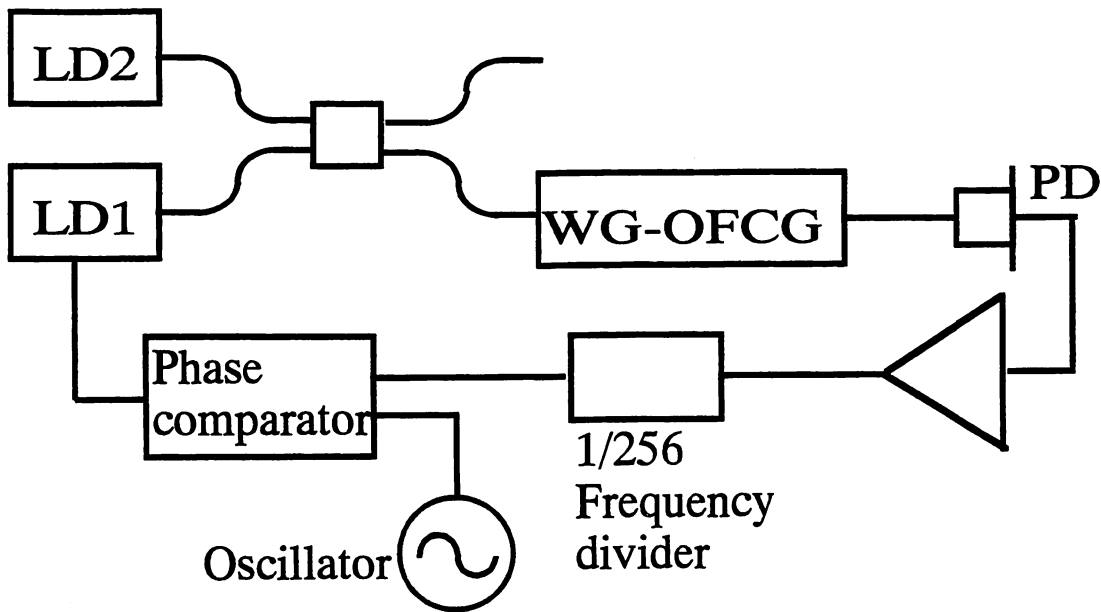


Figure 7 Frequency offset locked loop system

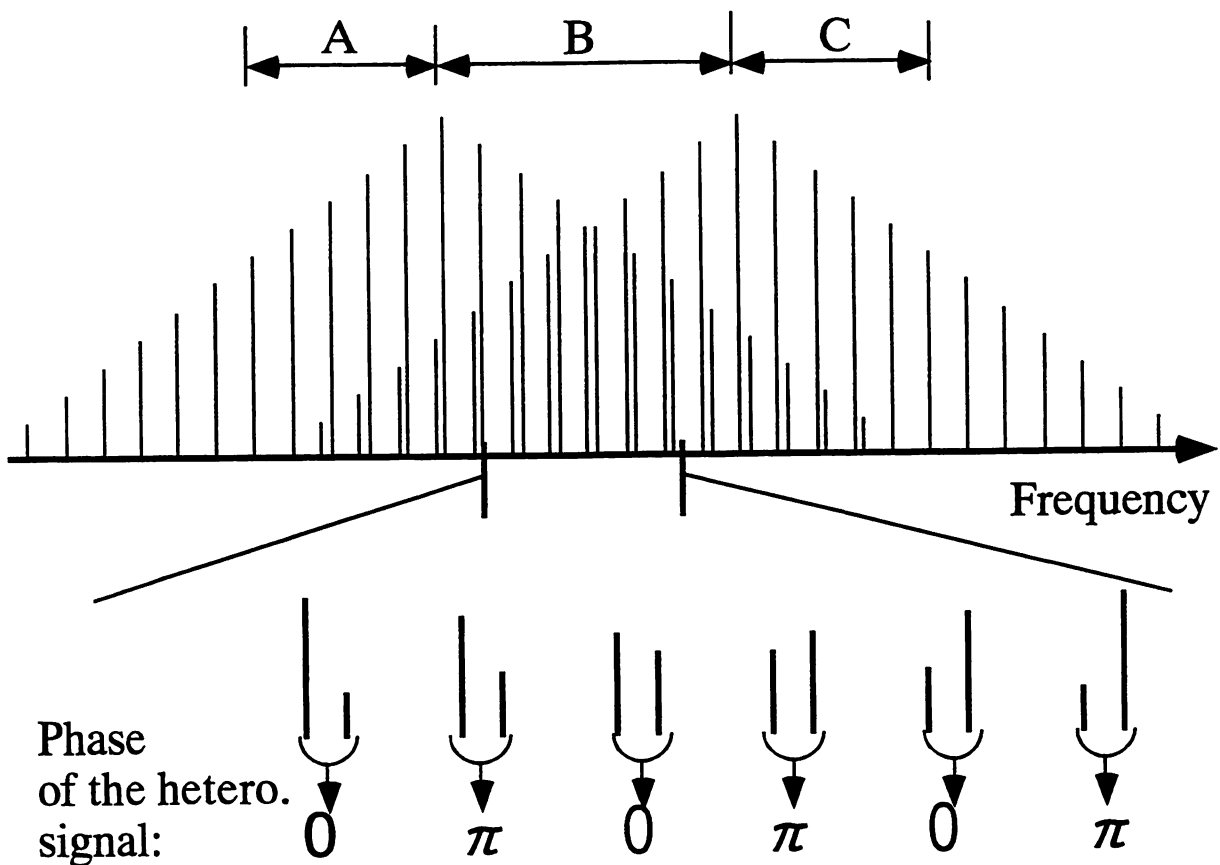


Figure 8 Schematic explanation of a heterodyne detection between two OFCs

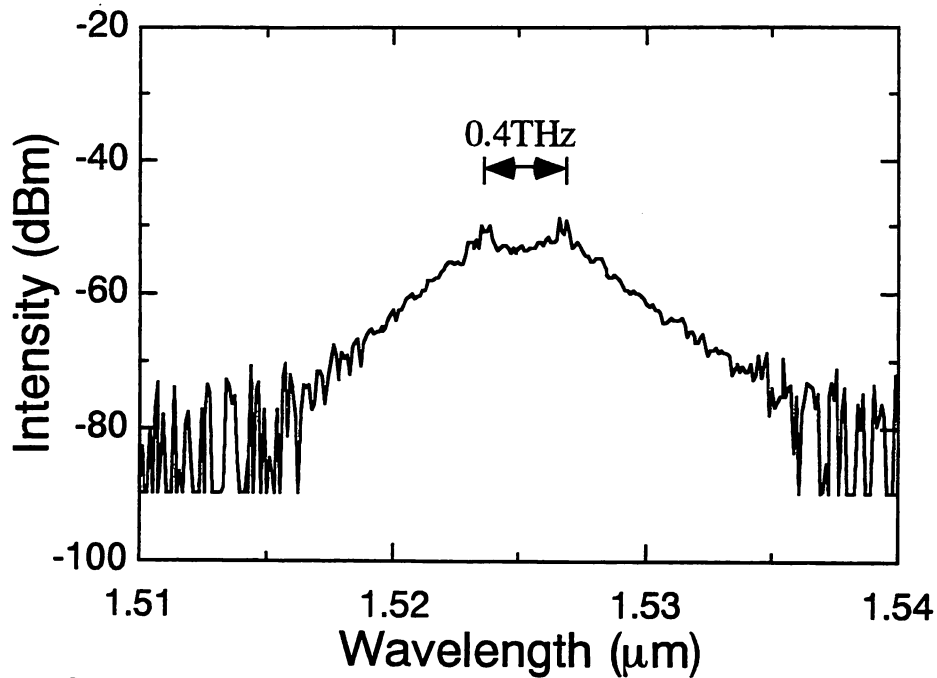


Figure 9 Envelopes of the two OFCs for heterodyne detection measured by an optical spectrum analyzer

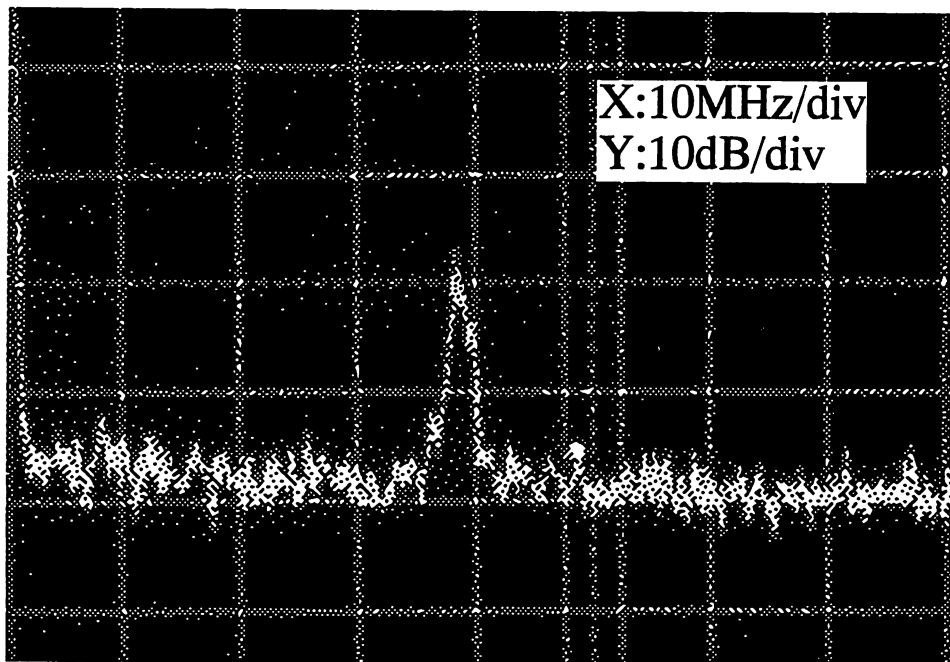


Figure 10 A heterodyne signal between two OFCs under the condition of frequency offset locking

TuJ1 (Invited)**8:30 am**

An optical-frequency comb generator for stable frequency reference grids and accurate frequency counting, M. Ohtsu,* *Graduate School, Tokyo Institute of Technology, 4259 Nagatsuta, Midori-ku, Yokohama, 227, Japan*. Performances of a monolithic cavity-type and waveguide-type optical-frequency comb generators with a span of several Terahertz are reviewed. Applications to stable frequency reference grids for a wide-range tunable-coherent diode laser systems and a novel frequency chain for accurate frequency counting are proposed.

**Photon Control Project, Kanagawa Academy of Science and Technology, Japan.*

TuJ2**9:00 am**

1.5- μm laser diode optical-frequency standards using sub-megahertz molecular saturated-absorption lines, M. de Labacherie, K. Nakagawa,* H. Sasada,** M. Ohtsu,* *On leave from LHA/CNRS, Bat. 221, Université Paris-Sud, 91405 Orsay Cedex, France. E-mail: michel@ip.titech.ac.jp*. Sub-megahertz molecular saturated-absorption lines at 1.5 μm have been obtained using 1-mW laser diodes. Such lines provide several tens of frequency discriminators with a kilohertz order sensitivity, between 1.52 and 1.56 μm . Application of such lines to laser diode high quality 1.5- μm optical-frequency standards is investigated.

Tokyo Institute of Technology, Japan;* *Keio University.*